Reactivity of Bio-Inspired Manganese-Oxygen Intermediates

By

Melissa C. Denler

Submitted to the graduate degree program in Chemistry and the Graduate Faculty of the University of Kansas in partial fulfillment of the requirements for the degree of Doctor of Philosophy.

_____

Chairperson: Dr. Timothy A. Jackson

_____

Dr. Mikhail V. Barybin

_____

Dr. James D. Blakemore

_____

Dr. David R. Benson

_____

Dr. Prajnaparamita Dhar

Date Defended: June 10, 2019

The Dissertation Committee for Melissa C. Denler
certifies that this is the approved version of the following dissertation:

Reactivity of Bio-Inspired Manganese-Oxygen Intermediates

_____
Chairperson: Dr. Timothy A. Jackson

Date approved: June 20, 2019

Abstract

Due to their ability to cycle between many stable oxidation states, Mn centers are employed by biological systems to react with oxygen and its reduced derivatives to mediate important chemical reactions. While these enzymes feature varied active-site structures, they utilize a common set of Mn-oxygen intermediates, which include oxygen ligands in the superoxo, peroxo, oxo, and hydroxo states. Taking inspiration from biology, Mn-based catalysts have been employed to perform C–H bond activation and olefin epoxidation using H_2O_2 as a cheap and environmentally-friendly oxidant. High-valent Mn-oxo centers are proposed to mediate difficult oxidation reactions for these catalysts. This dissertation focuses on the use of neutral, nitrogen-based ligands to support bio-inspired Mn^{III}-peroxo and Mn^{IV}-oxo adducts. These species are characterized with spectroscopic and computational methods, and kinetic studies are utilized to investigate reactivity with a variety of substrates.

A novel mononuclear Mn^{II} complex, $[Mn^{II}(L^7BQ)(OTf)_2]$ was shown to react with H_2O_2 in the presence of base to access a new Mn^{III}-peroxo species, $[Mn^{III}(O_2)(L^7BQ)]^+$. This intermediate was characterized by spectroscopic techniques, including electronic absorption and Mn K-edge X-ray absorption (XAS) methods. Aldehyde deformylation by $[Mn^{III}(O_2)(L^7BQ)]^+$ was only observed in the presence of acid. Aldehyde substrates often contain acid impurities that can protonate the Mn^{III}-peroxo center prior to deformylation, making it difficult to assign the reactive species.

Mn^{IV}-oxo species supported by derivatives of the N4py scaffold have allowed for direct investigation of structure-reactivity relationships. The introduction of benzimidazole moieties gave $[Mn^{IV}(O)(2pyN2B)]^{2+}$, which was characterized by electronic absorption, XAS, and electron paramagnetic resonance methods. Kinetic studies of this Mn^{IV}-oxo complex and others in the N4py

series has allowed access to a variety of equatorial field strengths. While the reactivity of Mn^{IV}-oxo centers in hydrogen atom transfer (HAT) has been studied extensively, much less is known about their oxygen atom transfer (OAT) reactivity. Recent calculations on the sulfoxidation of thioanisole by $[Mn^{IV}(O)(N4py)]^{2+}$ suggest multi-state reactivity, but there is minimal experimental evidence to evaluate this theory. Kinetic studies for the oxidation of thioanisole and its derivatives offers insights into the reaction mechanism, and how that relates to the computationally predicted multi-state reactivity pathway.

Acknowledgements

I would like to start by thanking my research advisor, Professor Tim Jackson. I will forever be grateful to you for taking me into your group. Switching research labs as a first year was a big (and scary) decision, but it was honestly one of the best decisions I have ever made. I have learned so much about the field of bioinorganic chemistry from you, and I have really enjoyed having you as a mentor.

Thank you to the NIH Chemical Biology Training Grant for allowing me to cross the gap between chemistry and biology. To all the graduate students I have interacted with on the training grant, thank you for teaching me to step outside of my field and helping me grow as a bio-inspired chemist. And to the training grant mentors, Paul, Tom and Audrey- thank you for supporting me throughout my graduate career.

I need to also thank my committee members. Professor Misha Barybin, I remember when I first considered switching research groups and your support helped solidify that joining the Jackson group was the right choice for me. I have enjoyed having you as both a professor and a mentor throughout my time at KU. Professor James Blakemore, I have appreciated speaking with you about science, graduate school and beyond. I look forward to seeing what science your group does in the coming years. To Professor David Benson, I am extremely thankful to you for the opportunities you have provided me to further my career in education. From working with you as a lecture TA to working alongside you as an instructor for Chem330, I have learned so much from you and what my values are as a future educator. Professor Prajna Dhar, thank you for serving on my defense committee as well as on my orals committee years ago, I have enjoyed having you be apart of my graduate career!

Thank you to Justin Douglas, I have learned so much about EPR from you the last few years, and I have always enjoyed talking about both science and running with you. Thank you to Sarah Neuenswander for being such a friendly and helpful person. To Victor Day, thank you for solving our crystal structures and being so helpful with writing up the science.

So much of my success has been thanks to past and current members of the Jackson group. To Hannah, you were such a strong mentor to me my first year in the Jackson group, I loved being able to be desk buddies your last year. Thank you to Derek for sharing the quiet office space with me, it was such a great time for me (sorry if I talked too much) but I learned so much from you over the years. Allyssa, I remember joining the Jackson group and being so excited to work with you. My lab bestie, I could not imagine graduate school without you. Thank you for all of the walks, weird lab moments, and of course thank you for teaching me so much in the lab. Jaycee and Liz, I am so proud of you guys, you both are great scientists, and I've enjoyed working with you. To Priya and Sam, I cannot believe your first year is coming to an end! It has been fun watching you guys get your footing in the lab and I am excited to see what work you do over the next few years. To Josh- we have been through so much together, and I know you are probably sick of me by this point, but I value having our friendship to help me get through graduate school. Abraham, your outlook on life and science is so contagious, and I really enjoy your laugh and singing voice when you are in lab. Javier, it has been great getting to know you while you do research in our lab, I wish you best of luck with your PhD. To Yuri, you are turning into such a great scientist and I have enjoyed watching you grow! I have learned so much from you as well and I am really am not sure I could have made it through the last few years without you.

To Ellie and Shannon, I have been so blessed to be able to work with you both in lab. I have loved watching you grow as scientists and I am SO PROUD of you both. I am excited to see

where you go next. To the Barybin group members, Mason, Jason and Nate, thank you for always being willing to talk about science and give advice when needed. Especially Nate, starting our PhDs together and both pursuing a future in education has been great, and I can't wait to be teaching together and giving each other pointers. To Tal, its been fun spending the last 5 years in grad school together, can't wait to meet up at future chemistry conferences! To Chris, thanks being my go-to coffee/dog-park/IKEA buddy, and for having a handsome dog for Harriet to be best friends with. To Xinyun, thank you for teaching me how to run a column, making me carry the 20L acetone drums for you, and for being a constant mentor to me throughout my graduate career. To Mary Smith, you have been someone I have looked up to since day one. You were easy to learn from and have played such a huge role in my career and personal life, thank you for helping to shape me into the scientist and person I am today.

To Andy Borovik, thank you for allowing me to spend three months in your group doing a research rotation. To the Borovik group members- Victoria, Justin, Jared, Deborah, Lisa, Sunny, Jay, Delores, Suman, Caleb- thank you for welcoming me with open arms into the group. Spending time in California was such a highlight from my graduate career. To Kelsey, I am so happy we found each other! We are mirror images, two peas in a pod, perfect friendship match (but you know Andy gets 100% credit for pairing us up!).

To my family- Mom and Dad, thank you for always answering the phone when I needed you. Thank you for supporting me in every aspect of my life, and for always being there for me. To Elizabeth, our random phone calls and FaceTime sessions are my absolute favorite. To Carly, thanks for letting me escape to Montana with you a couple times throughout graduate school and for always being a phone call or a text away.

To Harriet, thanks for all the puppy snuggles and dog park escapes when lab got to be too much. Lastly, I must thank Bryce. This has been such an adventure for us. The last five years has been a crazy roller coaster ride, but WOW it feels good to be at the end. Thank you for the kit-kats, the Nos, the Netflix binge sessions to de-stress, for being my sounding board and also my rock through all of this, and for the non-stop support you have given me in everything that I do. There is no way I would have made it through this without you, thank you for always having my back and providing me with unconditional love and support. I am so excited to see where we go next.

Table of Contents

Abbreviations and Acronyms

Abs	absorption
BDFE	bond dissociation free energy
CCA	cyclohexanecarboxaldehyde
CH_2Cl_2	dichloromethane
CT	charge transfer
CV	cyclic voltammetry
DFT	density functional theory
DHA	9,10-dihydroanthracene
EPR	electron paramagnetic resonance
ESI-MS	electrospray ionization mass spectrometry
EtBn	ethyl benzene
EtOAc	ethyl acetate
EXAFS	extended X-ray absorption fine structure
HAT	hydrogen atom transfer
HOTf	triflic acid
mCPBA	*meta*-chloroperoxybenzoic acid
MeCN	acetonitrile
MCD	magnetic circular dichroism
MLCT	metal to ligand charge transfer
Mn-LOX	manganese lipoxygenase
Mn-RNR	manganese ribonucleotide reductase
Mn-SOD	manganese superoxide dismutase
NMR	nuclear magnetic resonance
OAT	oxygen atom transfer

OEC	oxygen evolving center
OxDc	oxalate decarboxylase
OxOx	oxalate oxidase
PhIO	iodosobenzene
PPA	2-phenylpropionaldehyde
PPh_3	triphenylphosphine
PSII	Photosystem II
SSRL	Stanford Synchrotron Radiation Lightsource
TD-DFT	time dependent density functional theory
THF	tetrahydrofuran
TFE	2,2,2-trifluoroethanol
UV-Vis	ultraviolet-visible
VTVH	variable temperature variable field
XANES	X-ray absorption near-edge structure
XAS	X-ray absorption spectroscopy
XRD	X-ray diffraction
ZFS	zero field splitting

Chapter 1: Mn^{III}-Peroxo and Mn^{IV}-Oxo Intermediates in Biological and Synthetic Settings

1.1 Importance of Manganese in Biology

In nature, there are many examples of Mn-dependent enzymes, which commonly feature histidine and carboxylate residues as ligands. The redox-active Mn center allows for catalysis of important enzymatic reactions, often by reacting with molecular oxygen and its reduced derivatives (i.e. superoxide, hydrogen peroxide, and water). Mn-superoxide dismutase (Mn-SOD) protects aerobic organisms against oxidative damage by breaking down superoxide through a process known as disproportionation (forming O_2 and H_2O_2).[1] Mn-ribonucleotide reductase (Mn-RNR) also reacts with superoxide, but, in this case, plays an important role in generating a stable tyrosine radical that is required to initiate the conversion of nucleotides to deoxynucleotides, which are the precursors for DNA synthesis and repair.[2] While these enzymes both activate superoxide, the active sites for each are structurally very different. Mn-SOD utilizes a single Mn center whereas Mn-RNR utilizes a dinuclear Mn center (Figure 1.1).

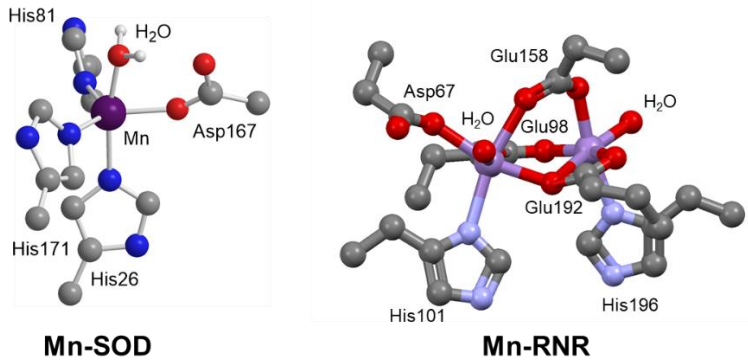

Figure 1.1. Crystal structures of the active sites for two Mn-dependent enzymes. Left: Human Mn-SOD (PDB: 1LUV) [3-4]. Right: Mn-RNR (PDB: 3N39).[2]

It is interesting to note that while each Mn-dependent enzyme found in nature possesses unique structure and function (Table 1.1), they all utilize a common set of Mn-oxygen reactive intermediates to catalyze their chemical transformations (Figure 1.2). These intermediates differ in their Mn oxidation states as well as the identity of the oxygen species bound. A few relevant

Mn-oxygen intermediates include Mn-superoxo, -peroxo, -oxo, and -hydroperoxo species (Figure 1.2).

Table 1.1. Common Mn-oxygen enzymes found in biological systems and their function.

Enzyme	Abbreviation	Biological Function
Mn-superoxide dismutase	*Mn-SOD*	Disproportionation of superoxide
Oxalate decarboxylase	*oxDc*	Decarboxylation of oxalate using O_2
Oxalate oxidase	*OxOx*	Oxidation of oxalate using O_2
Mn-ribonucleotide reductase	*Mn-RNR*	Generates tyrosine radical using superoxide
Oxygen-evolving complex	*OEC*	Splitting of H_2O
Mn-lipoxygenase	*Mn-LOX*	Oxidation of polyunsaturated fatty acids

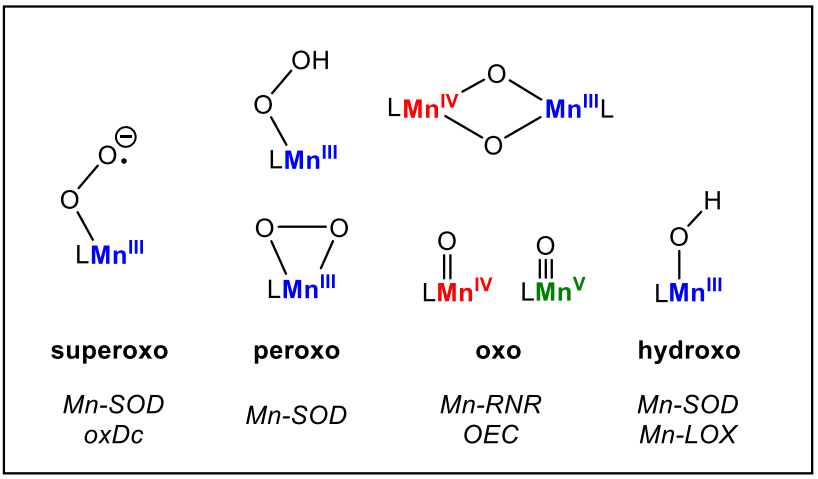

Figure 1.2. Common Mn-oxygen intermediates found in biological systems and the enzymes proposed to utilize them.

Another example of a Mn-dependent enzyme is the oxygen-evolving complex of photosystem II (OEC of PSII). This enzyme features an asymmetric Mn_4O_5Ca cubane active site that has been structurally characterized by X-ray diffraction (XRD) (Figure 1.3, left).[5] The OEC of PSII plays a key role in photosynthesis, as it is responsible for the splitting of water into protons, electrons and molecular oxygen. This enzymatic process is facilitated by the repeated oxidation of the Mn rich active site. After four oxidation reactions, and a number of proton transfer steps, the

oxygen atoms from two water molecules are converted into molecular oxygen.[6] Spectroscopic methods have been utilized to gain insight into key reactive intermediates in this transformation.[7] However, there is still much debate about the actual mechanism of water oxidation by the OEC.[8] It is commonly proposed that a high valent Mn-oxo center is important in the formation of the O–O bond central to the formation of dioxygen.[9] Towards the end of the catalytic cycle, a photooxidation of the active site produces a transient state, referred to as S_4, which presumably features an electrophilic Mn^V-oxo center (Figure 1.3, center).[10-11] In synthetic settings, Mn^V-oxo centers have been shown to be reactive for both hydrogen atom abstraction and oxygen atom transfer reactions.[12-13] While the OEC active site is surrounded by amino acid residues with a variety of C–H bonds that are susceptible to oxidation, the OEC can selectively control the reactivity of the putative Mn^V-oxo adduct to form an O–O bond through an OAT process (see Figure 1.3, right).[10]

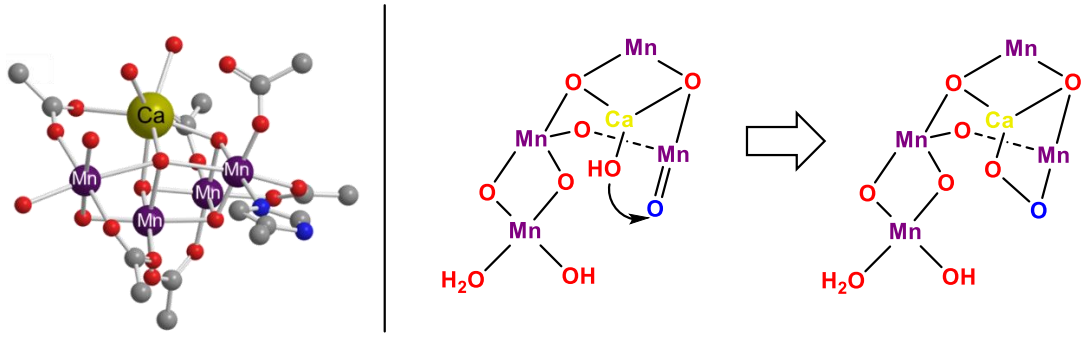

Figure 1.3. Left: Crystal structure of the resting state of the OEC of PSII, featuring a cubane active site, Mn_4O_5Ca (PDB: 3WU2).[5] Right: Hypothetical representation of the S_4 state of the active site in OEC. The arrow represents a possible route to formation of the O–O bond.

1.2 Synthetic Mn Catalysts

In organic chemistry, there is a need to develop efficient catalysts to mediate difficult oxidation reactions.[14] Specifically, there have been extensive efforts in the development of precious metal catalysts, including Pd and Pt catalysts.[15-16] These catalysts play a key role in the

refinement of crude oils and are also utilized to transform small organic molecules into pharmaceutical products.[17] Unfortunately, precious metals, by definition, lack abundance. This leads to high prices for these metals, and they also are quite toxic.[18] Alternatively, the use of first row-transition metals in catalysis provides several advantages. Because they are much more abundant compared to precious metals, they are much lower in cost, and they also have reduced toxicity, making them an environmentally friendly alternative.[18]

Taking cues from Mn-dependent enzymes that react with oxygenic substrates to facilitate critical transformations, synthetic chemists have turned to Mn-based catalysts to mediate oxidation reactions including epoxidation, hydroxylation, and alcohol oxidation.[19] With the use of an external oxidant, Mn-based catalysts have been shown to perform selective oxidation reactions. While simple soluble Mn salts such as $MnSO_4$ exhibit catalytic reactivity,[20] the use of nitrogen-based supporting ligand scaffolds can greatly enhance reactivity and selectivity.[21] Additionally, utilization of a cheap and environmentally friendly oxidant like H_2O_2 greatly increases the economic efficiency for these Mn-based catalysts.[22]

Activation of H_2O_2 by Mn-based catalysts is generally assumed to follow the peroxide-shunt pathway of the heme paradigm, as outlined in Figure 1.4. If starting from Mn^{II}, the cycle is initiated by 0.5 equivalent of H_2O_2 to give a Mn^{III} center. The binding of H_2O_2 gives a Mn^{III}-hydroperoxo species that is an acid/base equilibrium with the corresponding Mn^{III}-peroxo species. When protonated, the O–O bond of the peroxide is activated for heterolytic cleavage, expelling water and a reactive Mn^{V}-oxo species, which is proposed to serve as the active species in the catalytic oxidation reaction. Following reactivity with substrate, the Mn-species is converted back to the starting Mn^{III} center, thus allowing for catalytic oxidation.

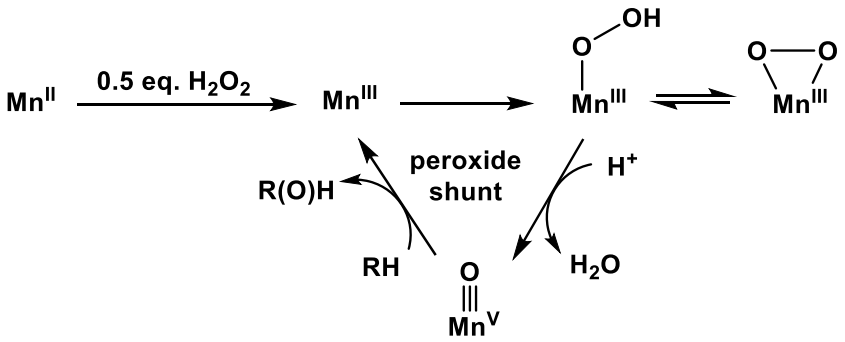

Figure 1.4. Proposed activation of H_2O_2 for Mn-based catalysts.

Manganese porphyrin complexes with H_2O_2 as a terminal oxidant have been extensively used for olefin epoxidation.[23] The tunability of porphyrins allows for extensive synthetic manipulation, which in turn can greatly affect reactivity. The robustness of these catalysts has been enhanced by the chlorination of the *meso*-positions, thus reducing catalyst decay, and also increasing catalytic efficiency.[24] On their own, these Mn porphyrin catalysts are unable to act efficiently in activating H_2O_2. However, through the addition of base or acid additives, reactivity is enhanced.[25-27]

Upon the addition of imidazole to Mn-based porphyrin catalysts and H_2O_2, higher reactivity and selectivity was observed for olefin epoxidation.[25-26] Specifically, the epoxidation of styrene by Mn(TPP)(Cl), Mn(TMP)(Cl), and Mn(TDCPP)(Cl) (where TPP = tetraphenylporphyrin, TMP = tetramesitylporphyrin, and TDCPP = tetra-2,6-dichlorophenylporphyrin) were investigated with varied amounts of imidazole. The experimental results showed that imidazole is required to facilitate the epoxidation of styrene (Table 1.2).[25] The importance of heterocyclic bases in the activation of H_2O_2 by Mn-based porphyrin catalysts could be attributed to their ability to coordinate to the Mn center axial to the peroxo adduct, thus activating the O–O bond for cleavage.

Table 1.2. Styrene epoxidation with 30% H_2O_2 in the presence of Mn-porphyrin catalysts and imidazole.

Catalyst	Equiv. of imidazole[a]	Styrene conversion (%)[b]	Styrene epoxide yield (%)[b]
No catalyst	0.6	ND	1
Mn(TPP)(Cl)	0.6	58	45
Mn(TMP)(Cl)	0.6	83	80
Mn(TMP)(Cl)	0	ND	1
Mn(TDCPP)(Cl)	0.6	100	93
Mn(TDCPP)(Cl)	0.1	ND	50
Mn(TDCPP)(Cl)	0	ND	1

[a]Compared to styrene. [b]Determined based on starting amount of styrene. Ligand abbreviations are as follows: TPP = tetraphenylporphyrin), TMP = tetramesitylporphyrin, and TDCPP = tetra-2,6-dichlorophenylporphyrin. Table created with data from reference [25].

The addition of carboxylic acids in H_2O_2 alkene epoxidation was also found to enhance reactivity for Mn(TDCPP)(Cl).[27] An important observation from this work was that the addition of an axial ligand, in this case a heterocyclic base, and a carboxylic acid were both required to facilitate alkene epoxidation (Table 1.3). The addition of benzoic acid provided the fastest conversion time for the H_2O_2 epoxidation of cyclooctene. It is proposed that the carboxylic acid serves to protonate the Mn^{III}-peroxo species and activate it for heterolytic cleavage of the O–O bond, thus enhancing the rate of alkene epoxidation.[27]

Table 1.3. Alkene epoxidation with 30% H_2O_2 and Mn(TDCPP)(Cl)

Alkene	H_2O_2[b]	Benzoic acid[b]	Conversion (%)	Epoxide yield (%)	Rxn time (min)
Cyclooctene	2	0.005	100	100	10
Dodec-1-ene	2	0.005	78	76	15
Dodec-1-ene	2	0.02	96	92	15
Trans-oct-4-ene	2	0.02	75	54	15
Trans-oct-4-ene	4	0.04	90	63	15

[a]Reaction conditions: at 0°C and pH 4.5-5.0 in CH_2Cl_2, with Mn(TDCPP)(Cl) (0.5 mol %), N-hexylimidazole (0.5 mol%). [b]Mol equiv. compared to alkene substrate.

Quici and co-workers designed a Mn-based porphyrin catalyst for H_2O_2 activation with a doubly tailed porphyrin, where they introduced functionality to alleviate the need for added acid and base to enhance epoxidation (Figure 1.5).[28] Their catalyst design allowed for the introduction

of a covalently-linked axial imidazole ligand that can bind the metal center and allow for a push effect, where electron density can be increased on the metal center, in turn stabilizing high-valent Mn-oxo centers.[29] They found that the covalent introduction of the carboxylic acid group to the porphyrin provided similar results compared to those where benzoic acid is introduced externally, suggesting they successfully designed a self-contained catalyst for H_2O_2 alkene epoxidation.[28]

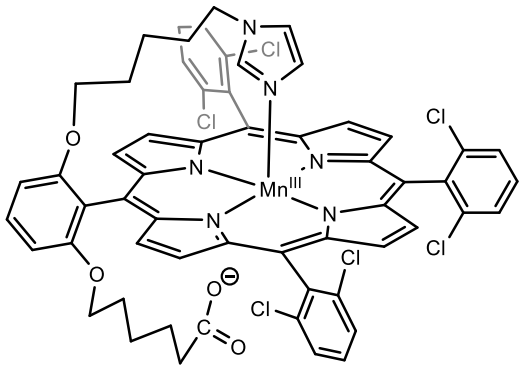

Figure 1.5. Porphyrin catalyst featuring an imidazole and a carboxylate group, connected through the 2 and 6 positions of the *meso*-aryl group.[28]

Nam and coworkers found that the reaction of $[Mn^{III}(TF_4TMAP)](CF_3SO_3)_5$ (TF_4TMAP = *meso*-tetrakis(2,3,5,6-tetrafluoroN,N,N-trimethyl-4-aniliniumyl)porphyrinato^{2-}) and H_2O_2 at pH 10.5 in an aqueous solution yielded a Mn^V-oxo species, which was characterized by electronic absorption and electron paramagnetic resonance (EPR) methods.[30] If an electron-withdrawing acylperoxide was used in place of H_2O_2, the same Mn^V-oxo species was observed. In contrast, a Mn^{IV}-oxo species was formed if $[Mn^{III}(TF_4TMAP)](CF_3SO_3)_5$ was treated with an electron-donating alkylperoxide. Together, these observations suggest that the identity of the peroxide substituent plays a role in the mechanism of O–O activation. Specifically, electron-withdrawing groups facilitate homolytic O–O bond cleavage to give a Mn^{IV}-oxo product, while electron-

donating groups facilitate heterolytic O–O bond cleavage to give a Mn^{V}-oxo product (Figure 1.6). In addition to different spectroscopic signatures, the Mn^{V}-oxo and Mn^{IV}-oxo intermediates exhibited very different reactivities with alkenes. The Mn^{V}-oxo species was found to be an efficient epoxidizing agent, whereas the Mn^{IV}-oxo species was unable to perform epoxidation.[30] To investigate the pH dependence for the activation of H_2O_2 by $[Mn^{III}(TF_4TMAP)](CF_3SO_3)_5$, Nam and co-workers also examined alkene epoxidation for a pH range of 3 to 11.[30] For the reaction of $[Mn^{III}(TF_4TMAP)](CF_3SO_3)_5$ with H_2O_2 in the presence of *cis*-stilbene, olefin epoxidation was observed at higher pH, but if the pH was below 7, no *cis*-stilbene oxide product was formed. These observations suggest that the lower the pH changed the O–O bond activation mechanism to homolytic cleavage, thus accessing a Mn^{IV}-oxo species that was unable to perform epoxidation (Figure 1.6).[30]

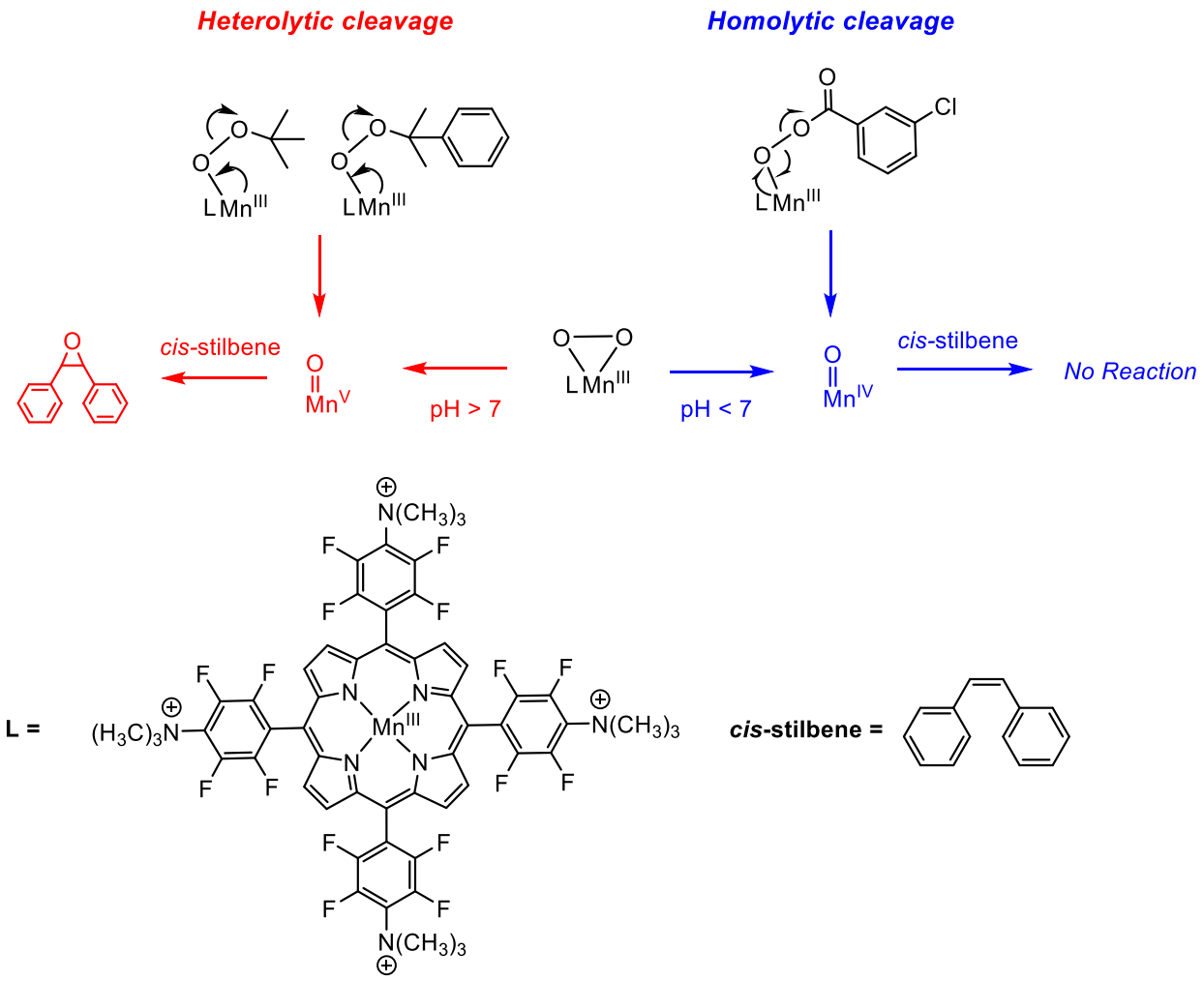

Figure 1.6. Possible mechanistic pathways for the O–O bond cleavage of Mn^{III}-peroxo centers

Stemming beyond porphyrin scaffold systems, Mn-based catalysts supported by bioinspired, non-porphyrin ligands have also been used as efficient catalysts for substrate oxidation reactions with H_2O_2 (Figure 1.7).[31] These catalysts have been shown to perform asymmetric epoxidation, selective C–H bond hydroxylation, and chemoselective oxidation of allylic olefins (i.e. either olefin epoxidation or alcohol oxidation) (Figure 1.7). Similar to what has been observed for Mn-based porphyrin catalysts, the use of external additives, including acids, bases, and axial

ligands, serve an important role in improving product yields, as well as stereo- and regioselectivity.[32]

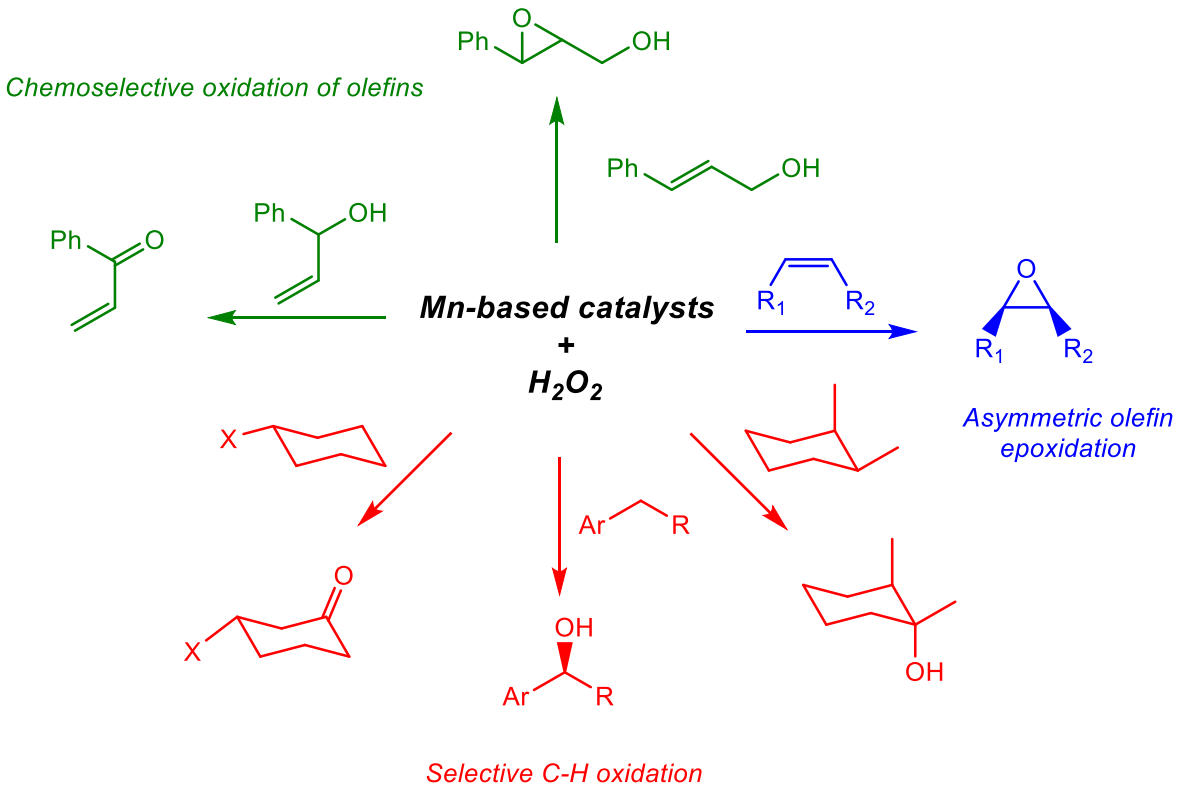

Figure 1.7. A handful of selective oxygenation reactions that Mn-aminopyridine catalysts have been able to mediate with H_2O_2.

Salen-based ligands developed in the 1990s to support Mn-centers showed promise for asymmetric epoxidation, but often exhibited low efficiency, and used toxic oxidants, such as hypochlorites (Figure 1.8, Ligand **1**).[33] Structurally similar to the salen scaffold is the β-ketoiminato-based ligand scaffold (Figure 1.8, Ligand **2**), which showed complementary catalytic activities and the ligand design allowed for structural manipulation.[34] More recently, tremendous advancements have been made in asymmetric epoxidation reactions of olefins by Mn-aminopyridine complexes.[35] In 2003, Stack *et al.* were able to generate an efficient Mn-catalyst for epoxidation of olefins using ligands **3** and **4** (Figure 1.8). In this system, peracetic acid was

used as an additive. The ability of these catalysts to perform asymmetric epoxidation was not reported.[36]

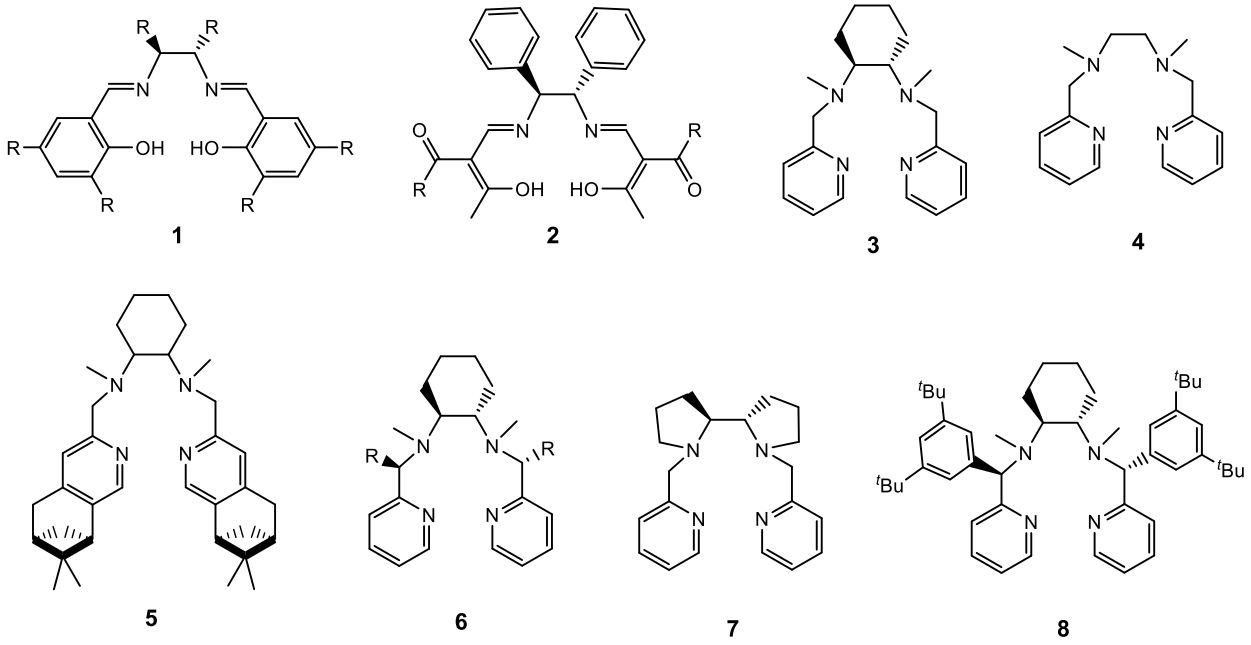

Figure 1.8. Structures of a few selected scaffold types used to support Mn-catalysts for asymmetric epoxidation and hydroxylation reactions with H_2O_2.[19, 33-35, 37-40]

In 2007, Costas and co-workers took the first step towards asymmetric epoxidation with Mn-based catalysts supported by chiral pinene-appended ligands, which were able to perform epoxidation by peracetic acid and PhIO for several alkenes (Figure 1.8, Ligand **5**).[19] Soon after, Sun and co-workers designed a series of chiral ligands, allowing for low catalyst loading and high enantioselective epoxidation (Figure 1.8, Ligand **6**).[37] Bryliakov and co-workers contributed to this ligand type with their design of a 2,2'-bipyrrolidine based ligand (Figure 1.8, Ligand **7**).[38] These scaffolds served as a jumping off point, with new ligands bearing tetradentate scaffolds with various modifications, including new chiral backbone designs, the introduction of various *N*-donor ligands in place of the pyridine moieties, and the introduction of steric bulk to effect reactivity.[35]

These examples highlight some of the breakthrough work that has been done in the field of Mn-based catalysts, specifically for the asymmetric epoxidation of olefins.[31, 35, 41-42]

The use of excess carboxylic acids is a common requirement for Mn-based catalysts to facilitate O–O bond cleavage in H_2O_2 activation, but recent efforts have been made to improve these reaction conditions. Nam and Sun recently reported on the asymmetric epoxidation of olefins by two Mn-centers supported by tetradentate N4 ligands (Figure 1.8, Ligands **6** and **8**).[39-40] In place of excess carboxylic acid, efficient substrate oxidation was observed with catalytic amounts of sulfuric acid.[39-40] While this decrease in the amount of acid required for efficient catalytic reactivity represents an improvement to the field, these results help to highlight the fact that external additives still play a crucial role in improving the activation of H_2O_2 by Mn-based catalysts.

Because there are many competing factors in controlling O–O bond cleavage for H_2O_2 activation reactions, it is not possible to propose a common mechanism for all catalytic systems. However, it is assumed that accessing a high-valent Mn-oxo center allows for these oxidation reactions. Therefore, it can be insightful to directly investigate these Mn-oxo centers to gain insight into their structure and electronic properties, which allow for better understanding of what makes an efficient oxidant in these types of transformations.

1.3 Mn-Peroxo Centers

Given their proposed importance in both synthetic and biological settings, model complexes of Mn^{III}-peroxo species have received much attention in the literature.[43] Common oxidants utilized to access Mn^{III}-peroxo intermediates include molecular oxygen, potassium superoxide, aqueous H_2O_2, and anhydrous H_2O_2. Metal-peroxo adducts feature two binding modes,

side-on (η^2) or end-on (η^1). To date there is no spectroscopic evidence for formation of end-on Mn^{III}-peroxo species, but rather all reports have been for side-on Mn^{III}-peroxo intermediates. Since the first side-on Mn^{III}-peroxo species was characterized by XRD in 1987,[44] six additional Mn^{III}-peroxo XRD structures have been reported.[45-50] Excluding these few examples, most Mn^{III}-peroxo model complexes are difficult to obtain in solid state due to their impaired thermal stability.[43] A majority of the other reported Mn^{III}-peroxo species have been synthesized under cryogenic conditions and have been characterized with a combined approach using both spectroscopic and computational methods.[43, 51-64] A selection of reported Mn^{III}-peroxo species are included in Figure 1.9.

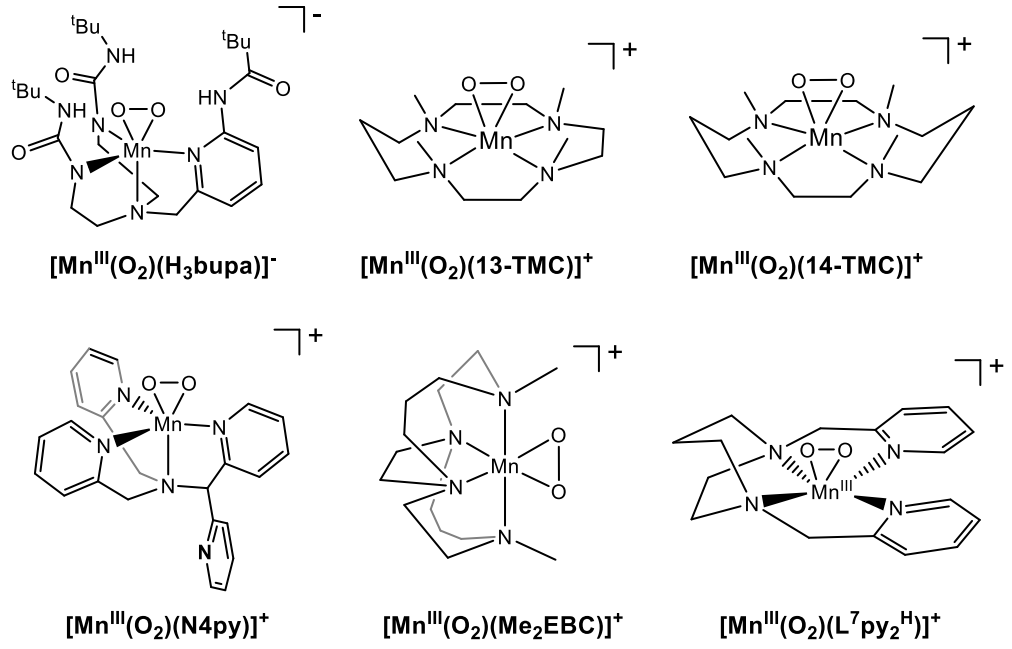

Figure 1.9. Structures of selected η^2-Mn^{III}-peroxo species.[47-48, 53, 56, 58-59, 61, 64]

Based on the handful of crystal structures reported for side-on Mn^{III}-peroxo species, Mn–O bond distances range from 1.84 – 1.90 Å, and O–O bond distances range from 1.40 – 1.43 Å.[43]

As an alternative to solid-state characterization, solution state Mn K-edge X-ray absorption (XAS) can be used to gain insight into Mn-ligand bond distances. Specifically, through analysis of the extended X-ray absorption fine structure (EXAFS) data, structural parameters for several Mn^{III}-peroxo species has been reported. In the case of $[Mn^{III}(O_2)(13\text{-TMC})]^+$ and $[Mn^{III}(O_2)(Me_2EBC)]^+$, EXAFS analysis revealed Mn–O bond distances of 1.88 and 1.86 Å, respectively, which are in excellent agreement with those Mn–O distances determined from XRD.[64-65]

Electronic absorption spectra for Mn^{III}-peroxo adducts typically exhibit weak features between 680 nm and 415 nm, with extinction coefficients between 60 M^{-1} cm^{-1} and 490 M^{-1} cm^{-1}. With the help of magnetic circular dichroism (MCD) and time-dependent density functional theory (TD-DFT) calculations, detailed investigations allowed for the spectral assignments of these weak features specifically for $[Mn^{III}(O_2)(L^7py_2^H)]^+$.[53] The two main features in the visible region were attributed to a peroxo-to-metal charge transfer (CT) transition (445 nm) and a Mn^{III} d-d ligand-field excitation (590 nm). Vibrational techniques have also helped to characterize several Mn^{III}-peroxo species. Unfortunately, resonance Raman experiments have proved difficult due to sample degradation upon irradiation with the laser.[49, 51] However, there are a few ν_{O-O} data reported from infrared spectroscopy, and these range from 885 – 892 cm^{-1}.[45-46, 56, 66]

To gain insight to the ground-state electronic structure, the ground-state spin Hamiltonian parameters have been determined for a handful of Mn^{III}-peroxo species. Specifically, parallel-mode X-band EPR experiments show six-line signals centered near 80 mT, exhibiting hyperfine splittings of 5.7 to 6.9 mT.[51-52, 61] Additionally, the zero-field splitting (ZFS) parameters for η^2-Mn^{III}-peroxo species exhibit *D* values between -1 to -2 cm^{-1}.[51-54 55-56, 58, 61, 66]

In addition to their unique structural and spectroscopic properties, Mn^{III}-peroxo species serve important roles for chemical transformations in biological and synthetic settings. In nature,

Mn-SOD is proposed to access a product-inhibited Mn^{III}-peroxo complex at high superoxide concentrations.[67] This species can slowly re-enter the catalytic cycle for disproportionation. Following the binding of superoxide, acid-promoted Mn–O bond cleavage releases H_2O_2 and a Mn^{III} center, resulting in reduction of superoxide.[4] In contrast to this enzymatic system, activation of H_2O_2 by synthetic Mn^{II} catalysts is proposed to be achieved by O–O bond cleavage to yield high-valent Mn-oxo species, as described in the previous section. The differences in reactivity observed for biological and synthetic systems has encouraged the investigation of what factors control O–O versus Mn–O bond cleavage for Mn^{III}-peroxo species.

Synthetic Mn^{III}-peroxo species have also been shown to perform aldehyde deformylation.[68] However, the mechanism for deformylation is not fully understood.[47-48, 54-56] Through the utilization of *para*-substituted benzaldehyde derivatives, the presence of electron-poor derivatives lead to faster decay of Mn^{III}-peroxo adducts, suggesting the mechanism follows a nucleophilic attack of substrate.[48, 54] Additionally, the aldehyde deformylation of cyclohexanecarboxyaldehdye (CCA) by metal-peroxo and metal-superoxo species has received much attention, allowing for a benchmark substrate to compare aldehyde deformylation reactivity between complexes.[47-48, 54, 56]

In addition to being nucleophilic, Mn^{III}-peroxo species have also been shown to act as hydrogen-atom acceptors.[56, 69] Specifically, Sastri and co-workers investigated the reactivity of a Mn^{III}-peroxo species supported by an amino-pyridyl ligand with 2-phenylpropionaldehyde (PPA).[69] They provide evidence suggesting that aldehyde deformylation of PPA by the Mn^{III}-peroxo species follows an initial hydrogen atom abstraction mechanism (Figure 1.10, left). Upon introduction of deuterium to the α-carbon, they observed a KIE of 5.4, suggesting abstraction of the C–H bond is a part of the rate determining step for aldehyde deformylation.[69] They were also able to perform a radical trapping experiment, allowing them to capture the PPA organic radical,

suggesting a hydrogen-atom abstraction step.[69] However, it must also be noted that this substrate may also be prone to nucleophilic attack by Mn^{III}-peroxo centers (Figure 1.10, right), making it difficult to pinpoint a single mechanistic pathway for all ligand systems.

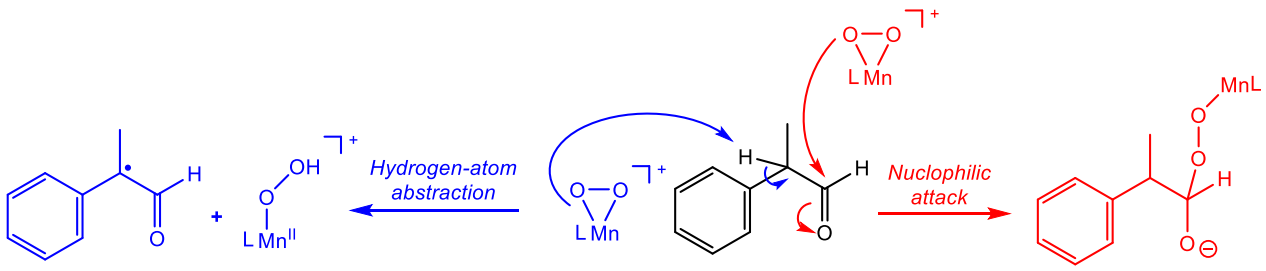

Figure 1.10. Possible mechanisms for aldehyde deformylation by Mn^{III}-peroxo species.

To complicate aldehyde deformylation by Mn^{III}-peroxo species further, aldehyde substrates often inherently contain small amounts of the corresponding carboxylic acid.[70] These acid impurities can be an issue because metal-peroxo species can be protonated. Further highlighting the sensitivity of metal-peroxo species to acid, Nam and co-workers have recently reported on the conversion of the η^2-Mn^{III}-peroxo species, $[Mn^{III}(O_2)(14\text{-TMC})]^+$ and $[Mn^{III}(O_2)(13\text{-TMC})]^+$ (where 14-TMC = 1,4,8,11-tetramethyl-1,4,8,11-tetraazacyclotetradecane and 13-TMC = 1,4,7,10-tetramethyl-1,4,7,10-tetraazacyclotridecane), to the corresponding η^1-Mn^{III}-hydroperoxo species, $[Mn^{III}(OOH)(14\text{-TMC})]^+$ and $[Mn^{III}(OOH)(13\text{-TMC})]^+$ by the addition of $HClO_4$ (Figure 1.11). The Mn^{III}-hydroperoxo species could be converted back to the Mn^{III}-peroxo complex through the addition of triethylamine.[65, 71] Formation of the Mn^{III}-hydroperoxo centers is rapid, and kinetic investigations with CCA support that these centers are more reactive than their Mn^{III}-peroxo counterparts.[65, 71] These observations suggest that acid impurities present in aldehyde substrates could easily protonate metal-peroxo species, resulting in confused reactivity. Therefore, kinetic analysis with the use of aldehydes must be done with

caution, as identifying the reactive center responsible for reactivity can be difficult due to the acid impurities present in aldehyde substrates.

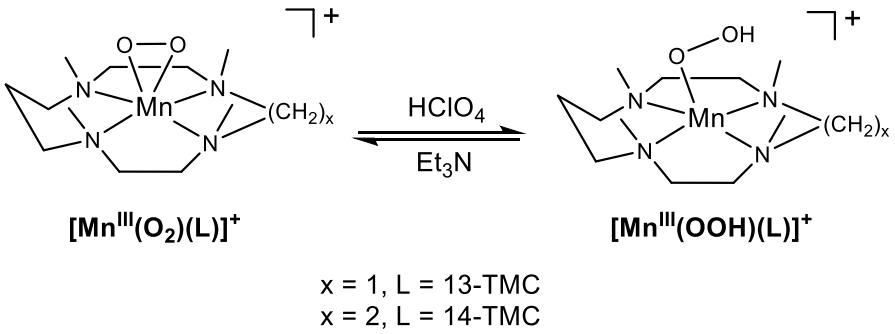

Figure 1.11. Reversible conversion of TMC-supported Mn^{III}-peroxo species to the corresponding Mn^{III}-hydroperoxo species through proton transfer reactions.

1.4 Mn-Oxo Centers

While activation of H_2O_2 by Mn-based catalysts is proposed to utilize high valent Mn-oxo species for substrate oxidation, it can be difficult to trap and characterize these important intermediates. The peroxide shunt pathway (described in an earlier section) suggests that the Mn-center is cycling through several oxidation states as it activates H_2O_2 and performs substrate oxidation. The presence of multiple Mn centers in different oxidation states complicates trapping and characterization of Mn-oxo intermediates. Alternatively, these Mn-oxo centers can be generated in high yields using oxygen-atom transfer reagents in the absence of substrate to allow for spectroscopic characterization. [57, 72-85] Supporting ligand scaffolds can be designed specifically to enhance stability of reactive centers, allowing them to be trapped. Unfortunately, ligand design is often a balancing act, because enhancement of stability can also result in reduced reactivity.[86]

High-valent Mn-oxo centers can be accessed directly through the addition of O-atom transfer agents, including ArIO and NaOCl, to starting Mn^{II} and Mn^{III} species to give Mn^{IV}-oxo and Mn^{V}-oxo species, respectively.[30, 72] These centers can be generated in high yields, allowing

for characterization with a variety of techniques. In contrast to the analogous Fe^{IV}-oxo systems that have been extensively characterized by XRD,[87-88] there is currently a single crystal structure reported for a Mn^{IV}-oxo complex. The structure of $[Mn^{IV}(O)(ditox)_3]^-$ was reported by Halbach *et al.* in 2018, and the all anionic oxygen ligand framework serves to stabilize the Mn-center, allowing for XRD characterization (Figure 1.12). Unfortunately, this stability also leads to decreased HAT reactivity compared to other Mn^{IV}-oxo complexes.[77]

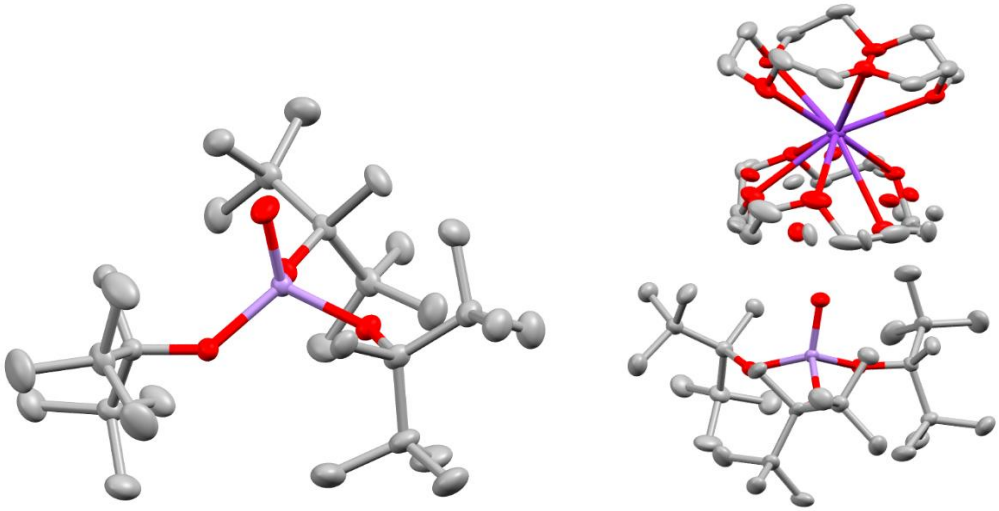

Figure 1.12. X-ray crystal structure of $[Mn^{IV}(O)(ditox)_3]^-$, where ditox = $^tBu_2MeCOH$.[77] Left: Anionic portion of the crystal structure. Right: Anionic and cationic portions of the crystal structure.

Focusing solely on non-porphyrin ligand scaffolds, there are several Mn^{IV}-oxo species reported in the literature (Figure 1.13). While none of these species have been characterized by XRD characterization, structural parameters for many of these species have been obtained from analysis of Mn K-edge XAS data. Analysis of the EXAFS data reveal Mn–O bond distances for several Mn^{IV}-oxo species that range from 1.58 to 1.74 Å. [73-75, 78-80] Typically these values are in good agreement with the distances determined from density functional theory (DFT) calculations.

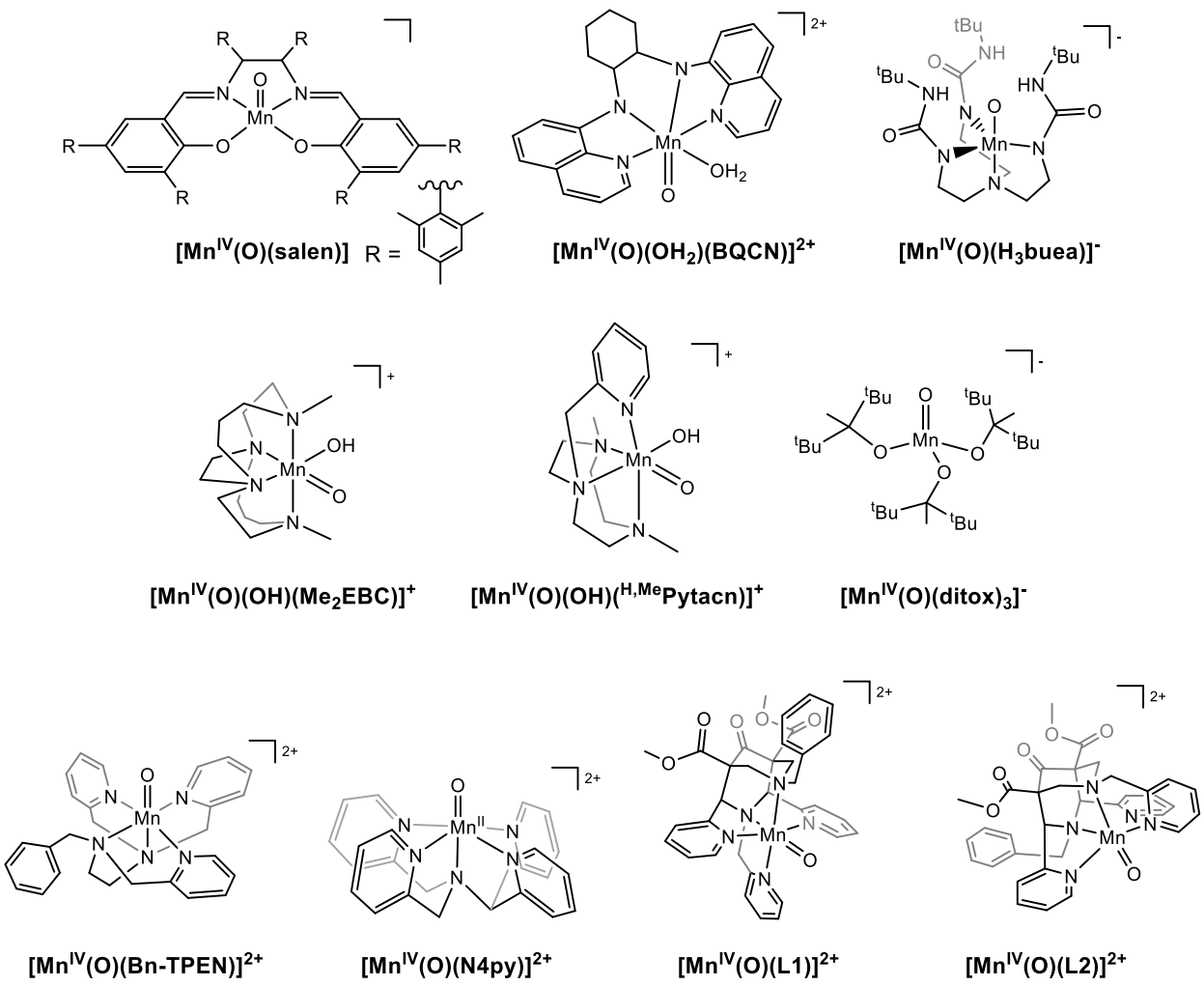

Figure 1.13. Molecular structures for Mn^{IV}-oxo species.[57, 72-85] While only the XRD structure for $[Mn^{IV}(O)(ditox)_3]^-$ has been reported, the remaining structures are inferred from spectroscopic techniques as well as DFT computations (for some complexes). L1 and L2 represent bispidine ligands from reference [81].

In addition to their unique structural and spectroscopic properties, Mn^{IV}-oxo species have also been shown to be useful for substrate oxidation, performing both hydrogen and oxygen atom transfer reactions.[72-76] Synthetic Mn^{IV}-oxo complexes can be used specifically to gain insight into Fe-dependent enzymes that utilize analogous Fe^{IV}-oxo centers for their oxidation reactions. It has long been assumed that the mechanism of Mn^{IV}-oxo and Fe^{IV}-oxo species are similar. Mechanistic insight into the hydrogen atom transfer (HAT) reactivity of synthetic Mn^{IV}-oxo complexes can be

compared to enzymatic systems, such as taurine/α-ketoglutarate dioxygenase (TauD), which utilizes an Fe^{IV}-oxo center to abstract a C–H bond from the small molecule taurine to initiate the elimination of sulfite, which serves as a source of sulfur.[89-90]

The set of non-porphyrinic Mn^{IV}-oxo species reported in the literature feature very diverse ligand frameworks (Figure 1.13), which gives rise to different coordination numbers, overall complex charges, as well as complex geometries.[57, 72-85] Unfortunately, the large variations in supporting ligand structures makes it difficult to rationalize observed reactivity trends. However, the use of neutral, pentadentate ligand scaffolds in the case of $[Mn^{IV}(O)(Bn\text{-}TPEN)]^{2+}$ and $[Mn^{IV}(O)(N4py)]^{2+}$ lead to dramatically enhanced HAT reactivity compared to other Mn^{IV}-oxo species in the literature.[73-75] These Mn^{IV}-oxo species can cleave strong C–H bonds (Bond Dissociation Free Energies, or BDFEs, between 73 and 99 kcal/mol[91]) at rates approaching those seen for the analogous Fe^{IV}-oxo centers.[73-75, 92-93] Specifically, our group has previously proposed that the enhanced reactivity for $[Mn^{IV}(O)(N4py)]^{2+}$ with substrates such as dihydroanthracene (Figure 1.14, top) is based on the thermodynamic favorability of the HAT reaction.[73] In support of this proposal, the $Mn^{IV/III}$ reduction potential for $[Mn^{IV}(O)(N4py)]^{2+}$ is ~700 mV higher than that of other Mn^{IV}-oxo complexes.[83-85] However, to conduct a full thermodynamic analysis for HAT reactions by $[Mn^{IV}(O)(N4py)]^{2+}$, we need insight into the basicity of the Mn^{IV}-oxo species. Unfortunately, pK_a values for the Mn^{III}-hydroxo product following hydrogen atom abstraction by the Mn^{IV}-oxo adduct of the N4py and Bn-TPEN ligands are not known.

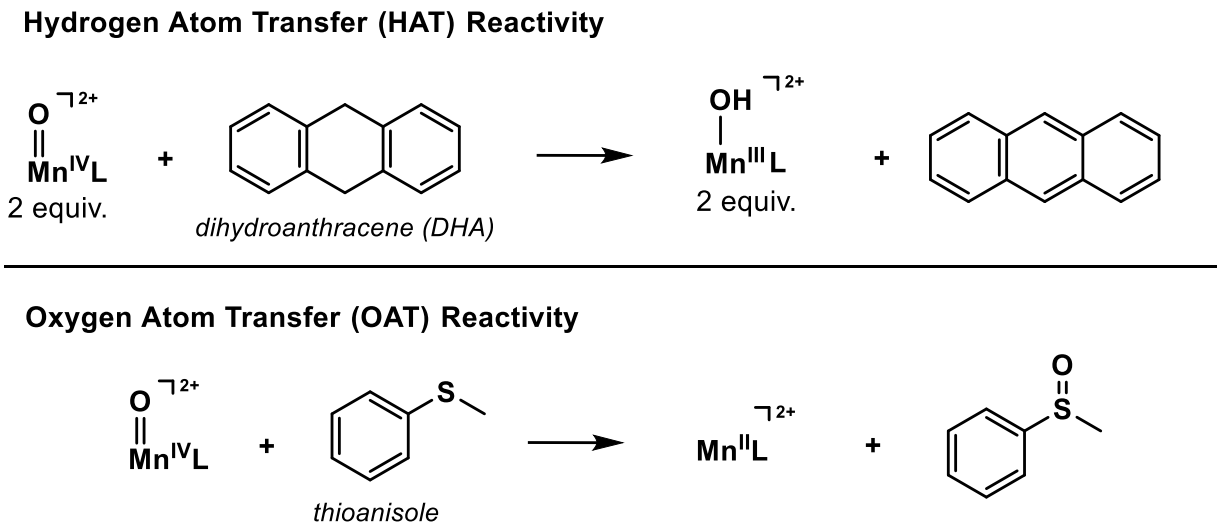

Figure 1.14. General reaction scheme for the sulfoxidation of thioanisole by Mn^{IV}-oxo species.

Based on DFT calculations, it has alternatively been proposed that the enhanced reactivity for $[Mn^{IV}(O)(Bn\text{-}TPEN)]^{2+}$ and $[Mn^{IV}(O)(N4py)]^{2+}$ can be explained by a multi-state reactivity model, where a low-lying excited state crosses with the ground state along the HAT reaction coordinate.[94] Specifically, it is proposed that a single electron excitation from the Mn=O π^*_{xz} orbital into the $Mn–N_{equatorial}$ $\sigma^*_{x2\text{-}y2}$ orbital creates a ^4E state that has a lower barrier for HAT than the $^4B_1$ ground state (Figure 1.15).[94]

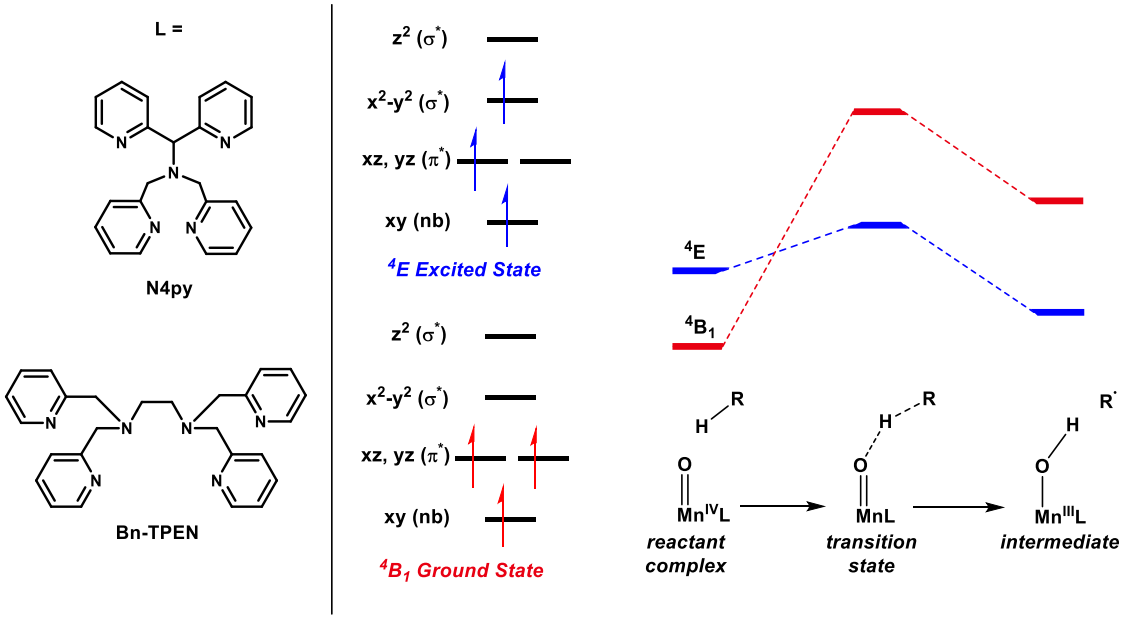

Figure 1.15. Reaction coordinates and computed electronic configurations for HAT from the $^4B_1$ and ^4E states by Mn^{IV}-oxo centers

In addition to HAT reactions, the ^4E excited state has been proposed to play a role in oxygen atom transfer (OAT) reactions.[95] However, calculations for the sulfoxidation of thioanisole by $[Mn^{IV}(O)(N4py)]^{2+}$ reveal a much more complex reaction landscape, potentially involving three states. For the OAT reaction to proceed, the Mn^{IV}-oxo (S = 3/2) reactant species must undergo a spin flip somewhere along the reaction pathway to access the Mn^{II} product (S = 5/2) species (Figure 1.14, bottom, see Chapter 6 for a more in-depth discussion). While calculations by Nam *et al.* predict that the sulfoxidation of thioanisole by $[Mn^{IV}(O)(N4py)]^{2+}$ involves a multi-state pathway involving the $^4B_1$ ground state, ^4E excited state, and a sextet state, little has been done to probe this prediction experimentally.[95]

To shed light on the excited state reactivity model, our group has recently used electronic absorption, magnetic circular dichroism (MCD) spectroscopy, and DFT calculations to assign the ^4E excited state for $[Mn^{IV}(O)(N4py)]^{2+}$.[96] Collectively, these data allowed for the assignment of the ^4E excitation to a near-IR feature at 950 nm. To evaluate the excited state reactivity proposal,

our group generated a series of Mn^{IV}-oxo species to understand how equatorial ligand perturbations directly tune the energy of the ^4E excitation and the HAT and OAT reactivity (Figure 1.16).[72] By introducing quinoline moieties in place of the pyridine arms of the parent N4py complex, the steric crowding around $[Mn^{IV}(O)(2pyN2Q)]^{2+}$ served to weaken the equatorial field. This resulted in a red-shift in the ^4E transition and an enhancement was observed for HAT and OAT reactivity. In contrast, by introducing electron-donating groups to the *para*- and *meta*-positions of the parent N4py pyridine arms to give $[Mn^{IV}(O)(^{DMM}N4py)]^{2+}$, there was a blue-shift in the ^4E transition, which suggests strengthening of the ligand-field, and a corresponding decrease in HAT and OAT reactivity. While these observations are in line with the multi-state reactivity proposal, tuning of the ligand field can directly alter other properties of the Mn^{IV}-oxo centers, including their reduction potential, which also supports the thermodynamic argument for enhanced reactivity.[72] Thus, there are still gaps in our knowledge that prevent us from determining what is causing enhanced reactivity.

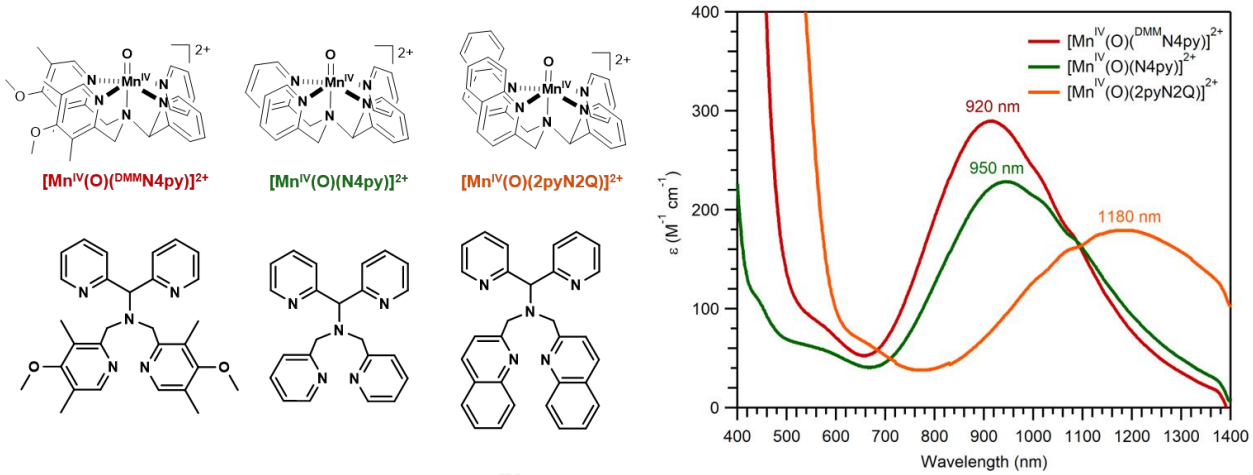

Figure 1.16. Ligand structure and Mn^{IV}-oxo species for a series of N4py derivatives. Electronic absorption spectrum for the series of Mn^{IV}-oxo species, highlighting the ^4E excitation in the near-IR region. λ_{max} values for are included on the graph.

In comparing reactivity for this series of Mn^{IV}-oxo species, $[Mn^{IV}(O)(2pyN2Q)]^{2+}$ exhibits reaction rates with dihydroanthracene (DHA) that were ca. 100-fold faster than those of the slowest complex, $[Mn^{IV}(O)(^{DMM}N4py)]^{2+}$ (Figure 1.17, left). A larger, 4000-fold rate enhancement was observed for thioanisole oxidation by $[Mn^{IV}(O)(2pyN2Q)]^{2+}$ compared to $[Mn^{IV}(O)(^{DMM}N4py)]^{2+}$ (Figure 1.17, right). In the OEC of PSII, a high-valent Mn-oxo species exhibits fast O–O bond formation, thus avoiding C–H abstraction of nearby amino acid residues and water molecules. Therefore, the enhanced OAT ability of $[Mn^{IV}(O)(2pyN2Q)]^{2+}$ could provide insight into how nature supports centers that are able to favor certain reactivity pathways.

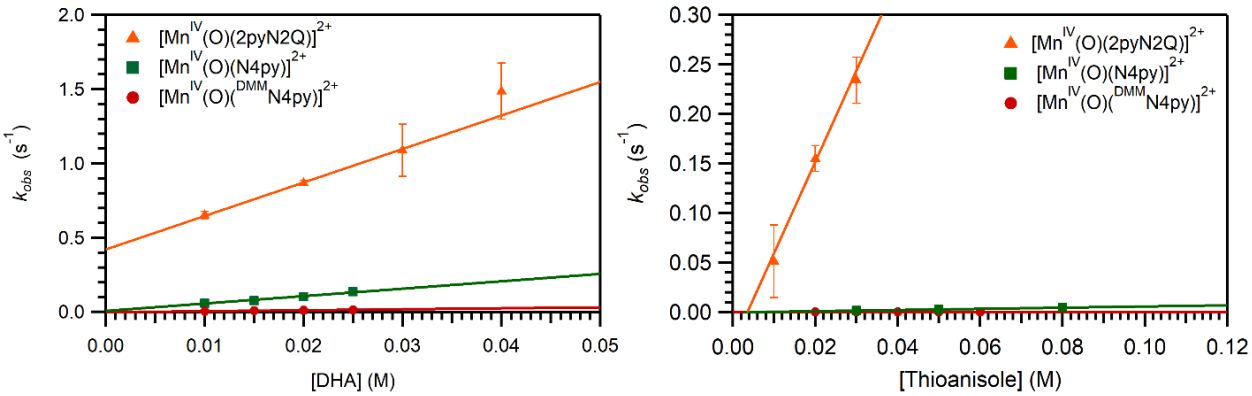

Figure 1.17. Pseudo-first-order rate constants (k_{obs}) versus DHA (left) and thioanisole (right) concentrations. The lines represent the best fits to the data used to determine the second-order rate constants (k_2) for each complex and substrate. Data are from references [72] and [73].

1.5 Fe^{IV}-Oxo Versus Mn^{IV}-Oxo Species

There are a handful of examples in the literature where direct comparisons have been made between Fe^{IV}-oxo and Mn^{IV}-oxo species at parity of coordination sphere. Specifically, Georgiev *et al*. have computationally investigated the reactivity of two dioxygenase enzymes containing Fe and Mn centers, which experimentally exhibit similar reactivity for the catabolism of aromatic compounds.[97] However, their DFT calculations predicted very different rate-determining steps. Their analysis showed that, while both enzymes follow the same reaction path, the rate-limiting step for the Fe-based enzyme involved a proton transfer step, whereas in the case of Mn-based

enzyme, a spin transition determines the activation barrier for the rate-determining homolytic O–O bond cleavage step.[97]

Experimental evidence is also available to suggest that Mn^{IV}-oxo and Fe^{IV}-oxo species may show subtle, yet important, differences in HAT reactions. Comba and co-workers designed two isomeric bispidine ligands, termed L1 and L2 (Figure 1.18, bottom right), to place different amine groups *trans* to the oxo moiety.[81, 98] Kinetic studies for Mn^{IV}-oxo species supported by this ligand system were performed for both HAT and OAT reactions, with $[Mn^{IV}(O)(L2)]^{2+}$ showing the fastest reactivity (Figure 1.18, left). In stark contrast, when a similar ligand scaffold system was employed for Fe^{IV}-oxo centers, with methyl functionality in place of the benzyl group (Figure 1.18, right), $[Fe^{IV}(O)(L1)]^{2+}$ exhibited the fastest reactivity.[98] Computational studies on these systems predict that the two metal-oxo species go through different transition state structures for C–H abstraction. Specifically, the Mn^{IV}-oxo species is predicted to go through a π–pathway, where substrate interacts with the Mn=O π^* molecular orbital (MO) and must approach at an angle of 90 degrees (Figure 1.19, left). Calculations predict that for this pathway, steric factors dominate the transition state structure. In contrast, the Fe^{IV}-oxo species is predicted to go through the σ-pathway, where substrate interacts with the Fe=O σ^* MO and must approach at 180 degrees through a sterically less-demanding pathway (Figure 1.19, right). Therefore, the unique architecture of the ligand scaffolds played varied roles in the transition states for HAT performed by Mn-oxo and Fe-oxo species supported by similar ligands.[81, 98]

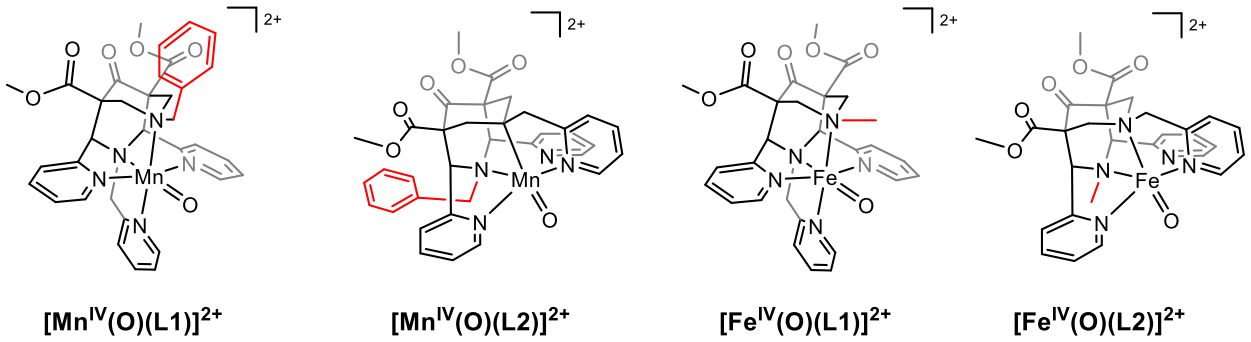

Figure 1.18. Mn^{IV}-oxo and Fe^{IV}-oxo species supported by bispidine-based ligands.

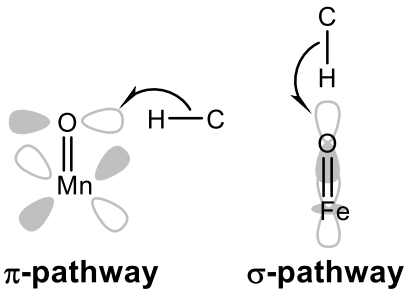

Figure 1.19. Orbital representations of the hydrogen-atom abstraction step by Mn^{IV}-oxo (left) and Fe^{IV}-oxo (right) species supported by bispidine-based ligands.

Additional work has shown that Mn and Fe-oxo species exhibit different sensitivity to acids at parity of coordination sphere, suggesting the basicity of the metal-oxo species is very different.[99-100] Specifically in the case of the ^{H,Me}Pytacn ligand system, the $[Mn^{IV}(O)(OH)(^{H,Me}Pytacn)]^+$ species can be readily protonated to access $[Mn^{IV}(OH)_2(^{H,Me}Pytacn)]^+$, with pH titration experiments revealing a pK_a for this latter species of 7.1.[99] In contrast, even at a pH of 1, the $[Fe^{IV}(O)(OH)(^{H,Me}Pytacn)]^+$ is not protonated, suggesting very different basicity for the Mn^{IV}-oxo and Fe^{IV}-oxo species.[92]

Interestingly, while the Mn^{IV}-oxo species supported by N4py derivatives and Bn-TPEN require the use of TFE as a solvent for formation, Fe^{IV}-oxo species with analogous ligands can be formed in either TFE or MeCN. This observation could potentially be explained by the difference

in basicity between the two metal centers, which may suggest hydrogen-bonding interactions that are provided by a protic solvent such as TFE may help to support the Mn^{IV}-oxo species in solution.

1.6 References

1. Miller, A.-F., Superoxide dismutases: active sites that save, but a protein that kills. *Current Opinion in Chemical Biology* **2004,** *8* (2), 162-168.

2. Boal, A. K.; Cotruvo, J. A.; Stubbe, J.; Rosenzweig, A. C., Structural Basis for Activation of Class Ib Ribonucleotide Reductase. *Science* **2010,** *329* (5998), 1526.

3. Hearn, A. S.; Stroupe, M. E.; Cabelli, D. E.; Ramilo, C. A.; Luba, J. P.; Tainer, J. A.; Nick, H. S.; Silverman, D. N., Catalytic and Structural Effects of Amino Acid Substitution at Histidine 30 in Human Manganese Superoxide Dismutase: Insertion of Valine Cγ into the Substrate Access Channel. *Biochemistry* **2003,** *42* (10), 2781-2789.

4. Sheng, Y.; Abreu, I. A.; Cabelli, D. E.; Maroney, M. J.; Miller, A.-F.; Teixeira, M.; Valentine, J. S., Superoxide Dismutases and Superoxide Reductases. *Chem. Rev.* **2014,** *114* (7), 3854-3918.

5. Umena, Y.; Kawakami, K.; Shen, J.-R.; Kamiya, N., Crystal structure of oxygen-evolving photosystem II at a resolution of 1.9 Å. *Nature* **2011,** *473*, 55.

6. Yano, J.; Kern, J.; Sauer, K.; Latimer, M. J.; Pushkar, Y.; Biesiadka, J.; Loll, B.; Saenger, W.; Messinger, J.; Zouni, A.; Yachandra, V. K., Where Water Is Oxidized to Dioxygen: Structure of the Photosynthetic Mn_4Ca Cluster. *Science* **2006,** *314* (5800), 821-825.

7. Shen, J.-R., The Structure of Photosystem II and the Mechanism of Water Oxidation in Photosynthesis. *Annual Review of Plant Biology* **2015,** *66* (1), 23-48.

8. Vinyard, D. J.; Ananyev, G. M.; Charles Dismukes, G., Photosystem II: The Reaction Center of Oxygenic Photosynthesis. *Annual Review of Biochemistry* **2013,** *82* (1), 577-606.

9. McEvoy, J. P.; Gascon, J. A.; Batista, V. S.; Brudvig, G. W., The mechanism of photosynthetic water splitting. *Photochemical & Photobiological Sciences* **2005,** *4* (12), 940-949.

10. Cady, C. W.; Crabtree, R. H.; Brudvig, G. W., Functional Models for the Oxygen-Evolving Complex of Photosystem II. *Coordination chemistry reviews* **2008,** *252* (3-4), 444-455.

11. McEvoy, J. P.; Brudvig, G. W., Water-Splitting Chemistry of Photosystem II. *Chem. Rev.* **2006,** *106* (11), 4455-4483.

12. Taguchi, T.; Gupta, R.; Lassalle-Kaiser, B.; Boyce, D. W.; Yachandra, V. K.; Tolman, W. B.; Yano, J.; Hendrich, M. P.; Borovik, A. S., Preparation and Properties of a Monomeric High-Spin Mn^{V}–Oxo Complex. *J. Am. Chem. Soc.* **2012,** *134* (4), 1996-1999.

13. Guo, M.; Dong, H.; Li, J.; Cheng, B.; Huang, Y.-q.; Feng, Y.-q.; Lei, A., Spectroscopic observation of iodosylarene metalloporphyrin adducts and manganese(V)-oxo porphyrin species in a cytochrome P450 analogue. *Nature Communications* **2012,** *3*, 1190.

14. DeRosa, T. F., Catalysis. In *Advances in Synthetic Organic Chemistry and Methods Reported in US Patents*, DeRosa, T. F., Ed. Elsevier: Oxford, 2006; pp 205-210.

15. Kostić, N. M.; Dutcă, L. M., 6.4 - Palladium. In *Comprehensive Coordination Chemistry II*, McCleverty, J. A.; Meyer, T. J., Eds. Pergamon: Oxford, 2003; pp 555-672.

16. Rendina, L. M.; Hambley, T. W., 6.5 - Platinum. In *Comprehensive Coordination Chemistry II*, McCleverty, J. A.; Meyer, T. J., Eds. Pergamon: Oxford, 2003; pp 673-745.

17. Bullock, R. M., Reaction: Earth-Abundant Metal Catalysts for Energy Conversions. *Chem* **2017,** *2* (4), 444-446.

18. Ludwig, J. R.; Schindler, C. S., Catalyst: Sustainable Catalysis. *Chem* **2017,** *2* (3), 313-316.

19. Gómez, L.; Garcia-Bosch, I.; Company, A.; Sala, X.; Fontrodona, X.; Ribas, X.; Costas, M., Chiral manganese complexes with pinene appended tetradentate ligands as stereoselective epoxidation catalysts. *Dalton Trans.* **2007,** (47), 5539-5545.

20. Lane, B. S.; Vogt, M.; DeRose, V. J.; Burgess, K., Manganese-Catalyzed Epoxidations of Alkenes in Bicarbonate Solutions. *J. Am. Chem. Soc.* **2002,** *124* (40), 11946-11954.

21. Joergensen, K. A., Transition-metal-catalyzed epoxidations. *Chem. Rev.* **1989,** *89* (3), 431-458.

22. Lane, B. S.; Burgess, K., A Cheap, Catalytic, Scalable, and Environmentally Benign Method for Alkene Epoxidations. *J. Am. Chem. Soc.* **2001,** *123* (12), 2933-2934.

23. Lane, B. S.; Burgess, K., Metal-Catalyzed Epoxidations of Alkenes with Hydrogen Peroxide. *Chem. Rev.* **2003,** *103* (7), 2457-2474.

24. Baciocchi, E.; Boschi, T.; Cassioli, L.; Galli, C.; Lapi, A.; Tagliatesta, P., Epoxidation and hydroxylation reactions catalysed by β-tetrahalogeno and β-octahalogeno manganese porphyrins. *Tetrahedron Letters* **1997,** *38* (41), 7283-7286.

25. Renaud, J.-P.; Battioni, P.; Bartoli, J. F.; Mansuy, D., A very efficient system for alkene epoxidation by hydrogen peroxide: catalysis by manganese-porphyrins in the presence of imidazole. *Journal of the Chemical Society, Chemical Communications* **1985,** (13), 888-889.

26. Battioni, P.; Renaud, J. P.; Bartoli, J. F.; Reina-Artiles, M.; Fort, M.; Mansuy, D., Monooxygenase-like oxidation of hydrocarbons by hydrogen peroxide catalyzed by manganese porphyrins and imidazole: selection of the best catalytic system and nature of the active oxygen species. *J. Am. Chem. Soc.* **1988,** *110* (25), 8462-8470.

27. Anelli, P. L.; Banfi, S.; Montanari, F.; Quici, S., Synergistic effect of lipophilic carboxylic acids and heterocyclic axial ligands in alkene epoxidation by hydrogen peroxide catalysed by manganese(III) tetra-aryl porphyrins. *Journal of the Chemical Society, Chemical Communications* **1989,** (12), 779-780.

28. Anelli, P. L.; Banfi, S.; Legramandi, F.; Montanari, F.; Pozzi, G.; Quici, S., Tailed Mn-tetraarylporphyrins bearing an axial ligand and/or a carboxylic group: self-consistent catalysts for H_2O_2 or NaOCl alkene epoxidation. *Journal of the Chemical Society, Perkin Transactions 1* **1993,** (12), 1345-1357.

29. Dawson, J. H.; Holm, R. H.; Trudell, J. R.; Barth, G.; Linder, R. E.; Bunnenberg, E.; Djerassi, C.; Tang, S. C., Magnetic circular dichroism studies. 43. Oxidized cytochrome P-450. Magnetic circular dichroism evidence for thiolate ligation in the substrate-bound form. Implications for the catalytic mechanism. *J. Am. Chem. Soc.* **1976,** *98* (12), 3707-3709.

30. Nam, W.; Kim, I.; Lim, M. H.; Choi, H. J.; Lee, J. S.; Jang, H. G., Isolation of an Oxomanganese(V) Porphyrin Intermediate in the Reaction of a Manganese(III) Porphyrin Complex and H2O2 in Aqueous Solution. *Chemistry – A European Journal* **2002,** *8* (9), 2067-2071.

31. Bryliakov, K. P., Catalytic Asymmetric Oxygenations with the Environmentally Benign Oxidants H_2O_2 and O_2. *Chem. Rev.* **2017,** *117* (17), 11406-11459.

32. Guo, M.; Corona, T.; Ray, K.; Nam, W., Heme and Nonheme High-Valent Iron and Manganese Oxo Cores in Biological and Abiological Oxidation Reactions. *ACS Central Science* **2019,** *5* (1), 13-28.

33. Irie, R.; Noda, K.; Ito, Y.; Matsumoto, N.; Katsuki, T., Catalytic asymmetric epoxidation of unfunctionalized olefins. *Tetrahedron Letters* **1990,** *31* (50), 7345-7348.

34. Nagata, T.; Imagawa, K.; Yamada, T.; Mukaiyama, T., Enantioselective Aerobic Epoxidation of Acyclic Simple Olefins Catalyzed by the Optically Active β-Ketoiminato Manganese(III) Complex. *Chemistry Letters* **1994,** *23* (7), 1259-1262.

35. Ottenbacher, R. V.; Talsi, E. P.; Bryliakov, K. P., Chiral Manganese Aminopyridine Complexes: the Versatile Catalysts of Chemo- and Stereoselective Oxidations with H2O2. *The Chemical Record* **2018,** *18* (1), 78-90.

36. Murphy, A.; Dubois, G.; Stack, T. D. P., Efficient Epoxidation of Electron-Deficient Olefins with a Cationic Manganese Complex. *J. Am. Chem. Soc.* **2003,** *125* (18), 5250-5251.

37. Wu, M.; Wang, B.; Wang, S.; Xia, C.; Sun, W., Asymmetric Epoxidation of Olefins with Chiral Bioinspired Manganese Complexes. *Organic Letters* **2009,** *11* (16), 3622-3625.

38. Ottenbacher, R. V.; Bryliakov, K. P.; Talsi, E. P., Non-Heme Manganese Complexes Catalyzed Asymmetric Epoxidation of Olefins by Peracetic Acid and Hydrogen Peroxide. *Advanced Synthesis & Catalysis* **2011,** *353* (6), 885-889.

39. Miao, C.; Wang, B.; Wang, Y.; Xia, C.; Lee, Y.-M.; Nam, W.; Sun, W., Proton-Promoted and Anion-Enhanced Epoxidation of Olefins by Hydrogen Peroxide in the Presence of Nonheme Manganese Catalysts. *J. Am. Chem. Soc.* **2016,** *138* (3), 936-943.

40. Miao, C.; Li, X.-X.; Lee, Y.-M.; Xia, C.; Wang, Y.; Nam, W.; Sun, W., Manganese complex-catalyzed oxidation and oxidative kinetic resolution of secondary alcohols by hydrogen peroxide. *Chem. Sci.* **2017,** *8* (11), 7476-7482.

41. Milan, M.; Salamone, M.; Costas, M.; Bietti, M., The Quest for Selectivity in Hydrogen Atom Transfer Based Aliphatic C–H Bond Oxygenation. *Acc. Chem. Res.* **2018,** *51* (9), 1984-1995.

42. Du, J.; Miao, C.; Xia, C.; Lee, Y.-M.; Nam, W.; Sun, W., Mechanistic Insights into the Enantioselective Epoxidation of Olefins by Bioinspired Manganese Complexes: Role of Carboxylic Acid and Nature of Active Oxidant. *ACS Catalysis* **2018,** *8* (5), 4528-4538.

43. Leto, D. F.; Jackson, T. A., Peroxomanganese complexes as an aid to understanding redox-active manganese enzymes. *JBIC Journal of Biological Inorganic Chemistry* **2014,** *19* (1), 1-15.

44. VanAtta, R. B.; Strouse, C. E.; Hanson, L. K.; Valentine, J. S., Peroxo(tetraphenylporphinato)manganese(III) and chloro(tetraphenylporphinato)manganese(II) anions. Synthesis, crystal structures, and electronic structures. *J. Am. Chem. Soc.* **1987,** *109* (5), 1425-1434.

45. Kitajima, N.; Komatsuzaki, H.; Hikichi, S.; Osawa, M.; Moro-oka, Y., A Monomeric Side-On Peroxo Manganese(III) Complex: $Mn(O_2)(3,5\text{-}iPr_2pzH)(HB(3,5\text{-}iPr_2pz)_3)$. *J. Am. Chem. Soc.* **1994,** *116* (25), 11596-11597.

46. Singh, U. P.; Sharma, A. K.; Hikichi, S.; Komatsuzaki, H.; Moro-oka, Y.; Akita, M., Hydrogen bonding interaction between imidazolyl N–H group and peroxide: Stabilization of Mn(III)-peroxo complex $Tp^{iPr2}Mn(\eta^2\text{-}O_2)(im^{Me}H)$ ($im^{Me}H$=2-methylimidazole). *Inorganica Chimica Acta* **2006,** *359* (13), 4407-4411.

47. Seo, M. S.; Kim, J. Y.; Annaraj, J.; Kim, Y.; Lee, Y.-M.; Kim, S.-J.; Kim, J.; Nam, W., $[Mn(tmc)(O_2)]^+$: A Side-On Peroxide Manganese(III) Complex Bearing a Non-heme Ligand. *Angew. Chem., Int. Ed.* **2007,** *46*, 377-380.

48. Annaraj, J.; Cho, J.; Lee, Y.-M.; Kim, S. Y.; Latifi, R.; de Visser, S. P.; Nam, W., Structural Characterization and Remarkable Axial Ligand Effect on the Nucleophilic Reactivity of a Nonheme Manganese(III)–Peroxo Complex. *Angew. Chem., Int. Ed.* **2009,** *48* (23), 4150-4153.

49. Kang, H.; Cho, J.; Cho, K.-B.; Nomura, T.; Ogura, T.; Nam, W., Mononuclear Manganese–Peroxo and Bis(μ-oxo)dimanganese Complexes Bearing a Common N-Methylated Macrocyclic Ligand. *Chemistry – A European Journal* **2013,** *19* (42), 14119-14125.

50. Cho, J.; Sarangi, R.; Nam, W., Mononuclear Metal–O2 Complexes Bearing Macrocyclic N-Tetramethylated Cyclam Ligands. *Acc. Chem. Res.* **2012,** *45* (8), 1321-1330.

51. Groni, S.; Blain, G.; Guillot, R.; Policar, C.; Anxolabéhère-Mallart, E., Reactivity of MnII with Superoxide. Evidence for a [Mn^{III}OO]+ Unit by Low-Temperature Spectroscopies. *Inorg. Chem.* **2007,** *46* (6), 1951-1953.

52. Groni, S.; Dorlet, P.; Blain, G.; Bourcier, S.; Guillot, R.; Anxolabéhère-Mallart, E., Reactivity of an Aminopyridine [$LMn^{II}]^{2+}$ Complex with H_2O_2. Detection of Intermediates at Low Temperature. *Inorg. Chem.* **2008,** *47* (8), 3166-3172.

53. Geiger, R. A.; Chattopadhyay, S.; Day, V. W.; Jackson, T. A., A Series of Peroxomanganese(III) Complexes Supported by Tetradentate Aminopyridyl Ligands: Detailed Spectroscopic and Computational Studies. *J. Am. Chem. Soc.* **2010,** *132* (8), 2821-2831.

54. Geiger, R. A.; Chattopadhyay, S.; Day, V. W.; Jackson, T. A., Nucleophilic reactivity of a series of peroxomanganese(iii) complexes supported by tetradentate aminopyridyl ligands. *Dalton Trans.* **2011,** *40* (8), 1707-1715.

55. Geiger, R. A.; Wijeratne, G. B.; Day, V. W.; Jackson, T. A., Steric and Electronic Influences on the Structures of Peroxomanganese(III) Complexes Supported by Tetradentate Ligands. *European Journal of Inorganic Chemistry* **2012,** *2012* (10), 1598-1608.

56. Shook, R. L.; Gunderson, W. A.; Greaves, J.; Ziller, J. W.; Hendrich, M. P.; Borovik, A. S., A Monomeric Mn^{III}–Peroxo Complex Derived Directly from Dioxygen. *J. Am. Chem. Soc.* **2008,** *130* (28), 8888-8889.

57. Shook, R. L.; Peterson, S. M.; Greaves, J.; Moore, C.; Rheingold, A. L.; Borovik, A. S., Catalytic Reduction of Dioxygen to Water with a Monomeric Manganese Complex at Room Temperature. *J. Am. Chem. Soc.* **2011,** *133* (15), 5810-5817.

58. Geiger, R. A.; Leto, D. F.; Chattopadhyay, S.; Dorlet, P.; Anxolabéhère-Mallart, E.; Jackson, T. A., Geometric and Electronic Structures of Peroxomanganese(III) Complexes Supported by Pentadentate Amino-Pyridine and -Imidazole Ligands. *Inorg. Chem.* **2011,** *50* (20), 10190-10203.

59. Leto, D. F.; Chattopadhyay, S.; Day, V. W.; Jackson, T. A., Reaction landscape of a pentadentate N5-ligated MnII complex with $O2^{\cdot-}$ and H2O2 includes conversion of a peroxomanganese(iii) adduct to a bis(μ-oxo)dimanganese(iii,iv) species. *Dalton Trans.* **2013,** *42* (36), 13014-13025.

60. Borovik, A. S., Bioinspired Hydrogen Bond Motifs in Ligand Design: The Role of Noncovalent Interactions in Metal Ion Mediated Activation of Dioxygen. *Acc. Chem. Res.* **2005,** *38* (1), 54-61.

61. El Ghachtouli, S.; Vincent Ching, H. Y.; Lassalle-Kaiser, B.; Guillot, R.; Leto, D. F.; Chattopadhyay, S.; Jackson, T. A.; Dorlet, P.; Anxolabéhère-Mallart, E., Electrochemical formation of Mn^{III}-peroxo complexes supported by pentadentate amino pyridine and imidazole ligands. *Chem. Commun.* **2013,** *49* (50), 5696-5698.

62. Du, J.; Xu, D.; Zhang, C.; Xia, C.; Wang, Y.; Sun, W., Synthesis, characterization, and reactivity of a side-on manganese(iii)–peroxo complex bearing a pentadentate aminopyridine ligand. *Dalton Trans.* **2016,** *45* (25), 10131-10135.

63. Du, J.; Miao, C.; Xia, C.; Sun, W., A novel manganese(III)-peroxo complex bearing a proline-derived pentadentate aminobenzimidazole ligand. *Chinese Chemical Letters* **2018,** *29* (12), 1869-1871.

64. Colmer, H. E.; Howcroft, A. W.; Jackson, T. A., Formation, Characterization, and O–O Bond Activation of a Peroxomanganese(III) Complex Supported by a Cross-Clamped Cyclam Ligand. *Inorg. Chem.* **2016,** *55* (5), 2055-2069.

65. So, H.; Park, Y. J.; Cho, K.-B.; Lee, Y.-M.; Seo, M. S.; Cho, J.; Sarangi, R.; Nam, W., Spectroscopic Characterization and Reactivity Studies of a Mononuclear Nonheme Mn(III)–Hydroperoxo Complex. *J. Am. Chem. Soc.* **2014,** *136* (35), 12229-12232.

66. Shook, R. L.; Borovik, A. S., Role of the Secondary Coordination Sphere in Metal-Mediated Dioxygen Activation. *Inorg. Chem.* **2010,** *49* (8), 3646-3660.

67. Bull, C.; Niederhoffer, E. C.; Yoshida, T.; Fee, J. A., Kinetic studies of superoxide dismutases: properties of the manganese-containing protein from Thermus thermophilus. *J. Am. Chem. Soc.* **1991,** *113* (11), 4069-4076.

68. Sisemore, M. F.; Selke, M.; Burstyn, J. N.; Valentine, J. S., Metalloporphyrin Peroxo Complexes of Iron(III), Manganese(III), and Titanium(IV). Comparative Studies Demonstrating That the Iron(III) Complex Is Extremely Nucleophilic. *Inorg. Chem.* **1997,** *36* (6), 979-984.

69. Barman, P.; Upadhyay, P.; Faponle, A. S.; Kumar, J.; Nag, S. S.; Kumar, D.; Sastri, C. V.; de Visser, S. P., Deformylation Reaction by a Nonheme Manganese(III)–Peroxo Complex via Initial Hydrogen-Atom Abstraction. *Angew. Chem., Int. Ed.* **2016,** *55* (37), 11091-11095.

70. Ure, A. D.; McDonald, A. R., Nucleophilic Reactivity of a Metal-Bound Superoxide Ligand. *Synlett* **2015,** *26* (15), 2060-2066.

71. Sankaralingam, M.; Lee, Y.-M.; Jeon, S. H.; Seo, M. S.; Cho, K.-B.; Nam, W., A mononuclear manganese(iii)-hydroperoxo complex: synthesis by activating dioxygen and reactivity in electrophilic and nucleophilic reactions. *Chem. Commun.* **2018,** *54* (10), 1209-1212.

72. Massie, A. A.; Denler, M. C.; Cardoso, L. T.; Walker, A. N.; Hossain, M. K.; Day, V. W.; Nordlander, E.; Jackson, T. A., Equatorial Ligand Perturbations Influence the Reactivity of Manganese(IV)-Oxo Complexes. *Angew. Chem. Int. Ed.* **2017,** *56* (15), 4178-4182.

73. Leto, D. F.; Ingram, R.; Day, V. W.; Jackson, T. A., Spectroscopic properties and reactivity of a mononuclear oxomanganese(iv) complex. *Chem. Commun.* **2013,** *49* (47), 5378-5380.

74. Chen, J.; Lee, Y.-M.; Davis, K. M.; Wu, X.; Seo, M. S.; Cho, K.-B.; Yoon, H.; Park, Y. J.; Fukuzumi, S.; Pushkar, Y. N.; Nam, W., A Mononuclear Non-Heme Manganese(IV)–Oxo Complex Binding Redox-Inactive Metal Ions. *J. Am. Chem. Soc.* **2013,** *135* (17), 6388-6391.

75. Wu, X.; Seo, M. S.; Davis, K. M.; Lee, Y.-M.; Chen, J.; Cho, K.-B.; Pushkar, Y. N.; Nam, W., A Highly Reactive Mononuclear Non-Heme Manganese(IV)–Oxo Complex That Can Activate the Strong C–H Bonds of Alkanes. *J. Am. Chem. Soc.* **2011,** *133* (50), 20088-20091.

76. Denler, M. C.; Massie, A. A.; Singh, R.; Stewart-Jones, E.; Sinha, A.; Day, V. W.; Nordlander, E.; Jackson, T. A., Mn^{IV}-Oxo complex of a bis(benzimidazolyl)-containing N5 ligand reveals different reactivity trends for Mn^{IV}-oxo than Fe^{IV}-oxo species. *Dalton Trans.* **2019,** *48* (15), 5007-5021.

77. Halbach, R. L.; Gygi, D.; Bloch, E. D.; Anderson, B. L.; Nocera, D. G., Structurally characterized terminal manganese(iv) oxo tris(alkoxide) complex. *Chem. Sci.* **2018,** *9* (19), 4524-4528.

78. Leto, D. F.; Massie, A. A.; Colmer, H. E.; Jackson, T. A., X-Band Electron Paramagnetic Resonance Comparison of Mononuclear Mn^{IV}-oxo and Mn^{IV}-hydroxo Complexes and Quantum Chemical Investigation of Mn^{IV} Zero-Field Splitting. *Inorg. Chem.* **2016,** *55* (7), 3272-3282.

79. Charnock, J. M.; Garner, C. D.; Trautwein, A. X.; Bill, E.; Winkler, H.; Ayougou, K.; Mandon, D.; Weiss, R., Characterization of an Oxo(porphyrinato)manganese(IV) Complex by X-ray Absorption Spectroscopy. *Angew. Chem. Int. Ed.* **1995,** *34* (3), 343-346.

80. Kurahashi, T.; Kikuchi, A.; Tosha, T.; Shiro, Y.; Kitagawa, T.; Fujii, H., Transient Intermediates from Mn(salen) with Sterically Hindered Mesityl Groups: Interconversion between Mn^{IV}-Phenolate and Mn^{III}-Phenoxyl Radicals as an Origin for Unique Reactivity. *Inorg. Chem.* **2008,** *47* (5), 1674-1686.

81. Barman, P.; Vardhaman, A. K.; Martin, B.; Wörner, S. J.; Sastri, C. V.; Comba, P., Influence of Ligand Architecture on Oxidation Reactions by High-Valent Nonheme Manganese Oxo Complexes Using Water as a Source of Oxygen. *Angew. Chem., Int. Ed.* **2015,** *54* (7), 2095-2099.

82. Leto, D. F.; Jackson, T. A., Mn K-Edge X-ray Absorption Studies of Oxo- and Hydroxomanganese(IV) Complexes: Experimental and Theoretical Insights into Pre-Edge Properties. *Inorg. Chem.* **2014,** *53*, 6179-6194.

83. Garcia-Bosch, I.; Company, A.; Cady, C. W.; Styring, S.; Browne, W. R.; Ribas, X.; Costas, M., Evidence for a Precursor Complex in C−H Hydrogen Atom Transfer Reactions Mediated by a Manganese(IV) Oxo Complex. *Angew. Chem., Int. Ed.* **2011,** *50* (25), 5648-5653.

84. Parsell, T. H.; Yang, M.-Y.; Borovik, A. S., C−H Bond Cleavage with Reductants: Re-Investigating the Reactivity of Monomeric $Mn^{III/IV}$−Oxo Complexes and the Role of Oxo Ligand Basicity. *J. Am. Chem. Soc.* **2009,** *131* (8), 2762-2763.

85. Yin, G.; Danby, A. M.; Kitko, D.; Carter, J. D.; Scheper, W. M.; Busch, D. H., Oxidative Reactivity Difference among the Metal Oxo and Metal Hydroxo Moieties: pH Dependent Hydrogen Abstraction by a Manganese(IV) Complex Having Two Hydroxide Ligands. *J. Am. Chem. Soc.* **2008,** *130* (48), 16245-16253.

86. Neu, H. M.; Baglia, R. A.; Goldberg, D. P., A Balancing Act: Stability versus Reactivity of Mn(O) Complexes. *Acc. Chem. Res.* **2015,** *48* (10), 2754-2764.

87. Nam, W., Synthetic Mononuclear Nonheme Iron–Oxygen Intermediates. *Acc. Chem. Res.* **2015,** *48* (8), 2415-2423.

88. Puri, M.; Que, L., Toward the Synthesis of More Reactive S = 2 Non-Heme Oxoiron(IV) Complexes. *Acc. Chem. Res.* **2015,** *48* (8), 2443-2452.

89. Price, J. C.; Barr, E. W.; Glass, T. E.; Krebs, C.; Bollinger, J. M., Evidence for Hydrogen Abstraction from C1 of Taurine by the High-Spin Fe(IV) Intermediate Detected during Oxygen Activation by Taurine:α-Ketoglutarate Dioxygenase (TauD). *J. Am. Chem. Soc.* **2003,** *125* (43), 13008-13009.

90. Eichhorn, E.; van der Ploeg, J. R.; Kertesz, M. A.; Leisinger, T., Characterization of α-Ketoglutarate-dependent Taurine Dioxygenase from Escherichia coli. *Journal of Biological Chemistry* **1997,** *272* (37), 23031-23036.

91. Warren, J. J.; Tronic, T. A.; Mayer, J. M., Thermochemistry of Proton-Coupled Electron Transfer Reagents and its Implications. *Chem. Rev.* **2010,** *110* (12), 6961-7001.

92. Yoon, H.; Morimoto, Y.; Lee, Y.-M.; Nam, W.; Fukuzumi, S., Electron-transfer properties of a nonheme manganese(iv)-oxo complex acting as a stronger one-electron oxidant than the iron(iv)-oxo analogue. *Chem. Commun.* **2012,** *48* (91), 11187-11189.

93. Yoon, H.; Lee, Y.-M.; Wu, X.; Cho, K.-B.; Sarangi, R.; Nam, W.; Fukuzumi, S., Enhanced Electron-Transfer Reactivity of Nonheme Manganese(IV)–Oxo Complexes by Binding Scandium Ions. *J. Am. Chem. Soc.* **2013,** *135* (24), 9186-9194.

94. Cho, K.-B.; Shaik, S.; Nam, W., Theoretical Investigations into C–H Bond Activation Reaction by Nonheme $Mn^{IV}O$ Complexes: Multistate Reactivity with No Oxygen Rebound. *J. Phys. Chem. Lett.* **2012,** *3* (19), 2851-2856.

95. Chen, J.; Cho, K.-B.; Lee, Y.-M.; Kwon, Y. H.; Nam, W., Mononuclear nonheme iron(iv)–oxo and manganese(iv)–oxo complexes in oxidation reactions: experimental results prove theoretical prediction. *Chem. Commun.* **2015,** *51* (66), 13094-13097.

96. Leto, D. F.; Massie, A. A.; Rice, D. B.; Jackson, T. A., Spectroscopic and Computational Investigations of a Mononuclear Manganese(IV)-Oxo Complex Reveal Electronic Structure Contributions to Reactivity. *J. Am. Chem. Soc.* **2016,** *138* (47), 15413-15424.

97. Georgiev, V.; Borowski, T.; Blomberg, M. R. A.; Siegbahn, P. E. M., A comparison of the reaction mechanisms of iron- and manganese-containing 2,3-HPCD: an important spin transition for manganese. *JBIC Journal of Biological Inorganic Chemistry* **2008,** *13* (6), 929.

98. Jaccob, M.; Comba, P.; Maurer, M.; Vadivelu, P.; Venuvanalingam, P., A combined experimental and computational study on the sulfoxidation by high-valent iron bispidine complexes. *Dalton Trans.* **2011,** *40* (42), 11276-11281.

99. Yin, G.; McCormick, J. M.; Buchalova, M.; Danby, A. M.; Rodgers, K.; Day, V. W.; Smith, K.; Perkins, C. M.; Kitko, D.; Carter, J. D.; Scheper, W. M.; Busch, D. H., Synthesis, Characterization, and Solution Properties of a Novel Cross-Bridged Cyclam Manganese(IV) Complex Having Two Terminal Hydroxo Ligands. *Inorg. Chem.* **2006,** *45* (20), 8052-8061.

100. Company, A.; Prat, I.; Frisch, J. R.; Mas-Ballesté, D. R.; Güell, M.; Juhász, G.; Ribas, X.; Münck, D. E.; Luis, J. M.; Que, L.; Costas, M., Modeling the cis-Oxo-Labile Binding Site Motif of Non-Heme Iron Oxygenases: Water Exchange and Oxidation Reactivity of a Non-Heme Iron(IV)-Oxo Compound Bearing a Tripodal Tetradentate Ligand. *Chemistry - A European Journal* **2011,** *17* (5), 1622-1634.

Chapter 2. Mn^{III}-Peroxo Adduct Supported by a New Tetradentate Ligand Shows Acid-Sensitive Aldehyde Deformylation Reactivity

This work has been reproduced from: Denler, M. C., Wijeratne, G. B., Rice, D. B., Colmer, H. E., Day, V. W., Jackson, T.A. *Dalton Trans*. **2018**, *47*, 13442-13458

2.1 Introduction

In nature, there are many examples of manganese-dependent enzymes that are proposed to utilize peroxomanganese(III) adducts as key intermediates for catalyzing important biological transformations. Such enzymes include manganese superoxide dismutase,[1-2] manganese dioxygenase,[3-4] oxalate oxidase[5-6] and oxalate decarboxylase.[7-8] Peroxo-level adducts have also been proposed for the dinuclear enzymes manganese catalase[9] and the manganese-dependent version of ribonucleotide reductase (Mn-RNR).[10-11] Unfortunately, the mechanism by which these transformations take place is not well understood, which warrants detailed studies of synthetic model systems. To this end, small molecule model complexes have long served as useful tools in understanding the mechanisms of metalloenzymes.[12-14] In addition to these biological motivations, a better understanding of the structure and reactivity of peroxomanganese(III) intermediates is also of relevance for synthetic manganese catalysts used in substrate oxidation reactions.[15-21]

Solid-state X-ray diffraction structures have been reported for several peroxo-manganese species, including both side-on (η^2) peroxomanganese(III) adducts,[22-28] and end-on (η^1) alkylperoxomanganese(III) adducts.[29-30] Apart from these, the majority of peroxomanganese(III) species have been observed under cryogenic conditions and have been thoroughly characterized using a combination of spectroscopic and computational methods.[31-41] Complementary investigations of the chemical reactivity of peroxomanganese(III) complexes have revealed several modes of reactivity, including common decay pathways (such as the formation of dimers), which are summarized in Scheme 2.1.

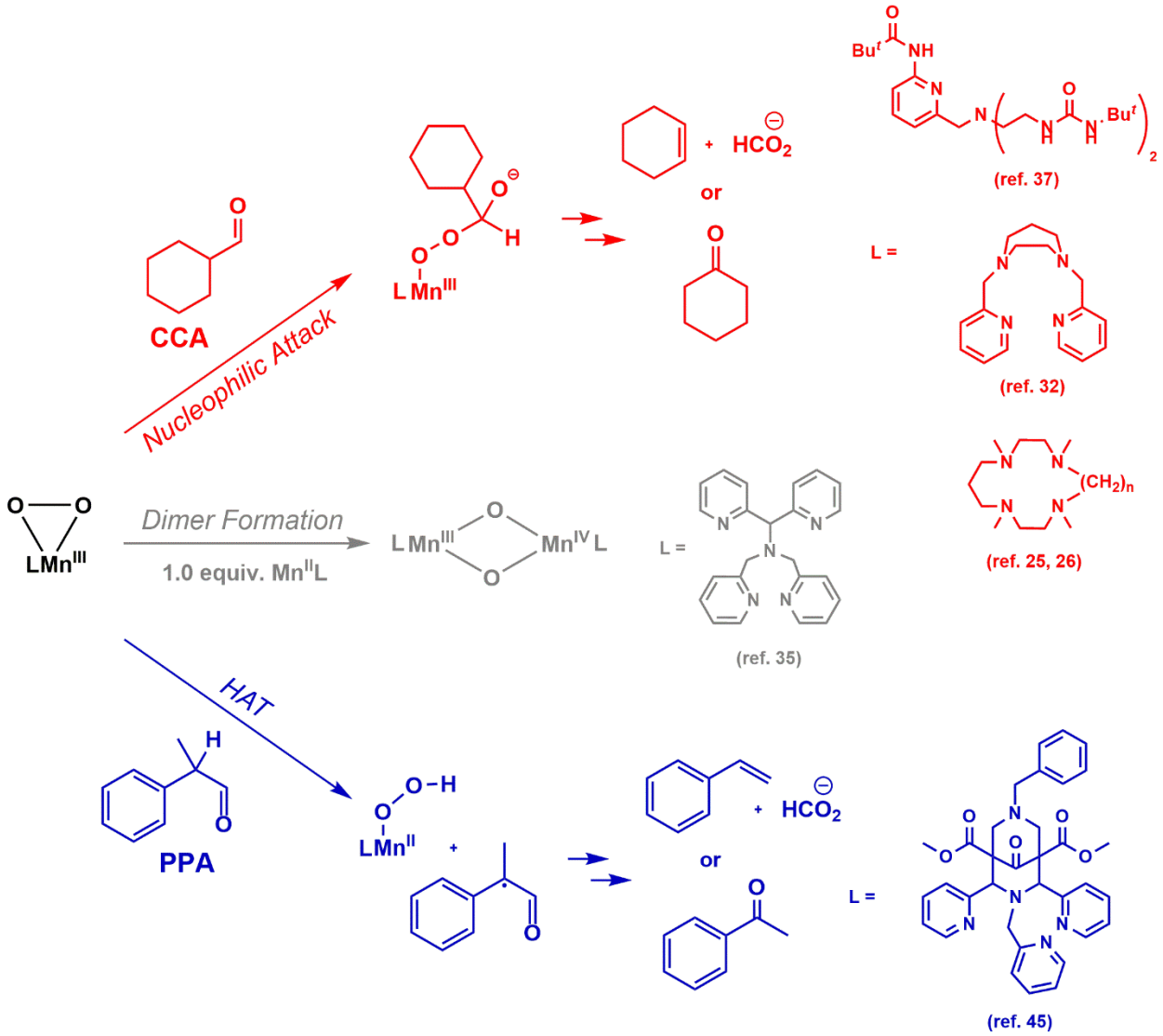

Scheme 2.1. Common reactions for peroxomanganese(III) complexes.

The ability of peroxomanganese(III) complexes to perform aldehyde deformylation has been known for some time.[42] There are several reports of Mn^{III}-peroxo adducts that deformylate cyclohexanecarboxaldehyde (CCA; see Scheme 2.1, top), although the mechanism for deformylation is not fully understood.[25-26, 32, 34, 37] Support for nucleophilic attack of the peroxo ligand on the aldehyde carbonyl carbon comes from kinetic studies that showed faster decay of Mn^{III}-peroxo adducts in the presence of electron-poor, *para*-substituted benzaldehydes. Hammett analyses of these systems yielded ρ^+ values from +1.5 to +2.5.[26, 32]

The nucleophilicity of Mn^{III}-peroxo adducts is likely also responsible for a commonly identified decay pathway, where the Mn^{III}-peroxo unit attacks unreacted Mn^{II} complex to form oxo-bridged $Mn^{III}Mn^{IV}$ product (Scheme 2.1, center). For example, the peroxomanganese(III) complex, $[Mn^{III}(O_2)(\kappa^4\text{-N4py})]^+$ (where N4py is the neutral N_5 ligand *N*,*N*-bis(2-pyridylmethyl)-*N*-bis(2-pyridyl)methylamine) was observed to convert to a bis(μ-oxo)dimanganese(III,IV) complex upon addition of $[Mn^{II}(N4py)(OTf)]^+$.[35] More recently, we have reported spectroscopic studies of the reaction of $[Mn^{III}(O_2)(Me_2EBC)]^{2+}$ (where Me_2EBC is the cross-clamped macrocyclic ligand 4,11-dimethyl-1,4,8,11-tetraazabicyclo[6.6.2]-hexadecane) with $[Mn^{II}(Cl)_2(Me_2EBC)]$, which provided evidence for the formation of a mixture of mononuclear Mn^{IV} and Mn^{III} products.[43] Both of these reactions are presumed to proceed through a μ-peroxodimanganese(II,III) intermediate. Quite recently, McDonald and co-workers have provided spectroscopic evidence for a μ-peroxodimanganese(II,III) species supported by the dinucleating ligand HPTB (HPTB = *N*,*N*,*N*′,*N*′-tetrakis(2-(benzimidazolyl))-2-hydroxy-1,3-diaminopropane).[44]

In contrast to these modes of reactivity that rely on the nucleophilicity of the Mn^{III}-peroxo unit, there are several examples of peroxomanganese(III) adducts acting as hydrogen-atom acceptors (Scheme 2.1, bottom). Borovik and co-workers showed that a peroxomanganese(III) adduct supported by a tripodal ligand with a hydrogen-bonding cavity forms a hybrid Mn^{III}-oxo/hydroxo species after reaction with the hydrogen-atom donor diphenylhydrazine.[37] More recently, Sastri and co-workers showed that a Mn^{III}-peroxo supported by an aminopyridyl ligand effects the deformylation of 2-phenylpropionaldehyde (PPA) by a hydrogen-atom transfer mechanism.[45] This alternate mechanism for deformylation was supported by the observation of an H/D kinetic isotope effect when the benzylic C–H bond of PPA was substituted for deuterium.

The ability of the Mn^{III}-peroxo unit to abstract hydrogen atoms from benzylic C–H bonds, such as those of PPA, offers a new perspective on the decay pathways of Mn^{III}-peroxo adducts supported by aminopyridyl ligands. This includes the decay reaction of the $[Mn^{III}(O_2)(MeTPEN)]^+$ complex (where MeTPEN is *N*-methyl-*N*,*N*′,*N*′-tris(2-pyridylmethyl)ethane-1,2-diamine; see Scheme 2.2),[41] which resulted in the eventual formation of a Mn^{II} complex coordinated by two pyridinecarboxylate ligands (Scheme 2.2) derived from the oxidation of the parent MeTPEN ligand. Anxolabéhère-Mallart and co-workers postulated that this decay pathway, which required the addition of strong acid, proceeded through a Mn^{III}-hydroperoxo species that underwent O–O cleavage to afford a strong oxidant (i.e., a high-valent Mn^{IV}-oxo adduct) capable of initiating oxidation of the MeTPEN ligand at the benzylic linkers.[41] In light of the more recent studies that suggest that Mn^{III}-peroxo and Mn^{III}-hydroperoxo adducts can attack benzylic C–H bonds, it is unclear if it is necessary to invoke formation of a high-valent manganese-oxo species to rationalize the observed chemistry.

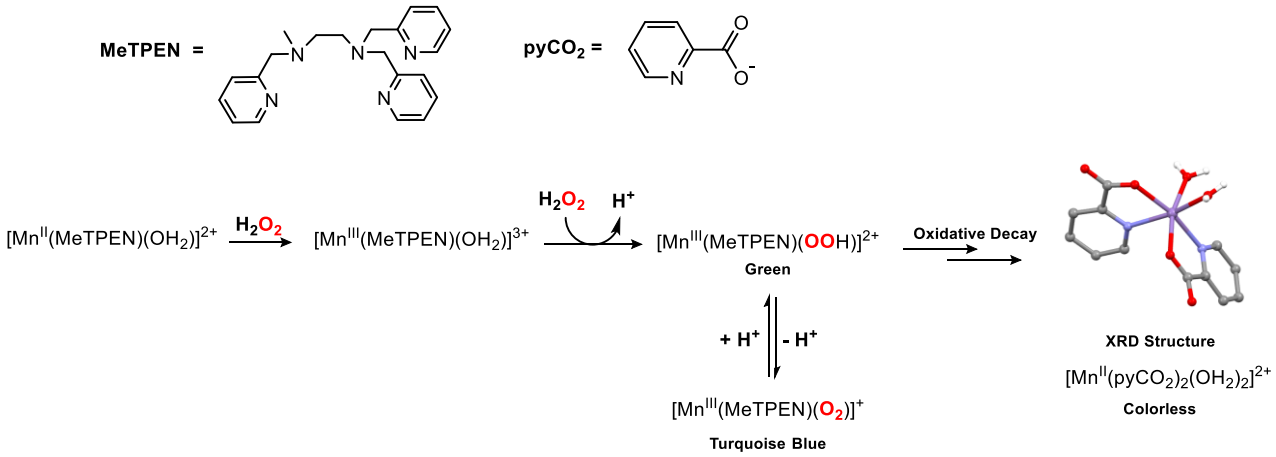

Scheme 2.2. The proposed formation and ligand oxidation pathway of a Mn^{III}-peroxo and Mn^{III}-hydroperoxo species supported by the *N*-methyl-*N*,*N*′,*N*′-tris(2-pyridylmethyl)ethane-1,2-diamine ligand (MeTPEN). The XRD structure, taken from reference 41, shows the final manganese decay product in the presence of acid, where the metal center is coordinated to two pyridine carboxylate molecules ($pyCO_2^-$) that resulted from ligand oxidation.

Because of the potential for Mn^{III}-peroxo and Mn^{III}-hydroperoxo adducts to attack C–H bonds of moderate strength (ca. 80 – 85 kcal/mol), the design and synthesis of a novel ligand platform excluding benzylic $–CH_2$ linkers is of interest, as this ligand could avoid hydrogen atom abstraction as a decay pathway. To develop such a ligand, we chose a ligand topology quite similar to that of the $L^7py_2^R$ family that we had previously used to generate a series of Mn^{III}-peroxo adducts (Figure 2.1).[31-32, 34] In this study, we report the synthesis of the L^7BQ ligand (L^7BQ = 1,4-di(quinolin-8-yl)-1,4-diazepane), which lacks benzylic linkers, and describe the corresponding Mn^{II} complex, $[Mn^{II}(L^7BQ)(OTf)_2]$. As anticipated, the $[Mn^{II}(L^7BQ)(OTf)_2]$ complex reacts with H_2O_2 and Et_3N to generate the peroxomanganese(III) complex, $[Mn^{III}(O_2)(L^7BQ)]^+$, which has been characterized by a variety of spectroscopic techniques. Although the $[Mn^{III}(O_2)(L^7BQ)]^+$ complex does not show enhanced stability relative to the $[Mn^{III}(O_2)(L^7py_2^R)]^+$ analogues, the reactivity of this complex with respect to aldehydes is distinct and highly sensitive to the presence of acid, suggesting a ligand influence on reactivity.

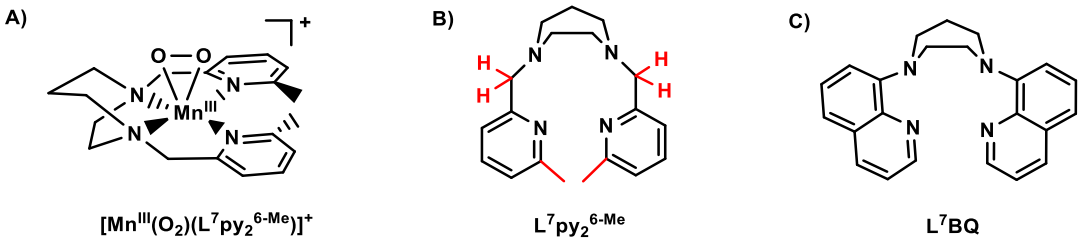

Figure 2.1. The schematic structures of A) $[Mn^{III}(O_2)(L^7py_2^{6\text{-}Me})]^+$ B) $L^7py_2^{6\text{-}Me}$ ligand (with benzylic groups potentially susceptible to oxidation highlighted in red), and C) the new L^7BQ ligand described in this work.

2.2 Experimental Methods

Materials. Unless otherwise noted, all chemicals and solvents were obtained from commercial vendors at ACS grade or better and were used without further purification. Acetonitrile, methanol, and ether were dried and degassed using a Pure Solv (2010) solvent

purification system. Toluene was made anaerobic by either sparging and then drying over activated alumina using a PPT Glass Contour solvent purification system, or dry toluene (99% purity) from Acros Organics was degassed by four freeze-pump-thaw cycles using Schlenk techniques. All dried, degassed solvents were immediately taken into an argon-filled glove box and were stored in tightly-sealed Schlenk glassware until use. CCA was distilled prior to use; however, a ^{1}H-NMR analysis of the material following distillation revealed the persistence of acid impurities (*vide infra*). Syntheses of $L^{7}BQ$ and $[Mn^{II}(L^{7}BQ)(OTf)_2]$ were carried out under inert conditions, as described below. Product analysis for PPA was performed by running reaction mixtures through a silica plug with excess EtOAc, and 1,2,4,5-tetrachloro-3-nitrobenzene was used as an internal standard for ^{1}H NMR quantification in CD_3CN.

Instrumentation. NMR spectra were collected on a Bruker DRX 400 MHz spectrometer and a 600 MHz AVAN CE III spectrometer with a BBO probe or a QNP probe. Data were collected at room temperature in $CDCl_3$ (δ = 7.26 ppm), unless stated otherwise. Mass spectrometry experiments were performed using an LCT Primers MicroMass electrospray time-of-flight instrument. Electronic absorption spectra were obtained on a Varian Cary 50 Bio spectrophotometer interfaced with a Unisoku cryostat (USP-203-A) capable of maintaining temperatures between 150 and 373 K. EPR spectra were collected on an X-band (9 GHz) Bruker EMXPlus spectrometer equipped with an Oxford ESR900 continuous flow liquid helium cryostat and an Oxford ITC503 temperature system. Both parallel- and perpendicular-mode spectra were collected using a Bruker ER4116DM dual-mode cavity. All spectra were collected under nonsaturating conditions at 2.0 mW microwave power, 4 G modulation amplitude, 100 kHz modulation frequency and 83 ms time constant. Spin quantification of the product of $[Mn^{III}(O_2)(L^{7}BQ)]^{+}$ with cyclohexanecarboxylic acid (termed intermediate A) was determined

against a 2.5 mM sample of $[Mn^{II}(L^7BQ)(OTf)_2]$ in MeCN. Gas chromatography-mass spectrometry data were collected using a Quattro Micro GC quadrupole mass analyzer via an Agilent 6890 N gas chromatograph. A 5% phenyl methyl silicone stationary phase (HP-5 MS) 12 meter column was used along with a helium carrier gas at a flow rate of 2 ml min^{-1}. The injector port was heated to 240 ºC and 1 μL of sample was injected with a split ratio of 20:1. The GC thermal gradient was an initial 50 ºC, which was held for 1 minute before increasing 50 ºC min^{-1} to 300 ºC and held for two minutes. Elemental analysis was done through Micro-Analysis, Inc.

Synthesis of the L^7BQ Ligand. 8-bromoquinoline (500 mg, 2.4 mmol), homopiperazine (120 mg, 1.2 mmol), and NaO^tBu (324 mg, 3.4 mmol) were combined in a Schlenk tube in dry, degassed toluene (40 mL), along with 4 mol% $Pd_2(dba)_3$ (110 mg, 0.12 mmol), and 10 mol% BINAP (150 mg, 0.24 mmol) within an argon-filled glove box. The tube was sealed with an air-tight septum, and stirred at 110 ºC for three days. Although no difficulties were encountered, heating a sealed vessel can result in explosion of the reaction vessel. Because of this, all reactions were performed behind a blast shield. After heating for three days, the reaction mixture was cooled to room temperature and was diluted with excess diethyl ether. This mixture was filtered through celite and evaporated to dryness under reduced pressure. The crude product was purified by flash chromatography over silica gel using ethyl acetate and hexane (1 : 20) as the beginning eluent and the percentage of ethyl acetate was gradually increased over time. The clean ligand was isolated as a yellow oil in 69% yield (292 mg) and was characterized by ^1H NMR, ^{13}C NMR, HSQC and ESI-MS. ^1H NMR data (600 MHz instrument, Figure A2.1) for L^7BQ ($CDCl_3$, δ) = 8.86 (dd, *J* = 4.1, 1.9 Hz, 2H), 8.09 (dd, *J* = 8.3, 1.9 Hz, 2H), 7.40 (t, *J* = 7.8 Hz, 2H), 7.35 (dd, *J* = 8.2, 4.1 Hz, 2H), 7.31 (dd, *J* = 8.2, 1.3 Hz, 2H), 7.21 (dd, *J* = 7.6, 1.4 Hz, 2H), 4.09 (s, 4H), 3.96 – 3.76 (m, 4H), 2.38 (p, *J* = 5.7 Hz, 2H) ppm. ^{13}C NMR data (collected on a 400 MHz instrument at 100.62

MHz, Figure A2.2) for L^7BQ ($CDCl_3$, δ) = 149.85, 147.39, 142.61, 136.43, 130.03, 126.82, 120.81, 119.64, 115.61, 55.16, 53.55, 29.06 ppm. HSQC for L7BQ in included in the supporting information (Figure A2.3). ESI-MS (Figure A2.4): $[L^7BQ + H]^+$ *m/z* = 355.1902 (calc. = 355.1917).

Synthesis of $[Mn^{II}(L^7BQ)(OTf)_2]$. An equimolar mixture of L^7BQ and $[Mn^{II}(OTf)_2(MeCN)_2]_n$ produced high yields (>90%) of $[Mn^{II}(L^7BQ)(OTf)_2]$ when stirred overnight in MeCN under an inert atmosphere at room temperature. $[Mn^{II}(OTf)_2(MeCN)_2]_n$ was synthesized according to literature procedures.[25] A detailed procedure for the metalation of L^7BQ is as follows. To a stirred MeCN solution (5 mL) of L^7BQ (100 mg, 0.282 mmol), an equimolar quantity of $Mn^{II}(OTf)_2$ (99 mg, 0.282 mmol) was added in the same solvent (5 mL) and was stirred overnight under an inert atmosphere. The mixture was then filtered using a syringe filter and dried under reduced pressure. The solid product was recrystallized with MeCN and Et_2O by vapor diffusion. Light yellow crystals suitable for X-ray diffraction analysis were obtained by subsequent recrystallization with the same solvent system. $[Mn^{II}(L^7BQ)(OTf)_2]$ was further characterized by the effective magnetic moment analysis by the ^1H NMR method of Evans[46] in CD_3CN at 25 °C, and by ESI-MS and EPR methods. The effective magnetic moment of $[Mn^{II}(L^7BQ)(OTf)_2]$ at 25 °C was found to be 5.7 μ_B in CD_3CN (a diamagnetic correction, χ_D, of -277.24 x 10^{-6} emu mol^{-1} was included in the calculation of the molar magnetic susceptibility, χ_M).[47] This value agrees with the expected value (5.9 μ_B) for a monomeric high-spin Mn^{II} center. ESI-MS (Figure A2.5): $[Mn^{II}(L^7BQ)(OTf)]^+$ *m/z* = 558.0342 (calc. = 558.0745). The perpendicular-mode X-band EPR spectrum of a frozen MeCN solution of $[Mn^{II}(L^7BQ)(OTf)_2]$ exhibits features at 230 mT and 350 mT at 5 K (Figure A2.6, left), which are characteristic of a monomeric Mn^{II} species.[35] Additionally, the parallel-mode EPR spectrum shows no signal (Figure A2.6, right). Elemental Analysis

$[Mn^{II}(L^7BQ)(OTf)_2]\cdot H_2O$ $C_{25}H_{24}F_6MnN_4O_7S_2$ calc (%): C 41.38, H 3.33, N:7.72; Found (%): C 41.60, H: 3.23, N: 7.73.

X-ray diffraction data collection and analysis for $[Mn^{II}(L^7BQ)(OTf)_2]$. A light-yellow single-domain crystal of $[Mn^{II}(L^7BQ)(OTf)_2]$ was suspended with Paratone N oil on a MiteGen MicroMount and placed on a goniometer head in a cold nitrogen stream at 100 K for a single-crystal X-ray structure determination. Monochromatic X-rays were provided by a Bruker diffractometer equipped with Helios multilayer optics, an APEX II CCD detector, and a Bruker MicroStar microfocus rotating anode X-ray source operating at 45 kV and 60 mA. Intensity data (5238 0.5°-wide ω- or φ-scan frames with counting times of 2-3 seconds each) were collected with the Bruker program SMART,[48] and diffracted intensities were measured with the Bruker program SAINT.[49] The space group[50] and crystallographic data are summarized in Table A2.1. The Bruker software package SHELXTL was used to solve the structure and locate all nonhydrogen atoms with "direct methods" techniques. Hydrogen atoms were located from a difference Fourier and included in the structural model as independent isotropic atoms whose parameters were allowed to vary in least-squares refinement cycles. All stages of weighted full-matrix least-squares refinement were conducted using F_o^2 data with the SHELXTL Version 2010.3-0 software package.[51] The final structural model incorporated anisotropic thermal parameters for all non-hydrogen atoms and isotropic thermal parameters for all hydrogen atoms.

Generation and Characterization of $[Mn^{III}(O_2)(L^7BQ)]^+$. The peroxomanganese(III) complex $[Mn^{III}(O_2)(L^7BQ)]^+$ was generated by treating a 2.5 mM MeCN solution of $[Mn^{II}(L^7BQ)(OTf)_2]$ with 5 equiv. H_2O_2 and 1.0 equiv. Et_3N at -40 °C. Reactions using less than 5 equiv. hydrogen peroxide resulted in substantially lower formation of the Mn^{III}-peroxo adduct. We presume that water, which is added with the H_2O_2, is a strong enough base to remove the

second proton required for formation of the side-on peroxomanganese(III) species. When greater equiv. Et_3N were used, we observed the decay of $[Mn^{III}(O_2)(L^7BQ)]^+$ to be more rapid. One equiv. Et_3N gave the cleanest formation and the best thermal stability.

Because this species was sensitive to the temperature of the added reagents, syringes and stock solutions were chilled prior to addition in order to minimize any thermal decay. Additionally, the stock solutions were re-made often to avoid the base-catalyzed decomposition of hydrogen peroxide.[52] Characteristic changes in the electronic absorption spectrum were evident of the formation of $[Mn^{III}(O_2)(L^7BQ)]^+$, where the growth of two bands at 450 nm (ε = 260 M^{-1} cm^{-1}) and 660 nm (ε = 75 M^{-1} cm^{-1}) marked the formation of this species. ESI-MS $[Mn^{III}(O_2)(L^7BQ)]^+$ *m/z* = 441.1135 (calc. = 441.1123 *m/z*); $[Mn^{III}(^{18}O_2)(L^7BQ)]^+$ *m/z* = 445.1156 (calc. = 445.1208 *m/z*) (Figures A2.7 and A2.8). EPR samples of $[Mn^{III}(O_2)(L^7BQ)]^+$ were prepared at -40 °C in MeCN using cryogenic techniques and were analyzed at 5 K (Figure A2.9). Attempts to characterize $[Mn^{III}(O_2)(L^7BQ)]^+$ by vibrational methods were unsuccessful. We note that, to date, vibrational studies of side-on Mn^{III}-peroxo adducts have commonly been unsuccessful.[35, 40]

XAS Sample Preparation. Frozen solution samples of $[Mn^{II}(L^7BQ)(OTf)_2]$ at 11 mM and $[Mn^{III}(O_2)(L^7BQ)]^+$ at 2.5 mM were prepared from 400 μL of solution in MeCN that was frozen in a precooled sample cup. A frozen solution sample of the product of $[Mn^{III}(O_2)(L^7BQ)]^+$ with cyclohexanecarboxylic acid (termed intermediate A) was prepared from 400μL of a 2.5 mM solution in MeCN that was frozen in a precooled sample cup following the addition of cyclohexanecarboxylic acid to $[Mn^{III}(O_2)(L^7BQ)]^+$.

Product Analysis. GC-MS was used for analysis of organic products from the reactions of Mn complexes with CCA, and the percent yield of these reactions was determined by comparing the ratio of the product signal to that of an internal standard and comparing the ratio to a standard

curve for the product. A detailed procedure is a follows: a 2.5 mM solution of $[Mn^{III}(O_2)(L^7BQ)]^+$ was reacted with 165 equivalents of CCA at −40 °C in MeCN. When the reaction was completed, it was allowed to warm to room temperature, napthalene was added as an internal standard, and the reaction solution was run through a silica plug with excess EtOAc. The reaction was performed in triplicate. The work-up procedure was tested using a standard sample of known substrate and product concentrations, and the procedure was not found to change the substrate:product ratio.

XAS Data Collection. The Mn K-edge XAS data for all samples were collected over an energy range of 6300 to 7250 eV. Under all conditions, a manganese foil was used as reference for each scan by assigning the zero crossing of the second derivative of the K-edge energy of the foil to 6539.0 eV. All XAS data were obtained via fluorescence excitation. Data for $[Mn^{III}(O_2)(L^7BQ)]^+$ and the product of $[Mn^{III}(O_2)(L^7BQ)]^+$ with cyclohexanecarboxylic acid (termed intermediate A) were collected at beamline 9-3 at SSRL at 7 K using a Si(220) monochromator and a 100-element Ge array detector. Data for $[Mn^{II}(L^7BQ)(OTf)_2]$ were collected at beamline X3B at the National Synchrotron Light Source (NSLS) using a Si(111) monochromator and a 31-element Ge array detector.

XAS Data Analysis. Processing of the XAS data for $[Mn^{II}(L^7BQ)(OTf)_2]$ was done using EXAFSPAK[53] using previously described methods.[43] Analysis of EXAFS data for $[Mn^{III}(O_2)(L^7BQ)]^+$ and intermediate A were performed using *DEMETER*.[54] The *AUTOBK* algorithm, as implemented in *ATHENA*, was used for background removal. The edge-step normalization procedure was used for each data set. EXAFS refinement in *ARTEMIS* was carried out on $k^3\chi(k)$ data, using phase and amplitude functions obtained from *FEFF*, version 6,[55] and a structural model of $[Mn^{III}(O_2)(L^7BQ)]^+$ from DFT computations. For each fit, the parameters *r* (average distance between Mn and scattering atom), E_0 (a single value for all paths), and σ^2

(Debye-Waller factor) were optimized, while *n*, the number of atoms in the shell, was kept fixed. *n* was varied by integer steps systematically to achieve better goodness of fit. The goodness of fit was evaluated using the R-factor:

$$R = \sum_{i=1}^{N}(\chi_i^{data} - \chi_i^{fit})^2 \,/\, \sum_{i=1}^{N}(\chi_i^{data})^2$$

Fits of the pre-edge area were performed using the FityK software.[56] Pre-edge intensity was normalized relative to the most intense fluorescence peak. The pre-edge was fit using pseudo-Voight line shapes and varied full-width at half-maximum, energy position, and height. The contribution from the rising edge and the background were also fit using a pseudo-Voight function. Manganese K-edge energy values were determined based on the position of the inflection point of the rising edge upon taking the first derivative of the edge region.

Density Functional Theory. All calculations were performed using the *ORCA* 4.0 software package.[57] Geometries for $[Mn^{III}(O_2)(L^7BQ)]^+$ were performed starting from the Mn^{II} crystal structure and adding the peroxo moiety. The high-spin S = 2 spin state was used for all computations. Optimizations were carried out using the B3LYP functional with the inclusion of dispersion interactions via Grimme's D3 correction with the Becke-Johnson damping scheme.[58-61] The def2-TZVP basis set was utilized for Mn, N, and O and the def2-SVP basis set was used for C and H.[62-63] A larger DFT integration grid, Grid6 in ORCA nomenclature, was utilized. The RIJCOSX approximation was used with a larger COSX grid (GridX6) and the def2/J auxiliary basis sets. Solvent was included implicitly through the SMD solvation model with the default parameters in ORCA for acetonitrile.[64] Structures were confirmed to be a minima through numerical frequency calculations performed at the same level of theory.

The manganese pre-K-edge spectra of $[Mn^{III}(O_2)(L^7BQ)]^+$ models were calculated using time-dependent density functional theory (TD-DFT) within the Tamm-Dancoff approximation

using the B3LYP functional.[65-66] Calculations were performed using the zeroth-order approximation (ZORA) with the ZORA-def2-TZVP(-f) basis sets used for all atoms.[67-68] The pre-edge area was calculated using a previously published method based on calibration using a series of Mn^{II} and Mn^{III} complexes, where the origin adjusted intensity (I) is calculated from the sum of the electric dipole, electric quadrupole, and magnetic dipole contributions. These values are used in the empirically derived equation A = 6.01I + 1.79 for B3LYP.[69] Simulations of the spectra were performed with a 1 eV linewidth.

The electronic absorption spectra of $[Mn^{III}(O_2)(L^7BQ)]^+$ models were calculated using TD-DFT methods utilizing the B3LYP functional. The def2-TZVPP basis set was used for Mn, N, and O and the def2-TZVP basis set for C and H. Solvation was included implicitly using the SMD solvation model with the default values for acetonitrile.

2.3 Results and Analysis

Synthesis of L^7BQ ligand. Given the observed ligand oxidative decay pathway of $[Mn^{III}(O_2)(MeTPEN)]^+$,[41] the L^7BQ ligand was designed in order to generate a peroxomanganese(III) adduct lacking benzylic linkers. The synthesis of this ligand involved the coupling of two quinolinyl moieties with both secondary amine groups in homopiperazine (Scheme 2.3). Coupling of secondary amines with aryl halides can be attained via the Pd-catalyzed Buchwald-Hartwig cross-coupling reactions.[70-72] In this case, 8-bromoquinoline and homopiperazine could be coupled to generate the desired aminoquinolinyl L^7BQ ligand in moderate yields (~69%).

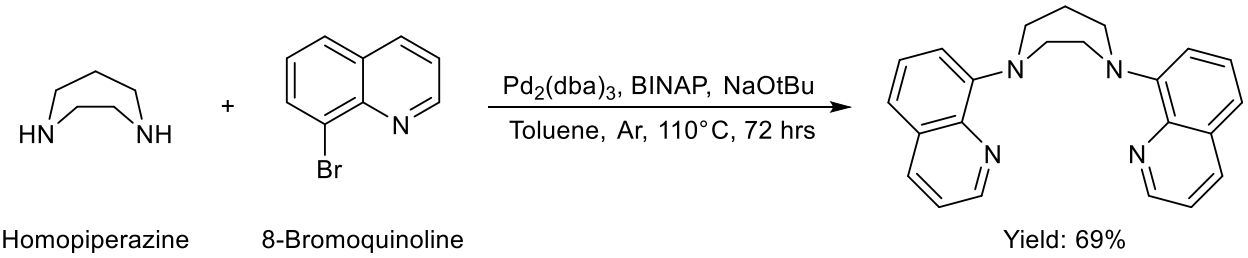

Scheme 2.3. Synthetic scheme for the L^7BQ ligand.

Structural Properties of $[Mn^{II}(L^7BQ)(OTf)_2]$. The $[Mn^{II}(L^7BQ)(OTf)_2]$ complex could be readily generated by the reaction of $[Mn(OTf)_2(MeCN)_2]_n$ with the L^7BQ ligand. The XRD structure of $[Mn^{II}(L^7BQ)(OTf)_2]$ contains a six-coordinate manganese center (Figure 2.2) in a pseudo-octahedral geometry. Significant bond lengths and angles of $[Mn^{II}(L^7BQ)(OTf)_2]$ are summarized in Table 2.1. In this structure, the L^7BQ ligand is coordinated in a tetradentate fashion occupying the equatorial plane (N1 - N4), with the Mn^{II} ion being displaced by 0.08 Å from the mean plane through these four coordinated nitrogens. The axial sites are occupied by the two triflate ions with an O11–Mn–O21 bond angle of 155.06°. The Mn–N distances vary between 2.2 – 2.3 Å, with the amine Mn–N distances being longer than the aromatic Mn–N distances; the Mn–O distances are ~2.2 Å (Table 2.1). All of these are values typical for high-spin Mn^{II} centers.[31, 34, 73] A highly distorted 6-coordinate geometry for the Mn^{II} center in $[Mn^{II}(L^7BQ)(OTf)_2]$ is indicated by the angles between coordinated atoms: N–Mn–N, 71° to 137°; O–Mn–N, 81° - 111°; and O–Mn–O, 155.06°. These angles for the MnO_2N_4 polyhedron more closely resemble a pentagonal bipyramid with a missing equatorial ligand than an octahedron. This polyhedron would ideally have equatorial N–Mn–N angles of 72° and 144°, O–Mn–N angles of 90° and an O–Mn–O angle of 180°. Nonbonded O---H interactions between coordinated triflates and the ethyl and propyl linkers joining N2 and N3 cause the triflates to move off the vertical axis in this molecule toward the "missing" equatorial coordination site. Even though the N1---N4 separation is 4.09 Å,

an acetonitrile solvent molecule of crystallization present in the asymmetric unit does not interact with the metal center (Mn–N distance of 6.729 Å) and is not shown in Figure 2.2. Hydrogen atoms on the two carbons adjacent to N1 and N4 are separated by 3.51 Å and block access to the fifth equatorial coordination site. The bond angles observed for $[Mn^{II}(L^7BQ)(OTf)_2]$ are very similar to those previously observed for Mn^{II} complexes of the $L^7py_2^R$ ligands.[31-32, 34]

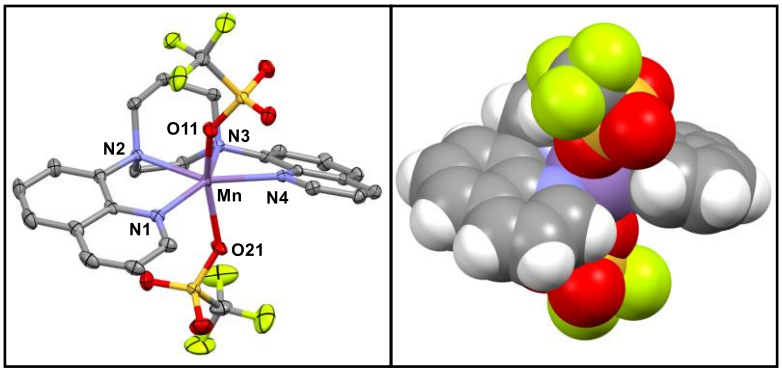

Figure 2.2. ORTEP diagram (left; 50% thermal probability) and space-filling model (right) for $[Mn^{II}(L^7BQ)(OTf)_2]$. Hydrogen atoms and the non-coordinating solvent molecule have been removed for clarity. Coordination bond lengths and angles are listed in Table 2.1.

Table 2.1. Selected Bond Lengths and Angles for $[Mn^{II}(L^7BQ)(OTf)_2]$.

Bond Length (Å)			
Mn–N1	2.1846(14)	Mn–N4	2.2109(14)
Mn–N2	2.3011(15)	Mn–N3	2.2841(14)
Mn–O11	2.1869(12)	Mn–O21	2.2152(13)
Bond Angle (°)			
O11–Mn–O21	155.05(5)	N4–Mn–O21	81.48(5)
N1–Mn–O11	85.22(5)	N1–Mn–N2	76.73(5)
N2–Mn–O11	95.27(5)	N2–Mn–N3	71.47(5)
N3–Mn–O11	111.49(5)	N3–Mn–N4	75.84(5)
N4–Mn–O11	88.82(5)	N1–Mn–N3	145.04(5)
N1–Mn–O21	86.37(5)	N2–Mn–N4	146.23(5)
N2–Mn–O21	105.57(5)	N1–Mn–N4	137.04(5)
N3–Mn–O21	88.43(5)		

Oxidation of $[Mn^{II}(L^7BQ)(OTf)_2]$ by H_2O_2. The electronic absorption spectrum of $[Mn^{II}(L^7BQ)(OTf)_2]$ in MeCN at 25 °C is featureless in the visible region, only showing the onset

of intense absorption features at wavelengths below 400 nm (Figure 2.3, left). The reaction of a 2.5 mM solution of $[Mn^{II}(L^7BQ)(OTf)_2]$ with 5 equiv. H_2O_2 and 1.0 equiv. Et_3N in MeCN at -40 ^oC gives rise to a new species characterized by two prominent absorption bands centered at 450 nm (ε = 260 M^{-1} cm^{-1}) and 660 nm (ε = 75 M^{-1} cm^{-1}; Figure 2.3, left).[74] The intensity of the feature at 450 nm and the peak to trough ratio between 560 and 660 nm were observed to vary to a small degree between sample preparations (0.7:1 – 1:1), due to the temperature sensitive nature of the peroxo. The positions and intensities of the bands at 450 and 660 nm are strikingly similar to those of other side-on peroxomanganese(III) complexes prepared using analogous N4 ligands and similar reaction conditions.[31-32, 34] The mass spectrum of the solution of $[Mn^{II}(L^7BQ)(OTf)_2]$ following treatment with H_2O_2 and Et_3N displays an ion peak at 441.1135 *m/z* (Figure A2.7), which compares well with that expected for $[Mn^{III}(O_2)(L^7BQ)]^+$ (calc. = 441.1123 *m/z*). When $H_2{}^{18}O_2$ was used to generate the peroxo intermediate, the corresponding ion peak shifted to 445.1156 *m/z* (Figure A2.8), providing further evidence for the presence of a peroxo ligand derived from H_2O_2. It should be noted that these peaks corresponding to the Mn^{III}-peroxo intermediates are of modest intensity in the mass spectrometric data collected at room temperature. This is anticipated, given the low thermal stability of this intermediate at temperatures higher than -40 ^oC (*vide infra*).

The $[Mn^{III}(O_2)(L^7BQ)]^+$ complex was further characterized by X-band EPR spectroscopy. As integer spin systems, high-spin Mn^{III} centers (S = 2) do not show signals in perpendicular-mode EPR experiments. Parallel-mode signals have been observed for some, but certainly not all, of the reported Mn^{III}-peroxo adducts.[37, 40-41, 75] A moderate zero-field splitting can render Mn^{III} centers silent even in parallel-mode at X-band frequencies. In contrast, mononuclear Mn^{II} and spin-coupled $Mn^{II}Mn^{III}$ and $Mn^{III}Mn^{IV}$ adducts will show prominent signals in perpendicular mode.

The perpendicular-mode EPR spectrum of $[Mn^{II}(L^7BQ)(OTf)_2]$ shows a positive feature at ca. 220 mT and a six-line signal centered near 350 mT. The six-line signal shows an average hyperfine splitting of 9.3 mT. The parallel-mode X-band EPR spectrum of $[Mn^{III}(O_2)(L^7BQ)]^+$ shows no features at 5 K, which can occur for Mn^{III} compounds with large zero-field splitting (Figure A2.9, top right).[76] The perpendicular mode X-band EPR spectra of $[Mn^{III}(O_2)(L^7BQ)]^+$ collected at 5 K (the red trace in Figure 2.3, right), reveals a low-intensity derivative-shaped signal at 350 mT and a weak feature at 220 mT (this latter feature is more apparent in a zoomed-in spectrum shown in Figure A2.9, bottom). These signals are most likely associated with unreacted $[Mn^{II}(L^7BQ)(OTf)_2]$, as an overlay of the perpendicular-mode EPR spectra of $[Mn^{II}(L^7BQ)(OTf)_2]$ with that of the $[Mn^{III}(O_2)(L^7BQ)]^+$ solution reveal strong similarities (Figure A2.9, bottom). The dominant hyperfine features of $[Mn^{II}(L^7BQ)(OTf)_2]$ are retained in the perpendicular-mode spectrum of the $[Mn^{III}(O_2)(L^7BQ)]^+$ solution (splitting of 9.7 mT). The additional fine structure (with a smaller splitting of 6.5 mT) could be due to superhyperfine interactions associated with the nitrogen ligands of L^7BQ, which are now resolved due to the lower concentration of Mn^{II}. Importantly, spin quantification shows that the perpendicular-mode EPR signal observed for the solution of $[Mn^{III}(O_2)(L^7BQ)]$ represents only 10% of the total Mn. Thus, the EPR signal arises from a minority species, clearly establishing that the bulk of Mn in the $[Mn^{III}(O_2)(L^7BQ)]^+$ solution is EPR silent.

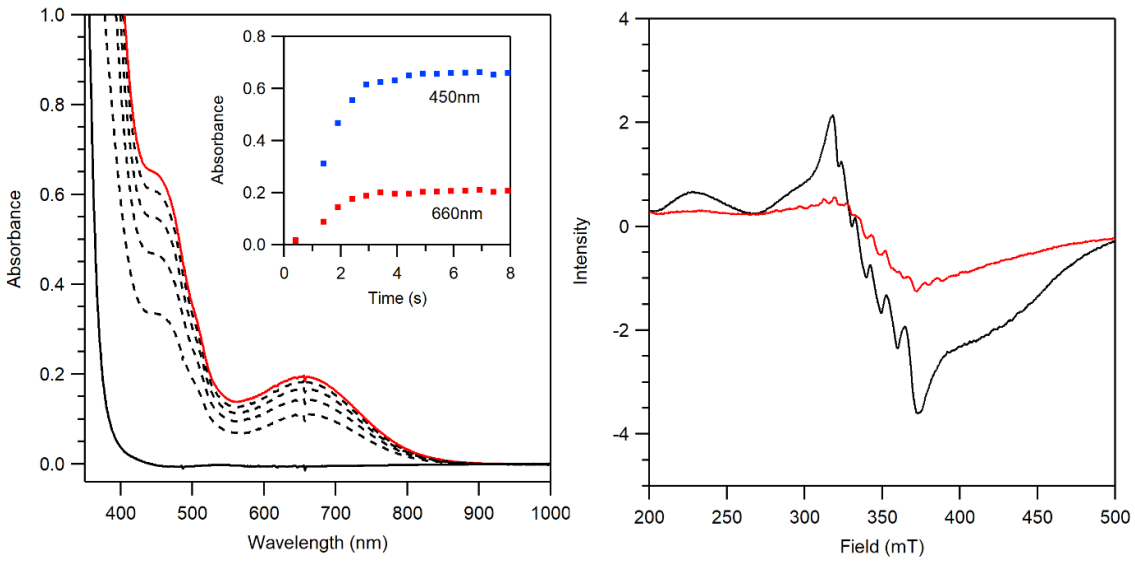

Figure 2.3. Left: Electronic absorption spectral changes of $[Mn^{II}(L^7BQ)(OTf)_2]$ (solid black trace) upon the addition of 5 equiv. H_2O_2 and 1.0 equiv. Et_3N in MeCN at -40 °C. Inset: Time evolution of absorption features at 450 nm and 660 nm. Right: Perpendicular mode X-band EPR spectra corresponding to 2.5 mM frozen MeCN solutions of $[Mn^{II}(L^7BQ)(OTf)_2]$ (solid black trace) and $[Mn^{III}(O_2)(L^7BQ)]^+$ (solid red trace) collected at 5 K.

XAS Characterization of $[Mn^{III}(O_2)(L^7BQ)]^+$. The $[Mn^{II}(L^7BQ)(OTf)_2]$ and $[Mn^{III}(O_2)(L^7BQ)]^+$ complexes showed Mn K-edge values of 6547.8 and 6549.2 eV, respectively (Table 2.2). The 1.6 eV lower edge energy for $[Mn^{II}(L^7BQ)(OTf)_2]$ compared to $[Mn^{III}(O_2)(L^7BQ)]^+$ is consistent with the higher Mn oxidation state for the latter complex. The edge shift is somewhat lower than that observed for other Mn^{II} and Mn^{III}-peroxo pairs (3.2 and 2.4 eV; see Table 2.2). However, the sample size for comparison is small, and the Mn^{II} complexes in these pairs all have different ligand spheres. Thus, variations in the Mn^{II} edges due to the different coordination environments could influence the observed shift between the Mn^{II} and Mn^{III}-peroxo species.

The pre-edge region of $[Mn^{II}(L^7BQ)(OTf)_2]$ shows one weak band at 6540.3 eV, with an area of 6.8 units. The pre-edge transitions of Mn coordination complexes arise from Mn 1s-to-3d transitions. These transitions are electric-dipole forbidden and, for low-symmetry complexes, their

intensity predominantly derives from Mn 3d-4p mixing aided by structural deviations from centrosymmetry. The small pre-edge area of $[Mn^{II}(L^7BQ)(OTf)_2]$ is consistent with a small degree of Mn 3d-4p mixing, as expected on the basis of the XRD structure (Figure 2.2). In contrast, the pre-edge region of $[Mn^{III}(O_2)(L^7BQ)]^+$ shows a prominent pre-edge peak at 6540.4 eV, with a shoulder at 6542.3 eV (Figure 2.4, inset). The total area of these peaks are 20.8 units, which is greatly increased relative to that of $[Mn^{II}(L^7BQ)(OTf)_2]$ (Table 2.2 and Figures 2.4 and A2.10). We had previously reported a ca. 2.5-fold increase in pre-edge area for the $[Mn^{III}(O_2)(Me_2EBC)]^+$ complex compared to its $[Mn(Cl)_2(Me_2EBC)]$ analogue (Table 2.2).[43] The intensity increase observed for the Mn^{II} and Mn^{III}-peroxo pair of the L^7BQ ligand is comparable, with a ca. 3-fold larger area for the latter complex.

Table 2.2. Edge and Pre-edge Energies (eV), Pre-edge Peak Heights and Areas for Mn^{II} and Mn^{III}-peroxo Complexes.

complex	medium	edge energy	pre-edge energy	height	area	reference
$[Mn^{II}(L^7BQ)(OTf)_2]$	MeCN	6547.8	6540.3	0.022	6.8	[a]
$[Mn^{III}(O_2)(L^7BQ)]^+$	MeCN	6549.2	6540.4, 6542.3	0.031, 0.056	20.8	[a]
$[Mn^{II}(Cl)_2(Me_2EBC)]$	solid	6547.1	6540.8	0.041	3.9	77
$[Mn^{III}(O_2)(Me_2EBC)]^+$	CH_2Cl_2	6550.3	6540.8	0.051	9.5	43
$[Mn^{II}(13\text{-TMC})]^{2+}$ [b]	CH_3CN	6545.5	NR [c]	NR [c]	NR [c]	78
$[Mn^{III}(O_2)(13\text{-TMC})]^+$ [b]	CH_3CN	6547.9	NR [c]	NR [c]	NR [c]	78

[a] This work. [b] 13-TMC = 1,4,7,10-tetramethyl-1,4,7,10-tetraazacyclotridecane. [c] Not reported.

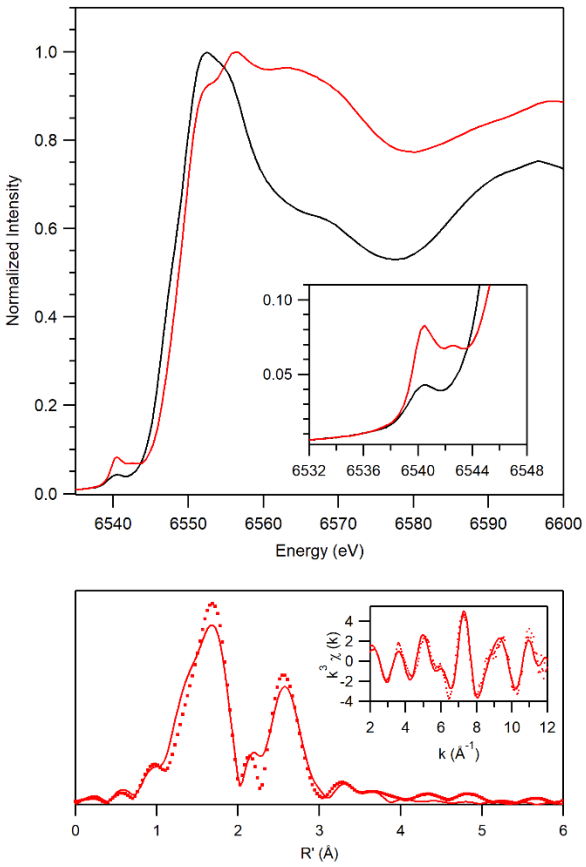

Figure 2.4. Top: Overlay of XANES regions for $[Mn^{II}(L^7BQ)(OTf)_2]$ (black) and $[Mn^{III}(O_2)(L^7BQ)]^+$ (red). Bottom: Fourier transform of Mn K-edge EXAFS data and raw EXAFS spectra (insets), experimental (···) and fits (—), for $[Mn^{III}(O_2)(L^7BQ)]^+$. The parameters used for the EXAFS fit are in Table 2.3.

The Fourier transform EXAFS spectrum of $[Mn^{III}(O_2)(L^7BQ)]^+$ consists of a prominent peak near 1.6 Å and a weaker feature at 2.7 Å (Figure 2.4, bottom). Results of fits to these data to obtain Mn-scatterer distances are summarized in Table 2.3. These features are best fit with an O shell at 1.85 Å (number of scatterers, n = 2), one N shell at 2.22 Å (n = 4) and two C shells at 3.10 and 3.59 Å (n = 5 and 3, respectively). The Mn–O distances are on the short end of those observed for crystallographically characterized Mn^{III}-peroxo adducts (Mn–O distances of 1.841 – 1.901 Å), while the Mn–N distances are typical for high-spin Mn^{III} complexes with amine, pyridine, and quinoline ligands.[12]

Table 2.3. EXAFS fitting results for $[Mn^{III}(O_2)(L^7BQ)]^+$ in MeCN ($\Delta k = 10$ Å^{-1}).

	Mn-O/N			Mn-N			Mn-C				
fit	n	r(Å)	σ^2	n	r(Å)	σ^2	n	r(Å)	σ^2	E_0	R
1	0			6	2.07	0.00404				-47.79	0.41
2	2	1.85	0.00413	4	2.22	0.00722				3.58	0.28
3	2	1.85	0.00367	4	2.23	0.00819	4	3.10	0.08631	4.87	0.13
4	2	1.85	0.00376	4	2.22	0.00792	4	3.59	0.00705	4.13	0.12
							6	3.10	0.00394		
5	2	1.85	0.00373	4	2.22	0.00802	3	3.59	0.00457	4.35	0.12
							6	3.10	0.00388		
6	**2**	**1.85**	**0.00373**	**4**	**2.22**	**0.00799**	**3**	**3.59**	**0.00420**	**4.13**	**0.11**
							5	**3.10**	**0.00256**		

DFT Structure of $[Mn^{III}(O_2)(L^7BQ)]^+$ and Pre-edge Properties from Time-Dependent (TD) DFT Computations. The structure of the L^7BQ ligand provides two unique faces for the peroxo unit to bind to the manganese center, one on the side of the ethyl linker and the other on the side of the propyl linker. Structures for these isomeric forms of $[Mn^{III}(O_2)(L^7BQ)]^+$ were optimized (Figure A2.11), and the structure with the peroxide bound on the propyl face is calculated to be 5 kcal mol^{-1} lower in energy than the structure with the peroxide bound on the ethyl face. This result is in agreement with similar computations for $[Mn^{III}(O_2)(L^7py_2^H)]^+$.[31] All values discussed here are from the lower energy structure of $[Mn^{III}(O_2)(L^7BQ)]^+$, but simulated XANES for both complexes are given in the Supporting Information (Figure A2.12). TD-DFT simulated UV-vis absorption spectra of $[Mn^{III}(O_2)(L^7BQ)]^+$ with the peroxide bound on the propyl face are also included in the Supporting Information (Figure A2.13).

Metric parameters for the DFT structure of $[Mn^{III}(O_2)(L^7BQ)]^+$ species with the peroxide bound on the propyl face are reported in the Supporting Information (Table A2.2). The Mn–O bond lengths are 1.862 Å and 1.856 Å, while the O–O bond is 1.418 Å. The calculated Mn–O distances are in excellent agreement with the best fit of the experimental EXAFS data, which included a 2 atom O shell at 1.85 Å (Table 2.3). The calculated Mn–O and O–O distances also

agree well with corresponding bond lengths for crystallographically characterized Mn^{III}-peroxo complexes, in which the Mn–O and O–O bond lengths range from 1.838 to 1.901 Å and 1.402 to 1.43 Å respectively.[12, 22-27] Additionally, the average Mn–N bond lengths of 2.22 Å for the DFT model of $[Mn^{III}(O_2)(L^7BQ)]^+$ is the same as the Mn–N distances from EXAFS (2.22 Å; see Table 2.3) and is accordant with corresponding bond lengths of other high-spin Mn^{III} complexes with nitrogen-based ligands. The two C shells from EXAFS analysis at 3.10 and 3.59 Å (n = 5 and 3, respectively) are also in good agreement with average distances of the closest carbons from the L^7BQ ligand determined in the DFT optimized structure, which come from the propyl and ethyl arms of the diazocycloalkane backbone as well as from several carbon atoms from the quinoline moieties (DFT distances of 2.98 – 3.54 Å).

The TD-DFT calculated pre-edge spectra for $[Mn^{III}(O_2)(L^7BQ)]^+$ shows two overlapping bands with energies of 6540.2 and 6541 eV, which is similar to the two peaks seen in the experimental pre-edge spectrum at 6540.8 and 6542.3 eV. Using a coordinate system where the Mn^{III}-O_2 unit lies in the xy plane, the first peak arises from excitations into the Mn^{III} β-$3d_{yz}$, $3d_{x2-y2}$, and $3d_{xz}$ orbitals, and the second peak arises from excitations into the Mn^{III} α-$3d_{xy}$ orbital and the Mn^{III} β-$3d_{z2}$ and $3d_{xy}$ orbitals (where α and β refer to majority and minority spin electrons, respectively). The calculated pre-edge area of 14.7 units underestimates the experimentally determined pre-edge area of 20.8 units, but reproduces an increase in area when compared to that previously calculated for the $[Mn^{III}(O_2)(Me_2EBC)]^+$ complex (Table 2.4). The summed Mn 4p character in the Mn 3d-based orbitals involved in the six pre-edge transitions of $[Mn^{III}(O_2)(L^7BQ)]^+$ is 3.6%, with significant contributions from multiple Mn^{III}-based orbitals. This 4p-3d mixing across the Mn^{III} 3d-manifold implies that geometric distortions induced by both the peroxo and L^7BQ ligands drive the large pre-edge area of $[Mn^{III}(O_2)(L^7BQ)]^+$. This mechanism

for orbital mixing is different than $[Mn^{III}(O_2)(Me_2EBC)]^+$, where a sizeable 4p contribution was observed only in the Mn–O peroxo σ-antibonding MO.[43]

Table 2.4. Experimental and TD-DFT-calculated Pre-edge Area and Mn 4p Contributions for $[Mn^{III}(O_2)(L^7BQ)]^+$ and $[Mn^{III}(O_2)(Me_2EBC)]^+$**.**

	experimental			calculated			ref
complex	pre-edge energy	height	area	pre-edge energy	area	Mn 4p (%)	
$[Mn^{III}(O_2)(L^7BQ)]^+$	6540.4	0.03	21	6540.2	14.7	3.6	[a]
	6542.3	0.06		6541			
$[Mn^{III}(O_2)(Me_2EBC)]^+$	6540.8	0.05	9.5	6541	6.1	3.0 [b]	43

[a]This work. [b]The percent Mn 4p-character differs from the previously published values; after re-evaluation of the computational output, it was determined that the previous value was in error.

Stability and Thermal Decay of $[Mn^{III}(O_2)(L^7BQ)]^+$. A 2.5 mM solution of $[Mn^{III}(O_2)(L^7BQ)]^+$ prepared using 5 equiv. H_2O_2 and 1.0 equiv. Et_3N in MeCN at -40 °C decays slowly over the course of an hour, with a half-life of ca. 10 minutes. In comparison, the $[Mn^{III}(O_2)(L^7py_2)]^+$ complex is shown to be stable for several hours at -40 °C ($t_{1/2}$ = 15 minutes at 0 °C), and the identity of the decay product was not determined.[31] The decay of $[Mn^{III}(O_2)(L^7BQ)]^+$ is characterized by an increase in absorbance at 450 and 550 nm, as shown in Figure 2.5. The perpendicular-mode X-band EPR spectrum of this decay species is quite similar to that of $[Mn^{III}(O_2)(L^7BQ)]^+$, showing only a low-intensity derivative-shaped signal at 350 mT, with a multi-line hyperfine pattern indicative of a multinuclear manganese species along with no features in parallel mode (see Figure A2.14). These data suggest that the decay product is EPR silent. Thus, the decay product could be a separate monomeric Mn^{III} species or an $S = 0$ antiferromagnetically coupled dimer. The rate of decay of $[Mn^{III}(O_2)(L^7BQ)]^+$ is sensitive to the amount of base used to prepare the Mn^{III}-peroxo adduct, as $[Mn^{III}(O_2)(L^7BQ)]^+$ formed using triethylamine in excess of 1.0 equiv. is observed to decay more rapidly.

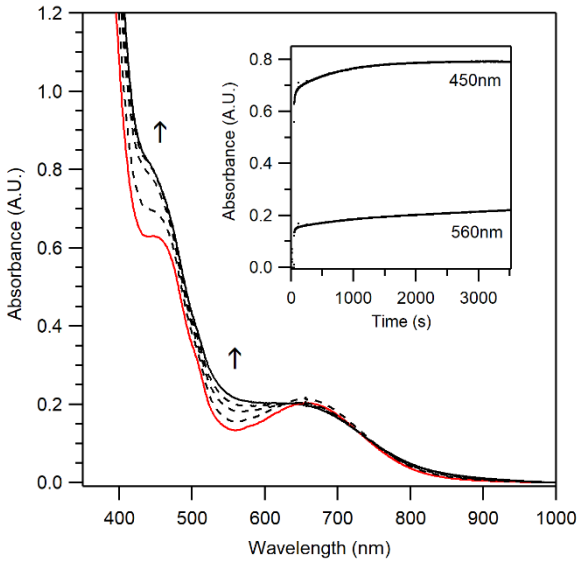

Figure 2.5. Electronic absorption spectral changes upon the self-decay of $[Mn^{III}(O_2)(L^7BQ)]^+$ (solid red trace) at -40°C in MeCN. Inset: Time evolution of absorption features at 450 nm and 560 nm, which highlights the formation of a decay species over 50 minutes.

We have previously reported that the decay pathways of the Mn^{III}-peroxo adducts $[Mn^{III}(O_2)(\kappa^4\text{-N4py})]^+$ and $[Mn^{III}(O_2)(Me_2EBC)]^+$ proceed by reaction of the Mn^{III}-peroxo center with unreacted Mn^{II} starting material.[35, 43] To investigate if this decay pathway is possible for the $[Mn^{III}(O_2)(L^7BQ)]^+$ complex, we added 1.0 equiv. of $[Mn^{II}(L^7BQ)(OTf)_2]$ to $[Mn^{III}(O_2)(L^7BQ)]^+$ at -40°C, after the latter had maximally formed. We observed no change in the electronic absorption spectrum upon the addition of the Mn^{II} complex, and the $[Mn^{III}(O_2)(L^7BQ)]^+$ species continued along its self-decay path (see Figure A2.15). Thus, the decay of $[Mn^{III}(O_2)(L^7BQ)]^+$ does not occur by reaction with the Mn^{II} starting material.

We also explored the formation of $[Mn^{III}(O_2)(L^7BQ)]^+$ over a variety of temperatures (-40 °C to room temperature) in different solvents (including methanol, propionitrile, butyronitrile, ethanol, dichloromethane, tetrahydrofuran and 2-methyltetrahydrofuran). Of these solvents, $[Mn^{III}(O_2)(L^7BQ)]^+$ could only be generated in propionitrile, but the species was much less stable. When formed in propionitrile at -40 °C, the electronic absorption bands associated with the Mn^{III}-

peroxo species at 450 and 660 nm loses definition within 15 seconds, indicating a substantially more rapid decay in this solvent (the half-life here is estimated to be ca. 1 minute). The limited variability of the solvent and temperature for $[Mn^{III}(O_2)(L^7BQ)]^+$ formation has prevented additional spectroscopic characterization. For example, characterization of $[Mn^{III}(O_2)(L^7BQ)]^+$ by magnetic circular dichroism (MCD) spectroscopy is not feasible due to the poor glassing capabilities of MeCN. We have previously shown that MCD spectroscopy can provide useful insights into understanding the geometric and electronic structures of peroxomanganese(III) species.[28, 31, 34] Furthermore, unlike the closely related $[Mn^{III}(O_2)(L^7py_2^R)]^+$ series of peroxo compounds,[31, 34] $[Mn^{III}(O_2)(L^7BQ)]^+$ could not be generated using KO_2 as the oxidant.

Reactivity of $[Mn^{III}(O_2)(L^7BQ)]^+$ with aldehydes. When a 2.5 mM solution of $[Mn^{III}(O_2)(L^7BQ)]^+$ at -40 °C in MeCN is treated with an excess (165 equivalents) of cylcohexanecarboxaldehyde (CCA), the absorption features for the peroxomanganese(III) species decay (Figure 2.6, left). Analysis of the resulting solution by GC-MS showed cyclohexanone in 38% yield compared to the starting concentration of $[Mn^{II}(L^7BQ)(OTf)_2]$. The formation and percent yield of cyclohexanone are similar to those previously reported for CCA deformylation by other Mn^{III}-peroxo complexes.[32, 37] We attempted to investigate the kinetics of the reaction of $[Mn^{III}(O_2)(L^7BQ)]^+$ with CCA by following the disappearance of the Mn^{III}-peroxo electronic absorption bands at 450 and 660 nm (Figure 2.6, left). This approach was used previously to determine second-order rate constants for the reactions of $[Mn^{III}(O_2)(L^7py_2^R)]^+$ complexes with CCA.[31] However, the disappearance of the electronic absorption bands associated with $[Mn^{III}(O_2)(L^7BQ)]^+$ upon the addition of excess CCA did not follow pseudo-first-order behavior. Instead, we observed a rapid initial drop in absorption intensity within the first 5 seconds of the reaction, followed by a slow decay (Figure 2.6, left inset). Furthermore, this rapid drop led to the

appearance of a new chromophore, which we have termed intermediate A, with band maxima at 595 and 450 nm (Figure 2.6, left, blue trace). This kinetic behavior suggests that $[Mn^{III}(O_2)(L^7BQ)]^+$ shows an initial rapid reaction with CCA to give a new intermediate that then more slowly decays.

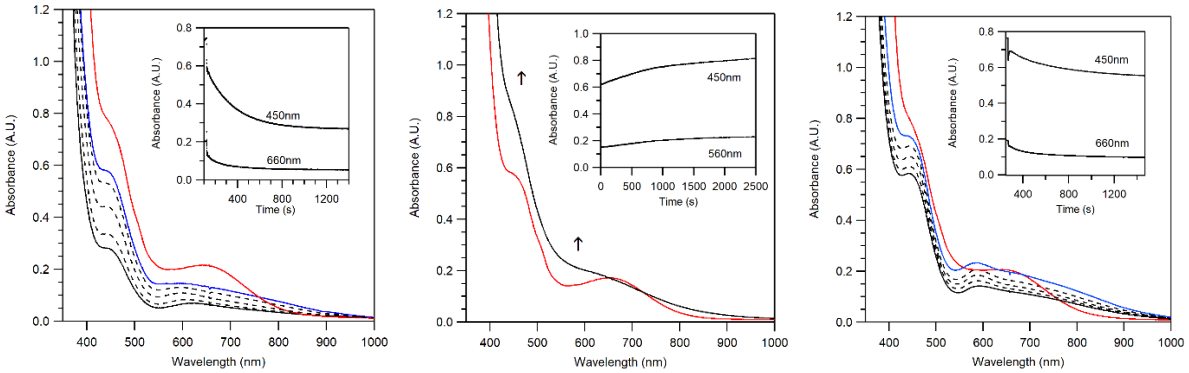

Figure 2.6. Left: Electronic absorption changes when 2.5 mM $[Mn^{III}(O_2)(L^7BQ)]^+$ are treated with 165 equiv. CCA in MeCN at -40°C. Center: Electronic absorption changes when 2.5 mM $[Mn^{III}(O_2)(L^7BQ)]^+$ are treated with 40 equiv. pure PPA in MeCN at -40°C. Right: Electronic absorption changes when 2.5 mM $[Mn^{III}(O_2)(L^7BQ)]^+$ are treated with 40 equiv. acid-contaminated PPA in MeCN at -40°C.

To better understand this deformylation chemistry, we also explored the reactivity of $[Mn^{III}(O_2)(L^7BQ)]^+$ with the aldehyde PPA. Unexpectedly, the addition of 40 equivalents of PPA to a 2.5 mM solution of $[Mn^{III}(O_2)(L^7BQ)]^+$ at -40 °C in MeCN did not show evidence of a reaction but instead followed the self-decay pathway of $[Mn^{III}(O_2)(L^7BQ)]^+$ (Figure 2.6, center). Additional analysis provided no evidence for the formation of the expected deformylation product (acetophenone) under these conditions. Further investigations showed that this lack of reactivity was highly dependent on the purity of PPA. Only in cases where PPA lacked any acid impurities did $[Mn^{III}(O_2)(L^7BQ)]^+$ fail to show a reaction with PPA. In cases where acid impurities were present (as assessed by ^{1}H-NMR investigations of PPA; see Figure A2.16), the addition of PPA to $[Mn^{III}(O_2)(L^7BQ)]^+$ resulted in electronic absorption changes very similar to those observed when $[Mn^{III}(O_2)(L^7BQ)]^+$ was treated with CCA. Specifically, the signals associated with

$[Mn^{III}(O_2)(L^7BQ)]^+$ show a rapid initial change to give an intermediate with features near 595 and 450 nm (blue trace), and this new chromophore would slowly decay (Figure 2.6, right). In addition, acetophenone formation was observed only for reactions of $[Mn^{III}(O_2)(L^7BQ)]^+$ with PPA containing acid contaminants.

On the basis of these observations, we attribute the initial rapid change in the electronic absorption spectrum of $[Mn^{III}(O_2)(L^7BQ)]^+$ when treated with CCA (or PPA with acid impurity) to a reaction of the Mn^{III}-peroxo unit with acid. McDonald and co-workers have noted that CCA commonly contains a small percentage of cyclohexanecarboxylic acid, which is challenging to completely remove by distillation.[79] ^{1}H-NMR experiments performed for CCA before and after distillation show the persistent of both formic acid and cyclohexanecarboxylic acid (Figure A2.17).

To test our hypothesis that an acid impurity accounts for the initial reaction of $[Mn^{III}(O_2)(L^7BQ)]^+$ with CCA, we investigated the reactivity of $[Mn^{III}(O_2)(L^7BQ)]^+$ with cyclohexanecarboxylic acid. For this reaction, we used concentrations of cyclohexanecarboxylic acid (2 equivalents relative to Mn) comparable to those present when 165 equivalents CCA are added to $[Mn^{III}(O_2)(L^7BQ)]^+$. From these experiments, we found that when a 2.5 mM solution of $[Mn^{III}(O_2)(L^7BQ)]^+$ is treated with 2.0 equivalents of cyclohexanecarboxylic acid in MeCN at -40 °C, the electronic absorption signals associated with $[Mn^{III}(O_2)(L^7BQ)]^+$ were replaced with new features at 580 and 450 nm (Figure 2.7, left). This process is complete within 10 seconds. The electronic absorption features of this new intermediate are almost identical to those of intermediate A (see Figure 2.7, right). Under these conditions, the intermediate formed from the reaction of $[Mn^{III}(O_2)(L^7BQ)]^+$ with cyclohexanecarboxylic acid is stable for over 100 seconds at -40 °C in MeCN, which permitted its further characterization by additional spectroscopic methods. On the

basis of the disappearance of the optical features of intermediate A, the half-life of this species is ca. 10 minutes.

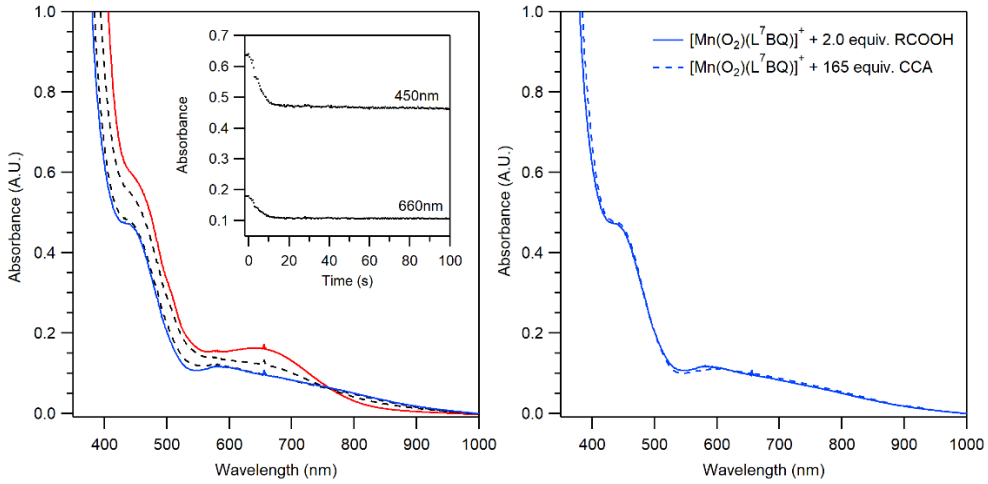

Figure 2.7. Left: Electronic absorption changes for $[Mn^{III}(O_2)(L^7BQ)]^+$ + 2 equiv. cyclohexanecarboxylic acid in MeCN at -40 °C to generate a new species (solid blue trace). Right: Overlay of electronic absorption features of the new species (solid blue trace) and intermediate A formed from the treatment of $[Mn^{III}(O_2)(L^7BQ)]^+$ with excess CCA (dashed blue trace).

Combined EPR and XAS characterization of intermediate A reveal spectroscopic signatures associated with $[Mn^{II}(L^7BQ)(OTf)_2]$ in MeCN. For example, no signals were observed for intermediate A in the parallel-mode spectrum at X-band frequency, but perpendicular-mode data revealed the presence of a six-line feature, centered at 350 mT, that is essentially identical in appearance to that of $[Mn^{II}(L^7BQ)(OTf)_2]$ in MeCN (Figure A2.18). Spin quantification of the 6-line signal of intermediate A relative to $[Mn^{II}(L^7BQ)(OTf)_2]$ in MeCN indicates that the signal represents 80 ± 15% of the Mn in the sample. However, as $[Mn^{II}(L^7BQ)(OTf)_2]$ is colorless, a minority species, which is not observed by EPR spectroscopy, must give rise to the electronic absorption signals of intermediate A at 450 and 595 nm. XAS data collected for intermediate A reveal XANES data significantly perturbed relative to $[Mn^{III}(O_2)(L^7BQ)]^+$, but very similar to those of $[Mn^{II}(L^7BQ)(OTf)_2]$ in MeCN (Figure A2.19). Notably, the XANES data of intermediate A are not identical to those of $[Mn^{II}(L^7BQ)(OTf)_2]$, suggesting the presence of additional Mn

species. Collectively, the EPR and XAS data suggest that the species responsible for the 450 and 595 nm electronic absorption bands of intermediate A represents a small fraction of the total Mn in the sample, with the bulk of Mn having reverted back to the Mn^{II} starting material.

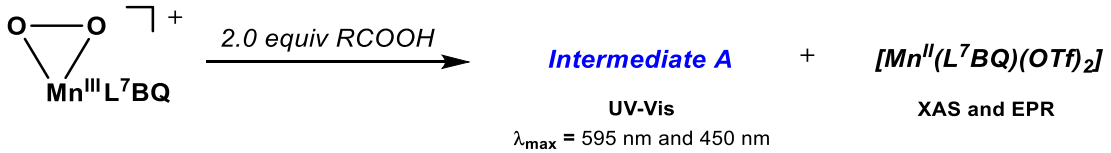

Scheme 2.4. Summary of reactivity observed upon addition of cyclohexanecaboxylic acid to $[Mn^{III}(O_2)(L^7BQ)]^+$.

As we can observe intermediate A by electronic absorption spectroscopy, we are able to monitor the response of this species to added aldehydes. When $[Mn^{III}(O_2)(L^7BQ)]^+$ with 2 equiv. cyclohexanecarboxylic acid are treated with 40 equivalents of PPA, we observe the formation of a small amount of acetophenone (10% relative to the starting Mn concentration). These observations suggest that intermediate A is competent for aldehyde deformylation.

2.4 Discussion

For a number of manganese-dependent enzymes, peroxomanganese(III) adducts are proposed as key intermediates. These peroxo-level centers are also proposed as important adducts for small-molecule manganese catalysts.[1-6, 15-16, 80] Unfortunately, the mechanistic understanding of these manganese-dependent biological processes are not as well understood as their analogous iron systems. There are examples of enzymatic studies for manganese systems, but there are numerous challenges involved. Often, enzyme active sites are buried deep within a protein environment. This requires the use of aqueous solutions, which limits the temperature at which these systems are investigated. Unfortunately, this makes it difficult to trap key intermediates that

may be important in the mechanism. The use of small-molecule model complexes of Mn enzymes allows for the use of a wider solvent scope, which also broadens the temperature range at which these reactive centers can be studied.[12, 34-35, 81-84] Although the most common type of Mn-peroxo species are η^2-peroxomanganese(III) complexes,[22-28, 31-41] η^1-alkylperoxomanganese(III), η^1-hydroperoxomanganese(III), and *trans*-μ-1,2-peroxo-bridged dimanganese(III,III) dimeric species have also been structurally and/ or spectroscopically characterized.[29-30, 85] However, characterization of the structural properties and chemical reactivity of these complexes is rather limited, because they often exhibit low chemical yields and impaired thermal stability.[12]

Sastri and co-workers have recently shown that a Mn^{III}-peroxo adduct supported by a neutral N_5 ligand is able to deformylate PPA by a hydrogen-atom transfer mechanism involving attack at the weak benzylic C–H bond of the substrate.[45] This work suggested that a Mn^{III}-peroxo adduct supported by a ligand with benzylic C–H bonds may be especially susceptible to ligand degradation. Motivated by these observations, we designed the L^7BQ ligand, which features a topology similar to that of the $L^7py_2^R$ family that has shown much success in supporting Mn^{III}-peroxo ligands, but lacks the benzylic arms, which may be prone to oxidation.[31-32, 34]

The Mn^{II} complex of the new L^7BQ ligand, $[Mn^{II}(L^7BQ)(OTf)_2]$, was structurally characterized by X-ray diffraction. As anticipated, the structure of this complex is similar to the related Mn^{II} salts of the $L^7py_2^R$ ligand family.[31-32, 34] When treated with 5 equiv. of H_2O_2 and 1.0 equiv. of triethylamine, $[Mn^{II}(L^7BQ)(OTf)_2]$ produced a new intermediate in MeCN solution at -40 °C. Electronic absorption and EPR spectroscopy, mass spectrometry, and Mn K-edge XAS data provide support for the formulation of this intermediate as the mononuclear Mn^{III}-peroxo adduct $[Mn^{III}(O_2)(L^7BQ)]^+$. This intermediate must be generated at cryogenic temperatures and decays over the course of 50 minutes at -40 °C in MeCN. Unlike several other Mn^{III}-peroxo adducts, the

decay of $[Mn^{III}(O_2)(L^7BQ)]^+$ does not appear to be through the reaction with the Mn^{II} starting material.

The half-life of $[Mn^{III}(O_2)(L^7BQ)]^+$ at -40 °C in MeCN is ca. 10 minutes. Thus, $[Mn^{III}(O_2)(L^7BQ)]^+$ does not display enhanced thermal stability relative to its $[Mn^{III}(O_2)(L^7py_2{}^R)]^+$ analogues (the $[Mn^{III}(O_2)(L^7py_2{}^H)]^+$ complex was stable for hours at -40 °C and had a half-life of 15 minutes at 0 °C).[31] For both $[Mn^{III}(O_2)(L^7BQ)]^+$ and $[Mn^{III}(O_2)(L^7py_2{}^R)]^+$ complexes, the products of thermal decay have not been identified.[31] In addition to the different thermal stabilities, the $[Mn^{III}(O_2)(L^7BQ)]^+$ complex also showed reactivity with aldehydes distinct from that of the $[Mn^{III}(O_2)(L^7py_2{}^R)]^+$ complexes. Treatment of the $[Mn^{III}(O_2)(L^7py_2{}^R)]^+$ complexes with aldehydes (such as CCA and benzaldehydes) led to a decay that followed pseudo-first-order behavior. Experiments using different concentrations of CCA showed an increased decay rate with increasing CCA concentration, which permitted the determination of second-order rate constants.[32]

Unlike those systems, the reaction of $[Mn^{III}(O_2)(L^7BQ)]^+$ and CCA did not follow pseudo-first-order kinetics. Instead, the addition of CCA led to the rapid formation of intermediate A, characterized by band maxima at 595 and 450 nm (Figure 2.6, left). This intermediate then slowly decayed. Nonetheless, analysis of the solution obtained at the end of the reaction provided evidence for roughly 40% cyclohexanone formation, suggestive of aldehyde deformylation. Additional experiments showed that the intermediate observed by electronic absorption spectroscopy (intermediate A) resulted from the reaction of $[Mn^{III}(O_2)(L^7BQ)]^+$ with acid impurity present in CCA.

McDonald and coworkers have previously emphasized the challenge in assigning the identity of the active metal species in reactions with aldehydes precisely because of the persistence of acid impurities in aldehyde substrates.[79] Our present observations underscore this point. Here,

we provide strong evidence that acid impurities in CCA convert the $[Mn^{III}(O_2)(L^7BQ)]^+$ species to a new, colored intermediate. Additional spectroscopic data also suggest the reaction of $[Mn^{III}(O_2)(L^7BQ)]^+$ with acid regenerates the corresponding Mn^{II} complex, with the chromophoric intermediate representing only ~20% of Mn in the sample (Scheme 2.4).

While the identity of this intermediate is unclear, we postulate that this new intermediate, and not $[Mn^{III}(O_2)(L^7BQ)]^+$, is responsible for the observed deformylation reactivity. Support for this proposal is provided by the reactions of $[Mn^{III}(O_2)(L^7BQ)]^+$ with PPA. When $[Mn^{III}(O_2)(L^7BQ)]^+$ is treated with purified PPA, lacking acid impurities, we observe no reaction. In contrast, when $[Mn^{III}(O_2)(L^7BQ)]^+$ is treated with PPA that contains acid impurities, we observe changes in the electronic absorption spectrum consistent with the formation of intermediate A, and this intermediate decays further. Moreover, $[Mn^{III}(O_2)(L^7BQ)]^+$ treated first with 2 equiv. cyclohexanecarboxylic acid and then PPA shows evidence for a small amount of acetophenone, the expected product of PPA deformylation.

One of several possibilities for the identity of intermediate A is a Mn^{III}-hydroxperoxo adduct. To the best of our knowledge, the only examples of well-characterized Mn^{III}-hydroxoperoxo adducts come from the work of Nam and coworkers.[78, 86] By protonating the corresponding Mn^{III}-peroxo species, they have generated the $[Mn^{III}(OOH)(14\text{-TMC})]^+$ and $[Mn^{III}(OOH)(13\text{-TMC})]^+$ complexes (where 13-TMC is 1,,4,7,10-tetramethyl-1,4,7,10-tetraazacyclotridecane and 14-TMC is 1,4,8,11-tetramethyl-1,4,8,11-tetraazacyclotetradecane).[78, 86] Kinetic investigations have revealed that the Mn^{III}-hydroperoxo adducts react more rapidly with CCA than their Mn^{III}-peroxo counterparts. Specifically, the second-order rate constants (k_2) for the reactions of $[Mn^{III}(OOH)(13\text{-TMC})]^+$ and $[Mn^{III}(O_2)(13\text{-TMC})]^+$ with CCA are, respectively, $1.2(1) \times 10^{-1}$ M^{-1} s^{-1} (at -10 °C) and $2.0(1) \times 10^{-2}$ M^{-1} s^{-1} (at 10 °C). In addition, the reaction of acid

with $[Mn^{III}(O_2)(14\text{-TMC})]^+$ to generate $[Mn^{III}(OOH)(14\text{-TMC})]^+$ was quite rapid compared to both of these processes. Thus, in cases where acid impurities are present in the aldehyde substrate, it could be that the metal-hydroperoxo adduct, rather than the metal-peroxo, is the active species for aldehyde deformylation.

Similar kinetic studies have been performed for iron systems, where there are also examples of interconversion of Fe^{III}-peroxo and Fe^{III}-hydroperoxo adducts using acid-base chemistry.[87-88] Most relevant to this present work are investigations of the reactivity of Fe^{III}-peroxo and Fe^{III}-hydroperoxo adducts of the 14-TMC ligand with aldehydes. Specifically, the $[Fe^{III}(OOH)(14\text{-TMC})]^+$ complex was observed to readily react with PPA at low temperatures, whereas the corresponding $[Fe^{III}(O_2)(14\text{-TMC})]^+$ complex only reacted with PPA at higher temperatures. The higher nucleophilic reactivity of the iron-hydroperoxo species was attributed to the end-on binding mode. The same trend was observed for electrophilic reactions, where the Fe^{III}-hydroperoxo was more active towards weak C–H bonds than the Fe^{III}-peroxo species.[88]

Thus, it has been seen in both Fe and Mn chemistry that metal(III)-peroxo and metal(III)-hydroperoxo adducts can have large, and somewhat unexpected, differences in reaction rates with aldehydes substrates. Given these collective observations, we echo McDonald in suggesting that the role of acid impurities in obfuscating understanding of aldehyde reactivity should be considered in all studies of aldehyde deformylation by metal-peroxo complexes.[79]

2.5 References

1. Miller, A.-F., Superoxide Dismutases: Active Sites that Save, but a Protein that Kills. *Curr. Opin. Chem. Biol.* **2004,** *8*, 162-168.

2. Grove, L. E.; Brunold, T. C., SECOND-SPHERE TUNING OF THE METAL ION REDUCTION POTENTIALS IN IRON AND MANGANESE SUPEROXIDE DISMUTASES. *Comments on Inorganic Chemistry* **2008,** *29* (5/6), 134-168.

3. Koehntop, K. D.; Emerson, J. P.; Que, L., Jr., The 2-His-1carboxylate facial triad: a versatile platform for dioxygen activation by mononuclear non-heme iron(II) enzymes. *J. Biol. Inorg. Chem.* **2005,** *10* (2), 87-93.

4. Gunderson, W. A.; Zatsman, A. I.; Emerson, J. P.; Farquhar, E. R.; Que, L.; Lipscomb, J. D.; Hendrich, M. P., Electron Paramagnetic Resonance Detection of Intermediates in the Enzymatic Cycle of an Extradiol Dioxygenase. *J. Am. Chem. Soc.* **2008,** *130* (44), 14465-14467.

5. Borowski, T.; Bassan, A.; Richards, N. G. J.; Siegbahn, P. E. M., Catalytic Reaction Mechanism of Oxalate Oxidase (Germin). A Hybrid DFT Study. *Journal of Chemical Theory and Computation* **2005,** *1* (4), 686-693.

6. Opaleye, O.; Rose, R.-S.; Whittaker, M. M.; Woo, E.-J.; Whittaker, J. W.; Pickersgill, R. W., Structural and Spectroscopic Studies Shed Light on the Mechanism of Oxalate Oxidase. *Journal of Biological Chemistry* **2006,** *281* (10), 6428-6433.

7. Tabares, L. C.; Gätjens, J.; Hureau, C.; Burrell, M. R.; Bowater, L.; Pecoraro, V. L.; Bornemann, S.; Un, S., pH-Dependent Structures of the Manganese Binding Sites in Oxalate Decarboxylase as Revealed by High-Field Electron Paramagnetic Resonance. *J. Phys. Chem. B* **2009,** *113* (26), 9016-9025.

8. Tanner, A.; Bowater, L.; Fairhurst, S. A.; Bornemann, S., Oxalate Decarboxylase Requires Manganese and Dioxygen for Activity: OVEREXPRESSION AND CHARACTERIZATION OF BACILLUS SUBTILIS YvrK AND YoaN. *J. Biol. Chem.* **2001,** *276* (47), 43627-43634.

9. Wu, A. J.; Penner-Hahn, J. E.; Pecoraro, V. L., Structural, Spectroscopic, and Reactivity Models for the Manganese Catalases. *Chem. Rev.* **2004,** *104* (2), 903-938.

10. Cotruvo, J. A.; Stich, T. A.; Britt, R. D.; Stubbe, J., Mechanism of Assembly of the Dimanganese-Tyrosyl Radical Cofactor of Class Ib Ribonucleotide Reductase: Enzymatic Generation of Superoxide Is Required for Tyrosine Oxidation via a Mn(III)Mn(IV) Intermediate. *J. Am. Chem. Soc.* **2013**.

11. Cotruvo, J. J. A.; Stubbe, J., Metallation and mismetallation of iron and manganese proteins in vitro and in vivo: the class I ribonucleotide reductases as a case study. *Metallomics* **2012,** *4* (10), 1020-1036.

12. Leto, D.; Jackson, T., Peroxomanganese complexes as an aid to understanding redox-active manganese enzymes. *Journal of Biological Inorganic Chemistry* **2014,** *19* (1), 1-15.

13. Baglia, R. A.; Zaragoza, J. P. T.; Goldberg, D. P., Biomimetic Reactivity of Oxygen-Derived Manganese and Iron Porphyrinoid Complexes. *Chem. Rev.* **2017,** *117* (21), 13320-13352.

14. Jasniewski, A. J.; Que, L., Dioxygen Activation by Nonheme Diiron Enzymes: Diverse Dioxygen Adducts, High-Valent Intermediates, and Related Model Complexes. *Chem. Rev.* **2018,** *118* (5), 2554-2592.

15. Sibbons, K. F.; Shastri, K.; Watkinson, M., The application of manganese complexes of ligands derived from 1,4,7-triazacyclononane in oxidative catalysis. *Dalton Trans.* **2006,** (5), 645-661.

16. Saisaha, P.; de Boer, J. W.; Browne, W. R., Mechanisms in manganese catalysed oxidation of alkenes with H_2O_2. *Chem. Soc. Rev.* **2013,** *42* (5), 2059-2074.

17. Ottenbacher, R. V.; Samsonenko, D. G.; Talsi, E. P.; Bryliakov, K. P., Enantioselective Epoxidations of Olefins with Various Oxidants on Bioinspired Mn Complexes: Evidence for Different Mechanisms and Chiral Additive Amplification. *ACS Catalysis* **2016,** *6* (2), 979-988.

18. Ottenbacher, R.; Talsi, E.; Bryliakov, K., Direct Selective Oxidative Functionalization of C–H Bonds with H_2O_2: Mn-Aminopyridine Complexes Challenge the Dominance of Non-Heme Fe Catalysts. *Molecules* **2016,** *21* (11), 1454.

19. Talsi, E. P.; Ottenbacher, R. V.; Bryliakov, K. P., Bioinspired oxidations of aliphatic C–H groups with H2O2 in the presence of manganese complexes. *Journal of Organometallic Chemistry* **2015,** *793*, 102-107.

20. Codola, Z.; Lloret-Fillol, J.; Costas, M., Aminopyridine iron and manganese complexes as molecular catalysts for challenging oxidative transformations. *Prog. Inorg. Chem.* **2014,** *59* (Copyright (C) 2016 American Chemical Society (ACS). All Rights Reserved.), 447-531.

21. Company, A.; Lloret-Fillol, J.; Costas, M. In *Small molecule models for nonporphyrinic iron and manganese oxygenases*, Elsevier B.V.: 2013; pp 487-564.

22. VanAtta, R. B.; Strouse, C. E.; Hanson, L. K.; Valentine, J. S., [Peroxotetraphenylporphinato]manganese(III) and [Chlorotetraphenylporphinato]manganese(II) Anions. Synthesis, Crystal Structures, and Electronic Structures. *J. Am. Chem. Soc.* **1987,** *109*, 1425-1434.

23. Kitajima, N.; Komatsuzaki, H.; Hikichi, S.; Osawa, M.; Moro-oka, Y., A Monomeric Side-On Peroxo Manganese(III) Complex: $Mn(O_2)(3,5\text{-}iPr_2pzH)(HB(3,5\text{-}iPr_2pz)_3)$. *J. Am. Chem. Soc.* **1994,** *116*, 11596-11597.

24. Singh, U. P.; Sharma, A. K.; Hikichi, S.; Komatsuzaki, H.; Moro-oka, Y.; Akita, M., Hydrogen bonding interaction between imidazolyl N-H group and peroxide: Stabilization of Mn(III)-peroxo complex $Tp^{iPr2}Mn(\eta^2\text{-}O_2)(im^{Me}H)$ ($im^{Me}H$ = 2-methylimidazole). *Inorg. Chim. Acta* **2006,** *359*, 4407-4411.

25. Seo, M. S.; Kim, J. Y.; Annaraj, J.; Kim, Y.; Lee, Y.-M.; Kim, S.-J.; Kim, J.; Nam, W., [Mn(tmc)(O2)]+: A Side-On Peroxido Manganese(III) Complex Bearing a Non-Heme Ligand. *Angew. Chem., Int. Ed.* **2007,** *46* (3), 377-380.

26. Annaraj, J.; Cho, J.; Lee, Y.-M.; Kim, S. Y.; Latifi, R.; de Visser, S. P.; Nam, W., Structural Characterization and Remarkable Axial Ligand Effect on the Nucleophilic Reactivity of a Nonheme Manganese(III)-Peroxo Complex. *Angew. Chem. Int. Ed.* **2009,** *48* (23), 4150-4153.

27. Kang, H.; Cho, J.; Cho, K.-B.; Nomura, T.; Ogura, T.; Nam, W., Mononuclear Manganese–Peroxo and Bis(μ-oxo)dimanganese Complexes Bearing a Common N-Methylated Macrocyclic Ligand. *Chem.--Eur. J.* **2013**, n/a-n/a.

28. Colmer, H. E.; Geiger, R. A.; Leto, D. F.; Wijeratne, G. B.; Day, V. W.; Jackson, T. A., Geometric and electronic structure of a peroxomanganese(iii) complex supported by a scorpionate ligand. *Dalton Trans.* **2014,** *43*, 17949-17963.

29. Coggins, M. K.; Kovacs, J. A., Structural and Spectroscopic Characterization of Metastable Thiolate-Ligated Manganese(III)–Alkylperoxo Species. *J. Am. Chem. Soc.* **2011,** *133* (32), 12470-12473.

30. Coggins, M. K.; Martin-Diaconescu, V.; DeBeer, S.; Kovacs, J. A., Correlation Between Structural, Spectroscopic, and Reactivity Properties Within a Series of Structurally Analogous Metastable Manganese(III)–Alkylperoxo Complexes. *J. Am. Chem. Soc.* **2013,** *135* (11), 4260-4272.

31. Geiger, R. A.; Chattopadhyay, S.; Day, V. W.; Jackson, T. A., A Series of Peroxomanganese(III) Complexes Supported by Tetradentate Aminopyridyl Ligands: Detailed Spectroscopic and Computational Studies. *Journal of the American Chemical Society* **2010,** *132* (8), 2821-2831.

32. Geiger, R. A.; Chattopadhyay, S.; Day, V. W.; Jackson, T. A., Nucleophilic reactivity of a series of peroxomanganese(III) complexes supported by tetradentate aminopyridyl ligands. *Dalton Trans.* **2011,** *40*, 1707-1715.

33. Geiger, R. A.; Leto, D. F.; Chattopadhyay, S.; Dorlet, P.; Anxolabéhère-Mallart, E.; Jackson, T. A., Geometric and Electronic Structures of Peroxomanganese(III) Complexes Supported by Pentadentate Amino-Pyridine and -Imidazole Ligands. *Inorg. Chem.* **2011,** *50* (20), 10190-10203.

34. Geiger, R. A.; Wijeratne, G.; Day, V. W.; Jackson, T. A., Steric and Electronic Influences on the Structures of Peroxomanganese(III) Complexes Supported by Tetradentate Ligands. *European Journal of Inorganic Chemistry* **2012**, 1598-1608.

35. Leto, D. F.; Chattopadhyay, S.; Day, V. W.; Jackson, T. A., Reaction landscape of a pentadentate N5-ligated MnII complex with O2[radical dot]- and H2O2 includes conversion of a peroxomanganese(iii) adduct to a bis([small mu]-oxo)dimanganese(iii,iv) species. *Dalton Trans.* **2013,** *42* (36), 13014-13025.

36. Borovik, A. S., Bioinspired Hydrogen Bond Motifs in Ligand Design: The Role of Noncovalent Interactions in Metal Ion Mediated Activation of Dioxygen. *Acc. Chem. Res.* **2004,** *38* (1), 54-61.

37. Shook, R. L.; Gunderson, W. A.; Greaves, J.; Ziller, J. W.; Hendrich, M. P.; Borovik, A. S., A Monomeric Mn^{III}-Peroxo Complex Derived Directly from Dioxygen. *J. Am. Chem. Soc.* **2008,** *130* (28), 8888-8889.

38. Shook, R. L.; Peterson, S. M.; Greaves, J.; Moore, C.; Rheingold, A. L.; Borovik, A. S., Catalytic Reduction of Dioxygen to Water with a Monomeric Manganese Complex at Room Temperature. *Journal of the American Chemical Society* **2011,** *133* (15), 5810-5817.

39. El Ghachtouli, S.; Vincent Ching, H. Y.; Lassalle-Kaiser, B.; Guillot, R.; Leto, D. F.; Chattopadhyay, S.; Jackson, T. A.; Dorlet, P.; Anxolabéhère-Mallart, E., Electrochemical formation of Mn^{III}-peroxo complexes supported by pentadentate amino pyridine and imidazole ligands. *Chem. Commun.* **2013,** *49* (50), 5696-5698.

40. Groni, S.; Blain, G.; Guillot, R.; Policar, C.; Anxolabéhère-Mallart, E., Reactivity of Mn^{II} with Superoxide. Evidence for a $[Mn^{III}OO]^{+}$ Unit by Low-Temperature Spectroscopies. *Inorg. Chem.* **2007,** *46* (6), 1951-1953.

41. Groni, S.; Dorlet, P.; Blain, G.; Bourcier, S.; Guillot, R.; Anxolabéhère-Mallart, E., Reactivity of an Aminopyridine $[LMn^{II}]^{2+}$ Complex with H_2O_2. Detection of Intermediates at Low Temperature. *Inorg. Chem.* **2008,** *47* (8), 3166-3172.

42. Sisemore, M. F.; Selke, M.; Burstyn, J. N.; Valentine, J. S., Metalloporphyrin Peroxo Complexes of Iron(III), Manganese(III), and Titanium(IV). Comparative Studies Demonstrating That the Iron(III) Complex Is Extremely Nucleophilic. *Inorg. Chem.* **1997,** *36* (6), 979-984.

43. Colmer, H. E.; Howcroft, A. W.; Jackson, T. A., Formation, Characterization, and O–O Bond Activation of a Peroxomanganese(III) Complex Supported by a Cross-Clamped Cyclam Ligand. *Inorg. Chem.* **2016,** *55* (5), 2055-2069.

44. Magherusan, A. M.; Zhou, A.; Farquhar, E. R.; García-Melchor, M.; Twamley, B.; Que, L.; McDonald, A. R., Mimicking Class I b Mn_2-Ribonucleotide Reductase: A Mn^{II}_2 Complex and Its Reaction with Superoxide. *Angew. Chem., Int. Ed. Engl.* **2018,** *57* (4), 918-922.

45. Barman, P.; Upadhyay, P.; Faponle, A. S.; Kumar, J.; Nag, S. S.; Kumar, D.; Sastri, C. V.; de Visser, S. P., Deformylation Reaction by a Nonheme Manganese(III)–Peroxo Complex via Initial Hydrogen-Atom Abstraction. *Angew. Chem., Int. Ed. Engl.* **2016,** *55* (37), 11091-11095.

46. Evans, D. F.; Jakubovic, D. A., Water-soluble hexadentate Schiff-base ligands as sequestrating agents for iron(III) and gallium(III). *J. Chem. Soc., Dalton Trans.* **1988,** (12), 2927-2933.

47. Bain, G. A.; Berry, J. F., Diamagnetic Corrections and Pascal's Constants. *J. Chem. Educ.* **2008,** *85* (4), 532.

48. Data Collection: SMART Software in APEX2 v2010.3-0 Suite. Bruker-AXS, E. C. P., Madison, WI 53711-5373 USA.

49. Data Reduction: SAINT Software in APEX2 v2010.3-0 Suite. Bruker-AXS, E. C. P., Madison, WI 53711-5373 USA.

50. International Tables for Crystallography, V. A., 4th ed., Kluwer: Boston (1996).

51. Refinement: SHELXTL v2010.3-0. Bruker-AXS, E. C. P., Madison, WI 53711-5373 USA.

52. Duke, F. R.; Haas, T. W., THE HOMOGENEOUS BASE-CATALYZED DECOMPOSITION OF HYDROGEN PEROXIDE1. *The Journal of Physical Chemistry* **1961,** *65* (2), 304-306.

53. George, G. N. *EXAFSPAK*, Stanford Synchrotron Radiation Laboratory; Stanford, CA, 1990.

54. Ravel, B.; Newville, M., ATHENA, ARTEMIS, HEPHAESTUS: data analysis for X-ray absorption spectroscopy using IFEFFIT. *J. Synchrotron Rad.* **2005,** *12* (4), 537-541.

55. Rehr, J. J.; Mustre de Leon, J.; Zabinsky, S. I.; Albers, R. C., Theoretical x-ray absorption fine structure standards. *Journal of the American Chemical Society* **1991,** *113* (14), 5135-5140.

56. Wojdyr, M., Fityk: a general-purpose peak fitting program. *J. Appl. Cryst.* **2010,** *43* (5 Part 1), 1126-1128.

57. Neese, F., Software update: the ORCA program system, version 4.0. *Wiley Interdisciplinary Reviews: Computational Molecular Science* **2018,** *8* (1), e1327.

58. Becke, A. D., Density-functional Thermochemistry. III. The Role of Exact Exchange. *J. Chem. Phys.* **1993,** *98* (7), 5648-5652.

59. Lee, C.; Yang, W.; Parr, R. G., Development of the Colle-Salvetti Correlation-energy Formula into a Functional of the Electron Density. *Phys. Rev. B* **1988,** *37* (2), 785-789.

60. Grimme, S.; Antony, J.; Ehrlich, S.; Krieg, H., A consistent and accurate ab initio parametrization of density functional dispersion correction (DFT-D) for the 94 elements H-Pu. *The Journal of Chemical Physics* **2010,** *132* (15), 154104.

61. Grimme, S.; Ehrlich, S.; Goerigk, L., Effect of the damping function in dispersion corrected density functional theory. *Journal of Computational Chemistry* **2011,** *32* (7), 1456-1465.

62. Weigend, F., Accurate Coulomb-fitting basis sets for H to Rn. *Physical Chemistry Chemical Physics* **2006,** *8* (9), 1057-1065.

63. Weigend, F.; Ahlrichs, R., Balanced basis sets of split valence, triple zeta valence and quadruple zeta valence quality for H to Rn: Design and assessment of accuracy. *Physical Chemistry Chemical Physics* **2005,** *7* (18), 3297-3305.

64. Marenich, A. V.; Cramer, C. J.; Truhlar, D. G., Universal Solvation Model Based on Solute Electron Density and on a Continuum Model of the Solvent Defined by the Bulk Dielectric Constant and Atomic Surface Tensions. *J. Phys. Chem. B* **2009,** *113* (18), 6378-6396.

65. Hirata, S.; Head-Gordon, M., Time-dependent Density Functional Theory for Radicals: An Improved Description of Excited States with Substantial Double Excitation Character. *Chem. Phys. Lett.* **1999,** *302*, 375-382.

66. Hirata, S.; Head-Gordon, M., Time-dependent Density Functional Theory within the Tamm–Dancoff Approximation. *Chem. Phys. Lett.* **1999,** *314*, 291-299.

67. Lenthe, E. v.; Baerends, E. J.; Snijders, J. G., Relativistic regular two-component Hamiltonians. *Journal of Chemical Physics* **1993,** *99* (6), 4597-4610.

68. van Wüllen, C., Molecular density functional calculations in the regular relativistic approximation: Method, application to coinage metal diatomics, hydrides, fluorides and chlorides, and comparison with first-order relativistic calculations. *Journal of Chemical Physics* **1998,** *109* (2), 392-399.

69. Roemelt, M.; Beckwith, M. A.; Duboc, C.; Collomb, M. N.; Neese, F.; DeBeer, S., Manganese K-edge X-ray absorption spectroscopy as a probe of the metal-ligand interactions in coordination compounds. *Inorg Chem* **2012,** *51* (1), 680-7.

70. Surry, D. S.; Buchwald, S. L., Dialkylbiaryl phosphines in Pd-catalyzed amination: a user's guide. *Chem. Sci.* **2011,** *2* (1), 27-50.

71. Childers, W. E.; Havran, L. M.; Asselin, M.; Bicksler, J. J.; Chong, D. C.; Grosu, G. T.; Shen, Z.; Abou-Gharbia, M. A.; Bach, A. C.; Harrison, B. L.; Kagan, N.; Kleintop, T.; Magolda, R.; Marathias, V.; Robichaud, A. J.; Sabb, A. L.; Zhang, M.-Y.; Andree, T. H.; Aschmies, S. H.; Beyer, C.; Comery, T. A.; Day, M.; Grauer, S. M.; Hughes, Z. A.; Rosenzweig-Lipson, S.; Platt, B.; Pulicicchio, C.; Smith, D. E.; Sukoff-Rizzo, S. J.; Sullivan, K. M.; Adedoyin, A.; Huselton, C.; Hirst, W. D., The Synthesis and Biological Evaluation of Quinolyl-piperazinyl Piperidines as Potent Serotonin 5-HT1A Antagonists. *J. Med. Chem.* **2010,** *53* (10), 4066-4084.

72. Ruiz-Castillo, P.; Buchwald, S. L., Applications of Palladium-Catalyzed C–N Cross-Coupling Reactions. *Chem. Rev.* **2016,** *116* (19), 12564-12649.

73. Leto, D. F.; Ingram, R.; Day, V. W.; Jackson, T. A., Spectroscopic properties and reactivity of a mononuclear oxomanganese(iv) complex. *Chem. Commun.* **2013,** *49* (47), 5378-5380.

74. These calculated extinction coefficients assume 100% conversion of the Mn^{II} species.

75. Shook, R. L.; Borovik, A. S., Role of the Secondary Coordination Sphere in Metal-Mediated Dioxygen Activation. *Inorg. Chem.* **2010,** *49* (8), 3646-3660.

76. Bencini, A.; Gatteschi, D., Inorganic Electronic Structure and Spectroscopy. In *Inorganic Electronic Structure and Spectroscopy*, Solomon, E. I.; Lever, A. B. P., Eds. John Wiley & Sons, Inc.: 2006; Vol. Volume I: Methodology, pp 93-155.

77. Leto, D. F.; Jackson, T. A., Mn K-Edge X-ray Absorption Studies of Oxo- and Hydroxo-manganese(IV) Complexes: Experimental and Theoretical Insights into Pre-Edge Properties. *Inorg. Chem.* **2014,** *53* (12), 6179-6194.

78. So, H.; Park, Y. J.; Cho, K.-B.; Lee, Y.-M.; Seo, M. S.; Cho, J.; Sarangi, R.; Nam, W., Spectroscopic Characterization and Reactivity Studies of a Mononuclear Nonheme Mn(III)–Hydroperoxo Complex. *Journal of the American Chemical Society* **2014,** *136* (35), 12229-12232.

79. Ure, A. D.; McDonald, A. R., Nucleophilic Reactivity of a Metal-Bound Superoxide Ligand. *Synlett* **2015,** *26* (15), 2060-2066.

80. Babcock, G. T. In *The oxygen-evolving complex in photosystem II as a metallo-radical enzyme*, Kluwer: 1995; pp 209-215.

81. Pecoraro, V. L.; Baldwin, M. J.; Gelasco, A., Interaction of Manganese with Dioxygen and Its Reduced Derivatives. *Chem. Rev.* **1994,** *94* (3), 807-826.

82. Goldsmith, C. R.; Cole, A. P.; Stack, T. D. P., C−H Activation by a Mononuclear Manganese(III) Hydroxide Complex: Synthesis and Characterization of a Manganese-Lipoxygenase Mimic *J. Am. Chem. Soc.* **2005,** *127* (27), 9904-9912.

83. Wijeratne, G. B.; Corzine, B.; Day, V. W.; Jackson, T. A., Saturation Kinetics in Phenolic O–H Bond Oxidation by a Mononuclear Mn(III)–OH Complex Derived from Dioxygen. *Inorg. Chem.* **2014,** *53* (14), 7622-7634.

84. Wijeratne, G. B.; Day, V. W.; Jackson, T. A., O-H bond oxidation by a monomeric MnIII-OMe complex. *Dalton Trans.* **2015,** *44* (7), 3295-3306.

85. Coggins, M. K.; Sun, X.; Kwak, Y.; Solomon, E. I.; Rybak-Akimova, E.; Kovacs, J. A., Characterization of Metastable Intermediates Formed in the Reaction between a Mn(II) Complex and Dioxygen, Including a Crystallographic Structure of a Binuclear Mn(III)–Peroxo Species. *J. Am. Chem. Soc.* **2013,** *135* (15), 5631-5640.

86. Sankaralingam, M.; Lee, Y.-M.; Jeon, S. H.; Seo, M. S.; Cho, K.-B.; Nam, W., A mononuclear manganese(iii)-hydroperoxo complex: synthesis by activating dioxygen and reactivity in electrophilic and nucleophilic reactions. *Chem. Commun.* **2018,** *54* (10), 1209-1212.

87. Y. N. Ho, R.; Que Jr, L.; Roelfes, G.; L. Feringa, B.; Hermant, R.; Hage, R., Resonance Raman evidence for the interconversion between an $[Fe^{III}–\eta^1\text{-}OOH]^{2+}$ and $[Fe^{III}–\eta^2\text{-}O_2]+$ species and mechanistic implications thereof. *Chem. Commun.* **1999,** (21), 2161-2162.

88. Cho, J.; Jeon, S.; Wilson, S. A.; Liu, L. V.; Kang, E. A.; Braymer, J. J.; Lim, M. H.; Hedman, B.; Hodgson, K. O.; Valentine, J. S.; Solomon, E. I.; Nam, W., Structure and reactivity of a mononuclear non-haem iron(III)–peroxo complex. *Nature* **2011,** *478*, 502.

Chapter 3. Tuning of the Equatorial Ligand Field for a Series of Mn^{IV}-Oxo Complexes

3.1 Introduction

High-valent Mn centers have been suggested as active oxidants for biological systems as well as synthetic catalysts. In nature, the oxygen-evolving complex (OEC) of photosystem II (PSII) utilizes four Mn ions as cofactors to catalyze the splitting of water into protons, electrons, and molecular oxygen.[1] Unfortunately, efforts to understand the mechanism for such biological processes is thwarted by the difficulty associated with trapping important enzymatic intermediates. Thus, the use of small molecule model complexes can aid in the characterization of otherwise reactive centers. Ligand scaffolds can be designed specifically to enhance stability and allow for characterization with a wide range of techniques. However, it can be difficult to generate stabilized intermediates that are still able to perform interesting chemical transformations.

To date, there are several reports of Mn^{IV}-oxo adducts that been characterized using spectroscopic techniques. Many of these centers have been shown to be efficient catalysts for a variety of oxidative transformations, including hydrogen atom transfer (HAT) and oxygen atom transfer (OAT).[2-9] There are a wide range of ligand types that have been utilized to support Mn^{IV}-oxo adducts, specifically nonporphyrinoid ligand scaffolds. Some centers slow sluggish reactivity towards highly activated C–H bonds, where in contrast, some centers have been shown to abstract the strong C–H bonds of toluene or cylcohexane.[2, 5-6, 10-15] The coordination motif, charge and geometry of the supporting ligand can have huge effects on the overall reactivity of Mn^{IV}-oxo species. Unfortunately, these large variations in supporting ligand scaffolds, as well as the varied reaction conditions reported, make it difficult to rationalize any observed reactivity trends.

Compared to other examples in the literature, the pentadentate ligands N4py and Bn-TPEN support Mn^{IV}-oxo species that show greatly enhanced reactivity.[2, 12, 16] Our group has previously proposed that the enhanced reactivity of $[Mn^{IV}(O)(N4py)]^{2+}$ could be based on thermodynamic

arguments, as the Mn $^{III/IV}$ reduction potential ($E_{1/2}$) is ~700 mV higher than those of other Mn^{IV}-oxo species.[4, 10-11] Unfortunately, the pK_a values for reactive Mn^{IV}-oxo centers are not reported, so the Mn^{III}-OH BDFE cannot be determined. Alternatively, density functional theory (DFT) studies performed by Nam and Shaik suggest that this enhanced reactivity of $[Mn^{IV}(O)(N4py)]^{2+}$ and $[Mn^{IV}(O)(Bn\text{-}TPEN)]^{2+}$ is due to a ^4E excited state that allows access to a lower barrier for both HAT and OAT compared to reactivity from the $^4B_1$ ground state.[17-18] With the help of magnetic circular dichroism, our group has recently assigned this ^4E excited state to a near-IR electronic absorption band at 950 nm.[19] Based on this reactivity model, the near-IR feature for these Mn^{IV}-oxo species could be used to predict reactivity prior to kinetic investigation.

To test this model, and systematically probe how ligand-field perturbations influence Mn^{IV}-oxo reactivity, our group has introduced ligand perturbations to the N4py scaffold. By functionalizing the picolyl arms of the parent N4py scaffold, the equatorial ligand field can be altered while keeping the pentadentate N_5 binding motif constant. The use of varied steric and electronic properties allows for tuning of the equatorial field strength (Figure 3.1). Specifically, the electron-rich di-3,5-methyl-4-methoxyl-pyridyl groups of the ^{DMM}N4py derivative (where DMM = dimethyl-methoxy) serve to strengthen the ligand field surrounding the Mn^{IV}-oxo adduct and results in a shift of the near-IR band to higher energy (Figure 3.2, left). In contrast, the systematic introduction of one and two quinoline groups for N3pyQ and 2pyN2Q respectively weaken the equatorial field through crowding of the oxo adduct. Spectroscopically, the introduction of the steric bulk results in shifts of the near-IR bands to lower energies (Figure 3.2, left). In addition to tuning the ligand field for these complexes, our group has found that these perturbations greatly affect HAT and OAT reactivity. Specifically, we have observed that a weaker ligand field correlates with increased reactivity for both HAT and OAT. However, in addition to

controlling spectroscopic properties, the supporting ligand can also directly tune electrochemical properties. Therefore, correlations can also be made between the redox properties of these Mn^{IV}-oxo species and their reactivity.

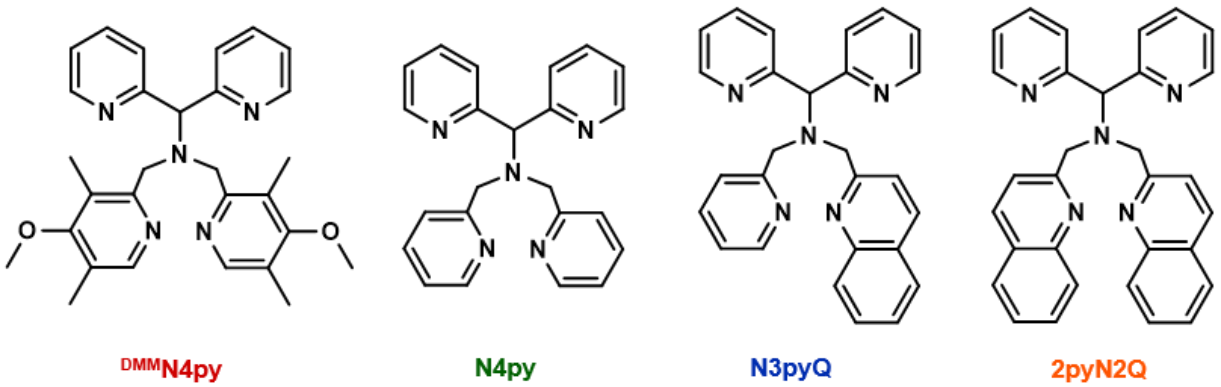

Figure 3.1. N4py and its ligand derivatives.

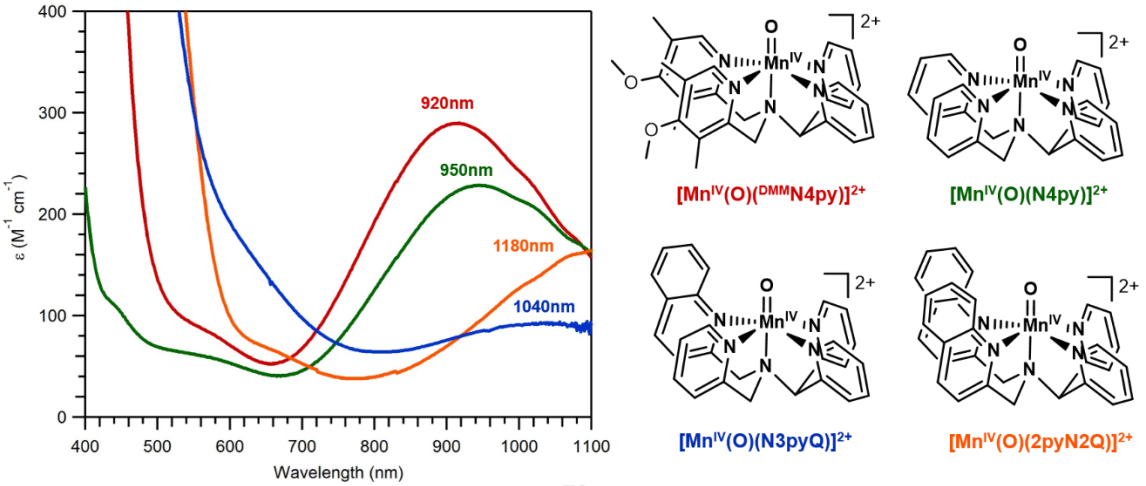

Figure 3.2. Left: UV-Vis spectra for Mn^{IV}-oxo complexes highlighting the near-IR feature attributed to the ^4E excited state. Right: Structures for the series of Mn^{IV}-oxo complexes supported by N4py and its derivatives.

3.2 Experimental Methods

Materials and Instrumentation. All solvents and chemicals were purchased from commercial vendors, and were used without further purification except for 9,10-dihydroanthracene (DHA) which was recrystallized from ethanol.[20] Iodosobenzene (PhIO) was prepared from iodosobenzene diacetate following a published procedure.[21] DHA-d_4 was prepared following a previously reported procedure.[22] $Mn^{II}(OTf)_2$•$2CH_3CN$ was generated according to a reported procedure.[23] Electronic absorption spectra for the kinetic reactions were obtained using a Cary 50 Bio or an Agilent 8453 spectrophotometer. Both spectrophotometers were interfaced with a Unisoku cryostat (USP-203-A). For O_2-free reactions, solvents were dried according to literature precedence and then degassed using freeze-pump-thaw methods.[20]

Synthesis of N4py. The pentadentate ligand N4py (N,N-bis(2-pyridylmethyl)-N-bis(2-pyridyl)methylamine) was prepared following previously described methods.[24-25]

Synthesis of ^{DMM}N4py. The pentadentate ligand ^{DMM}N4py (N,*N*-bis(4-methoxy-3,5-dimethyl-2-pyridylmethyl)-*N*-bis(2-pyridyl)methylamine) was synthesized based on a modified version of a previously published synthesis.[26] 2-chloromethyl-4-methoxy-3,5-dimethylpyridine hydrochloride (3.53 g, 15.9 mmol) was added to 5 mL of 5 M NaOH on ice. An additional 5 mL of H_2O and 5 mL of THF or acetone was added to facilitate dissolution of the pyridine salt. The bright pink solution was added to bis(2-pyridyl)methylamine (1.46 g, 7.88 mmol). The resulting solution was stirred for 48 hours, during which time the color changed to reddish-orange. To isolate crude ligand, 2.5 M NaOH was added in excess and the reaction mixture was extracted 3 X with CH_2Cl_2. The organic layer was dried with Na_2SO_4, filtered, and then solvent was removed under reduced pressure to give a reddish-brown oil. The crude ligand was purified by column chromatography (basic alumina). Initially, 100% CH_2Cl_2 was used to remove unreacted starting

material, and elution of the product was achieved using a MeOH gradient that was increased slowly to a maximum of 10%. Yield: 2.24 g (59%).

Synthesis of 2pyN2Q. The pentadentate ligand 2pyN2Q (bis(2-pyridyl)-N,N-bis(2 quinolylmethyl)methanamine) was prepared using a modified version of a previously published synthesis.[27] Two equivalents of 2-(chloromethyl)quinoline hydrochloride (0.512 g, 4.78 mmol) was dissolved in 1 mL 5 M NaOH on ice. THF was added slowly until all the salt was dissolved. This solution was added to one equivalent of bis(2-pyridyl)methylamine (0.443 g, 2.39 mmol). This reaction was stirred vigorously overnight to give a red solution the following day. To isolate the organic compounds, excess 2.5 M NaOH was added, and the reaction solution was washed 3 X with CH_2Cl_2. The organic layer was dried with Na_2SO_4, filtered, and solvent was removed to give a brown oil. To isolate pure ligand, column chromatography was performed on alumina. A gradient column from 100% CH_2Cl_2 to 10% MeOH/CH_2Cl_2 allowed for the separation of impurities to give a brown oil that turned blue/green the following day. However, ^{1}H NMR shows clean ligand, so the color can be attributed to a small amount of impurity. Yield: 0.683g (61%). ^{1}H NMR (500 MHz, $CDCl_3$) δ 8.59 (d, J = 4.3 Hz, 2H, py-H), 8.05 (d, J = 8.5 Hz, 2H, Qn-H), 8.01 (d, J = 8.5 Hz, 2H, Qn-H), 7.80 (d, J = 8.4 Hz, 2H, Qn-H), 7.75 – 7.71 (m, 4H, py-H, Qn-H), 7.70 – 7.62 (m, 4H, py-H, Qn-H), 7.45 (ddd, J = 8.2, 6.9, 1.1 Hz, 2H, Qn-H), 7.15 (ddd, J = 7.2, 4.7, 1.1 Hz, 2H, py-H), 5.47 (s, 1H, NCH), 4.24 (s, 4H, CH2Qn). 13C NMR (126 MHz, CDCl3) δ 160.42, 159.72, 149.29, 147.44, 136.32, 136.21, 129.25, 128.92, 127.38, 127.21, 126.01, 124.32, 122.18, 121.19 (Ar-C), 72.10 (CH), 58.23 (CH2). HRMS (in CH_3CN): m/z 468.2185 $[2pyN2Q+H]^+$, 490.2008 $[2pyN2Q+Na]^+$.

Synthesis of N3pyQ. N3py (N-[di(2-pyridinyl)methyl]-N-(2-pyridinylmethyl)amine) was prepared according to a previously published synthesis.[28] A slight excess of 2-

(chloromethyl)quinoline hydrochloride (0.578 g, 2.71 mmol) in 9 mL 5 M NaOH was added to N3py (0.68 g, 2,55 mmol) in 9 mL 5 M NaOH. The solution was refluxed at 80ºC for 24 hours, which resulted in a dark brown oil in suspension. After the reaction cooled, crude product was extracted 3 X with CH_2Cl_2. The organic layer was washed with 5 M NaOH, then dried over Na_2SO_4. After filtering off the solid, the solvent was removed under reduced pressure to give a brown oil. A gradient column from 100% CH_2Cl_2 to 20% MeOH/CH_2Cl_2 on silica was used to isolate clean ligand. Additionally, a separate batch of N3pyQ was obtained from the Nordlander group at Lund University in Sweden.

Synthesis of Metal Complexes. $[Mn^{II}(N4py)(OTf)](OTf)$, $[Mn^{II}(^{DMM}N4py)(OTf)](OTf)$, and $[Mn^{II}(2pyN2Q)(OTf)](OTf)$ complexes were prepared as previously reported.[15, 29] Under an intert atmosphere, equimolar amounts of ligand and $Mn^{II}(OTf)_2$•$2CH_3CN$ were combined in acetonitrile. After stirring overnight, the resulting solution was filtered through a membrane syringe filter and solvent was removed under reduced pressure. The resulting oil was dissolved in minimal acetonitrile layered slowly with diethyl ether. The isolated solid was then washed with diethyl ether and dried under reduced pressure. Further purification by repeated layering of vapor diffusion (acetonitrile and diethyl ether) allowed for pure samples of each metal complex to be obtained. $[Mn^{II}(N3pyQ)(OCl_4)](OCl_4)$ was obtained by combining equimolar amounts of N3pyQ ligand and manganese(II) perchlorate. After filtering through a membrane syringe filter, solvent was removed under reduced pressure. The resulting oil was dissolved in minimal MeCN and added dropwise to excess diethyl ether to crash out solid complex.

Synthesis of Mn^{IV}-oxo Species. $[Mn^{IV}(O)(2pyN2Q)]^{2+}$, $[Mn^{IV}(O)(N4py)]^{2+}$ and $[Mn^{IV}(O)(^{DMM}N4py)]^{2+}$ were all prepared *in situ* by reacting the corresponding Mn^{II} species with 10 equivalents, 2.5 equivalents and 1.2 equivalents of PhIO respectively in TFE.

Additionally, $[Mn^{IV}(O)(N3pyQ)]^{2+}$ was prepared in a similar fashion using 10 equivalents of PhIO. However, the formation of this new species has yet to be optimized due to difficulties in obtaining pure starting Mn^{II} complex.

Reactivity Towards C–H bonds. The reactivity of $[Mn^{IV}(O)(^{DMM}N4py)]^{2+}$ towards C–H bonds was investigated for the substrate dihydroanthracene (DHA). A 2mM solution of $[Mn^{IV}(O)(^{DMM}N4py)]^{2+}$ was prepared by combining solid $[Mn^{II}(^{DMM}N4py)(OTf)](OTf)$ in 1 mL deoxygenated CH_2Cl_2 with PhIO (1.2 equivalents) dissolved in 1 mL deoxygenated TFE in a UV-Vis cuvette. The cuvette was sealed under an argon atmosphere and the reaction mixture was placed into a temperature-controlled cryostat. The formation of $[Mn^{IV}(O)(^{DMM}N4py)]^{2+}$ was monitored by UV-Vis spectroscopy. At maximum formation of the band at 940nm, an appropriate amount of substrate was added in 100 μL CH_2Cl_2. The decay of the $[Mn^{IV}(O)(^{DMM}N4py)]^{2+}$ peak at 940 nm was monitored and fit to obtain first order rate constants, k_{obs}. Under these reaction conditions, the rates were observed to be first-order to at least five half-lives. Each trial was performed in at least triplicate. The k_{obs} values were determined at four substrate concentrations (20 – 50 mM). The observed rate constants were plotted against DHA concentration to obtain a second-order rate constant.

To determine the kinetic isotope effect (KIE) for $[Mn^{IV}(O)(^{DMM}N4py)]^{2+}$ with DHA, the k_2 was determined with deuterated DHA (DHA-d_4) using the same procedure outlined above, but at a concentration of 1 mM. Under these reaction conditions, the rates were observed to be first-order to at least five half-lives. Each trial was performed in at least triplicate. The k_{obs} values were determined at four substrate concentrations (10 – 40 mM).

To determine the activation parameters for HAT for the reaction of 1 mM $[Mn^{IV}(O)(^{DMM}N4py)]^{2+}$ with 10 mM DHA were determined from experiments in a 50:50 mix of

TFE/CH_2Cl_2 in the temperature range of 258.15 – 313.15 K. The decay of $[Mn^{IV}(O)(^{DMM}N4py)]^{2+}$ was monitored by electronic absorption. An Eyring analysis was performed by plotting 1/T versus $\ln(k_{obs}/T)$. Activation parameters were determined from the slope and intercept that were obtained by fitting the linear correlation.

Reactivity Towards Thioanisole. The OAT reactivity for the series of N4py derivatives was investigated using thioanisole as a substrate. For reach reaction, 1.0 mM of each Mn^{IV}-oxo species was generated in 100% TFE for $[Mn^{IV}(O)(^{DMM}N4py)]^{2+}$ and $[Mn^{IV}(O)(2pyN2Q)]^{2+}$ and 50:50 TFE/CH_2Cl_2 for $[Mn^{IV}(O)(N4py)]^{2+}$ by adding varying amounts of PhIO. Upon full formation, an aliquot of a solution containing thioanisole was added to the cuvette. Substrate concentrations were at least 10-fold compared to Mn concentration to attain pseudo-first order conditions. The decay of each oxo was followed by monitoring the near-IR feature, and the resulting time trace was fit to a pseudo-first order model to at least five half-lives. While rates for $[Mn^{IV}(O)(2pyN2Q)]^{2+}$ and $[Mn^{IV}(O)(N4py)]^{2+}$ could be determined using first-order fits, reactions involving $[Mn^{IV}(O)(^{DMM}N4py)]^{2+}$ lead to competing kinetic decay and oxo reformation beyond 2 half-lives. For this reason, an initial rate approximation was applied for the slower reactions (using 20% of initial disappearance of the near-IR peak). The initial rates given in AU/s were converted into s^{-1} by using the initial concentration of Mn (1.0 mM) and the extinction coefficient for $[Mn^{IV}(O)^{DMM}N4py]^{2+}$ (290 $M^{-1}cm^{-1}$). These initial rate approximations yielding k_{obs} values that agreed with those determined from a pseudo-first order fit for 40 equivalents of thioanisole with $[Mn^{IV}(O)(^{DMM}N4py)]^{2+}$. The observed rate constants for all complexes were plotted against thioanisole concentration to obtain second-order rate constants, and the concentration of substrate was corrected to the final total volume. The non-zero intercept for $[Mn^{IV}(O)(^{DMM}N4py)]^{2+}$ can be explained by its observed self-decay rate.

Analysis of organic products. Following the kinetic experiments with thioanisole, the reaction solutions were passed through a silica plug and eluted with excess ethyl acetate. 1,4-benzoquinone was added to the elutant as a standard. After solvent removal by rotary evaporation, the organic products were quantified by ^{1}H NMR experiments. Quantification of the products (Table 3.1) was determined by comparing resonance signals for the methyl protons of thioanisole (2.48 ppm) and its oxidized derivatives (sulfoxide, 2.73 ppm, and sulfone, 3.06 ppm) to the C–H protons of benzoquinone (6.80 ppm).[30] Previous investigation of the reaction of $[Mn^{IV}(O)(N4py)]^{2+}$ showed sulfoxide formation,[31] consistent with an oxygen-atom transfer process. Minimal thioanisole oxidation by PhIO was observed in control experiments lacking the Mn^{II} complex.

3.3 Results and Discussion

To assess how ligand perturbations impact reactivity for Mn^{IV}-oxo complexes supported by N4py and its derivatives, kinetic experiments were conducted for substrates that are expected to react by either HAT and OAT pathways. The HAT reactivity of $[Mn^{IV}(O)(^{DMM}N4py)]^{2+}$ was investigated using the substrate dihydroanthracene (DHA), which permits comparison with other Mn^{IV}-oxo species in the N4py series. Treatment of 2.0 mM $[Mn^{IV}(O)(^{DMM}N4py)]^{2+}$ in TFE with varying amounts of excess DHA at 25ºC led to pseudo-first order decay of the Mn^{IV}-oxo electronic absorption features. The observed rate constants were determined by fitting the decay of the signal at 920 nm. These rate constants, when plotted against substrate concentration, showed a linear increase as a function of DHA concentration. From this analysis, a second order rate constant (k_2) of 0.34(6) $M^{-1}s^{-1}$ was obtained. Compared to corresponding rates for $[Mn^{IV}(O)(N4py)]^{2+}$ and $[Mn^{IV}(O)(2pyN2Q)]^{2+}$, $[Mn^{IV}(O)(^{DMM}N4py)]^{2+}$ shows the slowest rate for the series (Figure 3.3

and Table 3.1). The fastest complex for DHA oxidation of the series is $[Mn^{IV}(O)(2pyN2Q)]^{2+}$, which is 6 times faster than $[Mn^{IV}(O)(N4py)]^{2+}$ and 68 times faster than $[Mn^{IV}(O)(^{DMM}N4py)]^{2+}$.

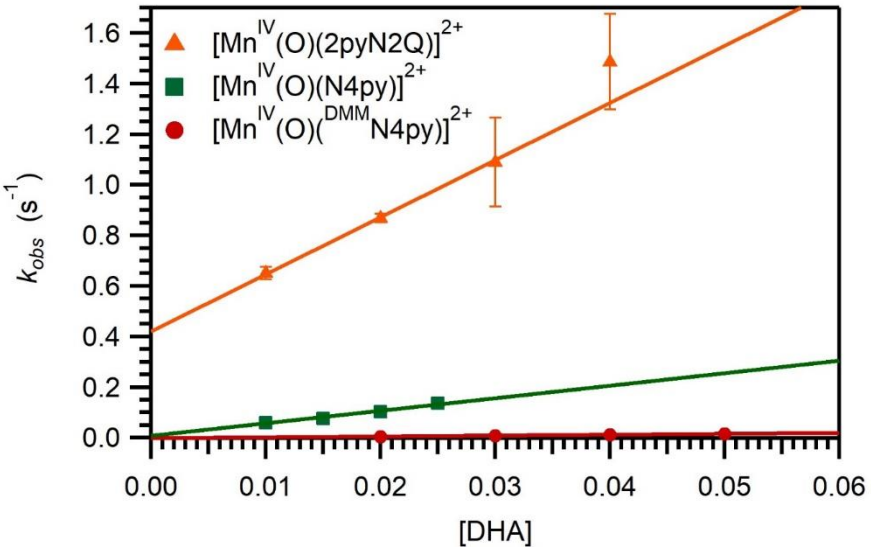

Figure 3.3. Plots of pseudo-first order rate constants (k_{obs}) versus DHA concentration for 2.0 mM of each complex in TFE at 298 K. Second order rate constants, k_2, were determined from the linear correlation between the concentration of DHA and the observed rate constants.

Table 3.1: Second-order Rate Constants (k_2) for the Reactions of Mn^{IV}-oxo Complexes with Thioanisole

complex[a]	k_2(DHA)[b]	k_2(thioanisole)[b]
$[Mn^{IV}(O)(2pyN2Q)]^{2+}$	23(3)	9.2(9)
$[Mn^{IV}(O)(N4py)]^{2+}$	3.6(4)	0.060(3)
$[Mn^{IV}(O)(^{DMM}N4py)]^{2+}$	0.34(6)	0.0023(4)

To further probe the mechanism of DHA oxidation by $[Mn^{IV}(O)(^{DMM}N4py)]^{2+}$, analogous reactions were performed with the use of deuterated DHA (DHA-d_4). Treatment of 1.0 mM $[Mn^{IV}(O)(^{DMM}N4py)]^{2+}$ in TFE at 25ºC with varying amounts of excess DHA-d_4 led to pseudo-first order decay of the Mn^{IV}-oxo electronic absorption features. A linear relationship between DHA-d_4 concentration and k_{obs} values yielded a k_2 of 0.035(2) $M^{-1}s^{-1}$ (Figure 3.4, dashed line). The reactions with DHA-d_4 were significantly slower than those observed for DHA, as can be seen in

Figure 3.4. By comparing the k_2 values, an H/D kinetic isotope effect (KIE) of 10.3 was observed. This is similar to the KIE of 11.2 that was previously observed for $[Mn^{IV}(O)(N4py)]^{2+}$, which was consistent with a tunneling contribution.[2]

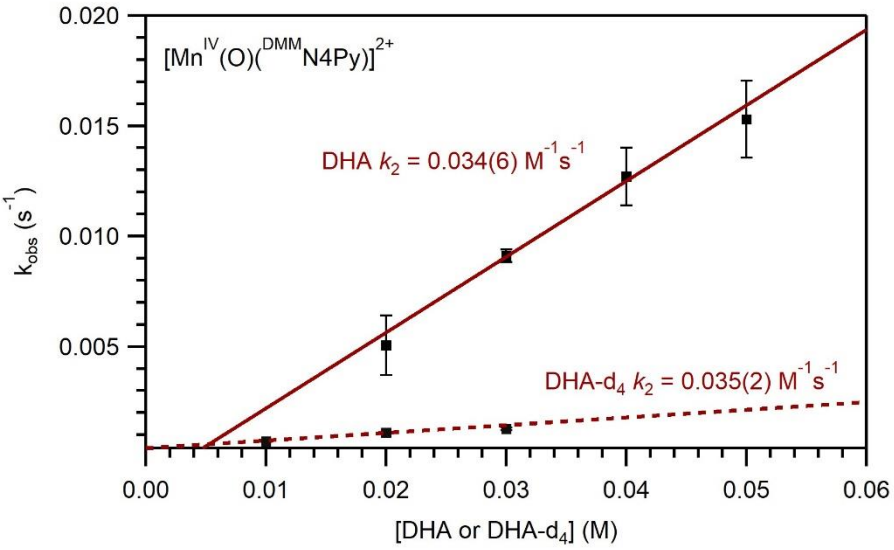

Figure 3.4. Plots of pseudo-first order rate constants (k_{obs}) versus DHA (solid line) and DHA-d_4 (dashed line) concentrations for $[Mn^{IV}(O)(^{DMM}N4py)]^{2+}$ in TFE at 25ºC. The lines each represent best fits to the data. This linear correlation was used to determine the second-order rate constants (k_2).

An Eyring analysis of the rate data for $[Mn^{IV}(O)(^{DMM}N4py)]^{2+}$ in the presence of DHA from 258 K – 313.15 K gave activation parameters $\Delta H^{\ddagger}$ and $\Delta S^{\ddagger}$ of 11.7(9) kcal/mol and -30(4) cal/ (mol K), respectively (Figure 3.5). These values can be compared to those previously determined for $[Mn^{IV}(O)(N4py)]^{2+}$, where activation parameters $\Delta H^{\ddagger}$ and $\Delta S^{\ddagger}$ of 9 kcal/mol and -35 cal/ (mol K) (Table 3.2) were reported. At 25ºC, the activation parameters for $[Mn^{IV}(O)(^{DMM}N4py)]^{2+}$ yield a $\Delta G^{\ddagger}$ value comparable to those reported previously for $[Mn^{IV}(O)(N4py)]^{2+}$, as well as for several other Mn^{IV}-oxo species as outlined in Table 3.2. It is important to note that the larger enthalpic barrier for $[Mn^{IV}(O)(^{DMM}N4py)]^{2+}$ compared to

$[Mn^{IV}(O)(N4py)]^{2+}$ is in line with what is observed experimentally, as $[Mn^{IV}(O)(^{DMM}N4py)]^{2+}$ exhibits much slower HAT reactivity with DHA.

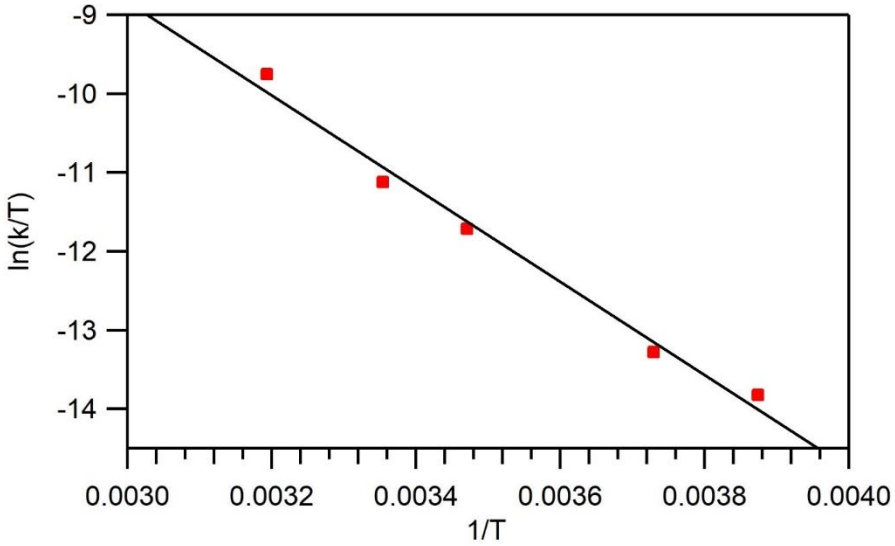

Figure 3.5. Eyring analysis, where 1/T (K^{-1}) is plotted against ln(k_{obs}/T) for the reaction of $[Mn^{IV}(O)(^{DMM}N4py)]^{2+}$ and DHA.

Table 3.2. Activation Parameters for the Reactions of Mn^{IV}-oxo Species with DHA

complex[a]	**concentration**	**Solvent System**	**Δ*G*‡**	**Δ*H*‡**	**Δ*S*‡**	**ref**
$[Mn^{IV}(O)(^{DMM}N4py)]^{2+}$	1.0 mM	TFE: CH_2Cl_2 (1:1)	20.5(9)	11.7(9)	-30(4)	[b]
$[Mn^{IV}(O)(N4py)]^{2+}$	1.0 mM	TFE: CH_2Cl_2 (1:1)	19.4(8)	9.0(8)	-35(3)	[2]
$[Mn^{IV}(O)(H_3buea)]^{-}$	0.6 mM	DMSO	19.6(1)	5(1)	-49(4)	[4]
$[Mn^{IV}(O)_2(Me_2EBC)]$	2.0 mM	$(CH_3)_2CO$:H_2O (4:1)	21.0(6)	13.7(6)	-25(2)	[32]
$[Mn^{IV}(O)(OH)(^{H,Me}Pytacn)]^{+}$	1.0 mM	MeCN:H_2O (4:1)	21.3(7)	10.3(7)	-37(2)	[11]

[a]Ligand abbreviations are as follows: ^{DMM}N4py = (N,N-bis(4-methoxy-3,5-dimethyl-2-pyridylmethyl)-N-bis(2-pyridyl)methylamine) ; N4py = N,N-bis(2-pyridylmethyl)-N-bis(2-pyridyl)methylamine; H_3buea = tris[(N′-tertbutylureaylato)-N-ethylene]aminato; Me_2EBC = 4,11-dimethyl-1,4,8,11tetraazabicyclo[6.6.2]hexadecane; ^{H,Me}Pytacn = 1-(2-pyridylmethyl)-4,7-dimethyl-1,4,7triazacyclononane. [b] This work. This table is reporduced from reference [2].

To assess the OAT reactivity of these Mn^{IV}-oxo species, kinetic experiments with thioanisole were conducted. Treatment of 1.0 mM of each Mn^{IV}-oxo complex with varying amounts of excess thioanisole at 25ºC led to pseudo-first order decay of the Mn^{IV}-oxo electronic absorption features. The observed rate constants were determined by fitting the decay of the near-IR feature for each complex. These rate constants, when plotted against substrate concentration,

showed a linear increase as a function of thioanisole concentration. From this analysis, k_2 values were obtained and are included in Table 3.1. Compared to HAT, a much larger rate variation was observed for the series of N4py Mn^{IV}-oxo derivatives, as can be seen in Figure 3.6. The reactivity of $[Mn^{IV}(O)(2pyN2Q)]^{2+}$ was 153 and 4000 times faster compared to $[Mn^{IV}(O)(N4py)]^{2+}$ and $[Mn^{IV}(O)(^{DMM}N4py)]^{2+}$, respectively. Additionally, a full spectrum view of Figure 3.6 is included in the appendix to highlight the large rate enhancement that is observed for $[Mn^{IV}(O)(2pyN2Q)]^{2+}$ (Figure A3.1).

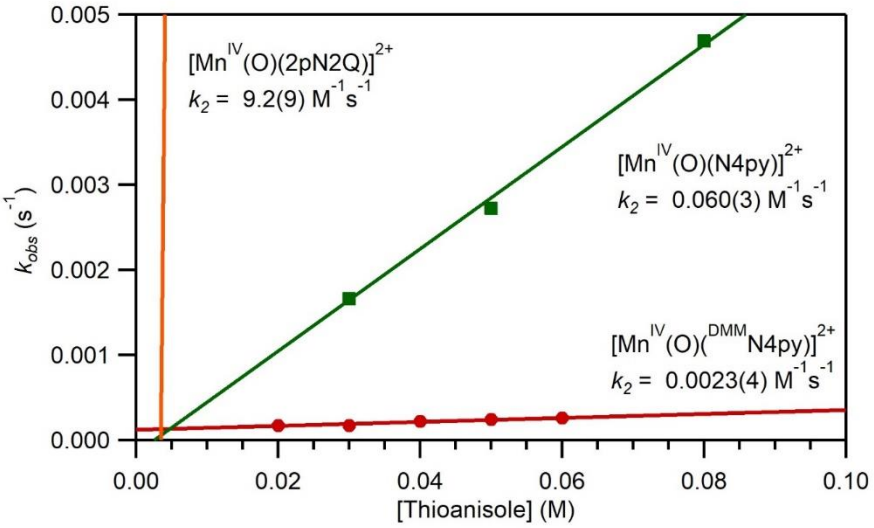

Figure 3.6. Plots of pseudo-first order rate constants (k_{obs}) versus thioanisole concentration for 1.0 mM of each complex in TFE at 298 K. Second order rate constants, k_2, were determined from the linear correlation between the concentration of thioanisole and the observed rate.

To further investigate the mechanism of OAT for the series of Mn^{IV}-oxo species, product analysis was conducted for the substrate thioansiole. The reaction of $[Mn^{IV}(O)(^{DMM}N4py)]^{2+}$ with thioanisole yielded ~0.94(5) equivalents of methyl phenyl sulfoxide ($PhSOCH_3$) relative to one equivalent of the Mn^{IV}-oxo, indicative of an OAT process. For the reaction of thioanisole with $[Mn^{IV}(O)(2pyN2Q)]^{2+}$, we observed formation of super-stoichiometric amounts of product relative to the Mn^{IV}-oxo concentration (Table 3.3). In addition to $PhSOCH_3$, the doubly oxidized product,

methyl phenyl sulfone ($PhSO_2CH_3$) was observed. These large amounts of oxidized product can be attributed to the use of excess (10 equiv. relative to Mn^{II}) of PhIO that is necessary to generate $[Mn^{IV}(O)(2pyN2Q)]^{2+}$. Since oxidation of thioanisole is a two-electron process, the complex reverted to the starting Mn^{II} species, is re-oxidized to the Mn^{IV}-oxo species, allowing another equivalent of thioanisole or $PhSOCH_3$ to be oxidized. This result suggests that the thioanisole oxidation by $[Mn^{IV}(O)(2pyN2Q)]^{2+}$ is catalytic.

Table 3.3. Product Quantification for Oxygen-atom Transfer Reactions.

Complex	**Additives (equiv)**		**Oxidized Products[a]**	
	PhIO	thioanisole	$PhSOCH_3$ (%)	$PhSO_2CH_3$ (%)
2pyN2Q	10	10	720(10)	18(5)
^{DMM}N4py	1.2	50	94(5)	0

[a] Percent determined relative to the concentration of Mn^{IV}-oxo complex.

The combined HAT and OAT kinetic data can be compared to the energy of the Mn^{IV}-oxo ^4E state to probe the excited state reactivity model. A plot of $\log(k_2)$ values for DHA oxidation versus ^4E energy shows a linear correlation, which is in line with the excited state reactivity proposal (Figure 3.7, left). This is suggestive that a lower energy ^4E state mediates faster HAT reactivity. However, there is a much stronger correlation between $\log(k_2)$ for DHA oxidation and the $Mn^{III/IV}$ peak potentials, which were reported previously (Figure 3.7, right).[15]

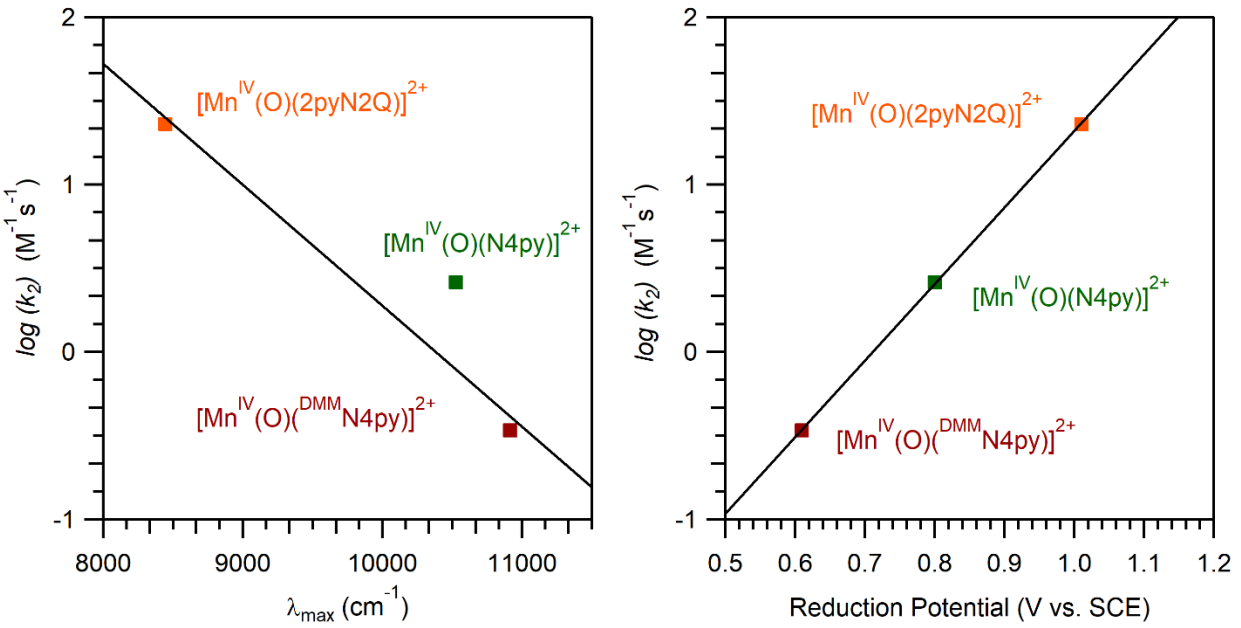

Figure 3.7. Plots of log(k_2) for DHA oxidation versus $Mn^{III/IV}$ reduction potentials (left) and near-IR band energies (right). The black line for each plot shows the fit between the three points.

Similar correlations can be made for OAT, where a plot of the ^4E energy against the log(k_2) with thioanisole shows a linear relationship (Figure 3.8, left). Once again, when the $Mn^{III/IV}$ peak potential is plotted against log(k_2), a much stronger correlation is observed (Figure 3.8, right). However, it is important to note that this correlation is unexpected. Thioanisole oxidation is presumed to occur by an OAT mechanism, which is overall a two-electron process.

These observed correlations for HAT and OAT reactivity for this series of Mn^{IV}-oxo species suggest that the equatorial ligand perturbations may be altering more than just the ^4E energy. In addition to spectroscopic changes, introduction of new steric and electronic properties to the N4py scaffold can also tune the electrochemical properties, as well as the basicity of the Mn^{IV}-adduct. Thus, it is difficult to pinpoint if there is a single parameter that is responsible for the enhanced reactivity for $[Mn^{IV}(O)(N4py)]^{2+}$ and its derivatives.

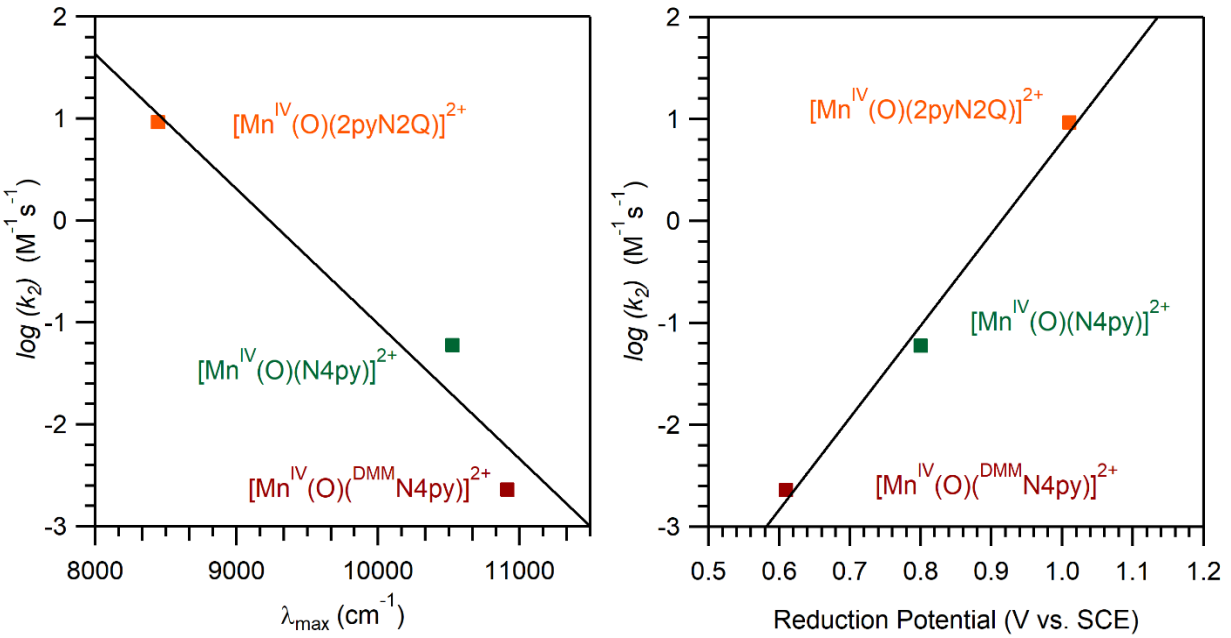

Figure 3.8. Plots of log(k_2) for thioanisole oxidation versus $Mn^{III/IV}$ reduction potentials (left) and near-IR band energies (right). The black line for each plot shows the fit between the three points.

Previously, our group has shown that $[Mn^{IV}(O)(N4py)]^{2+}$ shows a more positive $Mn^{III/IV}$ potential when compared to other less reactive Mn^{IV}-oxo complexes in the literature.[2] Additionally, $[Mn^{IV}(O)(2pyN2Q)]^{2+}$, the most reactive complex for this series, has the most positive $Mn^{III/IV}$ peak potential.[15] With what is known about the relationship between HAT rates and the thermodynamic driving force, this suggests the ability of these complexes to act as strong one-electron oxidants aids in its enhanced HAT reactivity. Unfortunately, an understanding of the proton affinity for these species is required for a full thermodynamic analysis.

To further investigate how reactivity is modulated for these types of Mn^{IV}-oxo species, it would be helpful to investigate a wider range of N4py derivatives. While ^{DMM}N4py and 2pyN2Q allow for the strengthening and weakening of the ligand field compared to N4py respectively, a correlation between three derivatives provides limited insight into what tunes reactivity for this class of Mn^{IV}-oxo adducts. Additionally, the near-IR feature of $[Mn^{IV}(O)(2pyN2Q)]^{2+}$ is red-

shifted 230 nm compared to $[Mn^{IV}(O)(N4py)]^{2+}$, making it an obvious outlier for this series. $[Mn^{IV}(O)(2pyN2Q)]^{2+}$ is also an outlier for OAT reactivity, as is apparent in the correlation plots in Figure 3.8. The reactivity of $[Mn^{IV}(O)(2pyN2Q)]^{2+}$ is much more enhanced compared to the other derivatives, leaving a large gap of unexplored reactivity. To gain more insight for reactive centers that lie between $[Mn^{IV}(O)(N4py)]^{2+}$ and $[Mn^{IV}(O)(2pyN2Q)]^{2+}$, a derivative where only a single quinoline arm is introduced could help to fill in this gap. To do this, we have designed $[Mn^{IV}(O)(N3pyQ)]^{2+}$, which possesses one pyridyl arm and one quinoline arm (Figure 3.9). Through the introduction of a single quinoline arm, this could give insight into how one sterically bulky group affects the Mn^{IV}-oxo adduct. The Mn^{II} complex for this derivative has been synthesized, but the formation of the oxo has yet to be optimized. As can be seen in Figure 3.9, the formation of $[Mn^{IV}(O)(N3pyQ)]^{2+}$ is marked by a near-IR feature at 1040 nm, however the intensity of this band is not as intense compared to the rest of the series. Work still needs to be done to optimize purification of the corresponding Mn^{II} species, as the solid is light brown, suggesting the presence of some unreacted ligand. Once formation of $[Mn^{IV}(O)(N3pyQ)]^{2+}$ is complete, the new derivative will need to be characterized using EPR, XAS, and ESI-MS.

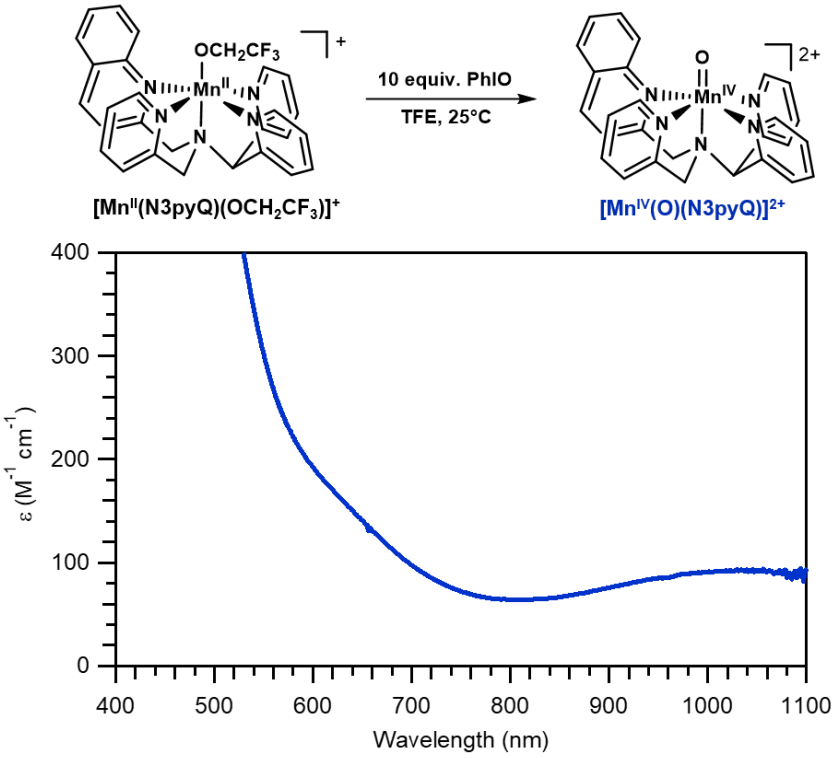

Figure 3.9. Electronic absorption spectrum for $[Mn^{IV}(O)(N3pyQ)]^{2+}$ upon the addition of 10 equiv. PhIO to the corresponding Mn^{II} complex.

Preliminary results show that the ^4E energy for $[Mn^{IV}(O)(N3pyQ)]^{2+}$ is 1040 nm (Figure 3.1), which lies in between that of $[Mn^{IV}(O)(2pyN2Q)]^{2+}$ (1180 nm) and $[Mn^{IV}(O)(N4py)]^{2+}$ (950nm). This is expected because its equatorial field lies halfway between N4py and 2pyN2Q due to the introduction of a single quinoline moiety. Further kinetic investigations for this derivative will help to further understand what tunes reactivity for the N4py series of Mn^{IV}-oxo complexes.

3.4 Conclusions

With this work, we have described a series of Mn^{IV}-oxo species supported by N4py derivatives with varied electronic and steric properties. In support of an excited state reactivity model, we have found that a weaker equatorial field correlates to faster reactivity for both HAT

and OAT. However, we have also found correlations between rates and $Mn^{III/IV}$ reduction potentials for both HAT and OAT. Therefore, there is much to be done to further investigate what controls reactivity for these Mn^{IV}-oxo species.

3.5 References

1. Yano, J.; Kern, J.; Sauer, K.; Latimer, M. J.; Pushkar, Y.; Biesiadka, J.; Loll, B.; Saenger, W.; Messinger, J.; Zouni, A.; Yachandra, V. K., Where Water Is Oxidized to Dioxygen: Structure of the Photosynthetic Mn_4Ca Cluster. *Science* **2006,** *314* (5800), 821-825.

2. Leto, D. F.; Ingram, R.; Day, V. W.; Jackson, T. A., Spectroscopic properties and reactivity of a mononuclear oxomanganese(iv) complex. *Chem. Commun.* **2013,** *49* (47), 5378-5380.

3. Sawant, S. C.; Wu, X.; Cho, J.; Cho, K.-B.; Kim, S. H.; Seo, M. S.; Lee, Y.-M.; Kubo, M.; Ogura, T.; Shaik, S.; Nam, W., Water as an Oxygen Source: Synthesis, Characterization, and Reactivity Studies of a Mononuclear Nonheme Manganese(IV) Oxo Complex. *Angew. Chem., Int. Ed. Engl.* **2010,** *49* (44), 8190-8194.

4. Parsell, T. H.; Yang, M.-Y.; Borovik, A. S., C−H Bond Cleavage with Reductants: Re-Investigating the Reactivity of Monomeric $Mn^{III/IV}$−Oxo Complexes and the Role of Oxo Ligand Basicity. *J. Am. Chem. Soc.* **2009,** *131* (8), 2762-2763.

5. Yin, G.; Danby, A. M.; Kitko, D.; Carter, J. D.; Scheper, W. M.; Busch, D. H., Understanding the Selectivity of a Moderate Oxidation Catalyst: Hydrogen Abstraction by a Fully Characterized, Activated Catalyst, the Robust Dihydroxo Manganese(IV) Complex of a Bridged Cyclam. *J. Am. Chem. Soc.* **2007,** *129* (6), 1512-1513.

6. Garcia-Bosch, I.; Company, A.; Cady, C. W.; Styring, S.; Browne, W. R.; Ribas, X.; Costas, M., Evidence for a Precursor Complex in C–H Hydrogen Atom Transfer Reactions Mediated by a Manganese(IV) Oxo Complex. *Angew. Chem., Int. Ed. Engl.* **2011,** *123* (25), 5766-5771.

7. Yoon, H.; Morimoto, Y.; Lee, Y.-M.; Nam, W.; Fukuzumi, S., Electron-transfer properties of a nonheme manganese(iv)-oxo complex acting as a stronger one-electron oxidant than the iron(iv)-oxo analogue. *Chem. Commun.* **2012,** *48* (91), 11187-11189.

8. Kurahashi, T.; Kikuchi, A.; Tosha, T.; Shiro, Y.; Kitagawa, T.; Fujii, H., Transient Intermediates from Mn(salen) with Sterically Hindered Mesityl Groups: Interconversion between Mn^{IV}-Phenolate and Mn^{III}-Phenoxyl Radicals as an Origin for Unique Reactivity. *Inorg. Chem.* **2008,** *47* (5), 1674-1686.

9. Comba, P.; Maurer, M.; Vadivelu, P., Oxidation of Cyclohexane by High-Valent Iron Bispidine Complexes: Tetradentate versus Pentadentate Ligands. *Inorg. Chem.* **2009,** *48* (21), 10389-10396.

10. Yin, G.; Danby, A. M.; Kitko, D.; Carter, J. D.; Scheper, W. M.; Busch, D. H., Oxidative Reactivity Difference among the Metal Oxo and Metal Hydroxo Moieties: pH Dependent Hydrogen Abstraction by a Manganese(IV) Complex Having Two Hydroxide Ligands. *Journal of the American Chemical Society* **2008,** *130* (48), 16245-16253.

11. Garcia-Bosch, I.; Company, A.; Cady, C. W.; Styring, S.; Browne, W. R.; Ribas, X.; Costas, M., Evidence for a Precursor Complex in C□H Hydrogen Atom Transfer Reactions Mediated by a Manganese(IV) Oxo Complex. *Angew. Chem., Int. Ed. Engl.* **2011,** *50* (25), 5648-5653.

12. Wu, X.; Seo, M. S.; Davis, K. M.; Lee, Y.-M.; Chen, J.; Cho, K.-B.; Pushkar, Y. N.; Nam, W., A Highly Reactive Mononuclear Non-Heme Manganese(IV)–Oxo Complex That Can Activate the Strong C–H Bonds of Alkanes. *J. Am. Chem. Soc.* **2011,** *133* (50), 20088-20091.

13. Massie, A. A.; Sinha, A.; Parham, J. D.; Nordlander, E.; Jackson, T. A., Relationship between Hydrogen-Atom Transfer Driving Force and Reaction Rates for an Oxomanganese(IV) Adduct. *Inorg. Chem.* **2018,** *57* (14), 8253-8263.

14. Denler, M. C.; Massie, A. A.; Singh, R.; Stewart-Jones, E.; Sinha, A.; Day, V. W.; Nordlander, E.; Jackson, T. A., Mn^{IV}-Oxo complex of a bis(benzimidazolyl)-containing N5 ligand reveals different reactivity trends for MnIV-oxo than FeIV-oxo species. *Dalton Trans.* **2019,** *48* (15), 5007-5021.

15. Massie, A. A.; Denler, M. C.; Cardoso, L. T.; Walker, A. N.; Hossain, M. K.; Day, V. W.; Nordlander, E.; Jackson, T. A., Equatorial Ligand Perturbations Influence the Reactivity of Manganese(IV)-Oxo Complexes. *Angew. Chem., Int. Ed. Engl.* **2017,** *56* (15), 4178-4182.

16. Chen, J.; Lee, Y.-M.; Davis, K. M.; Wu, X.; Seo, M. S.; Cho, K.-B.; Yoon, H.; Park, Y. J.; Fukuzumi, S.; Pushkar, Y. N.; Nam, W., A Mononuclear Non-Heme Manganese(IV)–Oxo Complex Binding Redox-Inactive Metal Ions. *J. Am. Chem. Soc* **2013,** *135* (17), 6388-6391.

17. Cho, K.-B.; Shaik, S.; Nam, W., Theoretical Investigations into C–H Bond Activation Reaction by Nonheme $Mn^{IV}O$ Complexes: Multistate Reactivity with No Oxygen Rebound. *J. Phys. Chem. Lett.* **2012,** *3* (19), 2851-2856.

18. Chen, J.; Cho, K.-B.; Lee, Y.-M.; Kwon, Y. H.; Nam, W., Mononuclear nonheme iron(iv)–oxo and manganese(iv)–oxo complexes in oxidation reactions: experimental results prove theoretical prediction. *Chem. Commun.* **2015,** *51* (66), 13094-13097.

19. Leto, D. F.; Massie, A. A.; Rice, D. B.; Jackson, T. A., Spectroscopic and Computational Investigations of a Mononuclear Manganese(IV)-Oxo Complex Reveal Electronic Structure Contributions to Reactivity. *J. Am. Chem. Soc.* **2016,** *138* (47), 15413-15424.

20. Armarego, W. L. F.; Perrin, D. D., *Purification of Laboratory Chemicals*. Butterworth-Heinemann: Oxford, U.K., 1997.

21. Saltzman, H.; Sharefkin, J. G., Iodosobenzene. *Org. Synth.* **1963,** *43*, 60.

22. Goldsmith, C. R.; Jonas, R. T.; Stack, T. D. P., C−H Bond Activation by a Ferric Methoxide Complex: Modeling the Rate-Determining Step in the Mechanism of Lipoxygenase. *J. Am. Chem. Soc* **2002,** *124* (1), 83-96.

23. Seo, M. S.; Kim, J. Y.; Annaraj, J.; Kim, Y.; Lee, Y.-M.; Kim, S.-J.; Kim, J.; Nam, W., $[Mn(tmc)(O_2)]^+$: A Side-On Peroxide Manganese(III) Complex Bearing a Non-heme Ligand. *Angew. Chem., Int. Ed. Engl.* **2007,** *46*, 377-380.

24. Chang, J.; Plummer, S.; Berman, E. S. F.; Striplin, D.; Blauch, D., Synthesis and Characterization of Bis(di-2-pyridylmethanamine)ruthenium(II). *Inorg. Chem.* **2004,** *43* (5), 1735-1742.

25. Lubben, M.; Meetsma, A.; Wilkinson, E. C.; Feringa, B.; Que Jr., L., Nonheme Iron Centers in Oxygen Activation: Characterization of an Iron(III) Hydroperoxide Intermediate. *Angewandte Chemie International Edition in English* **1995,** *34* (13-14), 1512-1514.

26. Rana, S.; Dey, A.; Maiti, D., Mechanistic elucidation of C–H oxidation by electron rich non-heme iron(iv)-oxo at room temperature. *Chem. Commun.* **2015,** *51* (77), 14469-14472.

27. Lo, W. K. C.; McAdam, C. J.; Blackman, A. G.; Crowley, J. D.; McMorran, D. A., The pentadentate ligands 2PyN2Q and N4Py, and their Cu(II) and Zn(II) complexes: A synthetic, spectroscopic and crystallographic structural study. *Inorganica Chimica Acta* **2015,** *426*, 183-194.

28. Roelfes, G.; Branum, M. E.; Wang, L.; Que, L.; Feringa, B. L., Efficient DNA Cleavage with an Iron Complex without Added Reductant. *Journal of the American Chemical Society* **2000,** *122* (46), 11517-11518.

29. Geiger, R. A.; Leto, D. F.; Chattopadhyay, S.; Dorlet, P.; Anxolabéhère-Mallart, E.; Jackson, T. A., Geometric and Electronic Structures of Peroxomanganese(III) Complexes Supported by Pentadentate Amino-Pyridine and -Imidazole Ligands. *Inorg. Chem.* **2011,** *50* (20), 10190-10203.

30. Paria, S.; Chatterjee, S.; Paine, T. K., Reactivity of an Iron–Oxygen Oxidant Generated upon Oxidative Decarboxylation of Biomimetic Iron(II) α-Hydroxy Acid Complexes. *Inorg. Chem.* **2014,** *53* (6), 2810-2821.

31. Chen, J.; Lee, Y.-M.; Davis, K. M.; Wu, X.; Seo, M. S.; Cho, K.-B.; Yoon, H.; Park, Y. J.; Fukuzumi, S.; Pushkar, Y. N.; Nam, W., A Mononuclear Non-Heme Manganese(IV)–Oxo Complex Binding Redox-Inactive Metal Ions. *J. Am. Chem. Soc.* **2013,** *135*, 6388-6391.

32. Wang, Y.; Shi, S.; Wang, H.; Zhu, D.; Yin, G., Kinetics of hydrogen abstraction by active metal hydroxo and oxo intermediates: revealing their unexpected similarities in the transition state. *Chem. Commun.* **2012,** *48* (63), 7832-7834.

Chapter 4. Mn^{IV}-Oxo Complex of a Bis(benzimidazolyl)-containing N5 Ligand Reveals Different Reactivity Trends for Mn^{IV}-Oxo than Fe^{IV}-Oxo Species

Portions of this chapter have been reproduced with permission from: Denler, M. C., Massie, A. A., Singh, R., Stewart-Jones, E., Sinha, A., Day, V. W., Nordlander, E., Jackson, T.A. *Dalton Trans*. **2019**, *48*, 5007-5021

4.1 Introduction

The use of earth-abundant metal catalysts to effect hydrocarbon oxidation has grown significantly in recent years. These efforts have led to new non-porphyrinoid Fe- and Mn-based catalysts for C–H bond functionalization.[1-5] Catalytic mechanisms for these systems typically feature substrate oxidation by hydrogen- or oxygen-atom transfer steps (HAT and OAT, respectively) initiated by high-valent metal-oxo species. Our understanding of these catalysts is aided by structure-reactivity relationships obtained through investigations of stoichiometric reactions of isolable metal-oxo species. For example, we recently reported that Mn^{IV}-oxo adducts supported by derivatives of the pentadentate N4py ligand display HAT and OAT reaction rates that are dependent on the equatorial ligand field strength (Figure 4.1).[6] The N4py derivatives previously considered were ^{DMM}N4py and 2pyN2Q (Figure 4.1), which respectively feature electron-rich di-3,5-methyl-4-methoxy-pyridyl groups and bulky quinolinyl groups that serve to increase (for ^{DMM}N4py) and decrease (for 2pyN2Q) the equatorial ligand field of the Mn center relative to the parent N4py ligand. A DFT structure of $[Mn^{IV}(O)(2pyN2Q)]^{2+}$ showed that the steric bulk of the quinolinyl groups also crowds the oxo coordination position, causing a N_{axial}–Mn=O angle of 170°, with the oxo ligand tilted away from the quinolinyl moieties (Figure 4.1). DFT structures for the corresponding $[Mn^{IV}(O)(N4py)]^{2+}$ and $[Mn^{IV}(O)(^{DMM}N4py)]^{2+}$ complexes showed N_{axial}–Mn=O angles of almost exactly 180°. The $[Mn^{IV}(O)(2pyN2Q)]^{2+}$ complex showed reaction rates with a variety of hydrocarbons that were ca. 100-fold faster than those of $[Mn^{IV}(O)(^{DMM}N4py)]^{2+}$ (Figure 4.1). A larger, 4000-fold rate enhancement was observed for thioanisole oxidation by $[Mn^{IV}(O)(2pyN2Q)]^{2+}$ compared to $[Mn^{IV}(O)(^{DMM}N4py)]^{2+}$.

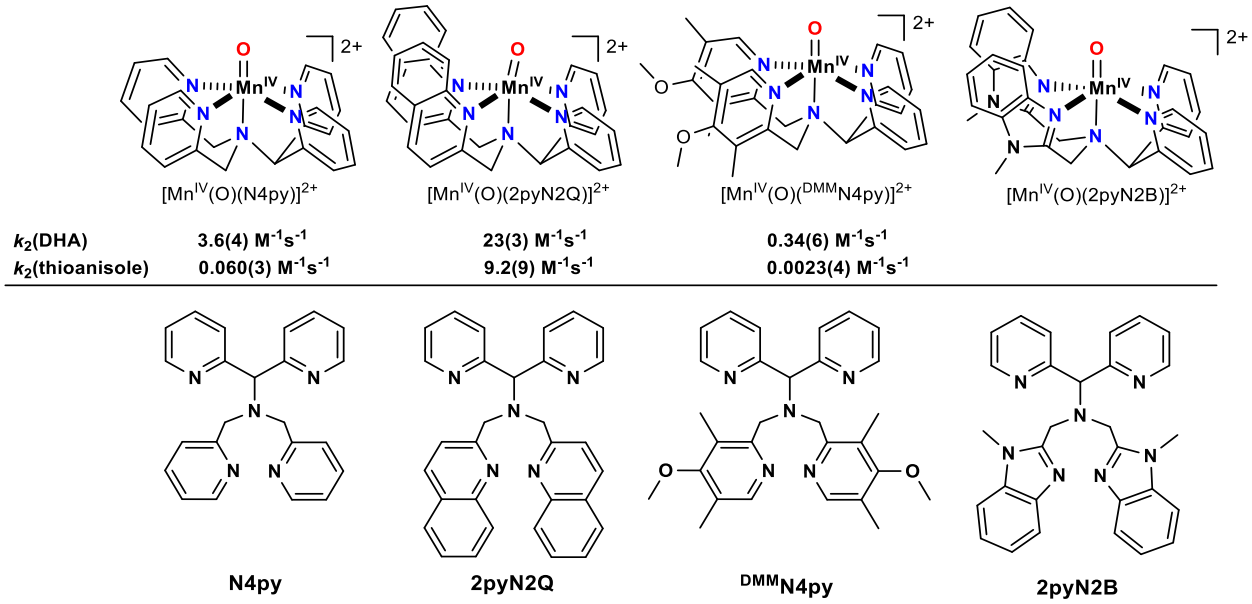

Figure 4.1. Mn^{IV}-oxo complexes and ligands based on the N4py framework. Ligand abbreviations are as follows: N4py is *N*,*N*-bis(2-pyridylmethyl)-*N*-bis(2-pyridyl)methylamine; ^{DMM}N4py is *N*,*N*-bis(4-methoxy-3,5-dimethyl-2-pyridylmethyl)-*N*-bis(2-pyridyl)methylamine; 2pyN2Q is *N*,*N*-bis(2-pyridyl)-*N*,*N*-bis(2-quinolylmethyl)methanamine; and 2pyN2B is *N*,*N*-bis(1-methyl-2-benzimidazolyl)methyl-*N*-(bis-2-pyridylmethyl)-amine.

More recently, Que and co-workers reported similar rate enhancements for the analogous Fe^{IV}-oxo series,[7] where $[Fe^{IV}(O)(2pyN2Q)]^{2+}$ reacts with hydrocarbons ca. 20-50-fold faster than $[Fe^{IV}(O)(^{DMM}N4py)]^{2+}$.[8] An X-ray crystal structure of $[Fe^{IV}(O)(2pyN2Q)]^{2+}$ showed a N_{axial}–Fe=O angle near 170°, consistent with our DFT predictions from the $[Mn^{IV}(O)(2pyN2Q)]^{2+}$ complex. This angle contrasts with the analogous N_{axial}–Fe=O angle found in the X-ray structure of $[Fe^{IV}(O)(2pyN2B)]^{2+}$, for which the value is 177° (2pyN2B is an N4py derivative with two pyridyl and two *N*-(methyl)benzimidazolyl functions (Figure 4.1)).[7] The Fe^{IV}-oxo rate enhancements were also correlated with the Fe^{IV} ligand-field strength, as a linear relationship was observed between the HAT energy barrier (from $\log(k_2)$) and the average Fe–N distance from the X-ray crystal structures of the Fe^{IV}-oxo complexes. The $[Fe^{IV}(O)(2pyN2B)]^{2+}$ complex showed HAT and OAT reaction rates approximately 1-2 orders of magnitude faster than the parent $[Fe^{IV}(O)(N4py)]^{2+}$ but 2-10 times slower than that of $[Fe^{IV}(O)(2pyN2Q)]^{2+}$.[7, 9]

To determine the influence of *N*-(methyl)benzimidazolyl ligation on a Mn^{IV}-oxo unit, we describe here the Mn^{IV}-oxo adduct supported by the 2pyN2B ligand, ($[Mn^{IV}(O)(2pyN2B)]^{2+}$; see Figure 4.1). To assess the influence of the 2pyN2B ligand on Mn^{IV}-oxo electronic structure and reactivity, we performed thorough spectroscopic investigations of $[Mn^{IV}(O)(2pyN2B)]^{2+}$, including characterization by electronic absorption, EPR, and Mn K-edge X-ray absorption near-edge spectroscopies. The reactivity of $[Mn^{IV}(O)(2pyN2B)]^{2+}$ was explored using thioanisole and 9,10-dihydroanthracene (DHA) as model substrates for OAT and HAT reactions, respectively. A comparison of the rates of $[Mn^{IV}(O)(2pyN2B)]^{2+}$ with those of related Mn^{IV}-oxo and Fe^{IV}-oxo complexes reveals a distinctly different relationship between ligand structure and reactivity for the Mn^{IV}-oxo adducts as compared to their Fe^{IV}-oxo analogues.

4.2 Experimental Methods

Materials and Instrumentation. All chemicals and solvents were purchased from commercial vendors and were ACS reagent-grade quality or better. 9-10-dihydroanthracene (DHA) and xanthene were recrystallized from ethanol.[10] All other chemicals were used as received, with the exception of MeCN and diethylether, which were sparged with argon and dried as described previously.[11] $Mn^{II}(OTf)_2 \bullet 2CH_3CN$, used for preparation of metal complexes, was synthesized according to a previously reported procedure.[12] For O_2-free reactions, solvents were dried following published procedures and degased by freeze-pump-thaw methods.[10] Iodosobenzene (PhIO) was prepared from iodosobenzene diacetate following a published procedure.[13]

Electronic absorption spectra for formation and kinetic reactions were obtained on a Varian Cary 50 Bio or an Agilent 8453 spectrophotometer. Both spectrophotometers were interfaced with

Unisoku cryostats (USP-203-A), capable of maintaining temperatures of 25 °C for all reactions. Electrospray-ionization mass spectrometry experiments were performed using an LCT Primers Micromass electrospray time-of-flight instrument. NMR data were collected on a Bruker AVIIIHD 400 MHz NMR instrument. EPR data were collected between 5 and 10 K on a 9 GHz Bruker EMXPlus spectrometer with an Oxford ESR900 continuous-flow liquid helium cryostat controlled by an Oxford ITC503 temperature system. Perpendicular-mode data were collected in a dual-mode Bruker ER4116DM cavity. Recording conditions were 9.637 GHz microwave frequency, 2.0 mW microwave power, 6 G modulation amplitude, 100 kHz modulation frequency, and 141 ms time constant.

Synthesis and Characterization. 2pyN2B was synthesized by a previously published method.[9] The $[Mn^{II}(OH_2)(2pyN2B)](OTf)_2$ complex ($C_{31}H_{29}F_6MnN_7O_7S_2$) was prepared by reacting equimolar amounts of the 2pyN2B free ligand and $Mn^{II}(OTf)_2 \bullet 2CH_3CN$ in CH_3CN under an argon atmosphere and stirring the resultant solution for 30 minutes to an hour. Solid $[Mn^{II}(OH_2)(2pyN2B)](OTf)_2$ was obtained by slow diffusion of diethyl ether into the $[Mn^{II}(OH_2)(2pyN2B)](OTf)_2$ acetonitrile solution under argon. Repeated recrystallizations yielded the $[Mn^{II}(OH_2)(2pyN2B)](OTf)_2$ salt in 52% yield. ESI-MS data for $[Mn^{II}(OH_2)(2pyN2B)](OTf)_2$ dissolved in MeCN shows a single peak at 563.13 corresponding to $[Mn^{II}(2pyN2B)(Cl)]^+$, in which the triflate ion was replaced by a chloride in the mass spectrometer (Figure A4.1). The effective magnetic moment (μ_{eff}) of $[Mn^{II}(OH_2)(2pyN2B)](OTf)_2$ was found to be 5.91 μ_b, which is in good agreement with the expected μ_{eff} of 5.92 μ_b for high-spin Mn^{II} centers. The perpendicular-mode EPR spectrum of a 1 mM solution of $[Mn^{II}(OH_2)(2pyN2B)](OTf)_2$ was collected at 10 K (Figure A4.2). The intermediate $[Mn^{IV}(O)(2pyN2B)]^{2+}$ ($C_{29}H_{27}MnN_7O$) was prepared *in situ* by reacting 1.7 mg (0.002 mmol) $[Mn^{II}(OH_2)(2pyN2B)](OTf)_2$ with 4.4 mg (0.02 mmol) PhIO in 2.0 mL 2,2,2-

trifluoroethanol (TFE). An ESI-MS sample of $[Mn^{IV}(O)(2pyN2B)]^{2+}$ was prepared by diluting 20 µL of the solution in pre-cooled MeCN (-40 ºC). ESI-MS data for isotopically-labeled $[Mn^{IV}(O)(2pyN2B)]^{2+}$ was obtained by incubating $[Mn^{IV}(O)(2pyN2B)]^{2+}$ with 15 µL $H_2{}^{18}O$ for 5 minutes to allow for water exchange. Because the stability of $[Mn^{IV}(O)(2pyN2B)]^{2+}$ is greatly reduced in MeCN, the dominant peaks in the mass spectra come from Mn^{II} decay products (Figure A4.3).

X-ray Crystallography of $[Mn^{II}(OH_2)(2pyN2B)](OTf)_2$. Crystals suitable for characterization by X-ray diffraction were obtained by vapor diffusion of diethyl ether into an acetonitrile solution of $[Mn^{II}(OH_2)(2pyN2B)](OTf)_2$. A full hemisphere of diffracted intensities (740 15-second frames with a scan width of 1.00°) was measured for a single-domain specimen using graphite-monochromated Mo Kα radiation (λ = 0.71073 Å) on a Bruker SMART APEX CCD Single Crystal Diffraction System.[14] The integrated data[15] were corrected empirically for variable absorption effects using equivalent reflections. The Bruker software package SHELXTL was used to solve the structure using "direct methods" techniques. All stages of the weighted full-matrix least-squares refinement were conducted using F_o^2 data with the SHELXTL XL v2014 software package.[16] The final structural model incorporated anisotropic thermal parameters for all nonhydrogen atoms and isotropic thermal parameters for all hydrogen atoms. All hydrogen atoms for the metal complex were located with a difference Fourier and initially included in the structural model as independent isotropic atoms whose parameters were allowed to vary in least-squares refinement cycles. The methyl group was eventually included as an idealized sp^3-hydridized rigid rotor that was allowed to rotate freely about its C-C bond in refinement cycles. Hydrogen atoms for the ether molecule of crystallization were placed at idealized riding model positions with C–H bond lengths of 0.97 – 0.98 Å and isotropic thermal parameters that were 1.2 (nonmethyl) or 1.5

(methyl) times the equivalent isotropic thermal parameter of the carbon atom to which they were covalently bonded. The methyl groups in the ether molecule were placed with idealized "staggered" orientations and the rigid rotor methyl group in the metal complex utilized C–H bond lengths of 0.97 Å. Crystal data and structure refinement details are given in Table A4.1. A checkCIF A-alert for $Mn^{II}(OH_2)(2pyN2B)](OTf)_2$ is likely due to a slight disordering of the ether solvent molecule of crystallization. This disorder produces larger thermal parameters for its atoms than those of the metal complex. The structure of $[Mn^{II}(OH_2)(2pyN2B)](ClO_4)_2 \bullet 2CH_3CN$ was also determined (CCDC entry 1891620).

Synthesis and Characterization of $[Mn^{II}(OH_2)(2pyN2B)](ClO_4)_2$. To a MeCN solution (10 ml) of the ligand (0.047 g, 0.1 mmol), $Mn(ClO_4)_2.6H_2O$ was added and the solution turned pale green. This solution was stirred for 4 hours and was left for slow evaporation of MeCN. After 4-5 days, white colored crystals were isolated. The crystals were washed with MeCN to remove any excess ligand. Crystals were obtained by slow evaporation in MeCN. ESI-MS data for $[Mn(OH_2)(2pyN2B)](ClO_4)_2$ dissolved in MeCN show the following peaks (m/z): 264.02 corresponding to $[Mn^{II}(2pyN2B)]^{2+}$ (calculated 264.08), 563.05 corresponding to $[Mn(2pyN2B)(OH)(H_2O)]^{+}$ (calculated 563.18) and 627.02 corresponding to $[Mn(2pyN2B)(OH)(H_2O)(CH3OH)_2]^{+}$ (calculated 627.23). The bond parameters of this structure do not differ significantly from $[Mn^{II}(OH_2)(2pyN2B)](OTf)_2$ (see Table A4.2).

Preparation of XAS Sample. A 15 mM sample of $[Mn^{II}(OH_2)(2pyN2B)](OTf)_2$ was prepared by dissolving 9.3 mg (0.012 mmol) $[Mn^{II}(OH_2)(2pyN2B)](OTf)_2$ in 0.8 mL of ethanol, transferring the solution to an XAS sample holder, and flash freezing the solution in liquid nitrogen. A 10 mM XAS sample of $[Mn^{IV}(O)(2pyN2B)]^{2+}$ was prepared by dissolving 13.3 mg (0.016 mmol) $[Mn^{II}(OH_2)(2pyN2B)](OTf)_2$ in 1.6 mL of a TFE solution containing 35.2 mg PhIO

(0.16 mmol). The reaction mixture was placed into a 0.2 cm cuvette, where the formation of $[Mn^{IV}(O)(2pyN2B)]^{2+}$ was monitored by electronic absorption spectroscopy. At maximum formation, two XAS samples were prepared and flash frozen in liquid nitrogen.

XAS Data Collection. Mn K-edge XAS data for $[Mn^{IV}(O)(2pyN2B)]^{2+}$ were collected at beamline 9-3 at the Stanford Synchrotron Radiation Light Source (SSRL). XAS spectra for $[Mn^{IV}(O)(2pyN2B)]^{2+}$ were obtained as fluorescence excitation spectra using a Canberra 100-element Ge array detector. Data for $[Mn^{II}(OH_2)(2pyN2B)](OTf)_2$ was collected at beamline 2-2 at SSRL using a Si(111) monochromator and a 13-element Ge array fluorescence detector. Mn K-edge X-ray absorption spectra were collected over an energy range of 6.3 to 7.4 keV (Si(220) monochromator). The frozen samples were maintained at 7 K during data collection by an Oxford liquid He cryostat. A reference spectrum of a manganese foil was collected for each scan and an internal calibration was performed by setting the zero crossing of the second derivative of the K-edge energy of the reference spectra to 6539.0 keV. The high flux at beamline 9-3 lead to photo-reduction for $[Mn^{IV}(O)(2pyN2B)]^{2+}$. When multiple scans were collected on a single spot of the frozen sample for $[Mn^{IV}(O)(2pyN2B)]^{2+}$, there was a noticeable shift of the edge to a lower energy. To reduce the effects of photoreduction, the beam was moved to different spots on the sample and only one scan was collected per spot. Three scans were collected for $[Mn^{IV}(O)(2pyN2B)]^{2+}$. Compared to conditions at beamline 9-3, beamline 2-2 has reduced X-ray flux. These conditions required the use of ethanol as the solvent rather than TFE, as the latter solvent leads to diminished X-ray fluorescence. The relatively low flux and smaller number of detectors at this beamline required the signal averaging of eighteen scans for $[Mn^{II}(OH_2)(2pyN2B)](OTf)_2$. XAS data was collected by Allyssa Massie.

XAS Data Analysis. XAS data analysis was performed using the Demeter software package.[17] Individual scans of raw data were analyzed and combined using Athena. Fits of the pre-edge area was performed using the FityK software.[18] Pre-edge intensity was normalized relative to the tail of the fluorescence signal. XAS data analysis was conducted by Allyssa Massie.

EPR Sample Preparation. A 1 mM sample of $[Mn^{II}(OH_2)(2pyN2B)](OTf)_2$ was prepared and flash frozen using liquid nitrogen in a 4 mm quartz EPR tube. A 10 mM sample of $[Mn^{IV}(O)(2pyN2B)]^{2+}$ was prepared by thawing the XAS sample at -20 °C and then immediately transferring 200 μL of this solution into a pre-cooled EPR tube and flash freezing the tube in liquid nitrogen. A second EPR sample of $[Mn^{IV}(O)(2pyN2B)]^{2+}$ was prepared as follows: 10 equivalents of PhIO were added to a 20 mM solution of $[Mn^{II}(OH_2)(2pyN2B)](OTf)_2$ in TFE to give a final concentration of 10 mM. The formation of $[Mn^{IV}(O)(2pyN2B)]^{2+}$ was monitored by UV-Vis spectroscopy. Upon maximum formation of the Mn^{IV}-oxo species, 200 μL of this solution were transferred into a pre-cooled EPR tube that was then flash frozen in liquid nitrogen.

Electronic Structure Computations. All computations were performed using the *ORCA* 3.0.3 software package.[19] DFT geometry optimizations of $[Mn^{IV}(O)(2pyN2B)]^{2+}$ and $[Mn^{IV}(O)(N4py)]^{2+}$ employed the TPSS functional,[20] TZVP (Mn, O, and N) and SVP (C, F, and H) basis sets,[21-23] and the COSMO solvation model (for TFE).[24] Tight optimization and SCF criteria were invoked using the TightOpt and TightSCF keywords. The RI approximation, with TZVP/J and SVP/J auxiliary basis sets, was used for geometry optimizations. This level of theory replicates that employed for previously reported geometries of $[Mn^{IV}(O)(2pyN2Q)]^{2+}$ and $[Mn^{IV}(O)(^{DMM}N4py)]^{2+}$,[6] allowing for a balanced structural comparison of these complexes. Structures were converged to the S = 3/2 spin states. Cartesian coordinates for $[Mn^{IV}(O)(2pyN2B)]^{2+}$ and $[Mn^{IV}(O)(N4py)]^{2+}$ are included in Tables A4.4 and A4.5.

HAT and OAT Reactivity Studies. In a typical reaction, when 1.0 mM of $[Mn^{IV}(O)(2pyN2B)]^{2+}$ was fully formed, an aliquot of a solution containing substrate (thioanisole in TFE and DHA or xanthene in CH_2Cl_2) was added to the cuvette for a final solution volume of 2.1 mL. The decay of the 940 nm feature of $[Mn^{IV}(O)(2pyN2B)]^{2+}$ was monitored, and the resulting time trace was fit to a pseudo-first order model. The observed rate constants were plotted against the substrate concentration to obtain a second-order rate constant. For DHA, 10 - 40 equivalents of substrate were added to determine the second-order rate constant for HAT reactivity. The reaction of $[Mn^{IV}(O)(2pyN2B)]^{2+}$ with deuterated [D_4]-DHA was used to determine a primary kinetic isotope effect. For xanthene, 20-50 equivalents of substrate were added to determine the second-order rate constant for HAT reactivity. 10 to 60 equivalents of thioanisole were used to determine the second-order rate constant for the OAT reaction. Reactions with thioanisole were conducted by Eleanor Stewart-Jones.

Product Analysis Experiments. Analysis of the product of the reaction between $[Mn^{IV}(O)(2pyN2B)]^{2+}$ and DHA was performed by removing the solvent under vacuum and then re-dissolving the isolated residue in cyclohexane. The product anthracene was observed and quantified using the published extinction coefficient for anthracene in cyclohexane.[25] Analysis of the product of the reaction of $[Mn^{IV}(O)(2pyN2B)]^{2+}$ and thioanisole was performed by ^{1}H-NMR experiments following previously described methods.[6] The only modification was the use of toluene as internal standard, which was added directly to the ^{1}H-NMR sample before analysis.

Cyclic Voltammetry Experiments. A glassy carbon working electrode, a platinum auxiliary electrode, and a Ag/AgCl quasi-reference electrode were used with an external ferrocene/ferrocenium potential as an external reference. Cyclic voltammograms were recorded on an Epsilon potentiostat. These experiments used 16.5 mg (0.02 mmol)

$[Mn^{II}(OH_2)(2pyN2B)](OTf)_2$, with 22.0 mg PhIO (0.1 mmol) in TFE with 0.1 M Bu_4NPF_6 electrolyte at 298 K. Fewer equivalents of PhIO were used in electrochemical experiments due to limited solubility of PhIO in TFE. Cyclic voltammetry experiments were conducted by Allyssa Massie.

Analysis of Multiline EPR Signal in the EPR Spectrum of $[Mn^{IV}(O)(2pyN2B)]^{2+}$. The perpendicular-mode EPR spectra of $[Mn^{IV}(O)(2pyN2B)]^{2+}$ shown in Figure 4.3 show a 16-line $Mn^{III}Mn^{IV}$ dimer impurity at g = 2.0, which presumably results from the thermal decay of $[Mn^{IV}(O)(2pyN2B)]^{2+}$. Because both the $Mn^{III}Mn^{IV}$ dimer and Mn^{IV}-oxo species show EPR signals in the g = 2.0 region, spin quantification cannot be used to determine the exact amount of $Mn^{III}Mn^{IV}$ dimer present in the sample. However, using a previously published protocol, we were able to prepare a separate EPR sample for the closely-related $[Mn^{III}Mn^{IV}(\mu\text{-}O)(^{DMM}N4py)_2)]^{2+}$ complex.[26] Recording conditions were 9.637 GHz microwave frequency, 2.0 mW microwave power, 4.55 G modulation amplitude, 100 kHz modulation frequency, and 141 ms time constant. As seen in Figure A4.21, the $Mn^{III}Mn^{IV}$ signal in the $[Mn^{IV}(O)(2pyN2B)]^{2+}$ sample (Figure 4.3 and A4.21) is very weak, consistent with our assumption that this signal represents a small fraction of Mn in the sample. Spin quantification was used to estimate that 4% of the total amount of Mn in solution is present as a dimer. However, it must be emphasized that this value is likely over estimated due to the overlapping Mn^{IV}-oxo signal at g = 2.0.

4.3 Results and Discussion

X-ray Diffraction Structure of $[Mn^{II}(OH_2)(2pyN2B)](OTf)_2$. The crystal structure of $[Mn^{II}(OH_2)(2pyN2B)](OTf)_2$ shows a mononuclear Mn^{II} center in a distorted octahedral environment with an axial water ligand and the 2pyN2B ligand bound in its expected pentadentate mode (Figure 4.2). The axial Mn–OH_2 distance of 2.087(3) Å is comparable to that observed for

$[Mn^{II}(OH_2)(2pyN2Q)](OTf)_2$ (2.091(2) Å).[6] However, the water ligand in $[Mn^{II}(OH_2)(2pyN2B)](OTf)_2$ is not as distorted from the idealized octahedral position as in $[Mn^{II}(OH_2)(2pyN2Q)](OTf)_2$ (N_{axial}–Mn–OH_2 angles of 177.9° and 163.8°, respectively). This difference in bond angles reflects the greater steric influence of the quinolinyl moieties in 2pyN2Q on the axial coordination position. In support, the closest contacts for the benzimidazolyl carbon atoms and the oxygen atom of the water ligand of $[Mn^{II}(OH_2)(2pyN2B)]^{2+}$ are 3.807 Å. These separations lead to corresponding CH···OH_2 interaction distances of 3.093 Å. In contrast, the previously reported XRD structure of $[Mn^{II}(OH_2)(2pyN2Q)](OTf)_2$ shows $C_{quinolinyl}$···OH_2 separations of 3.453 and 3.515 Å, which leads to much shorter CH···OH_2 interaction distances of 2.529 and 2.616 Å. The greater steric influence of the 2pyN2Q ligand as compared to 2pyN2B was also observed in the recently reported XRD structures for the Fe^{IV}-oxo complexes (*vide supra*).[7] As discussed by Que and coworkers, the steric influence exerted by the quinolinyl substituents leads to long metal-$N_{quinoline}$ distances and, consequently, weak quinolinyl donation to the metal.[2, 7]

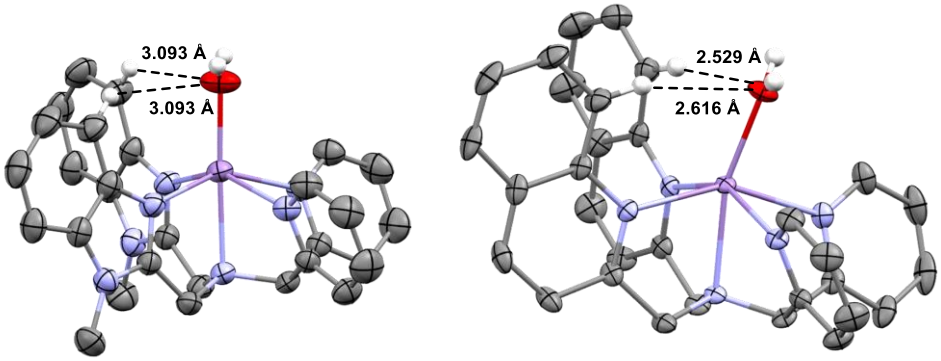

Figure 4.2. Molecular structures of $[Mn^{II}(OH_2)(2pyN2B)]^{2+}$ and $[Mn^{II}(OH_2)(2pyN2Q)]^{2+}$ cations. Thermal ellipsoids are shown at 50% probability and most hydrogen atoms and triflate counter anions have been removed for clarity.

The two Mn–$N_{benzimidazolyl}$ distances in $[Mn^{II}(OH_2)(2pyN2B)](OTf)_2$ are 2.193(2) Å, which are ca. 0.06 – 0.08 Å shorter than the corresponding Mn–$N_{pyridyl}$ distances of $[Mn^{II}(OTf)(N4py)]^+$, but similar to the Mn–$N_{3,5\text{-dimethyl-4-methoxypyridyl}}$ bond lengths of $[Mn^{II}(OTf)(^{DMM}N4py)]^+$ (Table 4.1).[6, 27] These short Mn–$N_{benzimidazolyl}$ distances are accordant with the greater basicity of benzimidazole than pyridine.[28] The Mn–$N_{pyridyl}$ distances of $[Mn^{II}(OH_2)(2pyN2B)](OTf)_2$ (2.298(2) Å) are comparable to those observed for the other Mn^{II} complexes (Table 4.1). Overall, the average Mn–$N_{equatorial}$ distance for $[Mn^{II}(OH_2)(2pyN2B)](OTf)_2$ is slightly less than that of $[Mn^{II}(OTf)(^{DMM}N4py)]^{2+}$ (2.246 and 2.251 Å, respectively), making the 2pyN2B ligand the *strongest* equatorial donor of this series. The largest Mn-ligand bond deviation for $[Mn^{II}(OH_2)(2pyN2B)](OTf)_2$ is in the Mn–N_{amine} bond distance (2.375(3) Å), which is nearly 0.09 Å longer than the corresponding distances for the other Mn^{II} structures (Table 4.1). The Fe^{II}–N_{amine} distance in $[Fe^{II}(2pyN2B)(NCMe)](ClO_4)_2$ showed a similar elongation of 0.067 Å relative to $[Fe^{II}(N4py)(NCMe)](ClO_4)_2$.[9] This variation in bond length was attributed to different angular requirements of the five-membered benzimidazolyl and six-membered pyridyl rings.[9] The same rationale can be applied to account for the elongated Mn–N_{amine} bond of $[Mn^{II}(OH_2)(2pyN2B)](OTf)_2$. When this elongated Mn–N_{amine} distance is considered, the average Mn–N distances of $[Mn^{II}(OH_2)(2pyN2B)](OTf)_2$ (Mn–N_{total} in Table 4.1) are just slightly less than those of $[Mn^{II}(OTf)(N4py)]^+$ and $[Mn^{II}(OH_2)(2pyN2Q)]^{2+}$, and longer than that of $[Mn^{II}(OTf)(^{DMM}N4py)]^+$ (Table 4.1). Collectively, these metric data show that 2pyN2B provides an equatorial ligand field comparable in strength to that of ^{DMM}N4py and stronger than that of N4py and 2pyN2Q but with markedly attenuated axial donation.

Table 4.1. Manganese-Ligand Bond Distances (Å) for Mn^{II} Complexes Supported by the 2pyN2B, N4py, ^{DMM}N4py, and 2pyN2Q Ligands.

	$[Mn^{II}(OH_2)(2pyN2B)]^{2+}$	$[Mn^{II}(OTf)(N4py)]^{+a}$	$[Mn^{II}(OTf)(^{DMM}N4py)]^{+b}$	$[Mn^{II}(OH_2)(2pyN2Q)]^{2+b}$
Mn–O	2.087(3)	2.125(3)	2.114(3)	2.091(2)
$Mn–N_X$ [c]	2.193(2)	2.255(4)	2.189(4)	2.250(2)
$Mn–N_X$ [c]	2.193(2)	2.271(4)	2.225(3)	2.265(2)
$Mn–N_{pyridyl}$	2.298(2)	2.271(4)	2.296(4)	2.297(2)
$Mn–N_{pyridyl}$	2.298(2)	2.278(4)	2.293(3)	2.303(2)
$Mn–N_{amine}$	2.375(3)	2.289(4)	2.278(4)	2.279(2)
$Mn–N_{equatorial}$ [d]	2.246	2.269	2.251	2.279
$Mn–N_{total}$ [e]	2.271	2.273	2.256	2.279

[a] From reference [27]. [b] From reference [6]. [c] N_X is $N_{benzimidazolyl}$ for $[Mn^{II}(OH_2)(2pyN2B)]^{2+}$, $N_{pyridyl}$ for $[Mn^{II}(OTf)(N4py)]^{+}$, $N_{3,5\text{-dimethyl-4-methoxypyridyl}}$ for $[Mn^{II}(OTf)(^{DMM}N4py)]^{+}$, and $N_{quinolinyl}$ for $[Mn^{II}(OH_2)(2pyN2Q)]^{2+}$. [d] Average of the Mn–N bond distances in the equatorial positions. [e] Average of all Mn–N bond distances.

The trend in $Mn–N_{equatorial}$ bond length observed for the manganese(II) complexes with the 2pyN2B, N4py, and ^{DMM}N4py ligands is more dramatic than that observed for the corresponding iron(II) complexes. Specifically, $[Fe^{II}(NCMe)(2pyN2B)](ClO_4)_2$, $[Fe^{II}(NCMe)(N4py)](ClO_4)_2$, and $[Fe^{II}(NCMe)(^{DMM}N4py)](OTf)_2$ showed average $Fe–N_{equatorial}$ distances within the narrow range of 1.971 Å to 1.978 Å. This 0.007 Å length span is much smaller than the 0.038 Å variation seen for the corresponding Mn^{II} complexes (Table 4.1). The Fe^{II} complexes are all low spin (S = 0) at the temperatures employed for the X-ray crystallography experiments, and it is therefore expected that the $Fe–N_{equatorial}$ distances should be less sensitive to perturbations in the equatorial ligand field than the high-spin (S = 5/2) Mn^{II} complexes, in which the metal $3d_{x^2-y^2}$ MO, which is metal-$N_{equatorial}$ σ-antibonding, will be populated. [8-9, 29]

Formation and characterization of $[Mn^{IV}(O)(2pyN2B)]^{2+}$. The addition of PhIO to a TFE solution of $[Mn^{II}(OH_2)(2pyN2B)](OTf)_2$ at 25 °C led to the formation of new electronic absorption bands at 940, 460, and 410 nm (Figure 4.3). These bands reached maximum intensity when 10 equivalents of PhIO were used. The energy and intensity of the near-IR absorption band at 940 nm (ε = 250 $M^{-1}cm^{-1}$, assuming 100% formation) is quite similar to that observed for Mn^{IV}-

oxo complexes of the N4py, ^{DMM}N4py, and 2pyN2Q ligands (λ_{max} = 920 - 1180 nm; ε = 179 – 290 $M^{-1}cm^{-1}$; Table 4.2).[6, 27] On the basis of this similarity, and strongly supported by additional data described below, we assign the chromophore formed by the reaction of $[Mn^{II}(OH_2)(2pyN2B)](OTf)_2$ with PhIO to $[Mn^{IV}(O)(2pyN2B)]^{2+}$. In previous investigations of $[Mn^{IV}(O)(N4py)]^{2+}$ and its derivatives, the near-IR absorption bands of these complexes were attributed to the $^4B_1 \rightarrow {}^4E$ transition, which corresponds to a one-electron excitation from the quasi-degenerate Mn^{IV} $3d_{xz}$ and $3d_{yz}$ MOs to the unoccupied $3d_{x^2-y^2}$ MO.[6, 30] These MOs are Mn=O π-antibonding and Mn–$N_{equatorial}$ σ-antibonding, respectively. Previous DFT computations for $[Mn^{IV}(O)(N4py)]^{2+}$ and its derivatives showed that variations in the energy of this electronic transition arise predominantly from perturbations in Mn–$N_{equatorial}$ bonding.[6, 30] As shown in Table 4.2, the near-IR absorption maxima of $[Mn^{IV}(O)(2pyN2B)]^{2+}$ (940 nm; 10 640 cm^{-1}) lies between those of $[Mn^{IV}(O)(^{DMM}N4py)]^{2+}$ (920 nm; 10 870 cm^{-1}) and $[Mn^{IV}(O)(N4py)]^{2+}$ (950 nm; 10 530 cm^{-1}). This position is consistent with the benzimidazolyl moieties being better σ-donors than an unmodified pyridine, as also manifested in the Mn^{II}–N_X distances of the corresponding Mn^{II} complexes (Table 4.1).

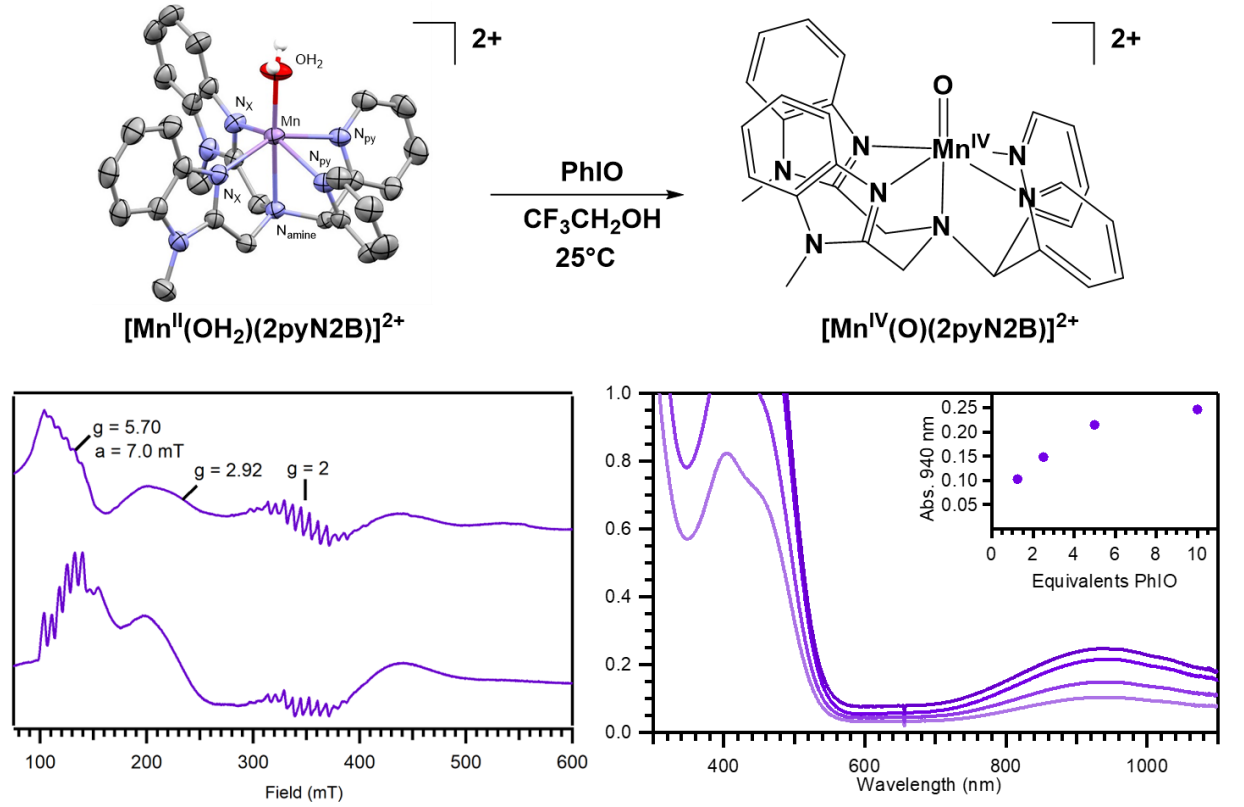

Figure 4.3. Top: Formation of $[Mn^{IV}(O)(2pyN2B)]^{2+}$ from PhIO oxidation of $[Mn^{II}(OH_2)(2pyN2B)]^{2+}$. Bottom right: Electronic absorption spectra showing the final spectra of $[Mn^{IV}(O)(2pyN2B)]^{2+}$ following the addition of 1 to 10 equivalents PhIO to $[Mn^{II}(OH_2)(2pyN2B)](OTf)_2$ (1.0 mM in TFE at 25 °C). The inset shows the intensity of the near-IR absorption band as a function of equivalents PhIO. Bottom left: Perpendicular-mode X-band EPR spectra of $[Mn^{IV}(O)(2pyN2B)]^{2+}$ at 10 K. The top trace represents data collected after thawing an XAS sample. The bottom trace is for data collected for a sample prepared by monitoring Mn^{IV}-oxo formation by UV-Vis spectroscopy.

Table 4.2. Electronic Absorption near-IR Band Maxima (nm), Extinction Coefficients (M^{-1} cm^{-1}), $t_{1/2}$ Values in TFE at 25°C (hours), EPR g-Values, Hyperfine Couplings (mT), XAS Edge and Pre-Edge Energies (eV), XAS Pre-Edge Areas, and CV Peak Potentials (V) for Mn^{IV}-oxo Complexes.

complex	λ_{max}	ε	$t_{1/2}$	g_{eff} [a]	a [b]	Edge	Pre-edge	area	$E_{p,c}$ [c]
$[Mn^{IV}(O)(^{DMM}N4py)]^{2+}$	920	290	6	4.38	7.7	6550.3	6541.3	19.6	0.61
$[Mn^{IV}(O)(2pyN2B)]^{2+}$	940	250	2.7	5.70	7.0	6549.6	6541.4	14.6	0.47
$[Mn^{IV}(O)(N4py)]^{2+}$	950	230	0.5	4.35	7.6	6550.8	6541.6	18.9	0.80
$[Mn^{IV}(O)(2pyN2Q)]^{2+}$	1180	179	0.2	4.30	7.2	6549.2	6541.2	17.0	1.01

[a] The g_{eff} value of the most intense, positive signal at low field (see Figure A4.6). [b] Hyperfine splitting of six-line signals observed near g = 5.7 – 5.8 (see Figure A4.6). [c]Cathodic peak potential versus SCE. Data for $[Mn^{IV}(O)(N4py)]^{2+}$ comes from reference [27] and data for $[Mn^{IV}(O)(^{DMM}N4py)]^{2+}$and $[Mn^{IV}(O)(2pyN2Q)]^{2+}$ comes from reference [6].

Even when using 10 equivalents PhIO, the rate of formation of $[Mn^{IV}(O)(2pyN2B)]^{2+}$ was relatively slow, taking about 20 minutes to reach completion. ESI-MS data for $[Mn^{IV}(O)(2pyN2B)]^{2+}$ show an ion peak at *m/z* of 272.08 (Figure A4.3), which agrees with that predicted for the Mn^{IV}-oxo adduct (*m/z* of 272.08). When $[Mn^{IV}(O)(2pyN2B)]^{2+}$ is incubated with $H_2{}^{18}O$, the ESI-MS shows a new peak at 273.08, which indicates water exchange to give the Mn^{IV}-^{18}O adduct (Figure A4.3). At 25 °C in TFE, a 1.0 mM solution of $[Mn^{IV}(O)(2pyN2B)]^{2+}$ showed a half-life of ~2.7 hours (Figure A4.4), which falls between those of $[Mn^{IV}(O)(2pyN2Q)]^{2+}$ and $[Mn^{IV}(O)(^{DMM}N4py)]^{2+}$ (half-lives of 0.2 and 6 hours, respectively). The thermal decay product of $[Mn^{IV}(O)(2pyN2B)]^{2+}$ is EPR silent and shows prominent ESI-MS peaks at 662.15 and 726.18, which correspond to $[Mn^{III}(2pyN2B)(OCH_2CF_3)(Cl)]^{+}$ and $[Mn^{III}(2pyN2B)(OCH_2CF_3)_2]^{+}$, respectively (Figure A4.5).

The X-band, perpendicular-mode EPR spectrum for $[Mn^{IV}(O)(2pyN2B)]^{2+}$ is characterized by a broad, positive feature centered at g_{eff} = 5.7, a weak derivative signal near g_{eff} = 2.9, and a multiline signal around g_{eff} = 2 (Figure 4.3, bottom left, two samples shown). The signal at g_{eff} = 5.7 shows a six-line hyperfine splitting with a = 7.0 mT. The multiline signal at g_{eff} = 2 likely derives from a multi-nuclear Mn species, which we assign as a $Mn^{III}Mn^{IV}$ dimer (Figure A4.21).[26] Although the g_{eff}-values for $[Mn^{IV}(O)(2pyN2B)]^{2+}$ are in the range expected for mononuclear, S = 3/2 Mn^{IV} species,[31] the spectrum is perturbed compared to those observed for the other N4py-based oxomanganese(IV) complexes (Figure A4.6 and Table 4.2).[6, 27] The down-field shift of the g_{eff} = 5.7 signal for $[Mn^{IV}(O)(2pyN2B)]^{2+}$, and the appearance of the weak signal at g_{eff} = 2.9, suggests that this oxomanganese(IV) complex has a larger rhombic component to its zero-field splitting tensor (*i.e.*, larger *E/D* parameter, where *D* and *E* are the axial and rhombic zero-field splitting parameters, respectively). The EPR spectrum of $[Mn^{IV}(O)(2pyN2B)]^{2+}$ is reminiscent of that

observed for $[Mn^{IV}(O)(OH)(Me_2EBC)]^+$ (Me_2EBC = 4,11-dimethyl-1,4,8,11-tetraazabicyclo[6.6.2]hexadecane), which had two overlapping six-line hyperfine features at g_{eff} = 5.95 and 4.99, and a derivative signal at g_{eff} = 2.62.[31]

In Figure 4.3, data for two different EPR spectra are shown. The top line represents data collected for a sample that was prepared by thawing an XAS sample and re-freezing the solution in an EPR tube. The bottom line represents data collected for a sample that was frozen immediately following full formation of $[Mn^{IV}(O)(2pyN2B)]^{2+}$ after monitoring by UV-Vis spectroscopy. The EPR spectrum for the latter sample shows that the positive feature centered at g = 5.70 can be attributed to two different signals. The appearance of eight hyperfine-lines (six of considerable intensity and two of modest intensity), is consistent with contributions from both the $m_s = \pm ½$ and $m_s = \pm 3/2$ Kramer's doublets.[31] Future work will include investigation of the temperature-dependence of these signals, because variable-temperature EPR experiments can provide insight into the ground-state zero-field splitting and ^{55}Mn hyperfine parameters.[32-36]

Cyclic voltammetry (CV) data for $[Mn^{IV}(O)(2pyN2B)]^{2+}$ show an irreversible one-electron reduction at -0.07 V vs. Cp_2Fe/Cp_2Fe^+ (+0.47 V vs. SCE; see Figure A4.7), which is attributed to the $Mn^{III/IV}$ couple. This process is irreversible, even at scan rates up to 1000 mV s^{-1}. The observed peak potential is slightly less than that of $[Mn^{IV}(O)(^{DMM}N4py)]^{2+}$ (0.06 V vs. Cp_2Fe/Cp_2Fe^+ or +0.61 V vs. SCE), and over 0.5 V less than $[Mn^{IV}(O)(2pyN2Q)]^{2+}$, which has the highest potential for this series (Table 4.2).[6] The low peak potential for $[Mn^{IV}(O)(2pyN2B)]^{2+}$ is consistent with the short $Mn–N_{benzimidazolyl}$ distances observed in the X-ray structure of $[Mn^{II}(OH_2)(2pyN2B)](OTf)_2$ (Figure 4.2), which suggest that the benzimidazolyl ligands are stronger donors than the pyridyl or quinolinyl ligands. Although peak potentials have not been reported for the analogous $[Fe^{IV}(O)(2pyN2B)]^{2+}$ complex, we can compare the shift observed between $[Mn^{IV}(O)(2pyN2B)]^{2+}$

and $[Mn^{IV}(O)(N4py)]^{2+}$ with that reported for their Fe^{II} analogues. In that case, the $[Fe^{II}(NCMe)(2pyN2B)]^{2+}$ complex had a potential 0.45 V less than that of $[Fe^{II}(NCMe)(N4py)]^{2+}$ (0.398 and 0.85 V versus Cp_2Fe/Cp_2Fe^+, respectively).[9] The 0.33 V lower potential of $[Mn^{IV}(O)(2pyN2B)]^{2+}$ than $[Mn^{IV}(O)(N4py)]^{2+}$ is comparable (Table 4.2).

Mn K-edge X-ray absorption data for $[Mn^{II}(OH_2)(2pyN2B)]^+$ and $[Mn^{IV}(O)(2pyN2B)]^{2+}$ show a 2.5 eV increase in edge energy for the latter complex (Figure 4.4), which is consistent with the higher Mn oxidation state. The edge energy of $[Mn^{IV}(O)(2pyN2B)]^{2+}$ (6549.6 eV) is also very similar to those observed for other Mn^{IV}-oxo complexes with neutral pentadentate ligands (6549.2 – 6550.8 eV).[6, 27] The observation that the edge energy of $[Mn^{IV}(O)(2pyN2B)]^{2+}$ is on the lower end of those observed for related Mn^{IV}-oxo adducts is congruent with the EPR data for this complex, which shows a weak multiline signal (Figure 4.3) due to the presence of some multinuclear species (potentially a $Mn^{III}Mn^{IV}$ dimer).

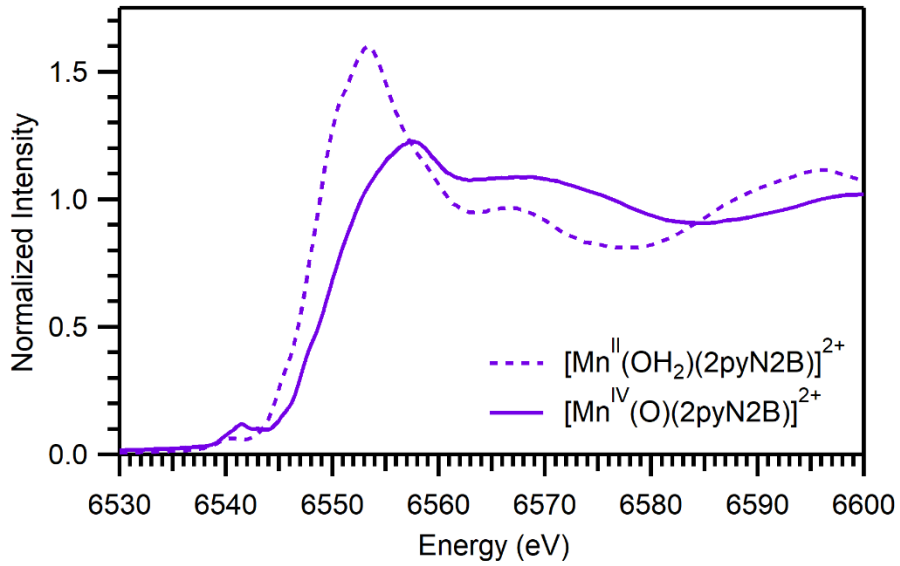

Figure 4.4. Experimental XANES data for frozen samples of $[Mn^{II}(OH_2)(2pyN2B)](OTf)_2$ in ethanol (dashed traces) and $[Mn^{IV}(O)(2pyN2B)]^{2+}$ in TFE (solid traces).

The XAS spectrum of $[Mn^{IV}(O)(2pyN2B)]^{2+}$ shows a prominent pre-edge feature centered at ca. 6541 eV (Figure 4.4) with an area of 14.6 units (Figure A4.8). This feature is readily attributed to a Mn^{IV} 1s-to-3d transition, which gains intensity through Mn^{IV} 3d-4p mixing induced by the short Mn=O distance. The previously described $[Mn^{IV}(O)(N4py)]^{2+}$, $[Mn^{IV}(O)(^{DMM}N4py)]^{2+}$, and $[Mn^{IV}(O)(2pyN2Q)]^{2+}$ complexes also showed pre-edge features near 6541 eV (Figure A4.9),[6, 27] with areas ranging from 17.0 – 19.6 units.

Electronic Structure Computations for $[Mn^{IV}(O)(2pyN2B)]^{2+}$. DFT calculations were carried out to further understand the geometric and electronic structure of $[Mn^{IV}(O)(2pyN2B)]^{2+}$. The DFT-optimized structure of $[Mn^{IV}(O)(2pyN2B)]^{2+}$ has a Mn=O bond length of 1.671 Å, which is very similar to those predicted for the Mn^{IV}-oxo complexes of the ^{DMM}N4py, N4py, and 2pyN2Q ligands (1.673 – 1.678 Å; see Figure 4.5 and Table A4.3). While the $Mn–N_{equatorial}$ distances of $[Mn^{IV}(O)(2pyN2B)]^{2+}$ are the shortest of the series (2.011 Å; see Figure 4.5 and Table A4.2), they are only slightly shorter than the $Mn–N_{equatorial}$ distances of $[Mn^{IV}(O)(^{DMM}N4py)]^{2+}$ and $[Mn^{IV}(O)(N4py)]^{2+}$ (2.015 and 2.018 Å, respectively). These predictions are consistent with the similar near-IR λ_{max} values of these complexes (Table 4.3), which we had previously shown reflect the equatorial ligand-field strength.[6, 30] Further, the $Mn–N_{equatorial}$ distances of $[Mn^{IV}(O)(2pyNQ)]^{2+}$ are significantly elongated at 2.054 Å, consistent with the larger perturbation in the near-IR λ_{max} of this complex (Table 4.2). These variations in metal-nitrogen equatorial bond lengths are qualitatively similar to that observed in the crystal structures of the corresponding Fe^{IV}-oxo complexes.[7] In that case, the average $Fe^{IV}–N_{equatorial}$ bond length of $[Fe^{IV}(O)(2pyN2Q)]^{2+}$ was significantly elongated (2.046 Å), while those of $[Fe^{IV}(O)(2pyN2B)]^{2+}$ and $[Fe^{IV}(O)(N4py)]^{2+}$ were quite similar (1.971 and 1.956 Å, respectively). Nonetheless, for the Fe^{IV}-oxo complexes, N4py provides a stronger equatorial ligand field than 2pyN2B, whereas DFT computations for the

corresponding Mn^{IV}-oxo complexes predicts 2pyN2B to be a stronger equatorial donor (Figure 4.5 and Table A4.3).

The Mn–N_{amine} bond in the DFT-optimized structure of $[Mn^{IV}(O)(2pyN2B)]^{2+}$ is elongated compared to the other Mn^{IV}-oxo complexes (Figure 4.5 and Table A4.3). This result is in agreement with the Mn^{II} XRD structures, where the Mn–N_{amine} bond of $[Mn^{II}(OH_2)(2pyN2B)](OTf)_2$ was also longer than that of the other Mn^{II} complexes. The DFT structure also demonstrates that the 2pyN2B ligand provides significantly less steric crowding of the oxo compared to the 2pyN2Q ligand. This is exemplified by the O–Mn–N_{amine} angle of 177.48°, which is less distorted than in $[Mn^{IV}(O)(2pyN2Q)]^{2+}$ (O–Mn–N_{amine} angle of 170.14°). For comparison, we note that $[Mn^{II}(OH_2)(2pyN2B)](OTf)_2$ also showed a less distorted O–Mn–N_{amine} angle of 177.9°, while the corresponding angle in $[Mn^{II}(OH_2)(2pyN2Q)](OTf)_2$ is 163.8°.

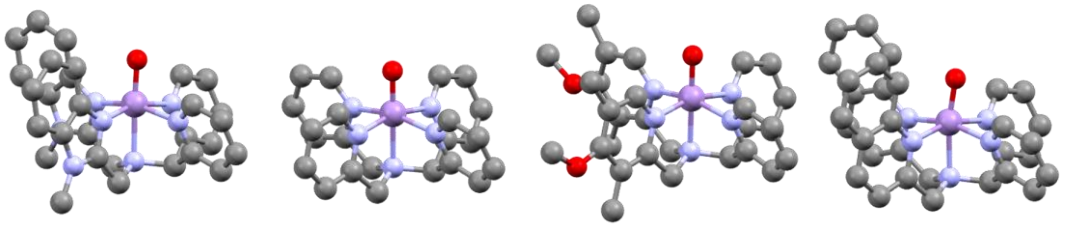

	$[Mn^{IV}(O)(2pyN2B)]^{2+}$	$[Mn^{IV}(O)(N4py)]^{2+}$	$[Mn^{IV}(O)(^{DMM}N4py)]^{2+}$	$[Mn^{IV}(O)(2pyN2Q)]^{2+}$
Mn–O	1.671 Å	1.673 Å	1.678 Å	1.678 Å
Mn–$N_{equatorial}$	2.011 Å	2.018 Å	2.015 Å	2.054 Å
Mn–N_{amine}	2.174 Å	2.118 Å	2.108 Å	2.109 Å
Mn–N_{total}	2.043 Å	2.038 Å	2.033 Å	2.065 Å
O–Mn–N_{amine}	177.48°	179.55°	179.76°	170.63°

Figure 4.5. Selected Bond Lengths (Å), Bond Angles (°) from DFT Computations. $N_{equatorial}$ is the average of the four equatorial Mn–N bond lengths. N_{amine} refers to the amine nitrogen *trans* to the oxo ligand. N_{total} refers to the average of all Mn–N bond distances. Data for $[Mn^{IV}(O)(^{DMM}N4py)]^{2+}$, $[Mn^{IV}(O)(2pyN2Q)]^{2+}$ and $[Mn^{IV}(O)(N4py)]^{2+}$ have been published previously.[6, 27]

Hydrocarbon and Thioanisole Oxidation by $[Mn^{IV}(O)(2pyN2B)]^{2+}$. To further compare $[Mn^{IV}(O)(2pyN2B)]^{2+}$ with other Mn^{IV}-oxo adducts, we investigated the reactivity of this complex with hydrocarbons and thioanisole. These reactions are expected to occur by different mechanisms (HAT and OAT, respectively), allowing us to understand the influence of the *N*-(methyl)benzimidazolyl functions in $[Mn^{IV}(O)(2pyN2B)]^{2+}$ on two separate reaction types. Our prior investigation of $[Mn^{IV}(O)(N4py)]^{2+}$, $[Mn^{IV}(O)(^{DMM}N4py)]^{2+}$, and $[Mn^{IV}(O)(2pyN2Q)]^{2+}$ revealed correlations between HAT and OAT reaction rates with both the near-IR absorption energy and the $Mn^{III/IV}$ reduction potentials of these complexes.[6] In each case, faster rates were associated with a more positive $Mn^{III/IV}$ reduction potential and a lower-energy near-IR absorption band. The basis for correlations with the near-IR absorption band are provided by DFT computations, which predict that HAT and OAT reactions for $[Mn^{IV}(O)(N4py)]^{2+}$ and related Mn^{IV}-oxo complexes involve crossing from the $^4B_1$ ground state to a ^4E excited state (arising from a Mn^{IV} $e(d_{xz}, d_{yz}) \rightarrow b_1(d_{x^2-y^2})$ one-electron excitation).[37-38] Our MCD investigations of $[Mn^{IV}(O)(N4py)]^{2+}$ assigned the near-IR absorption maxima of this complex as an excitation to the ^4E excited state.[30] Thus, according to this two-state reactivity model, complexes with lower-energy near-IR absorption bands (lower ^4E excited-state energies) should have lower transition states for HAT and OAT reactions. Alternatively, the $Mn^{III/IV}$ reduction potential represents a portion of the driving force for the HAT and OAT process, with more positive potentials being associated with a larger driving force. The $[Mn^{IV}(O)(2pyN2B)]^{2+}$ complex provides an interesting test for these correlations, as this complex shows the lowest $Mn^{III/IV}$ $E_{p,c}$ values for this series, but has a near-IR absorption maximum between those of $[Mn^{IV}(O)(N4py)]^{2+}$ and $[Mn^{IV}(O)(^{DMM}N4py)]^{2+}$ (Table 4.2).

Treatment of 1.0 mM $[Mn^{IV}(O)(2pyN2B)]^{2+}$ in TFE with an excess of 9,10-dihydroanthracene (DHA) at 25 °C led to the decay of the Mn^{IV}-oxo electronic absorption signals by pseudo-first-order and isosbestic behavior (Figure 4.6, top). The pseudo-first order rate constants, obtained by fitting the disappearance of the 940 nm band of $[Mn^{IV}(O)(2pyN2B)]^{2+}$ over time (Figure 4.6, top inset), showed a linear increase as a function of increasing DHA concentration (Figure 4.6, center). This analysis yielded a second-order rate constant (k_2) of 0.27(2) $M^{-1}s^{-1}$. To determine any solvent influence on this rate, we performed analogous kinetic investigations for the reaction of DHA with $[Mn^{IV}(O)(2pyN2B)]^{2+}$ in 1:1 (vol:vol) TFE:CH_2Cl_2, which yielded a smaller k_2 of 0.16(1) $M^{-1}s^{-1}$ (Figure A4.10). This slight influence of solvent on the rate is similar to that observed for $[Mn^{IV}(O)N4py]^{2+}$,[27] and reinforces other reports of modest enhancements for HAT reaction rates in TFE .[39] The rate of DHA oxidation by $[Mn^{IV}(O)(2pyN2B)]^{2+}$ in 1:1 TFE:CH_2Cl_2 is two-fold slower than that observed for $[Mn^{IV}(O)(^{DMM}N4py)]^{2+}$ (k_2 = 0.34(2) $M^{-1}s^{-1}$ in 1:1 TFE:CH_2Cl_2), which had shown the slowest rate of DHA oxidation for Mn^{IV}-oxo complexes of N4py and its derivatives (Table 4.3).[6, 27] To further compare the HAT reactivity of $[Mn^{IV}(O)(2pyN2B)]^{2+}$ with that of $[Mn^{IV}(O)(^{DMM}N4py)]^{2+}$, we determined the rate of reaction of $[Mn^{IV}(O)(2pyN2B)]^{2+}$ with xanthene, which has a weaker C–H bond than DHA (bond dissociation free energies of 73.3 kcal/mol vs 76.0 kcal/mol, respectively).[40] The oxidation of xanthene by $[Mn^{IV}(O)(2pyN2B)]^{2+}$ gave k_2 = 0.39(2) $M^{-1}s^{-1}$ in 1:1 TFE:CH_2Cl_2 (Figure A4.11). This rate is slightly slower than that observed for $[Mn^{IV}(O)(^{DMM}N4py)]^{2+}$ in 1:1 TFE:CH_2Cl_2 (k_2 of 0.62(6) $M^{-1}s^{-1}$), showing that $[Mn^{IV}(O)(2pyN2B)]^{2+}$ is the slower oxidant for two hydrocarbons.

To probe the mechanism of hydrocarbon oxidation by $[Mn^{IV}(O)(2pyN2B)]^{2+}$, analogous kinetic experiments were performed using deuterated [D_4]-DHA. The decay of the near-IR feature of $[Mn^{IV}(O)(2pyN2B)]^{2+}$ in the presence of [D_4]-DHA was significantly slower than that observed

for DHA (Figure A4.12 and A4.13), and a comparison of k_2 values yielded an H/D kinetic isotope effect of 12.5. This value is similar to that observed for $[Mn^{IV}(O)(^{DMM}N4py)]^{2+}$ and $[Mn^{IV}(O)(N4py)]^{2+}$ (10.2 and 11.2, respectively)[6, 27] and is suggestive of a HAT mechanism. Oxidation of 1.0 equivalent of DHA by $[Mn^{IV}(O)(2pyN2B)]^{2+}$ produced 0.4 equivalents anthracene per equivalent Mn^{IV}-oxo complex, also similar to that reported for DHA oxidation by $[Mn^{IV}(O)(N4py)]^{2+}$ and $[Mn^{IV}(O)(^{DMM}N4py)]^{2+}$.[6, 27] Additionally, ESI-MS of the solution following the reaction showed two prominent peaks at 563.14 and 662.15, corresponding to $[Mn^{II}(2pyN2B)(Cl)]^{+}$ and $[Mn^{III}(2pyN2B)(OCH_2CF_3)(Cl)]^{+}$ respectively (Figure A4.14). Thus, DHA oxidation by $[Mn^{IV}(O)(2pyN2B)]^{2+}$ gives a mixture of Mn^{II} and Mn^{III} products.

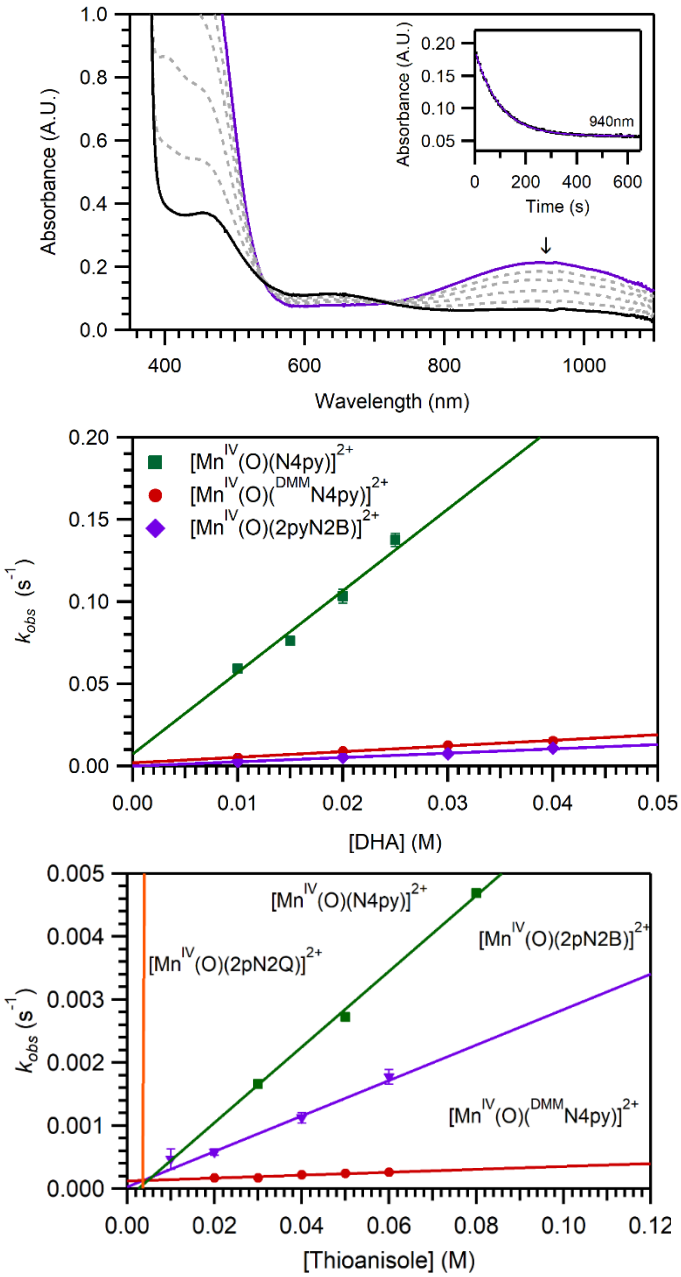

Figure 4.6. Top: Electronic absorption spectra showing the decay of 1.0 mM $Mn^{IV}(O)(2pyN2B)]^{2+}$ (purple trace) upon addition of 40 equivalents DHA in TFE at 25 °C. The inset shows the decay of the feature at 940 nm. Center: Pseudo-first-order rate constants (k_{obs}) vs. DHA concentration for Mn^{IV}-oxo species. Bottom: Pseudo-first-order rate constants (k_{obs}) versus thioanisole concentration for oxomanganese(IV) species. For the center and bottom plots, the lines represent best fits to the data used to determine the second-order rate constants (k_2). Data for $[Mn^{IV}(O)(^{DMM}N4py)]^{2+}$, $[Mn^{IV}(O)(N4py)]^{2+}$, and $[Mn^{IV}(O)(2pyN2Q)]^{2+}$ are from references [6] and [27]. As the rates of reaction for $[Mn^{IV}(O)(2pyN2Q)]^{2+}$ are substantially faster than those of the other complexes, the data points are off scale (see Figures A4.15 and A4.18 for plots with an expanded scale).

We also probed the reactivity of $[Mn^{IV}(O)(2pyN2B)]^{2+}$ with thioanisole. Unlike the hydrocarbons considered previously, thioanisole should react with this Mn^{IV}-oxo complex by an OAT mechanism. The addition of 40 equivalents thioanisole to a 1.0 mM solution of $[Mn^{IV}(O)(2pyN2B)]^{2+}$ in TFE at 25 °C led to a rapid disappearance of the electronic absorption bands at 405 and 940 nm by a first-order process for up to 3 half-lives (Figure A4.16). This reaction was accompanied by a slight increase in absorption intensity at 610 nm, with isosbestic points at 540 and 720 nm. We observed an increase in the decay rate of $[Mn^{IV}(O)(2pyN2B)]^{2+}$ as a function of thioanisole concentration, giving a second-order rate constant (k_2) of 0.028(3) $M^{-1}s^{-1}$ in TFE (Table 4.3 and Figure 4.6, bottom). This rate is intermediate between those of $[Mn^{IV}(O)(^{DMM}N4py)]^{2+}$ and $[Mn^{IV}(O)(N4py)]^{2+}$ (k_2 of 0.0023(4) and 0.060(3) $M^{-1}s^{-1}$, respectively), and is 300-fold slower than that of $[Mn^{IV}(O)(2pyN2Q)]^{2+}$ (k_2 = 9.2(9) $M^{-1}s^{-1}$).[6, 27] ^{1}H NMR analysis performed after the reaction of $[Mn^{IV}(O)(2pyN2B)]^{2+}$ with 60 equivalents of thioanisole showed methylphenylsulfoxide in 50% yield relative to the starting Mn^{II} concentration.

Table 4.3. Second-order Rate Constants (k_2) for the Reactions of Several Mn^{IV}-oxo Complexes with DHA and Thioanisole.

complex[a]	k_2(DHA)[b]	k_2(thioanisole)[b]	Solvent	Temp (°C)	Ref
$[Mn^{IV}(O)(2pyN2Q)]^{2+}$	23(3)	9.2(9)	TFE	25	6
$[Mn^{IV}(O)(N4py)]^{2+}$	3.6(4)	0.060(3)	TFE:CH_3CN (19:1)	25	27
$[Mn^{IV}(O)(^{DMM}N4py)]^{2+}$	0.34(6)	0.0023(4)	TFE:CH_2Cl_2 (DHA); TFE (thioanisole)	25	6
$[Mn^{IV}(O)(2pyN2B)]^{2+}$	0.27(2)	0.028(3)	TFE	25	c
$[Mn^{IV}(O)(OH_2)(BQCN)]^{2+}$	0.12	NR[d]	MeCN:H_2O(9:1)	0	41
$[Mn^{IV}(O)(H_3buea)]^{-}$	0.026(2)	NR[d]	DMSO	20	42
$[Mn^{IV}(O)(Bn\text{-}TPEN)]^{2+}$	NR[d]	1.3	TFE:CH_3CN (19:1)	0	43

[a]Ligand abbreviations as follows: BQCN is N,N′-dimethyl-N,N′-bis(8-quinolyl)cyclohexanediamine; H_3buea is tris[(N′-tert-butylureayl)-N-ethyl)]amine; Bn-TPEN is N-benzyl-N,N',N'-tris(2-pyridylmethyl)-1,2-diaminoethane). [b] $M^{-1}s^{-1}$ [c] This work [d] Not reported

Correlations for HAT and OAT Reactions of Mn^{IV}-oxo Species. The present data for HAT and OAT reactions of $[Mn^{IV}(O)(2pyN2B)]^{2+}$ allow us to revisit our prior correlations of these reaction rates with the λ_{max} of the near-IR absorbance feature of the Mn^{IV}-oxo complexes and the $Mn^{III/IV}$ reduction potentials.[1, 6] Figure 4.7 shows the relationships between the barriers for DHA oxidation by the Mn^{IV}-oxo complexes (represented as $\log(k_2)$) vs. the $Mn^{III/IV}$ reduction potential and the near-IR transition energy. DHA oxidation by $[Mn^{IV}(O)(2pyN2B)]^{2+}$ occurs at a rate expected on the basis of the reduction potential of this complex (Figure 4.7, squares), thereby reinforcing this correlation. In contrast, $[Mn^{IV}(O)(2pyN2B)]^{2+}$ is an outlier for the previously observed correlation between the near-IR transition energy and the rate of DHA oxidation via hydrogen atom transfer. While the near-IR λ_{max} of $[Mn^{IV}(O)(2pyN2B)]^{2+}$ lies midway between those of $[Mn^{IV}(O)(N4py)]^{2+}$ and $[Mn^{IV}(O)(^{DMM}N4py)]^{2+}$ (Table 4.2 and Figure 4.7), $[Mn^{IV}(O)(2pyN2B)]^{2+}$ shows a rate of reaction with DHA that is slower than that of both these complexes. Thus, for HAT reactions of these Mn^{IV}-oxo complexes with DHA, the $Mn^{III/IV}$ reduction potential is a better indicator of reactivity than the ^4E excited-state energy (taken as the near-IR λ_{max} value).

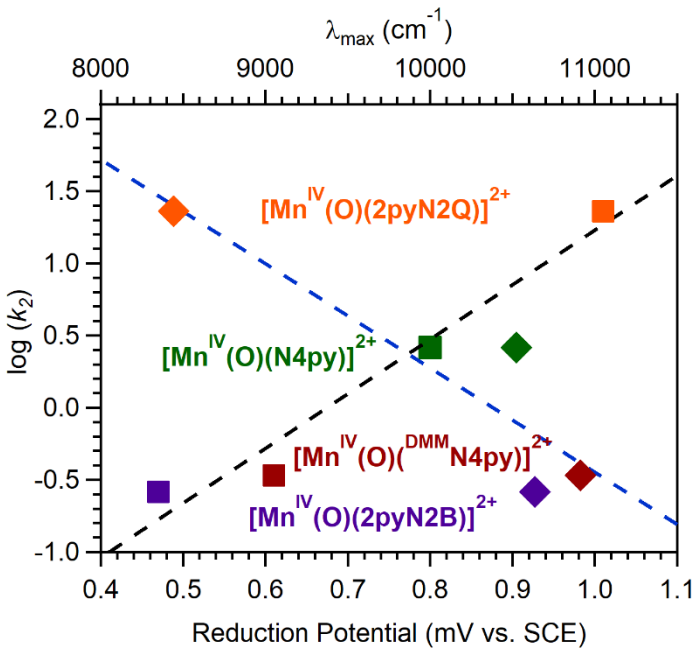

Figure 4.7. Experimental log(k_2) values for DHA oxidation (HAT) by Mn^{IV}-oxo complexes versus $Mn^{III/IV}$ reduction potentials (squares, black line, bottom abscissa) and near-IR electronic absorption band maxima (diamonds, blue line, top abscissa). The fitted lines show the correlation between these parameters.

A similar comparison of OAT reaction rates of Mn^{IV}-oxo complexes vs. $Mn^{III/IV}$ reduction potential and near-IR λ_{max} values is presented in Figure 4.8. For these OAT reactions, there is a close correlation between the OAT reaction barrier and the energy of the near-IR electronic absorption band (Figure 4.8, diamonds). In particular, $[Mn^{IV}(O)(2pyN2B)]^{2+}$ shows a near-IR band quite similar in energy to that of $[Mn^{IV}(O)(N4py)]^{2+}$, which is in keeping with their similar rates of reaction with thioanisole (Figure 4.8). This correlation is consistent with DFT predictions that the ^4E excited state is involved in OAT reactions of Mn^{IV}-oxo complexes.[37] In contrast, $[Mn^{IV}(O)(2pyN2B)]^{2+}$ has a rate substantially faster than expected on the basis of its reduction potential (Figure 4.8, squares). Specifically, $[Mn^{IV}(O)(2pyN2B)]^{2+}$ has a lower potential than $[Mn^{IV}(O)(^{DMM}N4py)]^{2+}$ and $[Mn^{IV}(O)(N4py)]^{2+}$ (by 0.14 and 0.33 V, respectively), but reacts with thioanisole 10-fold faster than $[Mn^{IV}(O)(^{DMM}N4py)]^{2+}$ and only 2-fold slower than $[Mn^{IV}(O)(N4py)]^{2+}$ (Table 4.2). The lack of a correlation between the thioanisole oxidation rate

and the $Mn^{III/IV}$ potentials of these Mn^{IV}-oxo complexes is not unexpected, as thioanisole oxidation presumably occurs by an OAT mechanism, which is a two-electron process.

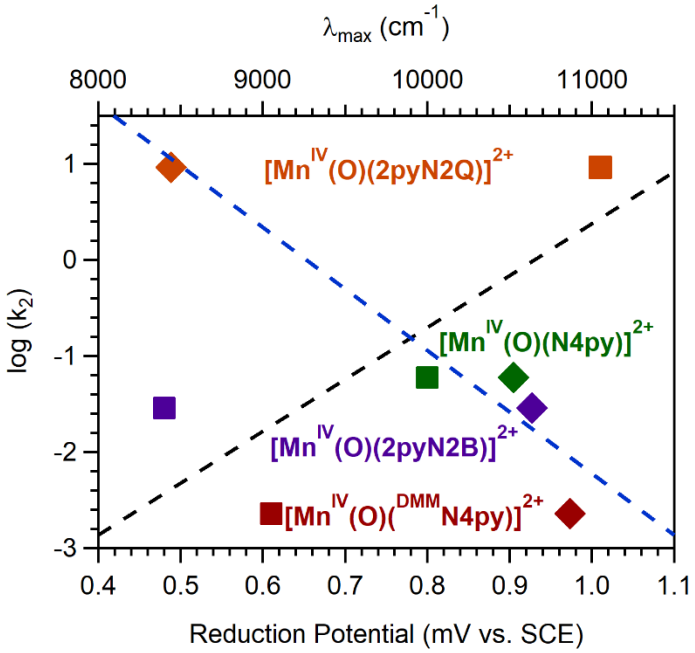

Figure 4.8. Experimental log(k_2) values for thioanisole oxidation (OAT) by Mn^{IV}-oxo complexes versus $Mn^{III/IV}$ reduction potentials (squares, black line, bottom abscissa) and near-IR electronic absorption band maxima (diamonds, blue line, top abscissa). The fitted lines show the correlation between these parameters.

Comparison of Mn^{IV}-oxo and Fe^{IV}-oxo Reactivity at Parity of Ligand Coordination Sphere. The present kinetic investigations of $[Mn^{IV}(O)(2pyN2B)]^{2+}$ also allow us to compare variations in HAT and OAT rates of these Mn^{IV}-oxo adducts with those of Fe^{IV}-oxo complexes supported by the same series of ligands. For the Mn^{IV}-oxo complexes, $[Mn^{IV}(O)(2pyN2Q)]^{2+}$ displays the fastest rate of reaction with DHA, with $[Mn^{IV}(O)(^{DMM}N4py)]^{2+}$ and $[Mn^{IV}(O)(2pyN2B)]^{2+}$ showing roughly similar rates that are the slowest for the series (Figure 4.9). These rates give an overall ligand ordering of 2pyN2Q > N4py > ^{DMM}N4py ≈ 2pyN2B for HAT reactions of the Mn^{IV}-oxo adducts. For the Fe^{IV}-oxo analogues, we can compare ligand effects using reaction rates for ethylbenzene oxidation, which show an ordering of 2pyN2Q > 2pyN2B > N4py ≈ ^{DMM}N4py (Figure 4.9). In this case, $[Fe^{IV}(O)(2pyN2Q)]^{2+}$ shows a rate of reaction with

ethylbenzene that is only 2-fold faster than that of $[Fe^{IV}(O)(2pyN2B)]^{2+}$.[7] Additionally, $[Fe^{IV}(O)(2pyN2B)]^{2+}$ reacts with ethylbenzene 12-fold faster than $[Fe^{IV}(O)(N4py)]^{2+}$, with even more dramatic rate enhancements observed for other substrates.[9] The HAT reactivity of $[Fe^{IV}(O)(^{DMM}N4py)]^{2+}$ and $[Fe^{IV}(O)(N4py)]^{2+}$ are quite similar, with the latter complex showing a faster rate of reaction with ethylbenzene (Figure 4.9) but a slower rate with cumene (Figure A4.20).[8, 44]

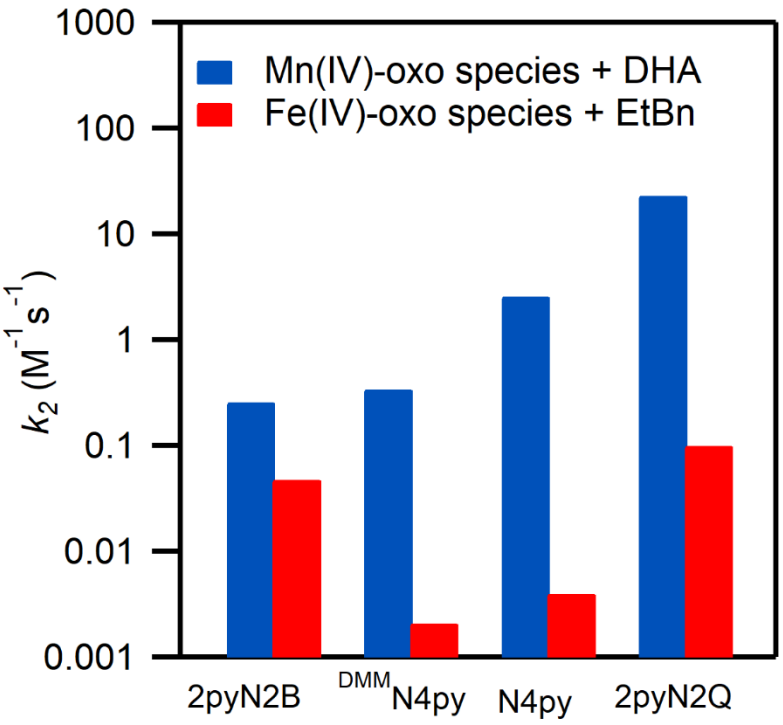

Figure 4.9. Blue: Comparison of the rates of reaction of DHA with oxomanganese(IV) species supported by N4py and its derivatives. Red: Comparison of the rates of reaction of ethylbenzene (EtBn) with oxoiron(IV) complexes supported by N4py and its derivatives. The sources of the rate data are as follows: $[Mn^{IV}(O)(^{DMM}N4py)]^{2+}$ and $[Mn^{IV}(O)(2pyN2Q)]^{2+}$ from reference [6]; $[Mn^{IV}(O)(N4py)]^{2+}$ from reference [27]; $[Fe^{IV}(O)(^{DMM}N4py)]^{2+}$ from reference [8]; $[Fe^{IV}(O)(N4py)]^{2+}$ from reference [44]; $[Fe^{IV}(O)(2pyN2B)]^{2+}$from reference [9], $[Fe^{IV}(O)(2pyN2Q)]^{2+}$ from reference.[7] For the oxoiron(IV) complexes, the reactivity trend is slightly different with cumene (Figure A4.19). Errors for the rates of the Mn^{IV}-oxo complexes are indicated in Table 4.3. Errors for the Fe^{IV}-oxo rate constants have not all been reported.

There is also data available to compare the OAT rates of Mn^{IV}-oxo and Fe^{IV}-oxo complexes supported by the N4py, 2pyN2B, and 2pyN2Q ligands. As was the case for the HAT reactions,

both $[Mn^{IV}(O)(2pyN2Q)]^{2+}$ and $[Fe^{IV}(O)(2pyN2Q)]^{2+}$ show greatly enhanced reactivity towards thioanisole (Figure A4.20). For the Fe^{IV}-oxo series, $[Fe^{IV}(O)(2pyN2B)]^{2+}$ showed the next highest reactivity with $[Fe^{IV}(O)(N4py)]^{2+}$ having the slowest rate.[9] In contrast, $[Mn^{IV}(O)(2pyN2B)]^{2+}$ displayed a thioanisole oxidation rate slightly less than that of $[Mn^{IV}(O)(N4py)]^{2+}$ (Table 4.3). Collectively, the rate data for both HAT and OAT reactions clearly demonstrates that identical ligand perturbations tune the reactivity of Fe^{IV}-oxo and Mn^{IV}-oxo complexes quite differently (Figure 4.9).

The observation that the oxometal(IV) complexes with 2pyN2Q ligation provide the fastest rates could be related to several unique features of these complexes. First, as shown in the DFT structure of $[Mn^{IV}(O)(2pyN2Q)]^{2+}$ and the X-ray crystal structure of $[Fe^{IV}(O)(2pyN2Q)]^{2+}$, the steric bulk of the quinolinyl moieties in these complexes crowds the oxo binding site, leading to a distortion in the N_{axial}–M=O bond angle from the 180° expected for an idealized six-coordinate complex.[6-7] For comparison, the $[Fe^{IV}(O)(2pyN2B)]^{2+}$ and $[Mn^{IV}(O)(2pyN2B)]^{2+}$ complexes show evidence of more modest steric interactions between the *N*(methyl)benzimidazolyl groups and the oxo ligand (Figure 4.5). Respective DFT and X-ray crystallographic results for these complexes show N_{axial}–M=O bond angles of 177°. The influence, if any, of this relatively small bond angle distortion on the reactivity of these complexes is unclear at present.

The second influence of the quinolinyl functions is to provide weaker metal-nitrogen bonds than the pyridyl and *N*(methyl)benzimidazolyl donors in the other complexes. For $[Mn^{IV}(O)(2pyN2Q)]^{2+}$, this effect is apparent in both the extremely low energy of the near-IR absorption band maxima (reflecting the stabilization of Mn^{IV} $3d_{x^2-y^2}$ MO that is σ-antibonding with respective to the equatorial ligands) and the high $Mn^{III/IV}$ reduction potential (Table 4.2). For $[Fe^{IV}(O)(2pyN2Q)]^{2+}$, Fe–$N_{quinolinyl}$ bond elongations relative to comparable Fe–N distances are

readily apparent in the X-ray crystal structure.[7] As has been discussed above, this is suggested to be a consequence of the steric interactions between the quinolinyl moieties and the $Fe^{IV}(O)$ entity, leading to a weaker effective field being exerted by these substituents. For the Fe^{IV}-oxo series, the relationship between these bond elongations and HAT and OAT reaction rates was displayed through a correlation between the average Fe^{IV}–N distances of these complexes and the barriers (expressed as $\log(k_2)$) for cyclohexane and thioanisole oxidation.[7] A similar correlation, using experimental Mn–N distances is not possible for the Mn^{IV}-oxo complexes, as experimental structural data are lacking for these complexes. The only common set of experimental metric parameters for the corresponding Mn systems comes from the X-ray crystal structures of the Mn^{II} complexes. Plots of the average Mn^{II}–N distance from these structures vs. $\log(k_2)$ for DHA and thioanisole oxidation show reasonable correlations, albeit with a fair amount of scatter (Figure 4.10, top-left panel). Far less scatter, especially for the DHA reactions, is observed when the average Mn^{II}–$N_{equatorial}$ distance is plotted versus the $\log(k_2)$ values (Figure 4.10, top-right panel). Analogous correlations developed using DFT-calculated Mn^{IV}–N distances show a fair degree of scatter (Figure 4.10, bottom panels). It should be noted that the variation in average Mn^{IV}–N distances is quite small (from 2.033 Å for $[Mn^{IV}(O)(^{DMM}N4py)]^{2+}$ to 2.065 Å for $[Mn^{IV}(O)(2pyN2Q)]^{2+}$. For comparison, the average crystallographic Fe–N distances of $[Fe^{IV}(O)(N4py)]^{2+}$ and $[Fe^{IV}(O)(2pyN2Q)]^{2+}$ vary by 0.08 Å (1.972 and 2.053 Å, respectively).

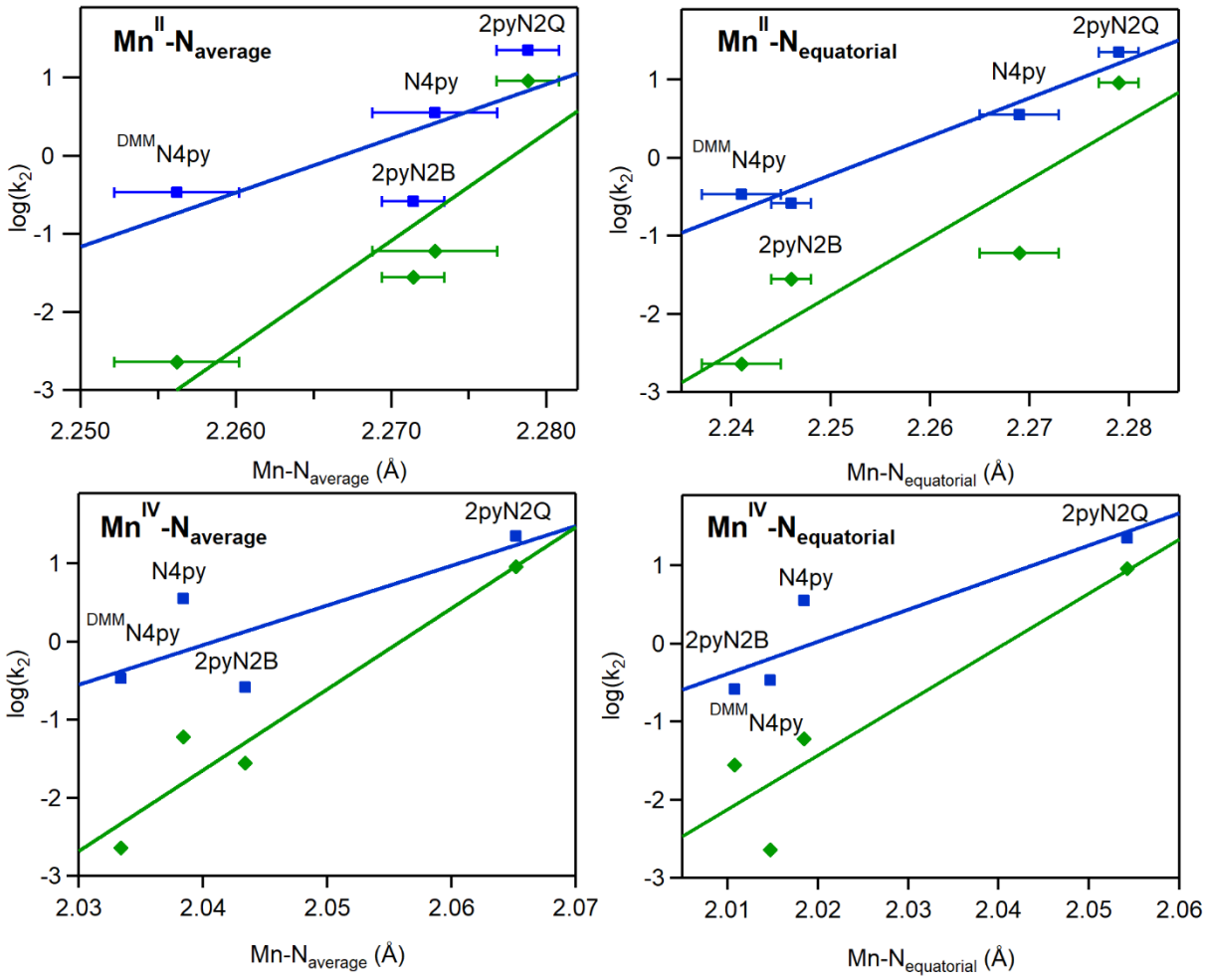

Figure 4.10. Comparison of the log(k_2) for DHA (blue) and thioanisole (green) and the average Mn–N distances (left panels) and Mn–N equatorial distances (right panels) for manganese(II) species (top panels) and manganese(IV)-oxo species (bottom panels) supported by N4py and its derivatives. Errors for the reaction rates can be found in Table 4.3.

Comba, Sastri, and co-workers have also observed a different pattern of reactivity for Mn^{IV}-oxo and Fe^{IV}-oxo complexes at parity of ligand sphere.[45-46] Their work employed pentadentate bispidine ligands (termed L_1 and L_2), whose different architectures place different amine functions *trans* to the oxo binding site.[46] Kinetic examination of thioanisole and 2,4-di-*tert*-butylphenol oxidation by $[Mn^{IV}(O)(L_1)]^{2+}$ and $[Mn^{IV}(O)(L_2)]^{2+}$ provided faster rates for the former complex. In contrast, the $[Fe^{IV}(O)(L_2)]^{2+}$ species is a more rapid oxidant than $[Fe^{IV}(O)(L_1)]^{2+}$.[45, 47-48] DFT analysis of cyclohexane oxidation by this set of metal-oxo species revealed that the Fe^{IV}-

oxo adducts react with this hydrocarbon through the so-called σ-pathway (linear Fe–O–H angle in the transition state), while the Mn^{IV}-oxo adducts utilize the π-pathway (bent Mn–O–H angle in the transition state). It was further proposed that, because of the distinctly different transition state structures, electronic factors dominate in the Fe^{IV}-oxo species, whereas steric factors are dominant for the Mn^{IV}-oxo species.[46] While intriguing, it is unclear whether this model can explain the different reactivity patterns of the Mn^{IV}-oxo and Fe^{IV}-oxo complexes considered in this present work. For example, Figure 4.7 shows a reasonable correlation between the HAT reaction barrier and the $Mn^{III/IV}$ reduction potential, suggesting that this electronic parameter, and not some steric factor, can account for the reactivity ordering of these complexes. Nonetheless, the basis for the disparate reactivity patterns of these Mn^{IV}-oxo and Fe^{IV}-oxo species is unclear at present. Further experimental and computational work is needed to fully explain these observations.

4.4 Conclusions.

In this work, we have described new Mn^{II} and Mn^{IV}-oxo complexes supported by the 2pyN2B ligand that features a mixture of amine, pyridyl, and *N*(methyl)benzimidazolyl donors. The $[Mn^{IV}(O)(2pyN2B)]^{2+}$ complex features a Mn^{IV}-oxo unit whose spectroscopic signatures resemble those of $[Mn^{IV}(O)(N4py)]^{2+}$ and its analogues $[Mn^{IV}(O)(^{DMM}N4py)]^{2+}$ and $[Mn^{IV}(O)(2pyN2Q)]^{2+}$. The near-IR electronic absorption band maxima of $[Mn^{IV}(O)(2pyN2B)]^{2+}$, which corresponds to a Mn^{IV} $e(d_{xz}, d_{yz}) \rightarrow b_1(d_{x^2-y^2})$ one-electron excitation, lies between those of $[Mn^{IV}(O)(^{DMM}N4py)]^{2+}$ and $[Mn^{IV}(O)(N4py)]^{2+}$, illustrating the higher donor strength of the *N*(methyl)benzimidazolyl functions compared to unsubstituted pyridyl groups. With regard to chemical reactivity, the rate of reaction of $[Mn^{IV}(O)(2pyN2B)]^{2+}$ with hydrocarbons was the slowest of the Mn^{IV}-oxo complexes supported by N4py and its derivatives. The slow rate was in

keeping with the lower reduction potential of this complex. In contrast, $[Mn^{IV}(O)(2pyN2B)]^{2+}$ reacted with thioanisole with a rate close to that of $[Mn^{IV}(O)(N4py)]^{2+}$ and roughly ten-fold faster than that of $[Mn^{IV}(O)(^{DMM}N4py)]^{2+}$. These trends in reactivity for this set of Mn^{IV}-oxo complexes contrast with that observed for the Fe^{IV}-oxo analogues. In those systems, the $[Fe^{IV}(O)(2pyN2B)]^{2+}$ complex is more reactive than $[Fe^{IV}(O)(^{DMM}N4py)]^{2+}$ and $[Fe^{IV}(O)(N4py)]^{2+}$. Although the basis for these disparate ligand influences are unclear at present, these observations illustrate that design principles developed for tuning the reactivity of Fe^{IV}-oxo complexes cannot be applied *carte blanche* to Mn^{IV}-oxo analogues, and *vice versa*.

4.5 References

1. Rice, D. B.; Massie, A. A.; Jackson, T. A., Manganese–Oxygen Intermediates in O–O Bond Activation and Hydrogen-Atom Transfer Reactions. *Acc. Chem. Res.* **2017,** *50* (11), 2706-2717.

2. Puri, M.; Que, L., Toward the Synthesis of More Reactive S = 2 Non-Heme Oxoiron(IV) Complexes. *Acc. Chem. Res.* **2015,** *48* (8), 2443-2452.

3. Nam, W.; Lee, Y.-M.; Fukuzumi, S., Hydrogen Atom Transfer Reactions of Mononuclear Nonheme Metal–Oxygen Intermediates. *Acc. Chem. Res.* **2018,** *51* (9), 2014-2022.

4. Oloo, W. N.; Que, L., Bioinspired Nonheme Iron Catalysts for C–H and C═C Bond Oxidation: Insights into the Nature of the Metal-Based Oxidants. *Acc. Chem. Res.* **2015,** *48* (9), 2612-2621.

5. Milan, M.; Salamone, M.; Costas, M.; Bietti, M., The Quest for Selectivity in Hydrogen Atom Transfer Based Aliphatic C–H Bond Oxygenation. *Acc. Chem. Res.* **2018,** *51* (9), 1984-1995.

6. Massie, A. A.; Denler, M. C.; Cardoso, L. T.; Walker, A. N.; Hossain, M. K.; Day, V. W.; Nordlander, E.; Jackson, T. A., Equatorial Ligand Perturbations Influence the Reactivity of Manganese(IV)-Oxo Complexes. *Angew. Chem., Int. Ed. Engl.* **2017,** *56* (15), 4178-4182.

7. Rasheed, W.; Draksharapu, A.; Banerjee, S.; Young, V. G.; Fan, R.; Guo, Y.; Ozerov, M.; Nehrkorn, J.; Krzystek, J.; Telser, J.; Que, L., Crystallographic Evidence for a Sterically Induced Ferryl Tilt in a Non-Heme Oxoiron(IV) Complex that Makes it a Better Oxidant. *Angew. Chem., Int. Ed. Engl.* **2018,** *57* (30), 9387-9391.

8. Rana, S.; Dey, A.; Maiti, D., Mechanistic elucidation of C–H oxidation by electron rich non-heme iron(iv)-oxo at room temperature. *Chem. Commun.* **2015,** *51* (77), 14469-14472.

9. Mitra, M.; Nimir, H.; Demeshko, S.; Bhat, S. S.; Malinkin, S. O.; Haukka, M.; Lloret-Fillol, J.; Lisensky, G. C.; Meyer, F.; Shteinman, A. A.; Browne, W. R.; Hrovat, D. A.; Richmond, M. G.; Costas, M.; Nordlander, E., Nonheme Fe(IV) Oxo Complexes of Two New Pentadentate Ligands and Their Hydrogen-Atom and Oxygen-Atom Transfer Reactions. *Inorg. Chem.* **2015,** *54* (15), 7152-7164.

10. Armarego, W. L. F.; Perrin, D. D., *Purification of Laboratory Chemicals*. Butterworth-Heinemann: Oxford, U.K., 1997.

11. Wijeratne, G. B.; Corzine, B.; Day, V. W.; Jackson, T. A., Saturation Kinetics in Phenolic O–H Bond Oxidation by a Mononuclear Mn(III)–OH Complex Derived from Dioxygen. *Inorg. Chem.* **2014,** *53* (14), 7622-7634.

12. Seo, M. S.; Kim, J. Y.; Annaraj, J.; Kim, Y.; Lee, Y.-M.; Kim, S.-J.; Kim, J.; Nam, W., $[Mn(tmc)(O_2)]^+$: A Side-On Peroxide Manganese(III) Complex Bearing a Non-heme Ligand. *Angew. Chem., Int. Ed. Engl.* **2007,** *46*, 377-380.

13. Saltzman, H.; Sharefkin, J. G., Iodosobenzene. *Org. Synth.* **1963,** *43*, 60.

14. *Data Collection: SMART Software in APEX2 v2014.11-0 Suite*. Bruker-AXS. 5465 E. Cheryl Parkway, Madison, WI 53711-5373 USA, 1998.

15. *Data Reduction: SAINT Software in APEX2 v2014.11-0 Suite*. Bruker-AXS, 5465 E. Cheryl Parkway, Madison, WI 53711-5373 USA.

16. *Refinement: SHELXTL Software in APEX2 v2014.11-0 Suite*. Bruker-AXS, 5465 E. Cheryl Parkway, Madison, WI 53711-5373 USA.

17. Ravel, B.; Newville, M., ATHENA, ARTEMIS, HEPHAESTUS: data analysis for X-ray absorption spectroscopy using IFEFFIT. *J. Synchrotron Rad.* **2005,** *12* (4), 537-541.

18. Wojdyr, M., Fityk: a general-purpose peak fitting program. *J. Appl. Cryst.* **2010,** *43* (5 Part 1), 1126-1128.

19. Neese, F., The ORCA program system. *WIREs Comput Mol Sci.* **2012,** *2* (1), 73-78.

20. Tao, J.; Perdew, J. P.; Staroverov, V. N.; Scuseria, G. E., Climbing the Density Functional Ladder: Nonempirical Meta-Generalized Gradient Approximation Designed for Molecules and Solids. *Phys. Rev. Lett.* **2003,** *91* (14), 146401.

21. Schäfer, A.; Horn, H.; Ahlrichs, R., Fully optimized contracted Gaussian basis sets for atoms Li to Kr. *J. Chem. Phys.* **1992,** *97* (4), 2571-2577.

22. Schäfer, A.; Huber, C.; Ahlrichs, R., Fully Optimized Contracted Gaussian Basis Sets of Triple Zeta Valence Quality for Atoms Li to Kr. *J. Chem. Phys.* **1994,** *100*, 5829-5835.

23. Weigend, F.; Ahlrichs, R., Balanced basis sets of split valence, triple zeta valence and quadruple zeta valence quality for H to Rn: Design and assessment of accuracy. *Phys. Chem. Chem. Phys.* **2005,** *7* (18), 3297-3305.

24. Marenich, A. V.; Cramer, C. J.; Truhlar, D. G., Universal Solvation Model Based on Solute Electron Density and on a Continuum Model of the Solvent Defined by the Bulk Dielectric Constant and Atomic Surface Tensions. *J. Phys. Chem. B* **2009,** *113* (18), 6378-6396.

25. Prahl, S. Anthracene. https://omlc.org/spectra/PhotochemCAD/html/022.html.

26. Lee, Y.; Jackson, T. A., Ligand Influence on Structural Properties and Reactivity of Bis(μ-oxo)dimanganese(III,IV) Species and Comparison of Reactivity with Terminal MnIV-oxo Complexes. *ChemistrySelect* **2018,** *3* (47), 13507-13516.

27. Leto, D. F.; Ingram, R.; Day, V. W.; Jackson, T. A., Spectroscopic properties and reactivity of a mononuclear oxomanganese(iv) complex. *Chem. Commun.* **2013,** *49* (47), 5378-5380.

28. Lõkov, M.; Tshepelevitsh, S.; Heering, A.; Plieger, P. G.; Vianello, R.; Leito, I., On the Basicity of Conjugated Nitrogen Heterocycles in Different Media. *Eur. J. Org. Chem.* **2017,** *2017* (30), 4475-4489.

29. Lubben, M.; Meetsma, A.; Wilkinson, E. C.; Feringa, B.; Que Jr., L., Nonheme Iron Centers in Oxygen Activation: Characterization of an Iron(III) Hydroperoxide Intermediate. *Angew. Chem., Int. Ed. Engl.* **1995,** *34* (13-14), 1512-1514.

30. Leto, D. F.; Massie, A. A.; Rice, D. B.; Jackson, T. A., Spectroscopic and Computational Investigations of a Mononuclear Manganese(IV)-Oxo Complex Reveal Electronic Structure Contributions to Reactivity. *J. Am. Chem. Soc.* **2016,** *138* (47), 15413-15424.

31. Leto, D. F.; Massie, A. A.; Colmer, H. E.; Jackson, T. A., X-Band Electron Paramagnetic Resonance Comparison of Mononuclear MnIV-oxo and MnIV-hydroxo Complexes and Quantum Chemical Investigation of MnIV Zero-Field Splitting. *Inorg. Chem.* **2016,** *55* (7), 3272-3282.

32. Gupta, R.; Taguchi, T.; Borovik, A. S.; Hendrich, M. P., Characterization of Monomeric $Mn^{II/III/IV}$–Hydroxo Complexes from X- and Q-Band Dual Mode Electron Paramagnetic Resonance (EPR) Spectroscopy. *Inorg. Chem.* **2013,** *52* (21), 12568-12575.

33. Telser, J.; Krzystek, J.; Ozarowski, A., High-frequency and high-field electron paramagnetic resonance (HFEPR): a new spectroscopic tool for bioinorganic chemistry. *JBIC Journal of Biological Inorganic Chemistry* **2014,** *19* (3), 297-318.

34. Duboc, C.; Collomb, M.-N., Multifrequency high-field EPR investigation of a mononuclear manganese(iv) complex. *Chem. Commun.* **2009,** (19), 2715-2717.

35. Duboc, C.; Ganyushin, D.; Sivalingam, K.; Collomb, M.-N.; Neese, F., Systematic Theoretical Study of the Zero-Field Splitting in Coordination Complexes of Mn(III). Density Functional Theory versus Multireference Wave Function Approaches. *The Journal of Physical Chemistry A* **2010,** *114* (39), 10750-10758.

36. Gupta, R.; Taguchi, T.; Lassalle-Kaiser, B.; Bominaar, E. L.; Yano, J.; Hendrich, M. P.; Borovik, A. S., High-spin Mn–oxo complexes and their relevance to the oxygen-evolving complex within photosystem II. *Proceedings of the National Academy of Sciences* **2015,** *112* (17), 5319-5324.

37. Chen, J.; Cho, K.-B.; Lee, Y.-M.; Kwon, Y. H.; Nam, W., Mononuclear nonheme iron(iv)–oxo and manganese(iv)–oxo complexes in oxidation reactions: experimental results prove theoretical prediction. *Chem. Commun.* **2015,** *51* (66), 13094-13097.

38. Cho, K.-B.; Shaik, S.; Nam, W., Theoretical Investigations into C–H Bond Activation Reaction by Nonheme $Mn^{IV}O$ Complexes: Multistate Reactivity with No Oxygen Rebound. *J. Phys. Chem. Lett.* **2012,** *3* (19), 2851-2856.

39. Massie, A. A.; Sinha, A.; Parham, J. D.; Nordlander, E.; Jackson, T. A., Relationship between Hydrogen-Atom Transfer Driving Force and Reaction Rates for an Oxomanganese(IV) Adduct. *Inorg. Chem.* **2018,** *57* (14), 8253-8263.

40. Warren, J. J.; Tronic, T. A.; Mayer, J. M., Thermochemistry of Proton-Coupled Electron Transfer Reagents and its Implications. *Chem. Rev.* **2010,** *110* (12), 6961-7001.

41. Sawant, S. C.; Wu, X.; Cho, J.; Cho, K.-B.; Kim, S. H.; Seo, M. S.; Lee, Y.-M.; Kubo, M.; Ogura, T.; Shaik, S.; Nam, W., Water as an Oxygen Source: Synthesis, Characterization, and Reactivity Studies of a Mononuclear Nonheme Manganese(IV) Oxo Complex. *Angew. Chem., Int. Ed. Engl.* **2010,** *49* (44), 8190-8194.

42. Parsell, T. H.; Yang, M.-Y.; Borovik, A. S., C−H Bond Cleavage with Reductants: Re-Investigating the Reactivity of Monomeric $Mn^{III/IV}$−Oxo Complexes and the Role of Oxo Ligand Basicity. *J. Am. Chem. Soc.* **2009,** *131* (8), 2762-2763.

43. Wu, X.; Seo, M. S.; Davis, K. M.; Lee, Y.-M.; Chen, J.; Cho, K.-B.; Pushkar, Y. N.; Nam, W., A Highly Reactive Mononuclear Non-Heme Manganese(IV)–Oxo Complex That Can Activate the Strong C–H Bonds of Alkanes. *J. Am. Chem. Soc.* **2011,** *133* (50), 20088-20091.

44. Kaizer, J.; Klinker, E. J.; Oh, N. Y.; Rohde, J.-U.; Song, W. J.; Stubna, A.; Kim, J.; Münck, E.; Nam, W.; Que Jr., L., Nonheme $Fe^{IV}O$ Complexes That Can Oxidize the C−H Bonds of Cyclohexane at Room Temperature. *J. Am. Chem. Soc* **2004,** *126* (2), 472-473.

45. Comba, P.; Maurer, M.; Vadivelu, P., Oxidation of Cyclohexane by High-Valent Iron Bispidine Complexes: Tetradentate versus Pentadentate Ligands. *Inorg. Chem.* **2009,** *48* (21), 10389-10396.

46. Barman, P.; Vardhaman, A. K.; Martin, B.; Wörner, S. J.; Sastri, C. V.; Comba, P., Influence of Ligand Architecture on Oxidation Reactions by High-Valent Nonheme Manganese Oxo Complexes Using Water as a Source of Oxygen. *Angew. Chem., Int. Ed. Engl.* **2015,** *54* (7), 2095-2099.

47. Bukowski, M. R.; Comba, P.; Lienke, A.; Limberg, C.; Lopez de Laorden, C.; Mas-Ballesté, R.; Merz, M.; Que Jr., L., Catalytic Epoxidation and 1,2-Dihydroxylation of Olefins with Bispidine–Iron(II)/H_2O_2 Systems. *Angew. Chem., Int. Ed. Engl.* **2006,** *45* (21), 3446-3449.

48. Jaccob, M.; Comba, P.; Maurer, M.; Vadivelu, P.; Venuvanalingam, P., A combined experimental and computational study on the sulfoxidation by high-valent iron bispidine complexes. *Dalton Trans.* **2011,** *40* (42), 11276-11281.

Chapter 5: Structural Characterization of a Series of N5-Ligated Mn^{IV}-oxo Species

5.1 Introduction

High-valent metal-oxo species are often utilized in biological and synthetic oxidation reactions. These reactive centers are important for hydrogen atom transfer (HAT) reactions, which can serve as an initial step for the hydroxylation, halogenation, or desaturation of substrate C–H bonds.[1-5] In cytochrome P450 enzymes, Fe^{IV}-oxo porphyrin radical centers are proposed as a key intermediate in the functionalization of a wide range of C–H bonds.[6] Additionally, taurine/α-ketoglutarate dioxygenase (TauD) is proposed to utilize an Fe^{IV}-oxo center for the functionalization of the small molecule taurine.[4-5, 7] The use of well-characterized Fe^{IV}-oxo model complexes has provided direct insight into the reactivity of these enzyme intermediates.[8-9] Importantly, these model systems have permitted detailed structural insights into Fe^{IV}-oxo complexes supported by a variety of ligand types. Since the first crystal structure of an Fe^{IV}-oxo center was published in 2003,[10] there have been more than 60 other Fe^{IV}-oxo complexes reported in the literature featuring non-porphyrinic supporting ligands.[8-9] These species have been investigated spectroscopically or structurally, and extensive work has been done to understand their reactivity for a broad range of oxidation reactions.

In contrast, there is far less information concerning the structural properties of Mn^{IV}-oxo centers. To date, there is only a single example of an X-ray diffraction (XRD) structure for a mononuclear Mn^{IV}-oxo complex, $[Mn^{IV}(O)(ditox)_3]^-$ (where Hditox = $^tBu_2MeCOH$). [11] The Mn^{IV}-oxo coordination sphere in this complex consists of three alkoxide ligands, to give a distorted pseudo-tetrahedral geometry with approximate C_{3v} symmetry. Presumably the all oxygen, trianionic ligand field stabilizes the Mn^{IV}-oxo unit. While this stabilization allowed for characterization by XRD, the strongly anionic ligand field also resulted in muted HAT reactivity.[11]

The most reactive Mn^{IV}-oxo centers reported to date feature neutral pentadentate ligands, and these complexes include $[Mn^{IV}(O)(N4py)]^{2+}$ and $[Mn^{IV}(O)(Bn\text{-}TPEN)]^{2+}$ (N4py = N,N-bis(2-pyridylmethyl)-N-bis(2-pyridyl)methylamine) and Bn-TPEN = N-benzyl-N,N',N'-tris(2-pyridylmethyl)-1,2-diaminoethane.[12-14] With the help of DFT calculations, the enhanced reactivity of these complexes was credited to a low-lying ligand-field excited state that offers a lower energy barrier for HAT than the ground state.[15-16] Inspired by this reactivity model, our group introduced ligand perturbations to directly tune the energy of this excited state and determine any corresponding change in reactivity. These efforts led to the generation of the $[Mn^{IV}(O)(^{DMM}N4py)]^{2+}$, $[Mn^{IV}(O)(2pyN2B)]^{2+}$, and $[Mn^{IV}(O)(2pyN2Q)]^{2+}$ complexes (Figure 5.1), which showed a range of reaction rates with hydrocarbons.[17-18]

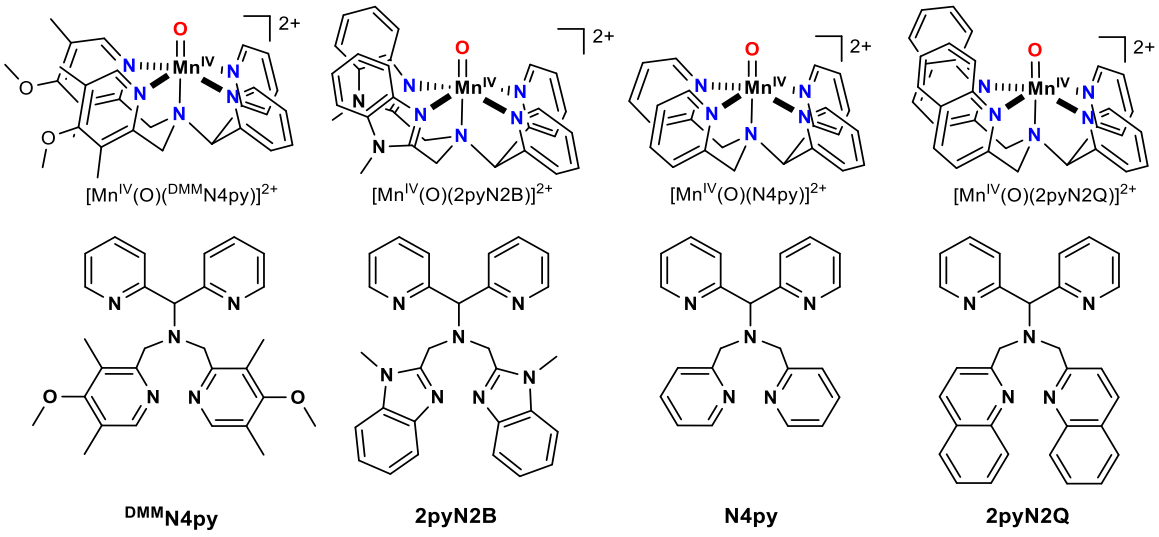

Figure 5.1. Mn^{IV}-oxo complexes and their corresponding ligands based on N4py ligand framework.

While this series of Mn^{IV}-oxo centers are all well-characterized spectroscopically, experimental insight into their structural properties is largely lacking. Although Mn K-edge X-ray absorption spectroscopy (XAS) has served as an extremely useful technique for characterization

for Mn^{IV}-oxo centers, this method has been incompletely applied to these complexes.[13-14, 19-21] Mn K-edge XAS data for Mn^{IV}-oxo complexes of the N4py, ^{DMM}N4py, 2pyN2B, and 2pyN2Q ligands were previously reported.[17-19] For $[Mn^{IV}(O)(N4py)]^{2+}$, a thorough analysis of both the pre-edge and EXAFS regions was described.[13, 19] For the Mn^{IV}-oxo complexes of the ^{DMM}N4py, 2pyN2B, and 2pyN2Q ligands, however, the prior analysis only included the edge and pre-edge regions.[17-18] Unfortunately, oxo formation for this series is dependent on the use of 2,2,2-trifluoroethanol (TFE) as either a solvent or co-solvent. Halogenated solvents are nearly opaque to lower energy X-rays, which interferes with the XAS measurements.[22] The solvent requirement for oxo formation could be attributed to the use of iodosobenzene (PhIO) as an oxidant for accessing the Mn^{IV}-oxo species, as PhIO exhibits limited solubility in most solvents and its dissolution requires the use of a protic solvent. However, another explanation could be that TFE provides a unique complex-solvent interaction that leads to stabilization of these Mn^{IV}-oxo adducts in solution.

In this present study, we describe the analysis of EXAFS data for Mn^{IV}-oxo complexes supported by the ^{DMM}N4py, 2pyN2B, and 2pyN2Q ligands in order to determine Mn-ligand metric parameters. These experimental metric parameters are in good agreement with those from DFT-derived models of the Mn^{IV}-oxo complexes that included second-sphere solvent (TFE) molecules. In each complex, these solvent molecules engage in strong hydrogen-bonding interactions with the oxo ligand, which leads to elongation in the Mn=O bond by ca. 0.02 Å. These results suggest the protic TFE solvent molecules could play an important role in stabilizing this class of Mn^{IV}-oxo adducts. DFT calculations performed to investigate analogous hydrogen-bonding interactions for the Fe^{IV}-oxo complex $[Fe^{IV}(O)(N4py)]^{2+}$ showed weaker hydrogen bonding when compared to the $[Mn^{IV}(O)(N4py)]^{2+}$ complex.

5.2 Experimental and Computational Methods

Materials, Instrumentation, and Synthesis. All chemicals and solvents were purchased from commercial vendors and were ACS reagent-grade quality or better. All chemicals were used as received, with the exception of MeCN and diethylether, which were sparged with argon and dried as described previously.[23] $Mn^{II}(OTf)_2$•$2CH_3CN$, used for preparation of metal complexes, was synthesized according to a previously reported procedure.[24] Iodosobenzene was prepared from iodosobenzene diacetate following a published procedure without modification.[25] Ligands and corresponding Mn^{II} complexes were prepared as described previously.[17-18, 26] The formation of the Mn^{IV}-oxo species were monitored by electronic absorption spectroscopy using either a Varian Cary 50 Bio or an Agilent 8453 spectrophotometer. Both spectrophotometers were interfaced with Unisoku cryostats (USP-203-A), capable of maintaining temperatures of 25 °C.

Preparation of XAS Samples. A 10 mM sample of $[Mn^{IV}(O)(^{DMM}N4py)]^{2+}$ was prepared by dissolving 12.5 mg (0.015 mmol) $[Mn^{II}(OTf)(^{DMM}N4py)](OTf)$ in 0.5 mL TFE and combining it with 6.6 mg (0.027 mmol) PhIO in 1 mL TFE and placing the reaction mixture into a 0.2 cm cuvette. The formation of $[Mn^{IV}(O)(^{DMM}N4py)]^{2+}$ was monitored by electronic absorption spectroscopy. At maximum formation, two XAS samples were prepared and flash frozen in liquid nitrogen.

A 10 mM XAS sample of $[Mn^{IV}(O)(2pyN2B)]^{2+}$ was prepared by dissolving 16.5 mg (0.020 mmol) $[Mn^{II}(OH_2)(2pyN2B)](OTf)_2$ in 2 mL of a TFE solution containing 44.0 mg (0.20 mmol) PhIO. The reaction mixture was placed into a 0.2 cm cuvette, where the formation of $[Mn^{IV}(O)(2pyN2B)]^{2+}$ was monitored by electronic absorption spectroscopy. At maximum formation, two XAS samples were prepared and flash frozen in liquid nitrogen.

A 10 mM sample of $[Mn^{IV}(O)(2pyN2Q)]^{2+}$ was prepared by dissolving 12.3 mg (0.015 mmol) $[Mn^{II}(OTf)(2pyN2Q)](OTf)$ in 0.5 mL TFE and 24.8 mg (0.11 mmol) PhIO in 1 mL TFE, which were mixed using a vortex mixer for 15 seconds. Two separate XAS samples were immediately prepared and flash frozen.

XAS Data Collection. XAS data for all samples were collected at beamline 9-3 at the Stanford Synchrotron Radiation Lightsource (SSRL). Mn K-edge X-ray absorption spectra were collected over an energy range of 6.3 to 7.4 keV (Si(220) monochromator). The frozen samples were maintained at 7 K during data collection by an Oxford liquid He cryostat. XAS spectra were obtained as fluorescence excitation spectra using a Canberra 100-element Ge array detector. A reference spectrum of a manganese foil was collected for each scan and an internal calibration was performed by setting the zero crossing of the second derivative of the K-edge energy of the reference spectra to 6539.0 keV. The high flux at beamline 9-3 lead to photo-reduction for the Mn^{IV}-oxo samples. When multiple scans were collected on a single spot of the frozen sample, there was a noticeable shift of the edge to a lower energy. To reduce the effects of photoreduction, the beam was moved to different spots on the sample and only one scan was collected per spot. Four scans were collected for $[Mn^{IV}(O)(^{DMM}N4py)]^{2+}$, while nine scans with a smaller horizontal gap were collected for $[Mn^{IV}(O)(2pyN2Q)]^{2+}$. Nine scans were collected for $[Mn^{IV}(O)(2pyN2B)]^{2+}$.

XAS Data Analysis. XAS data analysis was performed using the Demeter software package.[27] Individual scans of raw data were analyzed and combined using Athena, and extended X-ray absorption fine-structure (EXAFS) data were fit using Artemis. Phase and amplitude functions utilized in the fitting of the $k^3\chi(k)$ data were generated by *FEFF6*,[28] using density functional theory (DFT) optimized models (*vide infra*). For each fit, the parameters *r*, which describes the average scattering pathway distance, and σ^2 (Debye-Waller factor) were optimized

individually for each path, and E_0 (k = 0 point) was a common variable for all paths. The parameter describing the degeneracy of the scattering atom, n, was fixed for each fit and systematically varied between fits in order to achieve better goodness of fit. The goodness of fit was evaluated using the R-factor (Equation 1).

$$R = \sum_{i=1}^{N}(\chi_i^{data} - \chi_i^{fit})^2 \; / \; \sum_{i=1}^{N}(\chi_i^{data})^2 \qquad (1)$$

Fits of the pre-edge areas were performed using the FityK software.[29] Pre-edge intensity was normalized relative to the tail of the fluorescence signal.

Electronic Structure Computations. All computations were performed using the *ORCA* software package (versions 3.03 and 4.0.1.2).[30] DFT geometry optimizations employed the TPSS functional[31] with D3 corrections,[32-33] def2-TZVP (Mn, O, and N) and def2-SVP (C, F, and H) basis sets,[34-36] an SMD solvation model (for 2,2,2-trifluoroethanol),[37] and a dense integration grid (Grid6 in *ORCA*). Tight optimization and SCF criteria were invoked using the TightOpt and TightSCF keywords. The RI approximation, with def2-TZVP/J and def2-SVP/J auxiliary basis sets, was used for geometry optimizations. Structures of the Mn^{IV} complexes were converged to the 3/2 spin states, respectively. Optimizations of the Mn^{IV}-oxo complexes employed Frequency calculations for all Mn^{IV}-oxo species lacking second-sphere TFE molecules, and $[Mn^{IV}(O)(2pyN2Q)]^{2+}\cdot(TFE)_2$ showed no imaginary frequencies, ensuring that these structures represent true minima. The $[Mn^{IV}(O)(N4py)]^{2+}\cdot(TFE)_2$ and $[Mn^{IV}(O)(^{DMM}N4py)]^{2+}\cdot(TFE)_2$ structures each showed one small imaginary frequency (-7.30 and -25.18 cm^{-1}, respectively), associated with rotational modes of the methyl groups of TFE and the *para*-methoxy-pyridyl moieties, respectively. Attempts to eliminate these imaginary modes through the use of a denser integration grid or tighter convergence criteria were unsuccessful. Cartesian coordinates for all DFT optimized models are included as Supporting

Information (Tables A5.1 – A5.3). Pre-edge properties of the Mn^{IV}-oxo complexes were calculated using the TD-DFT method,[39] at a previously described level of theory.[21]

5.3 Results

Mn K-edge XAS Edge and Pre-edge Properties for Mn^{IV}-oxo Complexes. The Mn K-edge energies of the $[Mn^{IV}(O)(^{DMM}N4py)]^{2+}$, $[Mn^{IV}(O)(2pyN2B)]^{2+}$, $[Mn^{IV}(O)(N4py)]^{2+}$ and $[Mn^{IV}(O)(2pyN2Q)]^{2+}$ complexes fall within the narrow range of 6549.8 to 6550.8 eV (Table 5.1). The Mn K-edge of $[Mn^{IV}(O)(2pyN2Q)]^{2+}$ is ~0.5 eV lower than those of $[Mn^{IV}(O)(N4py)]^{2+}$, $[Mn^{IV}(O)(^{DMM}N4py)]^{2+}$ and $[Mn^{IV}(O)(2pyN2B)]^{2+}$. (Table 5.1). This difference can be appreciated in Figure 5.1, where the edge energy of $[Mn^{IV}(O)(2pyN2Q)]^{2+}$ is clearly lower than that of either $[Mn^{IV}(O)(^{DMM}N4py)]^{2+}$ or $[Mn^{IV}(O)(2pyN2B)]^{2+}$. Because the EPR spectra of $[Mn^{IV}(O)(2pyN2Q)]^{2+}$ shows a multiline signal due to the presence of some multi-nuclear species (potentially $Mn^{III}Mn^{IV}$ dimers), the lower edge energy of this complex is most likely due to the presence of this species. We note that the previously reported Mn K-edge energy for $[Mn^{IV}(O)(2pyN2Q)]^{2+}$, which was collected for a different sample, is 0.6 eV lower than that reported here (Table 5.1).[17] This variation in edge energy based on sample preparation further supports our hypothesis that reduced sample homogeneity for $[Mn^{IV}(O)(2pyN2Q)]^{2+}$ can account for the lower edges of these samples.

Table 5.1. Edge and Pre-edge Energies (eV) and Pre-edge Areas for Mn^{IV}-oxo Complexes.

complex	edge energy	pre-edge energy	pre-edge area
$[Mn^{IV}(O)(^{DMM}N4py)]^{2+}$	6550.5 (6550.3)[b]	6539.9, 6541.6, 6543.2 (6541.2)[b]	20.1[a]
$[Mn^{IV}(O)(2pyN2B)]^{2+}$	6550.2 (6549.6)[b]	6539.9, 6541.4, 6542.8 (6540.1, 6541.4, 6543.1)[b]	22.2
$[Mn^{IV}(O)(N4py)]^{2+}$ [c]	6550.8	6541.9	18.9
$[Mn^{IV}(O)(2pyN2Q)]^{2+}$	6549.8 (6549.2)[b]	6539.9, 6541.5[d] (6541.2)[b]	15.1[a]

[a] An analysis of previously published data using different samples provided the following edge areas: edge area for $[Mn^{IV}(O)(^{DMM}N4py)]^{2+}$ of 19.6; edge area for $[Mn^{IV}(O)(2pyN2B)]^{2+}$ of 14.6; edge area for $[Mn^{IV}(O)(2pyN2Q)]^{2+}$ of 17.0. [b] Edge and pre-edge energies in parentheses are from references [17] and [18]. [c] From reference [19]. The previously reported pre-edge area for $[Mn^{IV}(O)(N4py)]^{2+}$ (12.7) used a normalization relative to the most intense fluorescence peak. This present value was obtained by normalizing the intensity to the tail of the EXAFS region. [d] The pre-edge feature for $[Mn^{IV}(O)(2pyN2Q)]^{2+}$ can also be fit with 3 pseudo-Voigt functions, but the fit is of similar quality to the three-band fit presented here.

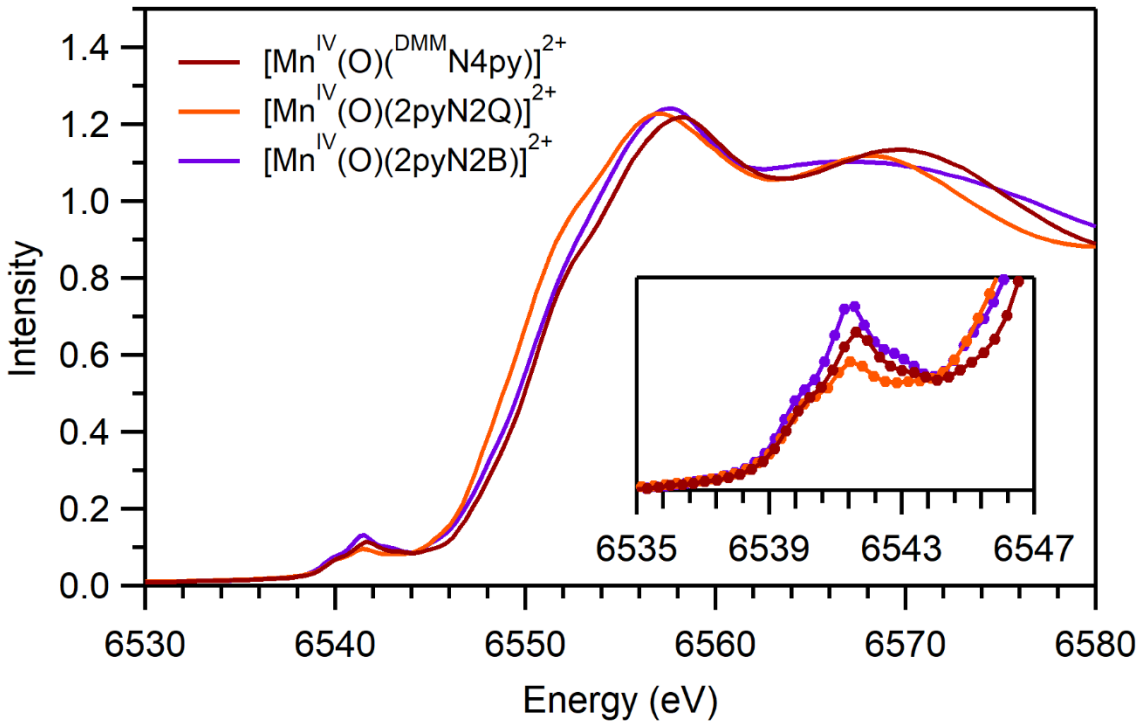

Figure 5.2. Comparison of experimental XANES regions for $[Mn^{IV}(O)(^{DMM}N4py)]^{2+}$, $[Mn^{IV}(O)2pyN2B)]^{2+}$, and $[Mn^{IV}(O)(2pyN2Q)]^{2+}$.

Each of the Mn^{IV}-oxo complexes shows a prominent pre-edge feature centered at ca. 6542 eV (Figure 5.2). This feature contains contributions from Mn^{IV} 1s-to-3d transition, which gain intensity through Mn^{IV} 3d-4p mixing induced by the short Mn=O distance.[19] The pre-edge features of $[Mn^{IV}(O)(N4py)]^{2+}$, $[Mn^{IV}(O)(^{DMM}N4py)]^{2+}$, and $[Mn^{IV}(O)(2pyN2Q)]^{2+}$ were previously fit with only one pseudo-Voigt function centered near 6541.2 eV.[17, 19] However, higher resolution pre-edge data collected for $[Mn^{IV}(O)(^{DMM}N4py)]^{2+}$, $[Mn^{IV}(O)(2pyN2Q)]^{2+}$, and $[Mn^{IV}(O)(2pyN2B)]^{2+}$ at beamline 9-3 (SSRL) clearly reveal multiple pre-edge peak maxima (Figure 5.2, inset). For example, the pre-edge region for $[Mn^{IV}(O)(^{DMM}N4py)]^{2+}$ shows a prominent peak at 6541.6 eV, with shoulders at 6539.9 and 6543.2 eV (Supporting Information, Figure A5.1). The pre-edge regions of $[Mn^{IV}(O)(2pyN2Q)]^{2+}$ and $[Mn^{IV}(O)(2pyN2B)]^{2+}$ are similar, although the latter sample appears to lack the shoulder at higher energy (Figure 5.2, inset).

The newly collected data were fit with two or three pseudo-Voigt functions (Supporting Information, Figure A5.1), giving pre-edge areas similar to those reported previously (Table 5.1). The exception is the pre-edge area for $[Mn^{IV}(O)(2pyN2B)]^{2+}$, which is now 22.2 a dramatic increase compared to the previously reported value of 14.6.[18] This increase in pre-edge area, along with the higher edge energy of the present sample (6550.2 versus 6549.6 eV), leads us to propose that the former sample was more heterogeneous, consisting of the Mn^{IV}-oxo center and secondary species.

The collective set of pre-edge areas determined from these present fits can be compared to values reported previously for $[Mn^{IV}(O)(N4py)]^{2+}$ and $[Mn^{IV}(O)(OH)(Me_2EBC)]^{2+}$, although this comparison must be performed with some caution, as the pre-edge data were normalized differently.[21] The pre-edge intensities for $[Mn^{IV}(O)(N4py)]^{2+}$ and $[Mn^{IV}(O)(OH)(Me_2EBC)]^{2+}$ were normalized relative to the most intense fluorescence peak, whereas the tail of the EXAFS

region was used to normalize data collected for $[Mn^{IV}(O)(^{DMM}N4py)]^{2+}$, $[Mn^{IV}(O)(2pyN2B)]^{2+}$, and $[Mn^{IV}(O)(2pyN2Q)]^{2+}$.[17, 19, 21] To assess the effects of this different normalization process on the pre-edge area, we applied the latter normalization process to XAS data previously reported for $[Mn^{IV}(O)(N4py)]^{2+}$. Normalization to the tail of the EXAFS region resulted in a pre-edge area of 18.9, a significant increase compared to that determined when normalizing relative to the most intense fluorescence peak (12.7 units).[17, 21] Using the older normalization protocol, $[Mn^{IV}(O)(OH)(Me_2EBC)]^{2+}$ had a pre-edge area higher than $[Mn^{IV}(O)(N4py)]^{2+}$ (14.2 versus 12.7). Therefore, if the pre-edge region for $[Mn^{IV}(O)(OH)(Me_2EBC)]^{2+}$ were normalized to the EXAFS tail, it would likely have the highest pre-edge area for this series of Mn^{IV}-oxo complexes.

EXAFS Data and Analysis for Mn^{IV}-oxo Species. The FT and raw EXAFS data for the $[Mn^{IV}(O)(^{DMM}N4py)]^{2+}$, $[Mn^{IV}(O)(2pyN2Q)]^{2+}$, and $[Mn^{IV}(O)(2pyN2B)]^{2+}$ complexes are shown in Figure 5.3, and best fits to date are collected in Table 5.2. More complete fitting information can be found in Tables A5.1 - A5.3. The FT spectrum of each Mn^{IV}-oxo complex is characterized by peaks at ca. 1.2, 1.6, and 1.9 Å that vary in intensity between the different complexes (Figure 5.3). Fits of the EXAFS data for $[Mn^{IV}(O)(^{DMM}N4py)]^{2+}$ and $[Mn^{IV}(O)(2pyN2B)]^{2+}$ reveal comparable metric parameters (Table 5.2). In particular, the set of FT EXAFS features from 1.2 – 1.9 Å are well fit with an O shell (n = 1) near 1.70 Å and two N shells near 1.93 and 2.10 Å (n = 2 and 3, respectively). Additional FT peaks from ca. 2.1 – 2.5 Å can be fit considering two sets of C shells near 2.74 and 2.93 Å. The Mn–O scatterer distances for $[Mn^{IV}(O)(^{DMM}N4py)]^{2+}$ and $[Mn^{IV}(O)(2pyN2B)]^{2+}$, (1.72 and 1.70 Å, respectively) are in excellent agreement with Mn–O distances previously reported from EXAFS analyses of Mn^{IV}-oxo complexes in a pseudo-octahedral environment, which range from 1.58 to 1.74 Å.[13-14, 19, 21, 38]

Table 5.2. Parameters derived from the best EXAFS fit for each Mn^{IV}-oxo complex

	Mn–O/N			Mn–N			Mn–C				
complex	*n*	r(Å)	σ^2	*n*	r(Å)	σ^2	*n*	r(Å)	σ^2	E_0	R
$[Mn^{IV}(O)(^{DMM}N4py)]^{2+}$	1	1.72	1.26	2	1.94	2.38	3	2.92	2.28	-1.79	0.208
				3	2.10	6.09	3	2.74	8.63		
$[Mn^{IV}(O)(2pyN2B)]^{2+}$	1	1.70	2.12	2	1.92	1.31	3	2.94	5.97	-4.01	0.304
				3	2.10	4.10	3	2.74	7.74		
$[Mn^{IV}(O)(2pyN2Q)]^{2+}$	1	1.76	7.06	3	2.06	6.31	4	2.91	7.34	-0.65	0.268
				2	2.25	5.73	3	2.71	8.17		

[a] Fourier Transform ranges are as follows: $[Mn^{IV}(O)(^{DMM}N4py)]^{2+}$: 2-14 $Å^{-1}$, $[Mn^{IV}(O)(2pyN2B)]^{2+}$: 2-13 $Å^{-1}$, $[Mn^{IV}(O)(2pyN2Q)]^{2+}$: 2-14 $Å^{-1}$. [b] σ^2 is in units of 10^3 $Å^2$.

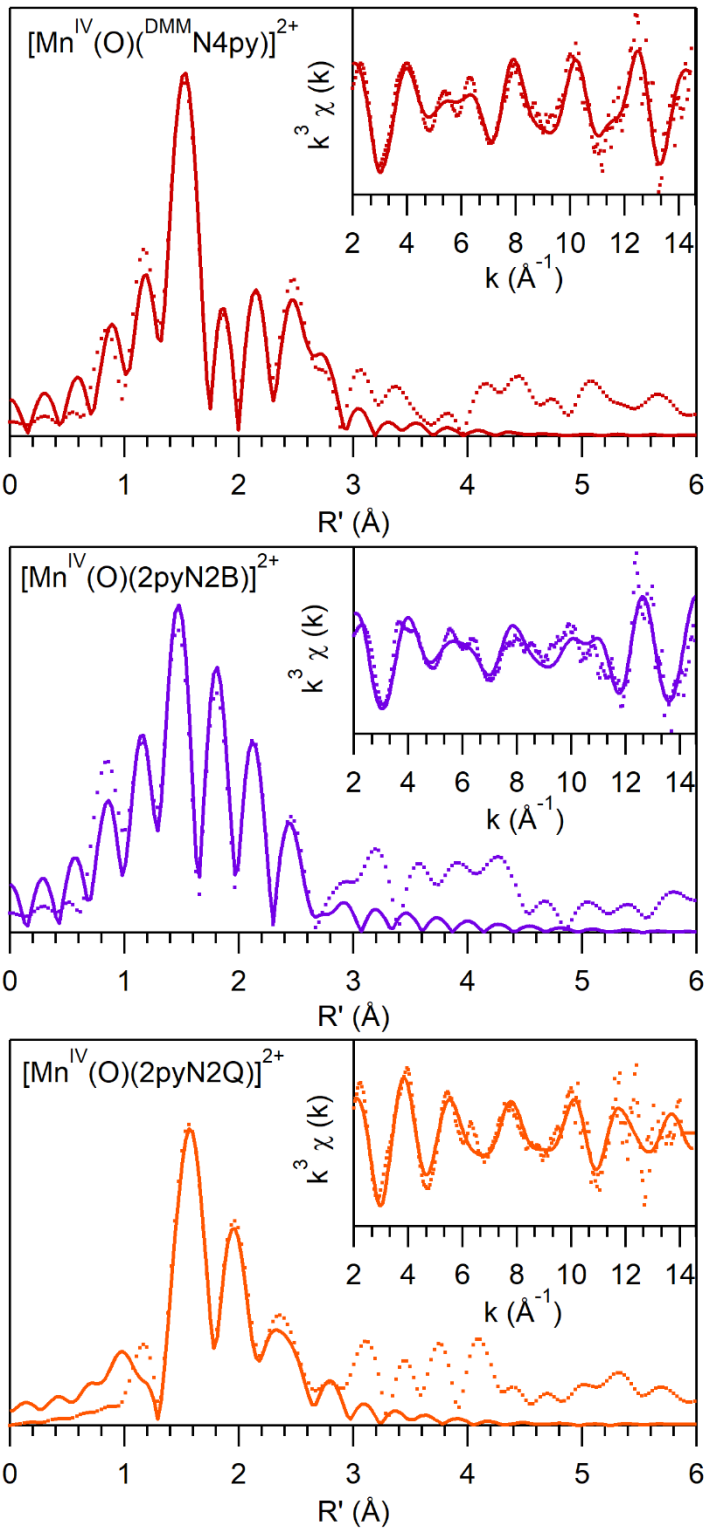

Figure 5.3. Fourier transforms of Mn K-edge EXAFS data and raw k^3 weighted EXAFS curves (insets) for the Mn^{IV}-oxo species. Experimental data is represented by dotted lines whereas fits are solid lines.

While the EXAFS analyses for $[Mn^{IV}(O)(^{DMM}N4py)]^{2+}$ and $[Mn^{IV}(O)(2pyN2B)]^{2+}$ yield metric parameters largely consistent with those of other Mn^{IV}-oxo complexes, the EXAFS fitting procedure for $[Mn^{IV}(O)(2pyN2Q)]^{2+}$ results in an O shell at the unrealistically long distance of 1.76 Å (Table 5.2). The Debye-Waller (σ^2) parameter for this shell is also unusually large for a single-atom shell at a short scattering distance. Given that $[Mn^{IV}(O)(2pyN2Q)]^{2+}$ has the fastest self-decay rate for this series of Mn^{IV}-oxo complexes, we attribute the unexpected EXAFS fits to the presence of secondary species. Thus, we conclude that the fit parameters for $[Mn^{IV}(O)(2pyN2Q)]^{2+}$ are not reflective of the true metric parameters of this complex.

Comparison of DFT and EXAFS Structures of Mn^{IV}-oxo Species. DFT computations were previously used to predict structures for $[Mn^{IV}(O)(^{DMM}N4py)]^{2+}$ and $[Mn^{IV}(O)(2pyN2B)]^{2+}$.[17-19] These computations predicted Mn-oxo distances of 1.68 and 1.66 Å for $[Mn^{IV}(O)(^{DMM}N4py)]^{2+}$ and $[Mn^{IV}(O)(2pyN2B)]^{2+}$, respectively. In each case, these values are 0.04 Å shorter than those obtained from the EXAFS fits (1.72 and 1.70 Å; see Table 5.3). Although some variance between experimental and DFT-predicted metric parameters is expected, typically DFT methods are most reliable at predicting distances for strong, short metal-ligand bonds, such as the Mn-oxo bonds considered here.[39] It is possible that partial photoreduction of the Mn^{IV}-oxo XAS samples could account for a Mn=O distance longer than that expected based on the DFT computations. Alternatively, the DFT treatment, which considers the Mn^{IV}-oxo dications in a solvent continuum (*i.e.*, with no explicit interactions with solvent), could be incomplete.

Because a protic solvent, such as TFE, could be reasonably considered to have hydrogen-bonding interactions with the oxo ligands, we performed DFT geometry optimizations for models of $[Mn^{IV}(O)(N4py)]^{2+}$, $[Mn^{IV}(O)(^{DMM}N4py)]^{2+}$, and $[Mn^{IV}(O)(2pyN2B)]^{2+}$ that included two TFE molecules. For completeness, we also considered a structure of $[Mn^{IV}(O)(2pyN2Q)]^{2+}$ with

explicit hydrogen-bonding interactions, although in this case we cannot compare the computational results to experimental distances. Our Mn^{IV}-oxo structures containing two TFE molecules are referred to as $[Mn^{IV}(O)(N4py)]^{2+}\cdot(TFE)_2$, $[Mn^{IV}(O)(^{DMM}N4py)]^{2+}\cdot(TFE)_2$, $[Mn^{IV}(O)(2pyN2Q)]^{2+}\cdot(TFE)_2$, and $[Mn^{IV}(O)(2pyN2B)]^{2+}\cdot(TFE)_2$. To provide a balanced comparison, we also re-optimized the structures of the Mn^{IV}-oxo complexes in the absence of added TFE using the same level of theory (our previous computational treatments lacked dispersion interactions, which we deemed important to include here to properly model solvent-solute interactions).[17-18] The result of these computations are summarized in Tables 5.3 and 5.4, and molecular structures of the complexes with hydrogen-bonded TFE molecules are shown in Figure 5.4.

Table 5.3. Comparison of DFT and EXAFS determined bond distances (Å) Mn^{IV}-oxo complexes.

complex	shell	DFT	EXAFS	DFT (H-bonding)
$[Mn^{IV}(O)(^{DMM}N4py)]^{2+}$	Mn–O (1)	1.68	1.72	1.70
	Mn–N (2)	1.99	1.95	1.98
	Mn–N (3)	2.04	2.10	2.03
$[Mn^{IV}(O)(2pyN2B)]^{2+}$	Mn–O (2)	1.66	1.70	1.68
	Mn–N (2)	1.97	1.92	1.96
	Mn–N (3)	2.20	2.10	2.08

Table 5.4. Selected Bond Lengths (Å), Bond Angles (°), and Hydrogen-Bonding Distances (Å) for Mn^{IV}-oxo Complexes $[Mn^{IV}(O)(N4py)]^{2+}$, $[Mn^{IV}(O)(^{DMM}N4py)]^{2+}$, and $[Mn^{IV}(O)(2pyN2Q)]^{2+}$ from DFT Computations.

	Mn–O	Mn–N_{eq}[a]	Mn–N_{amine}[b]	O–Mn–N_{amine}	O···H[c]
$[Mn^{IV}(O)(N4py)]^{2+}$	1.681	2.001	2.097	179.65	NA[d]
$[Mn^{IV}(O)(N4py)]^{2+}\cdot(TFE)_2$	1.699	2.001	2.077	178.27	1.641, 1.651
$[Mn^{IV}(O)(^{DMM}N4py)]^{2+}$	1.682	1.998	2.089	179.28	NA[d]
$[Mn^{IV}(O)(^{DMM}N4py)]^{2+}\cdot(TFE)_2$	1.702	1.997	2.069	177.97	1.622, 1.653
$[Mn^{IV}(O)(2pyN2B)]^{2+}$	1.661	2.055	2.335	176.03	NA[d]
$[Mn^{IV}(O)(2pyN2B)]^{2+}\cdot(TFE)_2$	1.680	1.999	2.155	178.24	1.739, 1.749
$[Mn^{IV}(O)(2pyN2Q)]^{2+}$	1.684	2.032	2.088	170.14	NA[d]
$[Mn^{IV}(O)(2pyN2Q)]^{2+}\cdot(TFE)_2$	1.703	2.030	2.070	170.44	1.678, 1.703

[a] The average of the four equatorial Mn–N bond lengths. [b] N_{amine} refers to the amine nitrogen *trans* to the oxo ligand. [c] Distances between the oxo ligand the alcohol hydrogen atoms of the TFE ligands. [d] Not applicable.

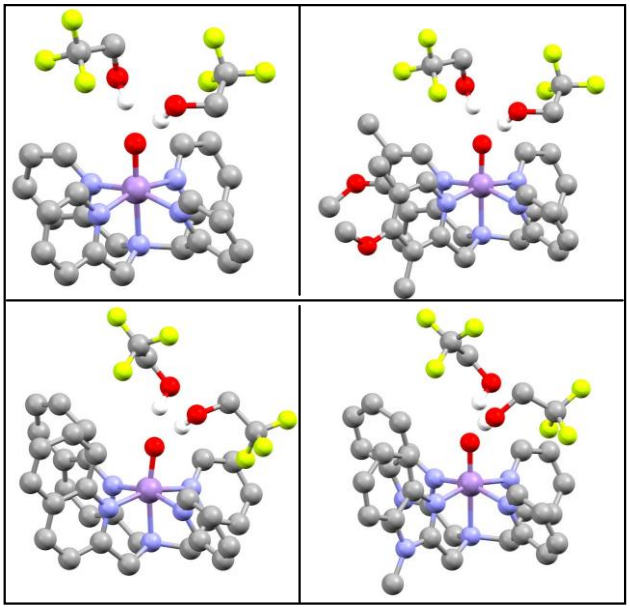

Figure 5.4. Molecular structures of Mn^{IV}-oxo complexes, $[Mn^{IV}(O)(N4py)]^{2+}\cdot(TFE)_2$ (top-left), $[Mn^{IV}(O)(^{DMM}N4py)]^{2+}\cdot(TFE)_2$ (top-right), $[Mn^{IV}(O)(2pyN2Q)]^{2+}\cdot(TFE)_2$ (bottom-left), and $[Mn^{IV}(O)(2pyN2B)]^{2+}\cdot(TFE)_2$ (bottom-right).

The structures of the Mn^{IV}-oxo complexes lacking the explicit TFE molecules are essentially identical to those previously reported.[17-18] In each case, the Mn=O distance is near 1.68 Å (except for $[Mn^{IV}(O)(2pyN2B)]^{2+}$, which has a shorter Mn=O distance of 1.66 Å) and the Mn–N_{eq} distances (which were obtained by averaging the equatorial Mn–N bond lengths), steadily

increase from $[Mn^{IV}(O)(^{DMM}N4py)]^{2+}$ to $[Mn^{IV}(O)(N4py)]^{2+}$ to $[Mn^{IV}(O)(2pyN2Q)]^{2+}$ (Table 5.4). In the case of $[Mn^{IV}(O)(2pyN2B)]^{2+}$, the average equatorial Mn–N_{eq} distances for the structure lacking the TFE molecules is at 2.055, which is the longest for this series. A previously determined structure of $[Mn^{IV}(O)(2pyN2B)]^{2+}$, which lacked dispersion corrections, predicted the average equatorial Mn–N_{eq} distance to be on the short end of the series. We speculate that the combination of dispersion corrections in the absence of explicit solvent interactions could lead to some errors in the DFT structure of $[Mn^{IV}(O)(2pyN2B)]^{2+}$. Finally, we note that the oxo ligand in $[Mn^{IV}(O)(2pyN2Q)]^{2+}$ is shifted away from the quinoline groups, giving an O–Mn–N_{amine} angle of 170°. The other Mn^{IV}-oxo complexes show far more modest deviations in O–Mn–N_{amine} angle from 180°.

The optimized structures of the $[Mn^{IV}(O)(N4py)]^{2+}\cdot(TFE)_2$, $[Mn^{IV}(O)(^{DMM}N4py)]^{2+}\cdot(TFE)_2$, $[Mn^{IV}(O)(2pyN2Q)]^{2+}\cdot(TFE)_2$, and $[Mn^{IV}(O)(2pyN2B)]^{2+}\cdot(TFE)_2$ complexes each show two TFE groups with strong hydrogen-bonding interactions with the oxo ligand (Figure 5.4). The distances between the oxo ligand and the alcohol hydrogen atom of the TFE molecules varies from 1.622 – 1.749 Å, which indicates strong hydrogen-bonding interactions. The longer oxo···$HOCH_2CF_3$ distances come from the $[Mn^{IV}(O)(2pyN2Q)]^{2+}\cdot(TFE)_2$ and $[Mn^{IV}(O)(2pyN2B)]^{2+}\cdot(TFE)_2$ structures (Table 5.4). Presumably, the steric bulk of the quinolinyl and benzimidazolyl groups prevent the TFE molecules from forming shorter hydrogen bonds with the oxo ligand. For each Mn^{IV}-oxo complex, the strong oxo···$HOCH_2CF_3$ interaction causes an elongation in the Mn=O distance of ca. 0.02 Å (Table 5.4). For $[Mn^{IV}(O)(2pyN2B)]^{2+}\cdot(TFE)_2$ and $[Mn^{IV}(O)(^{DMM}N4py)]^{2+}\cdot(TFE)_2$, this bond elongation leads to DFT-derived Mn=O bond lengths more consistent with those determined from fitting EXAFS data (Table 5.3).[19]

Using the DFT-optimized models of the Mn^{IV}-oxo complexes, we also calculated pre-edge transitions using the TD-DFT method.[39] The TD-DFT-computed spectra of these complexes are quite similar (Figure A5.2 and Table A5.4),[40] each dominated by two transitions, at ca. 6542 and 6543 eV, corresponding to Mn^{IV} 1s $\rightarrow$ $3d_{z^2}$ one-electron excitations in the α- and β-spin manifolds. The inclusion of hydrogen-bonding interactions with TFE solvent molecules leads to a minor (ca. 15%) reduction in pre-edge intensity compared to the models lacking interactions with TFE. Even in the presence of explicit hydrogen-bonding interactions, the short Mn–O bond lengths cause significant Mn^{IV} $3d_{z^2}$-$4p_z$ mixing, which accounts for the high relative intensity of excitations to the Mn^{IV} $3d_{z^2}$ orbitals (Tables 5.1 and Table A5.1). Notably, the DFT models including the TFE interactions give calculated pre-edge areas in excellent agreement with the experimental values (Table 5.5). The computations predict $[Mn^{IV}(O)(2pyN2B)]^{2+}$ to have the largest pre-edge area (24.7 units), in agreement with experiment (22.2 units). In addition, the energies of the TD-DFT transitions are within 0.5 eV of the higher-energy bands observed in the experimental spectra (Table 5.5). Each TD-DFT-computed spectrum also contains a cluster of transitions near 6541 eV, which could account for the low-energy shoulder observed experimentally (Table 5.1). The good agreement between calculated and experimental pre-edge properties for these Mn^{IV} centers is consistent with previous TD-DFT investigations.[21]

Table 5.5. Experimental and TD-DFT-Calculated Pre-edge Energies (eV) and Areas for the Series of Mn^{IV}-oxo Complexes.

	experimental		calculated pre-edge properties[a]			
complex	pre-edge	area	pre-edge energy	intensity	area	Mn 4p
$[Mn^{IV}(O)(^{DMM}N4py)]^{2+}$	6539.9	20.1	6541.0	2.58	17.3	3.1
	6541.6		6542.0			
	6543.2		6543.0			
$[Mn^{IV}(O)(2pyN2B)]^{2+}$	6539.9	22.2	6540.9	3.80	24.7	5.1
	6541.4		6541.9			
	6542.8		6542.9			
$[Mn^{IV}(O)(N4py)]^{2+}$	6541.9[b]	18.9[b]	6542.2	2.67	17.8	3.2
			6543.2			
$[Mn^{IV}(O)(2pyN2Q)]^{2+}$	6539.9	15.1	6541.6	2.34	15.9	2.0
	6541.5		6542.0			
			6542.9			

[a] From TD-DFT computations for models of the Mn^{IV}-oxo complexes with second-sphere TFE molecules hydrogen-bonding to the oxo ligand. Corresponding properties for models lacking the TFE molecules are included in the Supporting Information.[b] From references [19] and [13].

DFT Investigation of $[Fe^{IV}(O)(N4py)]^{2+}\cdot(TFE)_2$ Species. The Fe^{IV}-oxo analogue of $[Mn^{IV}(O)(N4py)]^{2+}$, $[Fe^{IV}(O)(N4py)]^{2+}$ has been generated in both the protic solvent TFE and in the aprotic solvent MeCN. To investigate the effects of hydrogen-bonding with solvent for $[Fe^{IV}(O)(N4py)]^{2+}$, and to compare Mn^{IV}-oxo and Fe^{IV}-oxo hydrogen-bonding interactions, we developed DFT structures for $[Fe^{IV}(O)(N4py)]^{2+}$ and $[Fe^{IV}(O)(N4py)]^{2+}\cdot(TFE)_2$. These computations employ the same level of theory as that used for the Mn^{IV}-oxo computations (*vide supra*). The DFT-optimized structure of $[Fe^{IV}(O)(N4py)]^{2+}$ shows an Fe=O distance of 1.649 Å, with average $Fe–N_{equatorial}$ distances of 1.965 Å, and an $Fe–N_{amine}$ distance of 2.046 Å. These metric parameters are in good agreement with experimental distances from X-ray crystallography (Figure A)[42] and with distances from previous DFT investigations.[43-45] In the DFT-optimized structure of $[Fe^{IV}(O)(N4py)]^{2+}\cdot(TFE)_2$, the two TFE molecules show strong hydrogen-bonding interactions with the oxo ligand (Figure 5.5). This interaction leads to a minor elongation in the Fe=O distance of 0.013 Å; minor changes are also observed in the Fe–N bond lengths. While the structure of

$[Fe^{IV}(O)(N4py)]^{2+}\cdot(TFE)_2$ does contain oxo-TFE hydrogen-bonding interactions, these interactions are not as strong as those observed in the $[Mn^{IV}(O)(N4py)]^{2+}\cdot(TFE)_2$ structure. Specifically, the oxo---H distances in $[Fe^{IV}(O)(N4py)]^{2+}\cdot(TFE)_2$ are 0.1 Å longer than those in $[Mn^{IV}(O)(N4py)]^{2+}\cdot(TFE)_2$ (1.75 and 1.65 Å, respectively; see Figure 5.5 and Table 5.4). These results are consistent with previous observations that suggest that, at parity of coordination sphere, Mn^{IV}-oxo centers are more basic than their Fe^{IV}-oxo analogues.[46-47]

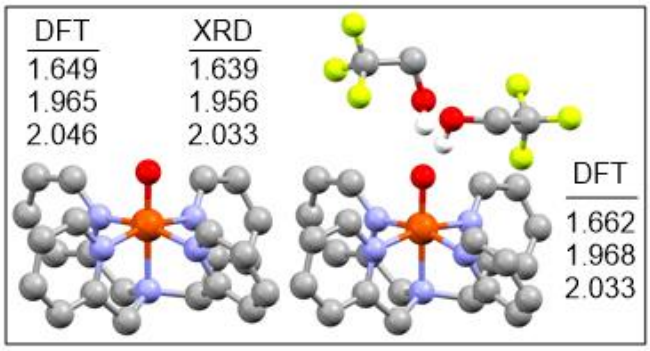

Figure 5.5. Molecular structures of $[Fe^{IV}(O)(N4py)]^{2+}$ (left) and $[Fe^{IV}(O)(N4py)]^{2+}\cdot(TFE)_2$ (right). Metric parameters from DFT computations and the X-ray diffraction (XRD) structure of $[Fe^{IV}(O)(N4py)](OTf)_2$ are provided. XRD data are from reference [42].

5.4 Discussion

EXAFS Analysis for Mn^{IV}-oxo species. To the best of our knowledge, only a single mononuclear Mn^{IV}-oxo complex has been structurally characterized by X-ray diffraction.[11] For the remainder of known Mn^{IV}-oxo complexes, Mn K-edge XAS has served as the sole technique for determining Mn-ligand bond distances. Herein, we utilized Mn K-edge XAS to determine metric parameters for a set of three Mn^{IV}-oxo species supported by N4py derivatives. Previous work had shown that these particular complexes display a range of rates for HAT and oxygen-atom transfer reactions, making the structures of these complexes of particular interest. Analysis of the EXAFS data for $[Mn^{IV}(O)(^{DMM}N4py)]^{2+}$ and $[Mn^{IV}(O)(2pyN2B)]^{2+}$ revealed Mn=O distances of 1.72 and 1.70 Å, respectively (Table 5.2). These distances are in excellent agreement with those of other Mn^{IV}-oxo species in a pseudo-octahedral geometry (Table 5.6). Specifically, $[Mn^{IV}(O)(N4py)]^{2+}$

and $[Mn^{IV}(O)(Bn\text{-}TPEN)]^{2+}$, which also both feature neutral N_5 ligands, both show comparable Mn=O distances of 1.69 Å.[14, 19] Mononuclear Mn^{IV}-oxo complexes supported by porphyrin ligands or with *cis* hydroxo ligands also display similar distances (1.69 and 1.71 Å, respectively). The Mn=O distance for $[Mn^{IV}(O)(2pyN2Q)]^{2+}$ determined by analysis of EXAFS data (1.76 Å) is a clear outlier. We attribute this long distance to sample heterogeneity, which is reasonable given that $[Mn^{IV}(O)(2pyN2Q)]^{2+}$ shows reduced stability compared to the other Mn^{IV}-oxo complexes in this series. Thus, we do not attribute the 1.76 Å distance as the Mn=O bond length. (We note that, while it would be illuminating to compare $Mn–N_{axial}$ and average $Mn–N_{equatorial}$ distances for this series of Mn^{IV}-oxo complexes, it is not possible to attribute particular Mn–N EXAFS shells to these ligand types.)

Table 5.6. Selected Bond Lengths (Å) for Mn^{IV}-oxo species in the literature.

Complex	Mn–O	Solvent	Reference
$[Mn^{IV}(O)(N4py)]^{2+}$	1.69, 1.70	TFE	19, 13
$[Mn^{IV}(O)(N4py)]^{2+}$–$(HOTf)_2$	1.74	TFE/MeCN	41
$[Mn^{IV}(O)(^{DMM}N4py)]^{2+}$	1.72	TFE	a
$[Mn^{IV}(O)(2pyN2B)]^{2+}$	1.70	TFE	a
$[Mn^{IV}(O)(OH)(Me_2EBC)]^{+}$	1.71	H_2O	12
$[Mn^{IV}(O)(Bn\text{-}TPEN)]^{2+}$	1.69	TFE	14
$[Mn^{IV}(O)(T_{piv}PP)]$	1.69	THF/DMF	42
$[Mn^{IV}(O)(salen)]$	1.58	PrCN	20

[a]This work

Potential Role of Trifluoroethanol in Stabilizing Mn^{IV}-oxo Species. While the Mn=O distances for $[Mn^{IV}(O)(^{DMM}N4py)]^{2+}$ and $[Mn^{IV}(O)(2pyN2B)]^{2+}$ determined from EXAFS fits agree well with other examples in the literature, these distances are in relatively poor agreement with the Mn=O distances from DFT calculations (Table 5.3). The computationally determined Mn=O distances for $[Mn^{IV}(O)(^{DMM}N4py)]^{2+}$ and $[Mn^{IV}(O)(2pyN2B)]^{2+}$ are each 0.04 Å lower than those determined from EXAFS analysis. Better agreement is achieved for calculations that included second-sphere TFE molecules, which form strong hydrogen-bonds with the oxo ligands.

The hydrogen-bonds result in a slight elongation of the Mn=O distances, putting the computationally determined Mn=O distances for $[Mn^{IV}(O)(^{DMM}N4py)]^{2+}$ and $[Mn^{IV}(O)(2pyN2B)]^{2+}$ within 0.02 Å of those determined from the analysis of EXAFS data.

The intimate interactions between the Mn^{IV}-oxo unit and solvent predicted by these computations could offer insight into the privileged role that TFE has played in stabilizing Mn^{IV}-oxo species with neutral, N_5 supporting ligands. Nam and co-workers were the first to observe that certain Mn^{IV}-oxo centers could form in excellent yield in TFE but not in other solvents (although some of these Mn^{IV}-oxo adducts can be formed in mixed solvents, these mixtures always include TFE, *i.e.*, TFE:CH_2Cl_2 or TFE:MeCN). We have used this knowledge to great advantage to make our present series of Mn^{IV}-oxo complexes. While we have previously suggested a role for TFE in helping to solubilize PhIO, allowing a for rapid reaction with the Mn^{II} precursor complex, our present computations suggest that hydrogen-bonding with TFE serves to stabilize the Mn^{IV}-oxo unit. One test of this proposed role of TFE as a hydrogen-bond donor would be to measure EXAFS data for one of these Mn^{IV}-oxo complexes in an aprotic solvent. Unfortunately, formation of members of this class of Mn^{IV}-oxo species in an aprotic solvent has not yet been achieved.

DFT Investigation of $[Mn^{IV}(O)(N4py)]^{2+}\cdot(HOTf)_2$ Species. Similar to our proposal of $[Mn^{IV}(O)(N4py)]^{2+}\cdot(TFE)_2$, Nam and Fukuzumi suggest the formation of $[Mn^{IV}(O)(N4py)]^{2+}\cdot(HOTf)_2$ when HOTf is added to $[Mn^{IV}(O)(N4py)]^{2+}$. EXAFS analysis shows a 0.04 Å elongation of the Mn=O distance upon addition of acid to $[Mn^{IV}(O)(N4py)]^{2+}$. This is very similar to our proposed structure in solution, $[Mn^{IV}(O)(N4py)]^{2+}\cdot(TFE)_2$, where two TFE solvent molecules serve to stabilize the Mn^{IV}-oxo intermediate through hydrogen-bonding interactions.

Upon the addition of HOTf to $[Mn^{IV}(O)(N4py)]^{2+}$, the near-IR feature at 940 nm decays and a shoulder grows in at 550 nm. These spectral changes are striking similar to those observed upon the addition of acid to the Mn^{IV}-oxo complex $[Mn^{IV}(O)(OH)(Me_2EBC)]^{2+}$. In this case, acid addition results in the formation of the $[Mn^{IV}(OH)_2(Me_2EBC)]^{2+}$, which has been well-characterized by a suite of methods, including XRD. The Mn^{IV}-dihydroxo complex $[Mn^{IV}(OH)_2(Me_2EBC)]^{2+}$ exhibits an electronic absorption feature at 550 nm. These changes in electronic transition energies were described in terms of the reduction in the Mn=O bond order, and the accompanied elimination of strong Mn-oxo π-interactions, upon protonation of the oxo ligand. Specifically, the near-IR absorption feature for these pseudo-octahedral Mn^{IV}-oxo complexes arises from a one-electron excitation from the Mn^{IV} d_{xz}, d_{yz} molecular orbitals (MOs), which are Mn=O π-antibonding, to the Mn^{IV} $d_{x^2-y^2}$ MO, which is $Mn–N_{equatorial}$ σ-antibonding. A shift of this near-IR absorption band to higher energy is consistent with a stabilization of the Mn^{IV} d_{xz}, d_{yz} donor orbitals through a weakening of Mn=O π-interactions. Thus, the similar spectral changes observed for similarity in band maxima between $[Mn^{IV}(O)(OH)(Me_2EBC)]^{2+}$ and $[Mn^{IV}(O)(N4py)]^{2+}$ upon the addition of acid could suggest the formation of Mn^{IV}-hydroxo products for both systems.[43]

DFT Calculations for analogous Fe oxo species in TFE. While the Mn^{IV}-oxo species supported by N4py derivatives and Bn-TPEN require the use of TFE as a solvent for formation, the analogous Fe complexes can be formed in either protic TFE or aprotic MeCN. Thus, TFE is not the privileged solvent for Fe^{IV}-oxo complexes as it is for Mn^{IV}-oxo analogous. Our DFT computations for $[Fe^{IV}(O)(N4py)]^{2+}$ in the presence of two second-sphere TFE molecules show reduced solvent-oxo hydrogen-bonding interactions when compared to the Mn^{IV}-oxo counterpart. Specifically, the DFT-optimized structures for $[Fe^{IV}(O)(N4py)]^{2+}\cdot(TFE)_2$ shows oxo···H

separations that are 0.1 Å longer than those for $[Mn^{IV}(O)(N4py)]^{2+}\cdot(TFE)_2$. Thus, solvent stabilization might not be as critical for the Fe^{IV}-oxo species.

Busch et al. determined that the bis-hydroxo species, $[Mn^{IV}(OH)_2(Me_2EBC)]^+$, is converted to the oxo-hydroxo species, $[Mn^{IV}(O)(OH)(Me_2EBC)]^{2+}$ by simply increasing the pH from 5.8 to 8.4.[43-44] With the help of Mn K-edge XAS, EXAFS analysis show that $[Mn^{IV}(O)(OH)(Me2EBC)]^{2+}$ is best fit with a single Mn–O shell at a distance of 1.80 Å. In contrast, EXAFS analysis of $[Mn^{IV}(O)(OH)(Me_2EBC)]^{2+}$ revealed a Mn=O bond distance of 1.71 Å and a Mn–OH distance of 1.84 Å. This supports deprotonation of one of the hydroxo ligands to give an oxo adduct. This change in bond order is apparent by the decrease in bond distance, suggesting double bond character. They can interconvert between these two species by altering the pH of the solution. With the help of pH titration experiments, a pK_a for $[Mn^{IV}(O)(OH)(Me_2EBC)]^{2+}$ was determined to be 6.86.[44]. This suggests that the introduction of strong acids could result in protonation of an oxo adduct depending on its basicity.

A similar observation was made by Costas et al for $[Mn^{IV}(OH)_2(^{H,Me}Pytacn)]^+$, where the conjugate base $[Mn^{IV}(O)(OH)(^{H,Me}Pytacn)]^+$ could be accessed by introducing an equivalent of *t*BuOK. This process was shown to be reversible upon the addition of an equivalent of CF_3SO_3H, which highlights the ease of converting between the oxo and hydroxo adducts for this system.[45] Additionally, pH titration experiments for $[Mn^{IV}(O)(OH)(^{H,Me}Pytacn)]^+$ revealed a pK_a of 7.1, which is similar to what was observed for $[Mn^{IV}(O)(OH)(Me_2EBC)]^+$.[44-45] It is interesting to note that the corresponding $[Fe^{IV}(O)(OH)(^{H,Me}Pytacn)]^+$ species exhibits very different acid-base reactivity. Even at pH ~1, this species does not undergo protonation of the oxo adduct, signifying that the corresponding pK_a is less than 1. These observations suggest that, at parity of coordination sphere, the Mn^{IV}-oxo adduct is at least 7 pK_a units more basic than the Fe^{IV}-oxo adduct.[46]

Other Fe^{IV}-oxo complexes supported by N4 and N5 ligands have been shown to be stable in the presence of excess acid, which provides further evidence for the low basicity of such complexes. Specifically, the addition of either 10 mM $HClO_4$ or 5 M CF_3COOH to $[Fe^{IV}(O)(N4py)]^{2+}$ results in minimal changes to the UV-Vis spectrum, which provides strong evidence that the Fe^{IV}-oxo adduct is not protonated under these conditions.[47-48] This behavior is in stark contrast to the analogous Mn^{IV}-oxo species, $[Mn^{IV}(O)(N4py)]^{2+}$, which exhibits spectral changes upon the addition of HOTf.

When considering a protonated Fe^{IV}-oxo species, an obvious site for protonation is at the oxo ligand. However, as has already been discussed, the pK_a values associated with Fe^{IV}-OH units are thought to be < 5.[49-51] When acid is added to $[Fe^{IV}(O)(H_3buea)]^-$, protonation likely occurs on the tripodal ligand rather than the oxo ligand. The ligand is proposed to undergo a structural change that takes place due to the new intramolecular H-bond with the oxo ligand within the active site center, which serves to stabilize the oxo unit. These findings were strongly supported by spectroscopic evidence, and this work suggests that caution must be taken when assigned high-valent Fe-OH species, as their existence may be questionable.[52]

At parity of coordination sphere, Mn and Fe centers exhibit strikingly different reactivities as well as differences in their sensitivity to acids. Specifically, there several Mn^{IV}-oxo species that are susceptible to protonation, whereas their analogous Fe^{IV}-oxo centers are not. DFT calculations on both $[Mn^{IV}(O)(N4py)]^{2+}$ and $[Fe^{IV}(O)(N4py)]^{2+}$ in the presence of TFE solvent molecules conducted in this work show that the Fe^{IV}-oxo center exhibits much weaker H-bonding interactions, suggesting that the Mn^{IV}-oxo center is inherently more basic. This observation may help to explain why Mn^{IV}-oxo species supported by N4py and other similar ligand scaffolds require

the use of a protic solvent system for formation, as the center is otherwise unstable and prone to decay.

5.5 Conclusions

Analysis of Mn K-edge XAS data for $[Mn^{IV}(O)(2pyN2B)]^{2+}$ and the related $[Mn^{IV}(O)(^{DMM}N4py)]^{2+}$ and $[Mn^{IV}(O)(2pyN2Q)]^{2+}$ complexes yield large pre-edge areas and relatively short Mn=O distances, which are hallmarks of mononuclear Mn^{IV}-oxo centers. Variations in pre-edge area are observed for this series, and these are well-reproduced by TD-DFT computations. The EXAFS-determined Mn=O bond lengths for these complexes are best reproduced by DFT models including second-sphere TFE molecules involved in strong hydrogen-bonding interactions with the oxo ligands. These interactions could shed light on the privileged status of TFE in stabilizing Mn^{IV}-oxo complexes. Weaker solvent-oxo hydrogen-bonding interactions were predicted for the Fe^{IV}-oxo complex $[Fe^{IV}(O)(N4py)]^{2+}$. This result is consistent with previous studies that suggest the Mn^{IV}-oxo unit is more basic than its Fe^{IV}-oxo counterpart. DFT investigations to understand the structure of $[Mn^{IV}(O)(N4py)]^{2+}$ in the presence of triflic acid lead to the postulate that the reactions of these species forms a Mn^{IV}-hydroxo center.

5.6 References

1. Rittle, J.; Green, M. T., Cytochrome P450 Compound I: Capture, Characterization, and C–H Bond Activation Kinetics. *Science* **2010,** *330* (6006), 933-937.

2. Huang, X.; Groves, J. T., Oxygen Activation and Radical Transformations in Heme Proteins and Metalloporphyrins. *Chem. Rev.* **2017**.

3. Wong, S. D.; Srnec, M.; Matthews, M. L.; Liu, L. V.; Kwak, Y.; Park, K.; Bell Iii, C. B.; Alp, E. E.; Zhao, J.; Yoda, Y.; Kitao, S.; Seto, M.; Krebs, C.; Bollinger, J. M.; Solomon, E. I., Elucidation of the Fe(iv)=O intermediate in the catalytic cycle of the halogenase SyrB2. *Nature* **2013,** *499*, 320.

4. Srnec, M.; Wong, S. D.; Matthews, M. L.; Krebs, C.; Bollinger, J. M.; Solomon, E. I., Electronic Structure of the Ferryl Intermediate in the α-Ketoglutarate Dependent Non-Heme Iron Halogenase SyrB2: Contributions to H Atom Abstraction Reactivity. *J. Am. Chem. Soc.* **2016,** *138* (15), 5110-5122.

5. Price, J. C.; Barr, E. W.; Glass, T. E.; Krebs, C.; Bollinger, J. M., Evidence for Hydrogen Abstraction from C1 of Taurine by the High-Spin Fe(IV) Intermediate Detected during Oxygen Activation by Taurine:α-Ketoglutarate Dioxygenase (TauD). *J. Am. Chem. Soc.* **2003,** *125* (43), 13008-13009.

6. Denisov, I. G.; Makris, T. M.; Sligar, S. G.; Schlichting, I., Structure and Chemistry of Cytochrome P450. *Chem. Rev.* **2005,** *105* (6), 2253-2278.

7. Hausinger, R. P., Fe(II)/α-Ketoglutarate-Dependent Hydroxylases and Related Enzymes. *Critical Reviews in Biochemistry and Molecular Biology* **2004,** *39* (1), 21-68.

8. Puri, M.; Que, L., Toward the Synthesis of More Reactive S = 2 Non-Heme Oxoiron(IV) Complexes. *Acc. Chem. Rev.* **2015,** *48* (8), 2443-2452.

9. Nam, W., Synthetic Mononuclear Nonheme Iron–Oxygen Intermediates. *Acc. Chem. Res.* **2015,** *48* (8), 2415-2423.

10. Rohde, J.-U.; In, J.-H.; Lim, M. H.; Brennessel, W. W.; Bukowski, M. R.; Stubna, A.; Münck, E.; Nam, W.; Que, L., Crystallographic and Spectroscopic Characterization of a Nonheme Fe(IV)=O Complex. *Science* **2003,** *299* (5609), 1037-1039.

11. Halbach, R. L.; Gygi, D.; Bloch, E. D.; Anderson, B. L.; Nocera, D. G., Structurally characterized terminal manganese(iv) oxo tris(alkoxide) complex. *Chemical Science* **2018,** *9* (19), 4524-4528.

12. Leto, D. F.; Massie, A. A.; Colmer, H. E.; Jackson, T. A., X-Band Electron Paramagnetic Resonance Comparison of Mononuclear Mn^{IV}-oxo and Mn^{IV}-hydroxo Complexes and Quantum Chemical Investigation of MnIV Zero-Field Splitting. *Inorg. Chem.* **2016,** *55* (7), 3272-3282.

13. Chen, J.; Lee, Y.-M.; Davis, K. M.; Wu, X.; Seo, M. S.; Cho, K.-B.; Yoon, H.; Park, Y. J.; Fukuzumi, S.; Pushkar, Y. N.; Nam, W., A Mononuclear Non-Heme Manganese(IV)–Oxo Complex Binding Redox-Inactive Metal Ions. *J. Am. Chem. Soc* **2013,** *135* (17), 6388-6391.

14. Wu, X.; Seo, M. S.; Davis, K. M.; Lee, Y.-M.; Chen, J.; Cho, K.-B.; Pushkar, Y. N.; Nam, W., A Highly Reactive Mononuclear Non-Heme Manganese(IV)–Oxo Complex That Can Activate the Strong C–H Bonds of Alkanes. *J. Am. Chem. Soc.* **2011,** *133* (50), 20088-20091.

15. Chen, J.; Cho, K.-B.; Lee, Y.-M.; Kwon, Y. H.; Nam, W., Mononuclear nonheme iron(iv)–oxo and manganese(iv)–oxo complexes in oxidation reactions: experimental results prove theoretical prediction. *Chem. Commun.* **2015,** *51* (66), 13094-13097.

16. Cho, K.-B.; Shaik, S.; Nam, W., Theoretical Investigations into C–H Bond Activation Reaction by Nonheme $Mn^{IV}O$ Complexes: Multistate Reactivity with No Oxygen Rebound. *J. Phys. Chem. Lett.* **2012,** *3* (19), 2851-2856.

17. Massie, A. A.; Denler, M. C.; Cardoso, L. T.; Walker, A. N.; Hossain, M. K.; Day, V. W.; Nordlander, E.; Jackson, T. A., Equatorial Ligand Perturbations Influence the Reactivity of Manganese(IV)-Oxo Complexes. *Angew. Chem., Int. Ed. Engl.* **2017,** *56* (15), 4178-4182.

18. Denler, M. C.; Massie, A. A.; Singh, R.; Stewart-Jones, E.; Sinha, A.; Day, V. W.; Nordlander, E.; Jackson, T. A., Mn^{IV}-Oxo complex of a bis(benzimidazolyl)-containing N5 ligand reveals different reactivity trends for Mn^{IV}-oxo than Fe^{IV}-oxo species. *Dalton Trans.* **2019,** *48* (15), 5007-5021.

19. Leto, D. F.; Ingram, R.; Day, V. W.; Jackson, T. A., Spectroscopic properties and reactivity of a mononuclear oxomanganese(iv) complex. *Chem. Commun.* **2013,** *49* (47), 5378-5380.

20. Kurahashi, T.; Kikuchi, A.; Tosha, T.; Shiro, Y.; Kitagawa, T.; Fujii, H., Transient Intermediates from Mn(salen) with Sterically Hindered Mesityl Groups: Interconversion between Mn^{IV}-Phenolate and Mn^{III}-Phenoxyl Radicals as an Origin for Unique Reactivity. *Inorg. Chem.* **2008,** *47* (5), 1674-1686.

21. Leto, D. F.; Jackson, T. A., Mn K-Edge X-ray Absorption Studies of Oxo- and Hydroxomanganese(IV) Complexes: Experimental and Theoretical Insights into Pre-Edge Properties. *Inorg. Chem.* **2014,** *53*, 6179-6194.

22. Penner-Hahn, J. E., X-ray Absorption Spectroscopy. In *Comprehensive Coordination Chemistry II*, Elsevier Ltd.: 2003; Vol. 2, pp 159-186.

23. Wijeratne, G. B.; Corzine, B.; Day, V. W.; Jackson, T. A., Saturation Kinetics in Phenolic O–H Bond Oxidation by a Mononuclear Mn(III)–OH Complex Derived from Dioxygen. *Inorg. Chem.* **2014,** *53* (14), 7622-7634.

24. Seo, M. S.; Kim, J. Y.; Annaraj, J.; Kim, Y.; Lee, Y.-M.; Kim, S.-J.; Kim, J.; Nam, W., $[Mn(tmc)(O_2)]^+$: A Side-On Peroxide Manganese(III) Complex Bearing a Non-heme Ligand. *Angew. Chem., Int. Ed. Engl.* **2007,** *46*, 377-380.

25. Saltzman, H.; Sharefkin, J. G., Iodosobenzene. *Org. Synth.* **1963,** *43*, 60.

26. Mitra, M.; Nimir, H.; Demeshko, S.; Bhat, S. S.; Malinkin, S. O.; Haukka, M.; Lloret-Fillol, J.; Lisensky, G. C.; Meyer, F.; Shteinman, A. A.; Browne, W. R.; Hrovat, D. A.; Richmond, M. G.; Costas, M.; Nordlander, E., Nonheme Fe(IV) Oxo Complexes of Two New Pentadentate Ligands and Their Hydrogen-Atom and Oxygen-Atom Transfer Reactions. *Inorg. Chem.* **2015,** *54* (15), 7152-7164.

27. Ravel, B.; Newville, M., ATHENA, ARTEMIS, HEPHAESTUS: data analysis for X-ray absorption spectroscopy using IFEFFIT. *J. Synchrotron Rad.* **2005,** *12* (4), 537-541.

28. Rehr, J. J.; Mustre de Leon, J.; Zabinsky, S. I.; Albers, R. C., Theoretical x-ray absorption fine structure standards. *Journal of the American Chemical Society* **1991,** *113* (14), 5135-5140.

29. Wojdyr, M., Fityk: a general-purpose peak fitting program. *J. Appl. Cryst.* **2010,** *43* (5 Part 1), 1126-1128.

30. Neese, F., The ORCA program system. *WIREs Comput Mol Sci.* **2012,** *2* (1), 73-78.

31. Tao, J.; Perdew, J. P.; Staroverov, V. N.; Scuseria, G. E., Climbing the Density Functional Ladder: Nonempirical Meta-Generalized Gradient Approximation Designed for Molecules and Solids. *Phys. Rev. Lett.* **2003,** *91* (14), 146401.

32. Grimme, S.; Antony, J.; Ehrlich, S.; Krieg, H., A consistent and accurate ab initio parametrization of density functional dispersion correction (DFT-D) for the 94 elements H-Pu. *J. Chem. Phys.* **2010,** *132* (15), 154104.

33. Grimme, S.; Ehrlich, S.; Goerigk, L., Effect of the damping function in dispersion corrected density functional theory. *J. Comput. Chem.* **2011,** *32* (7), 1456-1465.

34. Schäfer, A.; Horn, H.; Ahlrichs, R., Fully optimized contracted Gaussian basis sets for atoms Li to Kr. *J. Chem. Phys.* **1992,** *97* (4), 2571-2577.

35. Schäfer, A.; Huber, C.; Ahlrichs, R., Fully Optimized Contracted Gaussian Basis Sets of Triple Zeta Valence Quality for Atoms Li to Kr. *J. Chem. Phys.* **1994,** *100*, 5829-5835.

36. Weigend, F.; Ahlrichs, R., Balanced basis sets of split valence, triple zeta valence and quadruple zeta valence quality for H to Rn: Design and assessment of accuracy. *Phys. Chem. Chem. Phys.* **2005,** *7* (18), 3297-3305.

37. Marenich, A. V.; Cramer, C. J.; Truhlar, D. G., Universal Solvation Model Based on Solute Electron Density and on a Continuum Model of the Solvent Defined by the Bulk Dielectric Constant and Atomic Surface Tensions. *J. Phys. Chem. B* **2009,** *113* (18), 6378-6396.

38. Brink, C. P.; Crumbliss, A. L., Kinetics, Mechanism, and Thermodynamics of Aqueous Iron(III) Chelation and Dissociation: Influence of Carbon and Nitrogen Substituents in Hydroxamic Acid Ligands. *Inorg. Chem.* **1984,** *23* (26), 4708-4718.

39. Neese, F., A critical evaluation of DFT, including time-dependent DFT, applied to bioinorganic chemistry. *JBIC Journal of Biological Inorganic Chemistry* **2006,** *11* (6), 702-711.

40. Although little variation is seen in the transition energies between the Mn^{IV}-oxo models with or without the hydrogen-bonding TFE molecules, the models lacking the hydrogen-bonding interactions show slightly higher pre-edge intensities (increase of ca. 4 units; see Table A5.4). This increase in intensity is readily attributed to the shorter Mn-O distances for the models lacking the hydrogen-bonding interactions. Because of the minor variations between models with and without TFE molecules, we focus our discussion on the latter.

41. Chen, J.; Yoon, H.; Lee, Y.-M.; Seo, M. S.; Sarangi, R.; Fukuzumi, S.; Nam, W., Tuning the reactivity of mononuclear nonheme manganese(iv)-oxo complexes by triflic acid. *Chemical Science* **2015,** *6* (6), 3624-3632.

42. Charnock, J. M.; Garner, C. D.; Trautwein, A. X.; Bill, E.; Winkler, H.; Ayougou, K.; Mandon, D.; Weiss, R., Characterization of an Oxo(porphyrinato)manganese(IV) Complex by X-ray Absorption Spectroscopy. *Angewandte Chemie International Edition in English* **1995,** *34* (3), 343-346.

43. Chattopadhyay, S.; Geiger, R. A.; Yin, G.; Busch, D. H.; Jackson, T. A., Oxo- and Hydroxomanganese(IV) Adducts: A Comparative Spectroscopic and Computational Study. *Inorg. Chem.* **2010,** *49* (16), 7530-7535.

44. Yin, G.; McCormick, J. M.; Buchalova, M.; Danby, A. M.; Rodgers, K.; Day, V. W.; Smith, K.; Perkins, C. M.; Kitko, D.; Carter, J. D.; Scheper, W. M.; Busch, D. H., Synthesis, Characterization, and Solution Properties of a Novel Cross-Bridged Cyclam Manganese(IV) Complex Having Two Terminal Hydroxo Ligands. *Inorg. Chem.* **2006,** *45* (20), 8052-8061.

45. Garcia-Bosch, I.; Company, A.; Cady, C. W.; Styring, S.; Browne, W. R.; Ribas, X.; Costas, M., Evidence for a Precursor Complex in C–H Hydrogen Atom Transfer Reactions Mediated by a Manganese(IV) Oxo Complex. *Angew. Chem., Int. Ed. Engl.* **2011,** *50* (25), 5648-5653.

46. Company, A.; Prat, I.; Frisch, J. R.; Mas-Ballesté, D. R.; Güell, M.; Juhász, G.; Ribas, X.; Münck, D. E.; Luis, J. M.; Que, L.; Costas, M., Modeling the cis-Oxo-Labile Binding Site Motif of Non-Heme Iron Oxygenases: Water Exchange and Oxidation Reactivity of a Non-Heme Iron(IV)-Oxo Compound Bearing a Tripodal Tetradentate Ligand. *Chemistry - A European Journal* **2011,** *17* (5), 1622-1634.

47. Park, J.; Lee, Y.-M.; Nam, W.; Fukuzumi, S., Brønsted Acid-Promoted C–H Bond Cleavage via Electron Transfer from Toluene Derivatives to a Protonated Nonheme Iron(IV)-Oxo Complex with No Kinetic Isotope Effect. *Journal of the American Chemical Society* **2013,** *135* (13), 5052-5061.

48. Wang, D.; Zhang, M.; Bühlmann, P.; Que, L., Redox Potential and C−H Bond Cleaving Properties of a Nonheme Fe^{IV}═O Complex in Aqueous Solution. *Journal of the American Chemical Society* **2010,** *132* (22), 7638-7644.

49. Yosca, T. H.; Behan, R. K.; Krest, C. M.; Onderko, E. L.; Langston, M. C.; Green, M. T., Setting an Upper Limit on the Myoglobin Iron(IV)Hydroxide pKa: Insight into Axial Ligand Tuning in Heme Protein Catalysis. *Journal of the American Chemical Society* **2014,** *136* (25), 9124-9131.

50. Behan, R. K.; Green, M. T., On the status of ferryl protonation. *Journal of Inorganic Biochemistry* **2006,** *100* (4), 448-459.

51. Stoian, S. A.; Xue, G.; Bominaar, E. L.; Que, L.; Münck, E., Spectroscopic and Theoretical Investigation of a Complex with an [O═Fe^{IV}–O–Fe^{IV}═O] Core Related to Methane

Monooxygenase Intermediate Q. *Journal of the American Chemical Society* **2014,** *136* (4), 1545-1558.

52. Hill, E. A.; Weitz, A. C.; Onderko, E.; Romero-Rivera, A.; Guo, Y.; Swart, M.; Bominaar, E. L.; Green, M. T.; Hendrich, M. P.; Lacy, D. C.; Borovik, A. S., Reactivity of an Fe^{IV}-Oxo Complex with Protons and Oxidants. *Journal of the American Chemical Society* **2016,** *138* (40), 13143-13146.

Chapter 6. Oxygen Atom Transfer Reactivity for a Series of Mn^{IV}-oxo Species Supported by a Tunable Pentadentate Ligand Scaffold

Temperature dependence data in this chapter were collected by Eleanor Stewart-Jones.

6.1 Introduction

High-valent metal-oxo species are common oxidants in both biological systems and synthetic oxidation catalysts.[1-3] To understand the factors controlling the reactivity of these intermediates in substrate oxidation, metal-oxo species can be formed in the absence of substrate to allow for characterization with spectroscopic techniques, and the use of kinetic studies can allow for the development of structure-function relationships. Specifically, biomimetic studies of Mn^{IV}-oxo species in hydrogen atom transfer (HAT) and oxygen atom transfer (OAT) reactions has provided insight into the factors that drive reactivity for this type of oxidant.[4-9]

For OAT reactions in particular, advances have been made in understanding how $[Mn^{IV}(O)(N4py)]^{2+}$ and $[Mn^{IV}(O)(Bn\text{-}TPEN)]^{2+}$ facilitate the sufloxidation of thioanisole.[10-11] Upon the addition of excess thioanisole to these intermediates in 2,2,2-trifluoroethanol (TFE), the electronic absorption bands corresponding to the Mn^{IV}-oxo species disappear, leading to the formation of Mn^{II} products, which have been characterized by electronic absorption and EPR methods.[10-11] Product analysis for $[Mn^{IV}(O)(N4py)]^{2+}$ following the reaction with thioanisole revealed conversion of the substrate to methyl phenyl sulfoxide in stoichiometric yield compared to the starting Mn concentration.[11] Taken together, these results support a two-electron process for the sulfoxidation of thioanisole by these high-valent Mn^{IV}-oxo centers (Scheme 6.1). Further mechanistic understanding of the reactions for both $[Mn^{IV}(O)(Bn\text{-}TPEN)]^{2+}$ and $[Mn^{IV}(O)(N4py)]^{2+}$ was achieved by conducting a Hammett analysis with *para*-substituted thioanisole derivatives. These analyses yielding ρ values of -4.4 and -4.6, for $[Mn^{IV}(O)(Bn\text{-}TPEN)]^{2+}$ and $[Mn^{IV}(O)(N4py)]^{2+}$, respectively.[10-11] Thus, as the electron-withdrawing ability of the thioanisole substituent increased, a corresponding decrease in reaction rate was observed. This is consistent with the electrophilic character of the Mn^{IV}-oxo species.[10-11]

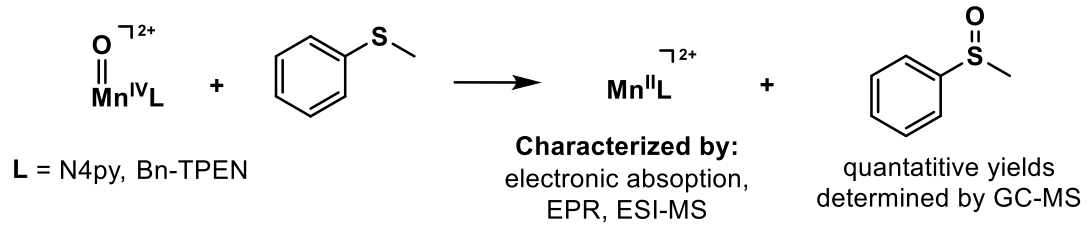

Scheme 6.1. Reaction of Mn^{IV}-oxo complexes with thioanisole.

Additional work for $[Mn^{IV}(O)(N4py)]^{2+}$ and $[Mn^{IV}(O)(Bn\text{-}TPEN)]^{2+}$ showed remarkable OAT rate enhancements of ca.10^7-fold in the presence of Lewis and Bronsted acids.[8, 10-11] Beyond altering the reactivity, the addition of these acids shifts the $Mn^{IV/III}$ reduction potentials to more positive values. Reduction potentials for $[Mn^{IV}(O)(N4py)]^{2+}$ and $[Mn^{IV}(O)(Bn\text{-}TPEN)]^{2+}$ shift from 0.80 V and 0.78 V to 1.42 V and 1.36 V, respectively, upon the addition of excess scandium (III) triflate.[11] Nam *et al.* postulate that the large OAT rate enhancement of Mn^{IV}-oxo centers in the presence acids is due to a change in sulfoxidation mechanism from a direct oxygen atom transfer (DOT) pathway to an electron transfer (ET) pathway (Figure 6.1).[8, 10-11]

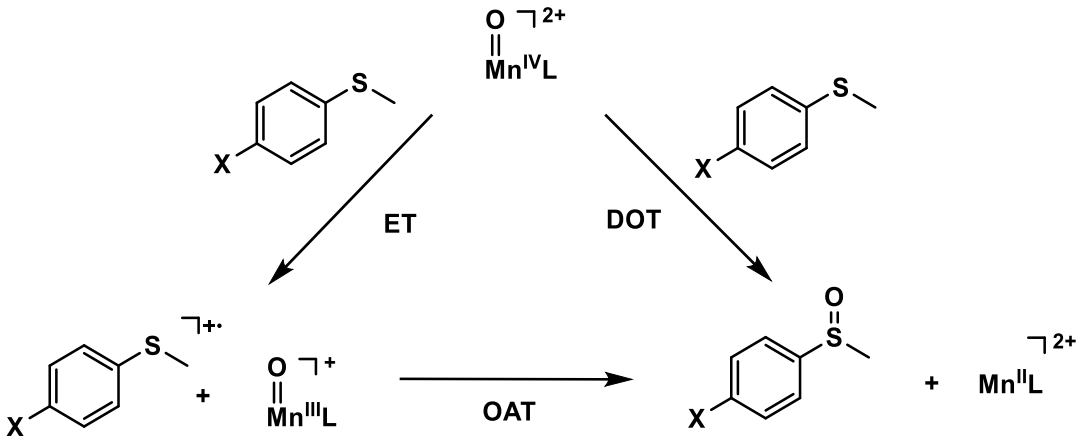

Figure 6.1. Proposed mechanistic pathways for the sulfoxidation of thioanisole derivatives by Mn^{IV}-oxo species.

Recently, density functional theory (DFT) calculations for $[Mn^{IV}(O)(N4py)]^{2+}$ predicted that, even for a direct OAT mechanism, the landscape was complicated by the involvement of multiple electronic states.[12] Similar complexity in oxidation reactions by Mn^{IV}-oxo adducts was first postulated for HAT reactions, where a low-lying ^4E excited state is predicted to cross with the $^4B_1$ ground state along the reaction coordinate.[13] The reaction of $[Mn^{IV}(O)(N4py)]^{2+}$ with thioanisole was also proposed to include a crossing of the ^4E excited state with the $^4B_1$ ground state, resulting in a lower energy barrier (Figure 6.2). However, the OAT reaction (Scheme 6.1) requires that the system undergo a spin-state crossing from Mn^{IV}-oxo (S = 3/2) to the Mn^{II} (S = 5/2) product (Figure 6.2). In the absence of any state crossing, the $^4B_1$ ground state has a calculated transition state barrier of 25 kcal/mol ($^4B_{1,TS}$, Figure 6.2). The corresponding transition state on the ^4E pathway has a lower barrier of 18.5 kcal/mol ($^4E_{TS}$, Figure 6.2). From either of these two transition states, a spin flip must occur to give the high-spin Mn^{II} (S = 5/2) product. Alternatively, a minimum energy crossing point between the ^4E state and a sextet state was predicted prior to the ^4E transition state ($^6\Gamma$, Figure 6.2).[12] Thus, depending on the spin flip barrier, the minimum energy crossing point could offer the lowest barrier at 15.2 kcal/mol ($^6\Gamma$-$^4E_{MECP}$, Figure 6.2). After this crossing, the $^6\Gamma$ state converts barrierlessly to the product. The k_2 value reported for the reaction of $[Mn^{IV}(O)(N4py)]^{2+}$ with thioanisole corresponds to a free energy barrier ($\Delta G^{\ddagger}$) of 18.5 kcal/mol at 273 K, which is in reasonable agreement with both the MECP barrier and the ^4E transition state energies. However, the DFT calculations rely on the electronic energy ($\Delta E^{\ddagger}$); thus, zero-point energies, dispersion energies, and entropic contributions were not considered (these terms were presumed to cancel, such that $\Delta E^{\ddagger} \approx \Delta G^{\ddagger}$).[12]

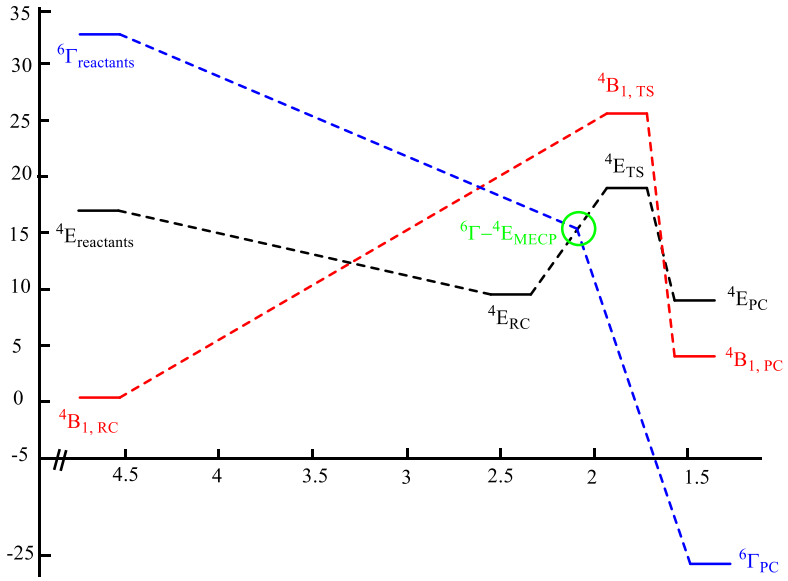

Figure 6.2. Simplified reaction energy profile for thioanisole sulfoxidation by $[Mn^{IV}(O)(N4py)]^{2+}$.

To understand the mechanism of OAT by Mn^{IV}-oxo species, our group introduced equatorial ligand perturbations to the N4py scaffold that directly modulate the ^4E excitation energy and the $Mn^{IV/III}$ reduction potential.[14-15] A weakening of the equatorial field lowers the ^4E energy, which correlates with faster reactivity for both HAT and OAT reactions.[14-15] Specifically, kinetic studies of thioanisole oxidation by $[Mn^{IV}(O)(2pyN2Q)]^{2+}$, $[Mn^{IV}(O)(N4py)]^{2+}$, $[Mn^{IV}(O)(^{DMM}N4py)]^{2+}$, and $[Mn^{IV}(O)(2pyN2B]^{2+}$ allowed for the correlation of $\log(k_2)$ to the ^4E excitation energy (Figure 6.3, bottom left). While this result is consistent with a multi-state reactivity pathway involving the ^4E state, a modest correlation was also obtained between $\log(k_2)$ and the reduction potential (Figure 6.3, bottom right). This result suggests that tuning of the equatorial field can alter several parameters, not only the energy of the ^4E state.

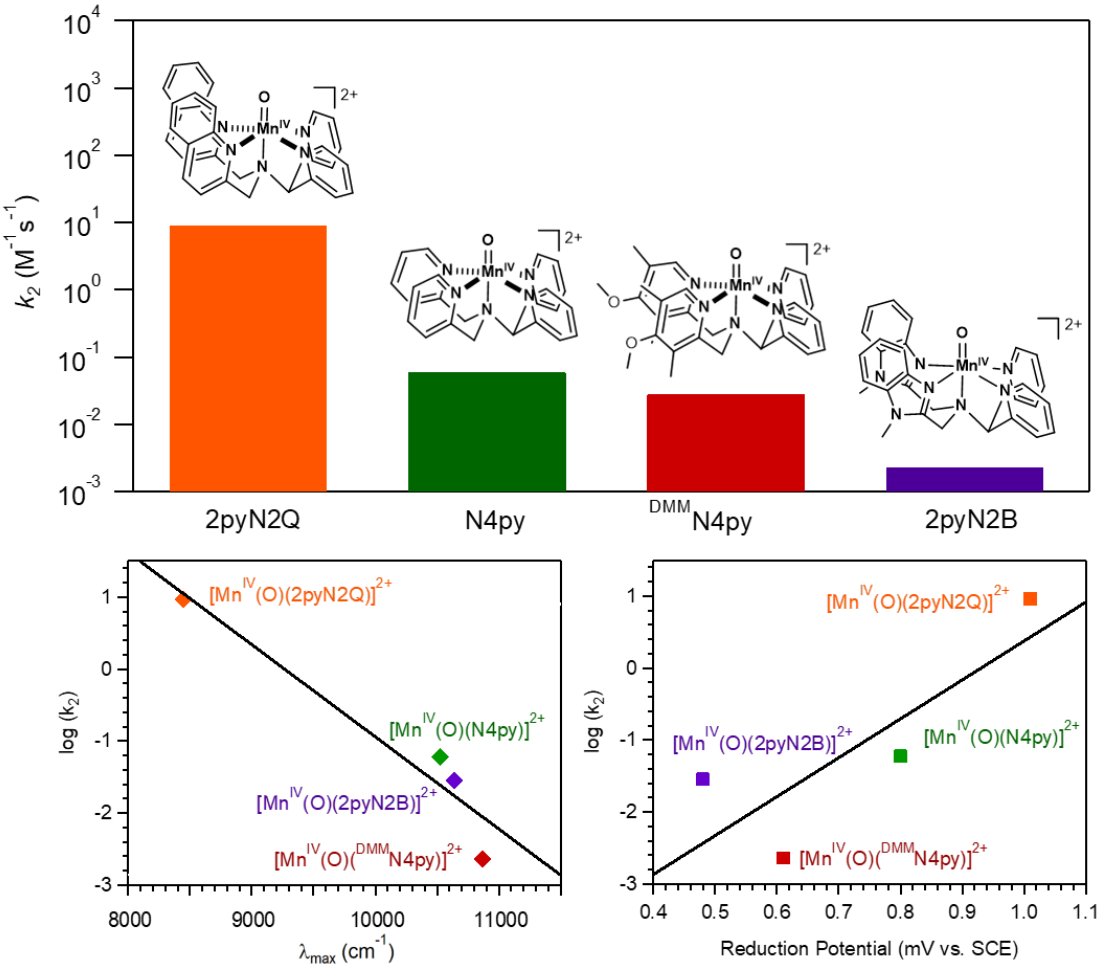

Figure 6.3. Top: Comparison of the rates of reaction of thioanisole with Mn^{IV}-oxo species supported by N4py and its derivatives. Bottom: Plots of experimental log(k_2) values for thioanisole oxidation (OAT) by Mn^{IV}-oxo complexes versus near-IR electronic absorption band maxima (left) and $Mn^{III/IV}$ reduction potentials (right)

To better understand the steric and electronic factors controlling the reactivity of Mn^{IV}-oxo species in OAT reactions, we used temperature-dependent kinetics to obtain activation parameters for thioanisole oxidation by a series of Mn^{IV}-oxo complexes, including $[Mn^{IV}(O)(2pyN2Q)]^{2+}$, $[Mn^{IV}(O)(N4py)]^{2+}$, $[Mn^{IV}(O)(2pyN2B)]^{2+}$, and $[Mn^{IV}(O)(^{DMM}N4py)]^{2+}$ These data are directly compared to computationally predicted energy barriers to gain insight into the OAT reaction landscape of Mn^{IV}-oxo species. Additionally, we establish the electrophilic character of this series through kinetic studies with *para*-substituted thioanisole derivatives. The OAT reactivity of

$[Mn^{IV}(O)(2pyN2Q)]^{2+}$ with further investigated with styrene to expand the scope of the oxidation reactions to epoxidation. Finally, cylcohexene and cyclooctene were investigated to gain insight into the chemoselectivity of $[Mn^{IV}(O)(2pyN2Q)]^{2+}$ for olefin substrates where both allylic C–H bond oxidation and C=C epoxidation are possible.

6.2 Experimental Methods

Materials and Instrumentation. All solvents and chemicals were purchased from commercial vendors and were used as received. Iodosobenzene (PhIO) was prepared from iodosobenzene diacetate following a published procedure.[16] Electronic absorption spectra for the kinetic reactions were obtained using a Cary 50 Bio or an Agilent 8453 spectrophotometer. The spectrophotometers were interfaced with either a Unisoku cryostat (USP-203-A) or a Quantum Northwest cryostat (t2 Sport).

Synthesis and Characterization. The 2pyN2Q, N4py, 2pyN2B and ^{DMM}N4py ligands and corresponding Mn^{II} species were synthesized according to previously published methods.[14-15, 17-22] $[Mn^{IV}(O)(2pyN2Q)]^{2+}$, $[Mn^{IV}(O)(N4py)]^{2+}$ $[Mn^{IV}(O)(2pyN2B)]^{2+}$ and $[Mn^{IV}(O)(^{DMM}N4py)]^{2+}$ were all prepared *in situ* by reacting the corresponding Mn^{II} species with 10, 2.5, 10, and 1.2 equivalents of iodosobenzene (PhIO), respectively, in 2,2,2-trifluoroethanol (TFE) at 25°C.

Reactivity with Thioanisole Derivatives. In a typical reaction, a solution of the appropriate Mn^{II} complex was dissolved in 1 mL TFE, transferred to a cuvette, and placed in a temperature-controlled cryostat at 25°C. Excess PhIO was dissolved in 1 mL TFE, and was added to the cuvette to give a final solution concentration of 1 mM. Formation of the Mn^{IV}-oxo complex was monitored by electronic absorption spectroscopy. Upon full formation (determined by comparing maximum formation of the near-IR feature associated with each Mn^{IV}-oxo complex to

its published extinction coefficient[14-15]), an aliquot of a solution (100 μL or 200 μL) containing thioanisole or a derivative in TFE (thioanisole, 4-fluorothioanisole) or CH_2Cl_2 (4-methoxythioanisole, 4-bromothioanisole) was added to the cuvette. Substrate concentrations were at least 10-fold excess compared to Mn concentration to maintain pseudo-first order conditions. The decay of each Mn^{IV}-oxo species was followed by monitoring the near-IR electronic absorption feature, and the resulting time trace was fit to a pseudo-first order model to at least three half-lives to yield pseudo-first order rate constants, k_{obs}. For each substrate, k_{obs} values were determined at a range of substrate concentrations. Linear fits obtained from the plots of k_{obs} versus the substrate concentration yielded second order rate constants (k_2). Because of the slow reactivity of $[Mn^{IV}(O)(^{DMM}N4py)]^{2+}$, the initial rate approximation was applied (using 20% of initial disappearance of the near-IR peak). The initial rates given in AU/s were converted to s^{-1} by using the initial concentration of manganese (1.0 mM) and the extinction coefficient for $[Mn^{IV}(O)^{DMM}N4py]^{2+}$ (290 $M^{-1}cm^{-1}$). The observed rate constants were plotted against substrate concentration to obtain second-order rate constants, and the concentration of substrate was corrected to the final total volume.

Activation Parameters for Thioanisole Oxidation. Kinetic studies were performed as described in the previous section, but a 100 μL aliquot of a TFE solution containing 40 equivalents of thioanisole was added to each reaction at varied, fixed temperatures. The addition of thioanisole led to the disappearance of the near-IR feature for each Mn^{IV}-oxo complex, and this disappearance was fit to a pseudo-first-order model to at least three half-lives. Each reaction was repeated in duplicate, and each complex was investigated at 4 different temperature points in the range of -15°C to 65°C. An Eyring analysis was performed by plotting $\ln(k_{obs}/T)$ versus 1/T (where temperature is in Kelvin), and the linear correlation was used to calculate $\Delta H^{\ddagger}$ and $\Delta S^{\ddagger}$.

$[Mn^{IV}(O)(2pyN2Q)]^{2+}$ Reactivity with Cyclohexene. To a 1.0 mM solution of $[Mn^{IV}(O)(2pyN2Q)]^{2+}$, varying amounts of cyclohexene (0.01 M – 0.04 M) in 100 μL of MeCN were added. The addition of cyclohexene led to the disappearance of the near-IR absorption feature for $[Mn^{IV}(O)(2pyN2Q)]^{2+}$, which was fit to a pseudo-first-order model to at least three half-lives to obtain k_{obs} values. Each reaction was repeated in duplicate. Plots of k_{obs} versus cyclohexene concentration yielded a k_2 value. Because of concerns regarding a reaction between $[Mn^{IV}(O)(2pyN2Q)]^{2+}$ and MeCN, kinetic experiments for $[Mn^{IV}(O)(2pyN2Q)]^{2+}$ were repeated with CH_2Cl_2 to dissolve substrate, which yielded a similar k_2 value. Additionally, a k_{obs} value was determined for the addition of 200 μL MeCN (~1740 equivalents) to $[Mn^{IV}(O)(2pyN2Q)]^{2+}$. Following the reaction of $[Mn^{IV}(O)(2pyN2Q)]^{2+}$ with 20 equivalents cyclohexene, the reaction was run through a silica plug with excess EtOAc, and the resulting solution was analyzed by gas-chromatography mass spectrometry.

Reactivity of Mn^{IV}-oxo species with Styrene, Cyclooctene, and Triphenylphosphine. To a 1.0 mM solution of $[Mn^{IV}(O)(2pyN2Q)]^{2+}$ in 100% TFE at 25°C, varying amounts of excess substrate (styrene and cyclooctene) were added. To a 1.0 mM solution of $[Mn^{IV}(O)(^{DMM}N4py)]^{2+}$ in TFE at 25°C, excess triphenylphosphine (PPh_3) was added. Substrate concentrations were as follows: styrene in TFE (0.02 M – 0.08 M), cyclooctene in CH_2Cl_2 (0.02 M – 0.08 M), PPh_3 in MeCN (0.01 M). The decay of the corresponding Mn^{IV}-oxo species was followed by monitoring the near-IR absorption feature, and the resulting time trace was fit to a pseudo-first order model to at least three half-lives. Each reaction was repeated in duplicate. For the reactions of $[Mn^{IV}(O)(2pyN2Q)]^{2+}$ with cyclohexene and cylcooctene, plots of k_{obs} versus substrate concentration yielded k_2 values. For $[Mn^{IV}(O)(^{DMM}N4py)]^{2+}$ and PPh_3, the k_{obs} was determined at a single concentration.

6.3 Results and Discussion

Activation Parameters for Reaction of Mn^{IV}-oxo with Thioanisole. An Eyring analysis of temperature dependence of pseudo-first order decay kinetics for $[Mn^{IV}(O)(^{DMM}N4py)]^{2+}$, $[Mn^{IV}(O)(N4py)]^{2+}$, $[Mn^{IV}(O)(2pyN2Q)]^{2+}$, and $[Mn^{IV}(O)(2pyN2B)]^{2+}$ allowed for the determination of experimental activation parameters. Each of these Mn^{IV}-oxo species exhibits a characteristic absorption feature in the near-IR region that decayed by a pseudo-first order process upon the addition of 40 equivalents thioanisole. The decay of each Mn^{IV}-oxo species was fit to give pseudo-first order rate constants (k_{obs}). The decay of each Mn^{IV}-oxo species was monitored for a range of temperatures between -15°C to 65°C, and plots of $\ln(k_{obs}/T)$ versus 1/T yielded linear correlations (Figure 6.4). Upon performing an Eyring analysis for each data set, experimental activation parameters $\Delta H^{\ddagger}$ and $\Delta S^{\ddagger}$ were obtained. The activation free energy ($\Delta G^{\ddagger}$), as well as the entropic contribution to the free energy ($T\Delta S^{\ddagger}$), was calculated for each complex at 298 K (Table 6.1).[15]

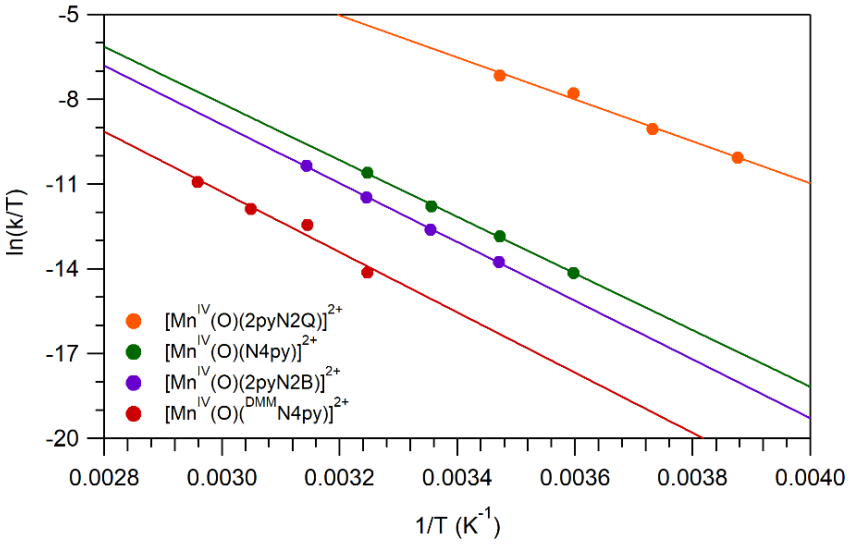

Figure 6.4. Plots of $\ln(k_{obs}/T)$ versus 1/T (K^{-1}) for the reaction of Mn^{IV}-oxo species and thioansiole. The lines show best fits to the Eyring equation.

Table 6.1. Rates and Activation Parameters for the Reactions of Several Mn^{IV}-oxo Complexes with Thioanisole.

Complex	k_2 ($M^{-1}s^{-1}$)	$\Delta G^{\ddagger}$ (kcal/mol)	$\Delta H^{\ddagger}$ (kcal/mol)	$T\Delta S^{\ddagger}$ (kcal/mol)
$[Mn^{IV}(O)(2pyN2Q)]^{2+}$	9.2(9)	17.7	14.7	-3.0
$[Mn^{IV}(O)(N4py)]^{2+}$	0.060(3)	21.0	19.9	-1.1
$[Mn^{IV}(O)(2pyN2B)]^{2+}$	0.028(3)	21.5	20.7	-0.9
$[Mn^{IV}(O)(^{DMM}N4py)]^{2+}$	0.0023(4)	23.0	21.2	-1.8

*$\Delta G^{\ddagger}$ and $T\Delta S^{\ddagger}$ were determined at 298 K

Previously, we reported k_2 values for the sulfoxidation of thioanisole by this series of Mn^{IV}-oxo complexes (Figure 6.3 and Table 6.1)[14-15] The trend in reactivity correlates well with the range of experimentally determined $\Delta G^{\ddagger}$ values (17.7 kcal/mol for $[Mn^{IV}(O)(2pyN2Q)]^{2+}$ to 23.0 kcal/mol for $[Mn^{IV}(O)(^{DMM}N4py)]^{2+}$, see Table 6.1). Our Eyring analysis shows that these variations in $\Delta G^{\ddagger}$ arise directly from changes in $\Delta H^{\ddagger}$ (Table 6.1). For each complex, the $T\Delta S^{\ddagger}$ contribution for these reactions at 298 K for each complex is small, further signifying that the $\Delta H^{\ddagger}$ barrier drives the previously reported trend in reactivity. While it is interesting to note that the largest $T\Delta S^{\ddagger}$ contribution was observed for the most sterically encumbered Mn^{IV}-oxo adduct, $[Mn^{IV}(O)(2pyN2Q)]^{2+}$, the net variations in $\Delta S^{\ddagger}$ are quite modest.

To date, there are limited examples of experimental activation parameters for sulfoxidation by Mn-oxo species. There are a few examples for Mn^{V}-oxo species, including the sulfoxidation of dibutyl sulfide by $Mn^{V}(O)(TDCPP)$[23] and the sulfoxdiation of 4-(methylthio)aniline by $[Mn^{V}(O)(TBP_8Cz)]$.[24] Regarding Mn^{IV}-oxo species, the closest comparison to the present system comes from Nam *et al.*, who investigated the oxidation of 4-(methylthio)benzonitrile by $[Mn^{IV}(O)(N4py)]^{2+}$ in the presence of 60 equivalents HOTf.[8] Activation parameters of $\Delta H^{\ddagger}$ = 15.1 kcal/mol and $\Delta S^{\ddagger}$ = -1.2 cal/mol·K ($T\Delta S^{\ddagger}$ = -0.4 kcal/mol at 298 K) were determined for this reaction. Nam and co-workers postulate that the small activation entropy ($\Delta S^{\ddagger}$ = -1.2 cal/mol·K) indicates an outer-sphere electron-transfer reaction, rather than a direct OAT mechanism.[25-26]

However, because the entropic contribution observed for $[Mn^{IV}(O)(N4py)]^{2+}$ in the presence of 60 equivalents HOTf is similar to that observed for $[Mn^{IV}(O)(N4py)]^{2+}$ here (which has been previously proposed by Nam *et al.* to follow an oxygen atom transfer mechanism),[8] the small $\Delta S^{\ddagger}$ may not be conclusive evidence for an electron transfer process.

Reactivity of Mn^{IV}-oxo Complexes with Thioanisole Derivatives. The reactivity of $[Mn^{IV}(O)(2pyN2Q)]^{2+}$, $[Mn^{IV}(O)(N4py)]^{2+}$, and $[Mn^{IV}(O)(^{DMM}N4py)]^{2+}$ with *para*-substituted thioanisole derivatives at 298 K was conducted to establish the electrophilic nature for this series. Upon the addition of 4-bromothioanisole, 4-fluorothioanisole and 4-methoxythioanisole to 1.0 mM solutions of the Mn^{IV}-oxo species, k_{obs} values were found to correlate to substrate concentration, allowing for the determination of k_2 values (Figure 6.5).

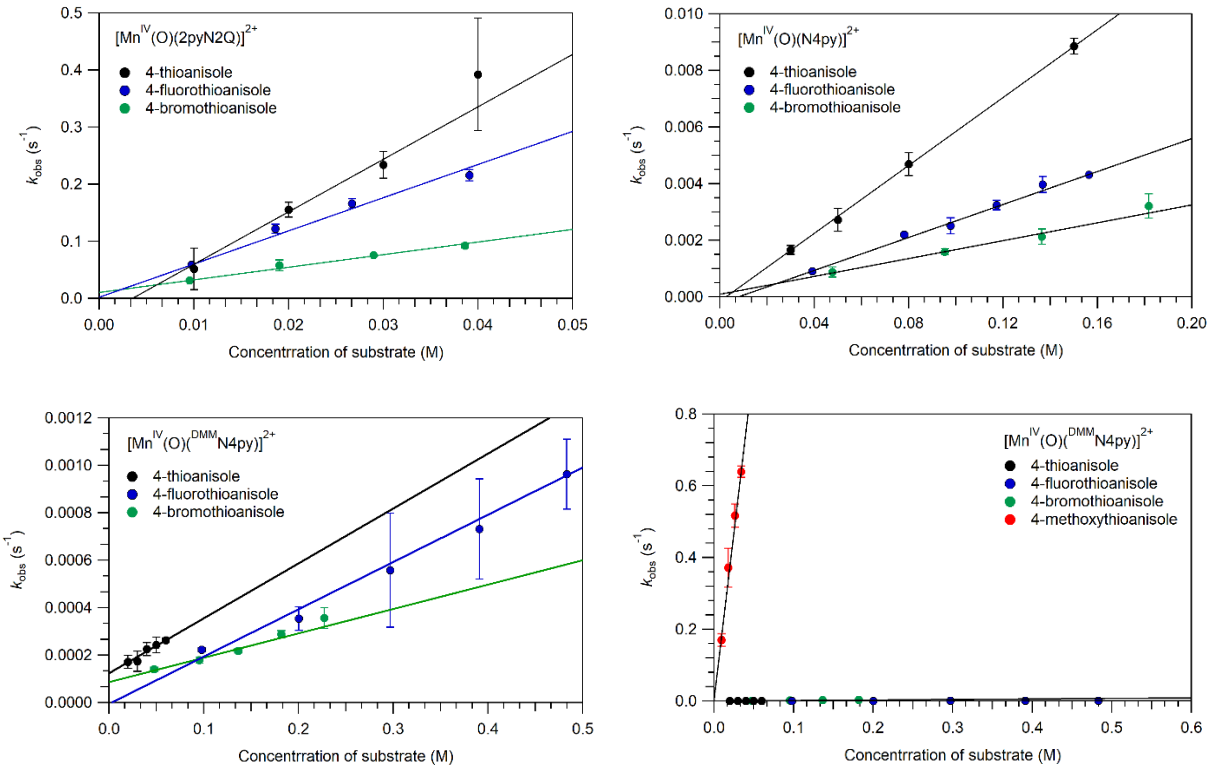

Figure 6.5. Plots of observed rates (k_{obs}) versus substrate concentration for $[Mn^{IV}(O)(2pyN2Q)]^{2+}$ (top left), $[Mn^{IV}(O)(N4py)]^{2+}$ (top right) and $[Mn^{IV}(O)(^{DMM}N4py)]^{2+}$ (bottom left = zoomed in, bottom right = full plot). Thioanisole data was previously reported.[15]

When log(k_2) was plotted against the σ_p values for each *para*-substituted thioanisole species, a negative ρ value was obtained for each complex. Specifically, $[Mn^{IV}(O)(2pyN2Q)]^{2+}$, $[Mn^{IV}(O)(N4py)]^{2+}$, and $[Mn^{IV}(O)(^{DMM}N4py)]^{2+}$ exhibit ρ values of -2.6(2), -2.3(7) and -2.66(3) (Figure 6.6). Because these numbers are so similar to one another, it can be postulated that these Mn^{IV}-oxo complexes oxidize these substrates by a direct OAT mechanism. Previously, Nam and co-workers conducted a Hammett analysis with *para*-substituted thioanisole derivatives for $[Mn^{IV}(O)(N4py)]^{2+}$ at 273 K, which exhibited a ρ value of -4.6, similar to what we observe here at 298 K (-2.7).[8] Additionally, the electron-tranfser driving force dependence of log(k_2) for the sulfoxidation thioanisole derivatives by $[Mn^{IV}(O)(N4py)]^{2+}$ showed a large deviation from that expected of an electron transfer process, suggesting the mechanism follows a direct OAT mechanism (Figure 6.1).[8]

It is interesting to note, that, upon the inclusion of the reaction rate of $[Mn^{IV}(O)(^{DMM}N4py)]^{2+}$ with 4-methoxythioanisole, this point is found to fall very far off the line for this complex. Unfortunately, this substrate could only be investigated for $[Mn^{IV}(O)(^{DMM}N4py)]^{2+}$, because the other complexes exhibited reaction rates that were too fast to monitor with our equipment. The point falling so far off the line may suggest a change in mechanism for oxidation of 4-methoxythioanisole by $[Mn^{IV}(O)(^{DMM}N4py)]^{2+}$. Thioanisole and and 4-methoxythioanisole exhibit reduction potentials of 1.18 V and 1.37 V (vs. SCE at 0°C in 19:1 TFE:MeCN)[11] respectively. Thus, the more easily oxidized substrate, 4-methoxythioanisole, may readily undergo a rate-determining electron transfer step that is followed by a fast oxygen atom transfer step (Figure 6.1).

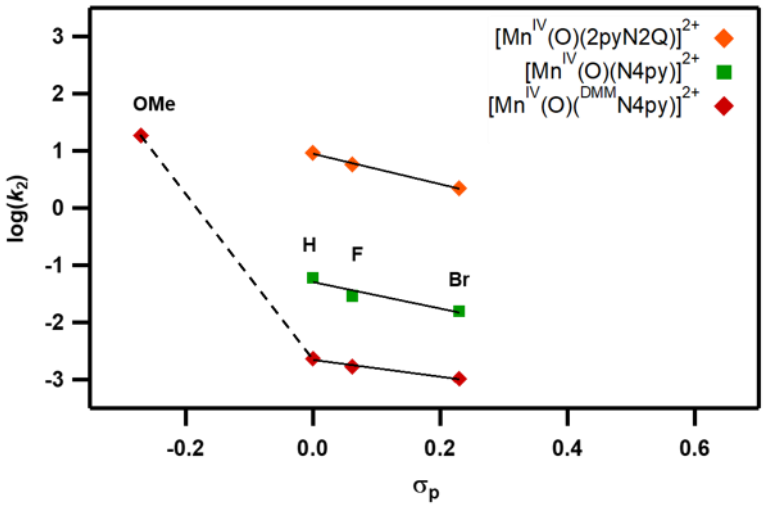

Figure 6.6. Hammett plot of log(k_2) for thioanisole oxidation plotted against the σ_p values for each thioanisole derivative.

Reactivity of $[Mn^{IV}(O)(^{DMM}N4py)]^{2+}$ with Triphenylphosphine. To investigate if the trends in the sulfoxidation of thioanisole observed for this series of Mn^{IV}-oxo species hold true for other OAT reactions, we attempted to use triphenylphosphine (PPh_3) as a substrate. Upon the addition of excess PPh_3 to $[Mn^{IV}(O)(^{DMM}N4py)]^{2+}$, electronic absorption spectrum changed within 0.5 seconds to give that of the corresponding Mn^{II}-species (Figure 6.7). These spectral changes suggest a two-electron oxidation of the substrate. Unfortunately, even with the slowest complex of the series, $[Mn^{IV}(O)(^{DMM}N4py)]^{2+}$, and only 10 equivalents of substrate, the reaction was complete in less than 0.5 seconds, thwarting any further kinetic investigation with this substrate.

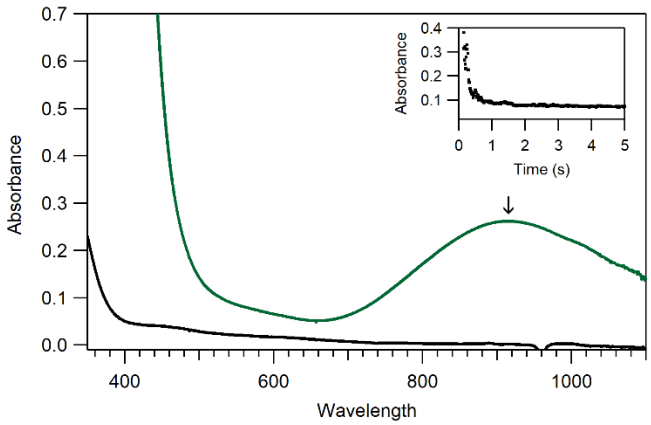

Figure 6.7. Reaction of 1.0 mM $[Mn^{IV}(O)(^{DMM}N4py)]^{2+}$ in TFE following the addition of 10 equivalents of PPh_3. Inset: decay of the feature at 920 nm over time.

Reactivity of $[Mn^{IV}(O)(2pyN2Q)]^{2+}$ with Olefins. To further probe the scope of reactivity for this series of Mn^{IV}-oxo species, several OAT substrates, including styrene, cyclohexene, and cyclooctene were investigated for $[Mn^{IV}(O)(2pyN2Q)]^{2+}$. Upon the addition of varied amounts of styrene to a 1.0 mM solution of $[Mn^{IV}(O)(2pyN2Q)]^{2+}$, the near-IR absorption feature decayed (Figure 6.8, left), and a plot of k_{obs} versus substrate concentration yielded a k_2 value of 0.7(1) M^{-1} s^{-1} (Figure 6.8, right). In contrast, the reactivity of $[Mn^{IV}(O)(^{DMM}N4py)]^{2+}$ with styrene exhibited very sluggish reactivity even upon the addition of 500 equivalents of styrene. As for $[Mn^{IV}(O)(N4py)]^{2+}$, the epoxidation of styrene was previously reported in TFE/MeCN (1:1) at 273 K to yield a k_2 of 3.3(3) x 10^{-4} M^{-1} s^{-1}.

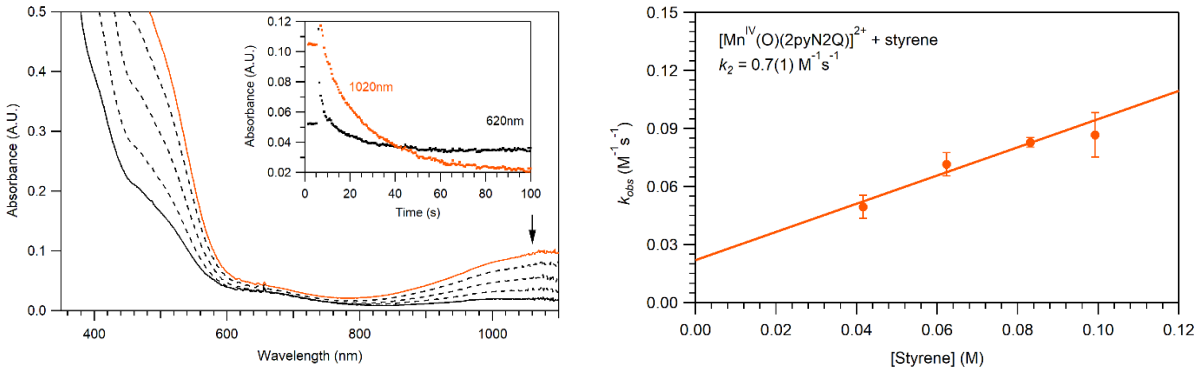

Figure 6.8. Left: Reaction of 1.0 mM $[Mn^{IV}(O)(2pyN2Q)]^{2+}$ with 45 equivalents of styrene in TFE. Inset: decay of the feature at 1020 nm over time, minimal change observed at 620 nm. Right: Plot of the pseudo-first order rate constants (k_{obs}) against the concentration of styrene.

The reactivity of $[Mn^{IV}(O)(2pyN2Q)]^{2+}$ with cylcohexene and cyclooctene was investigated. These substrates can be oxidized through the epoxidation of the C=C double bond, or through abstraction of the allylic C–H bond (Scheme 6.2, top). These substrates allow for the investigation of the chemoselectivity in the allylic oxidation of olefins. Upon the addition of excess cyclohexene dissolved in MeCN to a 1.0 mM solution of $[Mn^{IV}(O)(2pyN2Q)]^{2+}$ in TFE, the near-IR feature associated with the Mn^{IV}-oxo species disappeared (Figure 6.9, top). The k_{obs} values were found to be linearly dependent on substrate concentration, yielding a k_2 value of 0.46(1) M^{-1} s^{-1} (Figure 6.9, bottom left). However, it was later discovered that $[Mn^{IV}(O)(2pyN2Q)]^{2+}$ reacts with 200 μL of neat MeCN with a k_{obs} of 1.96×10^{-3} s^{-1} (Figure 6.10). To ensure the reaction between $[Mn^{IV}(O)(2pyN2Q)]^{2+}$ and solvent did not complicate the kinetic profile, the same kinetic investigation was performed, but with cyclohexene dissolved in CH_2Cl_2. These reactions yielded a k_2 of 0.52(3) M^{-1} s^{-1} (Figure 6.9, right), which is nearly identical to the k_2 determined with MeCN, suggesting substrate oxidation is faster than the self-decay in the 20:1 TFE/MeCN solvent mix. Spectral changes for electronic absorption for the reaction of $[Mn^{IV}(O)(2pyN2Q)]^{2+}$ suggest that allylic oxidation is the dominant process. Specifically, the Mn^{IV}-oxo features decay to give a new

intermediate with features at 500 nm and 620 nm, which is reminiscent of the Mn^{III}-OH species commonly seen for this complex following the reaction with HAT substrates.[15] It is clear that the decay of the feature at 1020 nm is related to the growth of the feature of 620 nm, as they exhibit similar k_{obs} values (Figure 6.9, top, inset). Following the reaction of 1.0 mM $[Mn^{IV}(O)(2pyN2Q)]^{2+}$ with 20 equivalents of cyclohexene, the reaction was run through a silica plug and analyzed by gas-chromatography to determine the organic products of the reaction. Based on the electronic absorption showing the fast formation of the Mn^{III}-product, this would suggest allylic oxidation occurring as the only oxidation reaction. However, a variety of products were observed, including epoxides. It is worth noting that the formation of $[Mn^{IV}(O)(2pyN2Q)]^{2+}$ is achieved with the use of 10 equivalents PhIO, which could lead to catalytic oxidation if the Mn^{IV}-oxo species is converted back to Mn^{II}. However, UV-Vis spectra suggest formation of a Mn^{III}-product, suggesting that there may be competing processes for olefin oxidation by $[Mn^{IV}(O)(2pyN2Q)]^{2+}$.

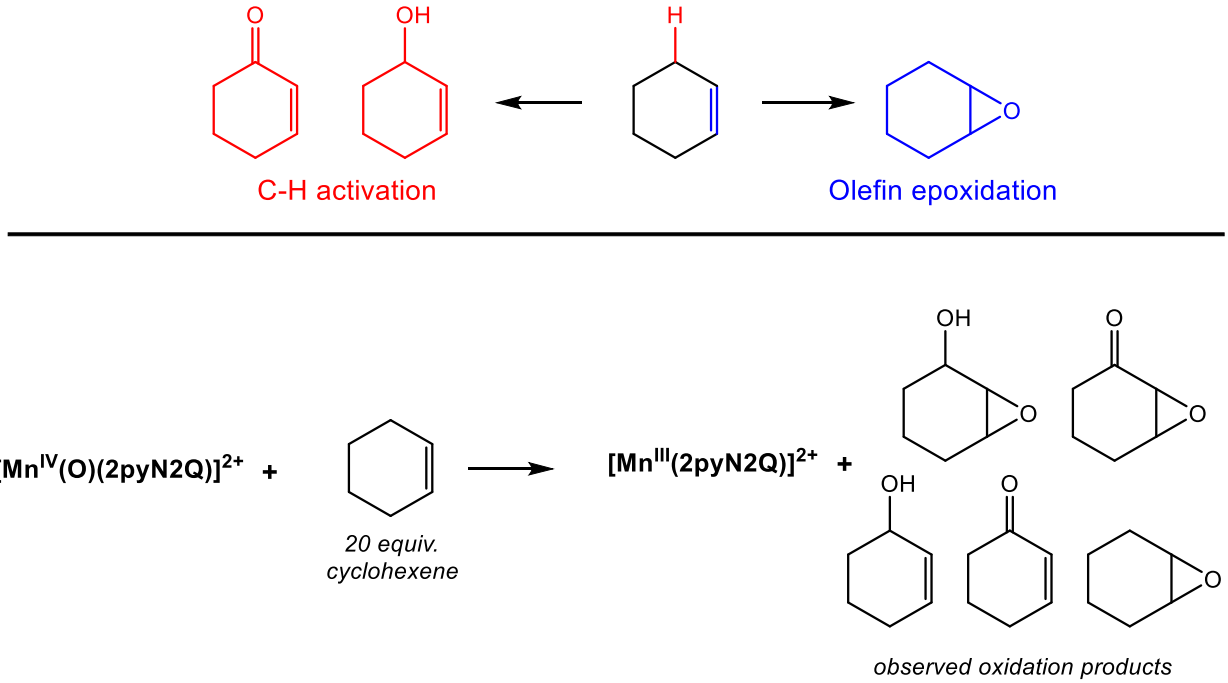

Scheme 6.2. Top: Chemoselective reactivity of cyclohexene, which is prone to olefin epoxidation and C–H bond activation. Bottom: Schematic representation of the reaction of 1.0 mM $[Mn^{IV}(O)(2pyN2Q)]^{2+}$ in TFE with 20 equivalents of cyclohexene.

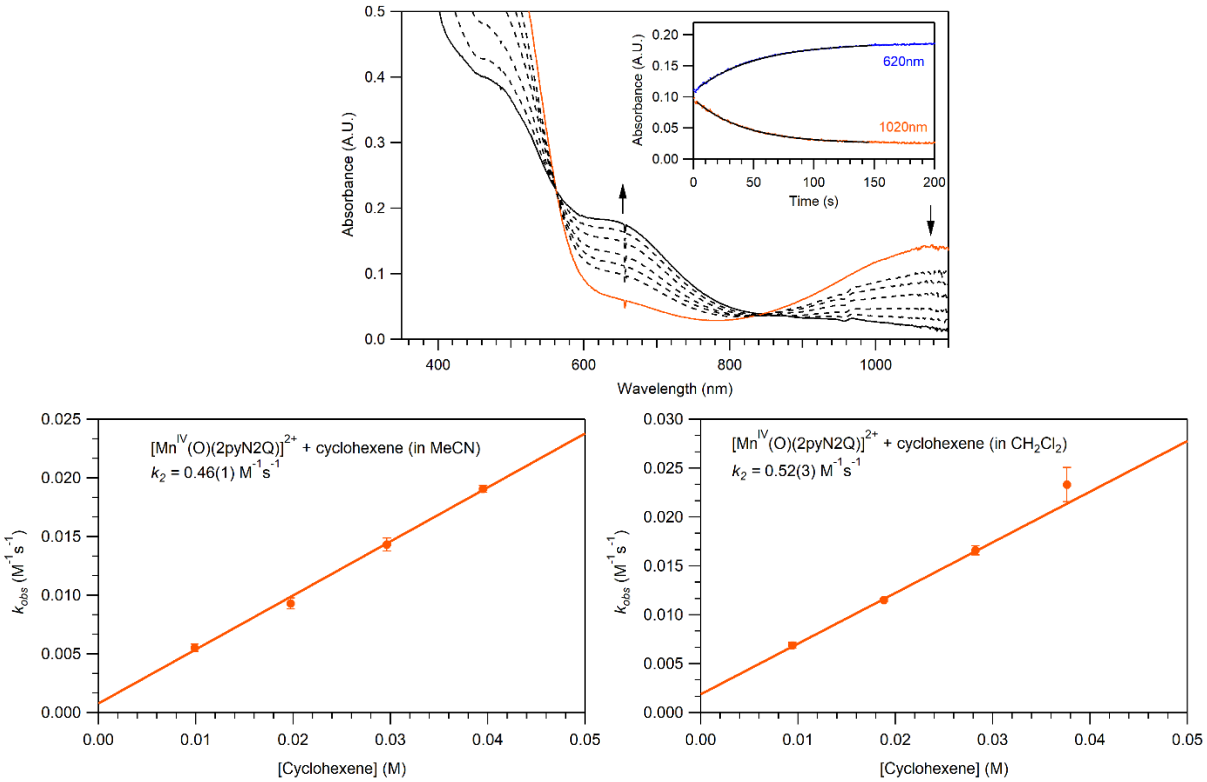

Figure 6.9. Top: Reaction of 1.0 mM $[Mn^{IV}(O)(2pyN2Q)]^{2+}$ with 40 equivalents of cylcohexene in TFE (cyclohexene dissolved in MeCN). Inset: decay of the feature at 1020 nm (k_{obs} = 0.024 s^{-1}) and the growth of the feature at 620 nm (k_{obs} = 0.021 s^{-1}). Bottom: Plots of the pseudo-first-order rate constants (k_{obs}) against substrate concentration for the reaction between $[Mn^{IV}(O)(2pyN2Q)]^{2+}$ and cyclohexene in TFE for substrate dissolved in MeCN (left) and CH_2Cl_2 (right).

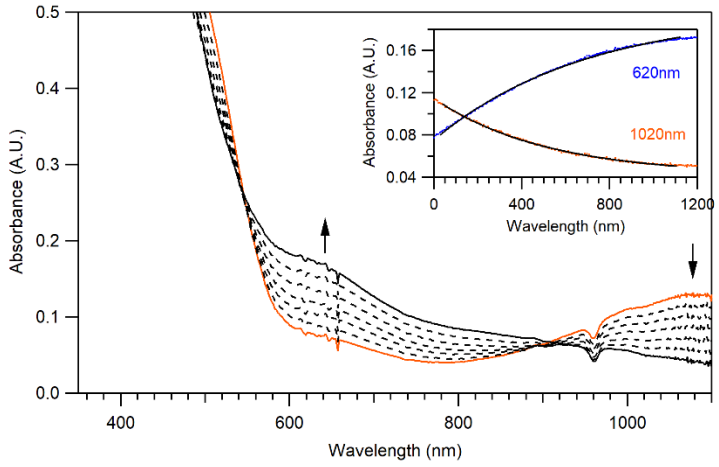

Figure 6.10. Electronic absorption spectra showing the reaction of 1.0 mM $[Mn^{IV}(O)(2pyN2Q)]^{2+}$ with 200µL MeCN (~1740 equivalents) in TFE at 25 °C. Inset: decay of the feature at 1020 nm (k_{obs} = 0.00196 M^{-1} s^{-1}) and the growth of the feature at 620 nm (k_{obs} = 0.001158 M^{-1} s^{-1}).

To further investigate the chemoselectivity of $[Mn^{IV}(O)(2pyN2Q)]^{2+}$ for allylic olefins, kinetic experiments with cycloocetene were performed. This substrate has a slightly stronger C–H bond compared to cyclohexene (83 kcal/mol and 80 kcal/mol, respectively).[27] Upon the addition of varied amounts of excess cyclooctene dissolved in CH_2Cl_2 to a 1.0 mM solution of $[Mn^{IV}(O)(2pyN2Q)]^{2+}$ in TFE, the near-IR feature at 1020 nm disappeared following pseudo-first order kinetics (Figure 6.11, left). Plots of k_{obs} values against substrate concentration yielded a k_2 value of 0.6(1) M^{-1} s^{-1} (Figure 6.11, right). Spectral changes to the UV-Vis suggest conversion of $[Mn^{IV}(O)(2pyN2Q)]^{2+}$ to the corresponding Mn^{II} complex. For the substrate cyclooctene, this rules out allylic oxidation and is suggestive of a two-electron process, presumably favoring epoxidation. However, the slow growth of the feature at 620 nm suggests that re-oxidation of the Mn^{II} center may allow for reformation of $[Mn^{IV}(O)(2pyN2Q)]^{2+}$, which may be able to perform allylic C–H bond activation in small amounts.

Taking cues from the electronic absorption spectra for the reaction of $[Mn^{IV}(O)(2pyN2Q)]^{2+}$ with cyclohexene and cyclooctene, very different mechanistic pathways are favored. In the case of cyclohexene, which has a BDFE of 80 kcal/mol, it seems $[Mn^{IV}(O)(2pyN2Q)]^{2+}$ selectively performs allylic C–H bond abstraction. In the case of cyclooctene, which has a slightly stronger C–H bond of 83 kcal/mol, epoxidation of the olefin is favored, thus signifying the chemoselectivity of $[Mn^{IV}(O)(2pyN2Q)]^{2+}$ for these two substrates. However, the products observed in the reaction of $[Mn^{IV}(O)(2pyN2Q)]^{2+}$ and cyclohexene suggest there may be a competing epoxidation product happening as well (Scheme 6.2).

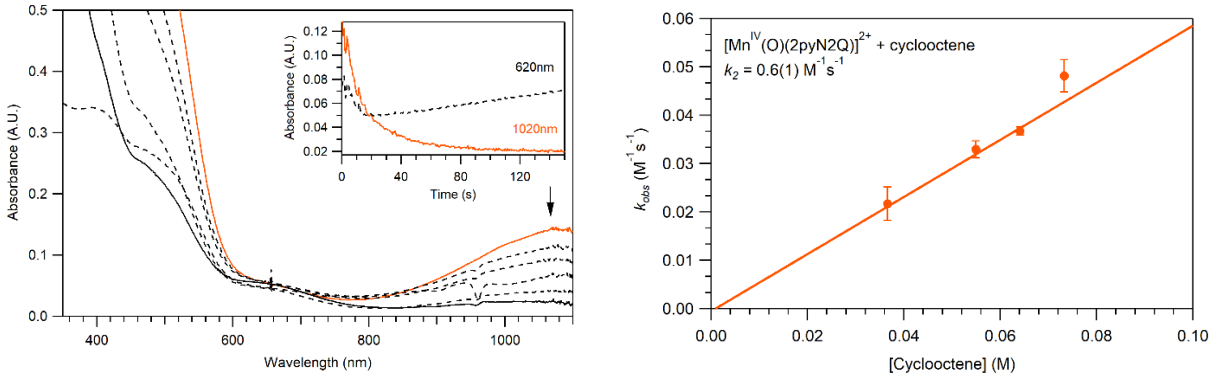

Figure 6.11. Left: Plots of the pseudo-first-order rate constants (k_{obs}) against substrate concentration for the reaction between $[Mn^{IV}(O)(2pyN2Q)]^{2+}$ and cyclooctene in TFE. Inset: decay of the feature at 920 nm and the minimal growth of the feature at 620 nm. Plots of the pseudo-first-order rate constants (k_{obs}) against substrate concentration for the reaction between $[Mn^{IV}(O)(2pyN2Q)]^{2+}$ and cyclooctene in TFE.

6.4 References

1. Ray, K.; Pfaff, F. F.; Wang, B.; Nam, W., Status of Reactive Non-Heme Metal–Oxygen Intermediates in Chemical and Enzymatic Reactions. *Journal of the American Chemical Society* **2014,** *136* (40), 13942-13958.

2. Neu, H. M.; Baglia, R. A.; Goldberg, D. P., A Balancing Act: Stability versus Reactivity of Mn(O) Complexes. *Acc. Chem. Res.* **2015,** *48* (10), 2754-2764.

3. Guo, M.; Corona, T.; Ray, K.; Nam, W., Heme and Nonheme High-Valent Iron and Manganese Oxo Cores in Biological and Abiological Oxidation Reactions. *ACS Central Science* **2019,** *5* (1), 13-28.

4. Rice, D. B.; Massie, A. A.; Jackson, T. A., Manganese–Oxygen Intermediates in O–O Bond Activation and Hydrogen-Atom Transfer Reactions. *Acc. Chem. Res.* **2017,** *50* (11), 2706-2717.

5. Liu, W.; Groves, J. T., Manganese Catalyzed C–H Halogenation. *Acc. Chem. Res.* **2015,** *48* (6), 1727-1735.

6. Yin, G.; Danby, A. M.; Kitko, D.; Carter, J. D.; Scheper, W. M.; Busch, D. H., Oxidative Reactivity Difference among the Metal Oxo and Metal Hydroxo Moieties: pH Dependent Hydrogen Abstraction by a Manganese(IV) Complex Having Two Hydroxide Ligands. *Journal of the American Chemical Society* **2008,** *130* (48), 16245-16253.

7. Garcia-Bosch, I.; Company, A.; Cady, C. W.; Styring, S.; Browne, W. R.; Ribas, X.; Costas, M., Evidence for a Precursor Complex in C–H Hydrogen Atom Transfer Reactions Mediated by a Manganese(IV) Oxo Complex. *Angew. Chem., Int. Ed. Engl.* **2011,** *50* (25), 5648-5653.

8. Chen, J.; Yoon, H.; Lee, Y.-M.; Seo, M. S.; Sarangi, R.; Fukuzumi, S.; Nam, W., Tuning the reactivity of mononuclear nonheme manganese(iv)-oxo complexes by triflic acid. *Chemical Science* **2015,** *6* (6), 3624-3632.

9. Jung, J.; Kim, S.; Lee, Y.-M.; Nam, W.; Fukuzumi, S., Switchover of the Mechanism between Electron Transfer and Hydrogen-Atom Transfer for a Protonated Manganese(IV)–Oxo Complex by Changing Only the Reaction Temperature. *Angew. Chem., Int. Ed. Engl.* **2016,** *55* (26), 7450-7454.

10. Wu, X.; Seo, M. S.; Davis, K. M.; Lee, Y.-M.; Chen, J.; Cho, K.-B.; Pushkar, Y. N.; Nam, W., A Highly Reactive Mononuclear Non-Heme Manganese(IV)–Oxo Complex That Can Activate the Strong C–H Bonds of Alkanes. *J. Am. Chem. Soc.* **2011,** *133* (50), 20088-20091.

11. Chen, J.; Lee, Y.-M.; Davis, K. M.; Wu, X.; Seo, M. S.; Cho, K.-B.; Yoon, H.; Park, Y. J.; Fukuzumi, S.; Pushkar, Y. N.; Nam, W., A Mononuclear Non-Heme Manganese(IV)–Oxo Complex Binding Redox-Inactive Metal Ions. *J. Am. Chem. Soc* **2013,** *135* (17), 6388-6391.

12. Chen, J.; Cho, K.-B.; Lee, Y.-M.; Kwon, Y. H.; Nam, W., Mononuclear nonheme iron(iv)–oxo and manganese(iv)–oxo complexes in oxidation reactions: experimental results prove theoretical prediction. *Chem. Commun.* **2015,** *51* (66), 13094-13097.

13. Cho, K.-B.; Shaik, S.; Nam, W., Theoretical Investigations into C–H Bond Activation Reaction by Nonheme $Mn^{IV}O$ Complexes: Multistate Reactivity with No Oxygen Rebound. *J. Phys. Chem. Lett.* **2012,** *3* (19), 2851-2856.

14. Denler, M. C.; Massie, A. A.; Singh, R.; Stewart-Jones, E.; Sinha, A.; Day, V. W.; Nordlander, E.; Jackson, T. A., Mn^{IV}-Oxo complex of a bis(benzimidazolyl)-containing N5 ligand reveals different reactivity trends for Mn^{IV}-oxo than Fe^{IV}-oxo species. *Dalton Trans.* **2019,** *48* (15), 5007-5021.

15. Massie, A. A.; Denler, M. C.; Cardoso, L. T.; Walker, A. N.; Hossain, M. K.; Day, V. W.; Nordlander, E.; Jackson, T. A., Equatorial Ligand Perturbations Influence the Reactivity of Manganese(IV)-Oxo Complexes. *Angew. Chem., Int. Ed. Engl.* **2017,** *56* (15), 4178-4182.

16. Saltzman, H.; Sharefkin, J. G., Iodosobenzene. *Org. Synth.* **1963,** *43*, 60.

17. Lo, W. K. C.; McAdam, C. J.; Blackman, A. G.; Crowley, J. D.; McMorran, D. A., The pentadentate ligands 2PyN2Q and N4Py, and their Cu(II) and Zn(II) complexes: A synthetic, spectroscopic and crystallographic structural study. *Inorganica Chimica Acta* **2015,** *426*, 183-194.

18. Chang, J.; Plummer, S.; Berman, E. S. F.; Striplin, D.; Blauch, D., Synthesis and Characterization of Bis(di-2-pyridylmethanamine)ruthenium(II). *Inorg. Chem.* **2004,** *43* (5), 1735-1742.

19. Lubben, M.; Meetsma, A.; Wilkinson, E. C.; Feringa, B.; Que Jr., L., Nonheme Iron Centers in Oxygen Activation: Characterization of an Iron(III) Hydroperoxide Intermediate. *Angew. Chem., Int. Ed. Engl.* **1995,** *34* (13-14), 1512-1514.

20. Rana, S.; Dey, A.; Maiti, D., Mechanistic elucidation of C–H oxidation by electron rich non-heme iron(iv)-oxo at room temperature. *Chem. Commun.* **2015,** *51* (77), 14469-14472.

21. Mitra, M.; Nimir, H.; Demeshko, S.; Bhat, S. S.; Malinkin, S. O.; Haukka, M.; Lloret-Fillol, J.; Lisensky, G. C.; Meyer, F.; Shteinman, A. A.; Browne, W. R.; Hrovat, D. A.; Richmond, M. G.; Costas, M.; Nordlander, E., Nonheme Fe(IV) Oxo Complexes of Two New Pentadentate Ligands and Their Hydrogen-Atom and Oxygen-Atom Transfer Reactions. *Inorg. Chem.* **2015,** *54* (15), 7152-7164.

22. Leto, D. F.; Ingram, R.; Day, V. W.; Jackson, T. A., Spectroscopic properties and reactivity of a mononuclear oxomanganese(iv) complex. *Chem. Commun.* **2013,** *49* (47), 5378-5380.

23. Song, W. J.; Seo, M. S.; DeBeer George, S.; Ohta, T.; Song, R.; Kang, M.-J.; Tosha, T.; Kitagawa, T.; Solomon, E. I.; Nam, W., Synthesis, Characterization, and Reactivities of Manganese(V)−Oxo Porphyrin Complexes. *Journal of the American Chemical Society* **2007,** *129* (5), 1268-1277.

24. Prokop, K. A.; Neu, H. M.; de Visser, S. P.; Goldberg, D. P., A Manganese(V)–Oxo π-Cation Radical Complex: Influence of One-Electron Oxidation on Oxygen-Atom Transfer. *Journal of the American Chemical Society* **2011,** *133* (40), 15874-15877.

25. Marcus, R. A., Chemical and Electrochemical Electron-Transfer Theory. *Annual Review of Physical Chemistry* **1964,** *15* (1), 155-196.

26. Marcus, R. A., Electron Transfer Reactions in Chemistry: Theory and Experiment (Nobel Lecture). *Angewandte Chemie International Edition in English* **1993,** *32* (8), 1111-1121.

27. Warren, J. J.; Tronic, T. A.; Mayer, J. M., Thermochemistry of Proton-Coupled Electron Transfer Reagents and its Implications. *Chem. Rev.* **2010,** *110* (12), 6961-7001.

Chapter 7. Summary and Future Directions

The work in this dissertation has focused on the formation, characterization, and reactivity of Mn^{III}-peroxo (Chapter 2) and Mn^{IV}-oxo (Chapter 3-6) species supported by tetradentate and pentadentate ligand scaffolds, respectively. Mn-based catalysts in the presence of H_2O_2 are known to mediate substrate oxidation reactions, including hydroxylation, epoxidation, and alcohol oxidation.[1] By studying Mn^{III}-peroxo species, we can begin to understand what modulates O–O bond cleavage, and this knowledge can be used to design catalysts that are more efficient at H_2O_2 activation. Additionally, investigation of Mn^{IV}-oxo species with varied coordination spheres can aid in the design of more reactive and selective catalysts for HAT and OAT reactions.

7.1 Investigation of a Mn^{III}-Peroxo Complex

A tetradentate L^7BQ ligand was shown to support a Mn^{III}-peroxo species, $[Mn^{III}(O_2)(L^7BQ)]^+$. This new intermediate was characterized with a variety of spectroscopic techniques, including electronic absorption, Mn K-edge X-ray absorption and electron paramagnetic resonance methods. Additionally, the aldehyde deformylation reactivity of $[Mn^{III}(O_2)(L^7BQ)]^+$ was assessed through reaction with cyclohexanecarboxaldehyde (CCA) and 2-phenylpropionaldehyde (PPA). From these experiments, it was determined that $[Mn^{III}(O_2)(L^7BQ)]^+$ only reacts with aldehydes in the presence of acid. The acid impurities may serve to access a new intermediate (i.e., a Mn^{III}-hydroperoxo to facilitate aldehyde deformylations). These observations underscore the challenges in identifying the reactive metal species in aldehyde deformylation reactions, and also serve to emphasize that care should be taken when assigning the identity of active metal in the presence of acid impurities.

7.2 Structure-Function Relationships for Mn^{IV}-Oxo Complexes

Previously, our group reported the formation of $[Mn^{IV}(O)(N4py)]^{2+}$, which was generated by treating the corresponding Mn^{II} complex with iodosobenzene (PhIO) in 2,2,2-trifluoroethanol (TFE).[2-3] Compared to other Mn^{IV}-oxo species reported in the literature, $[Mn^{IV}(O)(N4py)]^{2+}$ showed enhanced reactivity for hydrogen atom transfer (HAT) reactions. In addition to a thermodynamic basis for the enhanced reactivity of this complex,[2] there have been recent density functional theory (DFT) calculations that predict a multi-state reactivity model involving the ^4E excited state (see Chapter 6, Figure 1.14).[4] Our group has previously assigned this ^4E excitation for $[Mn^{IV}(O)(N4py)]^{2+}$ to a near-IR absorption feature, thus allowing for a λ_{max} that can be used to predict reactivity for this type of Mn^{IV}-oxo species.[5] Additional DFT calculations for the sulfoxidation of thioanisole also predict multi-state reactivity, where the ^4E state plays a role in offering a lower barrier for the reaction.[6] However, this oxygen atom transfer (OAT) reaction is predicted to involve three states, suggesting that the reaction is more complicated compared to HAT.

To date, little has been done experimentally to evaluate the multi-state reactivity model for HAT and OAT reactions. To further understand what causes the enhanced reactivity for these types of Mn^{IV}-oxo species, our group synthesized a series of Mn^{IV}-oxo species supported by N4py derivatives, where tuning of the equatorial field strength directly affected both the ^4E excitation energy as well as the HAT and OAT reactivity (Chapter 3).[3] The lowering of the ^4E energy for $[Mn^{IV}(O)(2pyN2Q)]^{2+}$ correlated to faster HAT and OAT reactivity, which is in line with the multi-state reactivity model. However, modifications to the ligand scaffold altered other properties of the Mn^{IV}-oxo species, including the $Mn^{IV/III}$ reduction potentials, with higher potentials correlating to faster reactivity.

To expand on this series of Mn^{IV}-oxo complexes, a new $[Mn^{IV}(O)(2pyN2B)]^{2+}$ complex with benzimidazole ligands was investigated (Chapters 4 and 5). Addition of a fourth derivative to this series allowed for expansion in our correlations between reactivity and the ^4E excitation and the $Mn^{IV/III}$ reduction potentials. Specifically, in the case of HAT reactions, a stronger correlation was obtained when reactivity was correlated to the reduction potential rather than the ^4E excitation. In the case of OAT reactions, we observed a strong correlation for the ^4E excitation and a more scattered correlation for the reduction potential. When comparing the reactivity for this series of Mn^{IV}-oxo species against analogous Fe^{IV}-oxo species, very different trends were observed.[7-9] While $[Mn^{IV}(O)(2pyN2B)]^{2+}$ is slower at both HAT and OAT reactions compared to $[Mn^{IV}(O)(N4py)]^{2+}$, $[Fe^{IV}(O)(2pyN2B)]^{2+}$ shows faster reactivity for HAT and OAT reactions compared to $[Fe^{IV}(O)(N4py)]^{2+}$. Although the basis for the reactivity differences at parity of coordination sphere are unclear, these observations demonstrate that principles developed to tune the reactivity for Fe^{IV}-oxo species cannot be applied directly to analogous Mn^{IV}-oxo species.

To further understand structure-function relationships for this type of Mn^{IV}-oxo species, $[Mn^{IV}(O)(N3pyQ)]^{2+}$ was synthesized (Chapter 3). The ^4E excitation for this complex falls in between those of $[Mn^{IV}(O)(N4py]^{2+}$ and $[Mn^{IV}(O)(2pyN2Q)]^{2+}$, which is expected because the new species possesses one quinoline arm and one pyridine arm. Upon further investigation of the HAT and OAT reactivity of $[Mn^{IV}(O)(N3pyQ)]^{2+}$, we should be able further evaluate trends between reactivity, the ^4E energy and the $Mn^{IV/III}$ reduction potential.

Because tuning the equatorial field directly alters reactivity, studying the geometric and electronic structure of the Mn^{IV}-oxo species can give direct insight into structure-function relationships. As Mn^{IV}-oxo species exhibit thermal instability, there is only a single report of an X-ray diffraction (XRD) structure.[10] As an alternative, Mn K-edge X-ray absorption spectroscopy

(XAS) is a useful technique to gain structural insight into complexes that cannot be obtained in crystalline form. Analysis of the extended X-ray absorption fine structure (EXAFS) region for $[Mn^{IV}(O)(2pyN2Q)]^{2+}$, $[Mn^{IV}(O)(^{DMM}N4py)]^{2+}$, and $[Mn^{IV}(O)(2pyN2B)]^{2+}$ revealed metal-ligand bond distances that could be compared to other Mn^{IV}- and Mn^{V}-oxo species in the literature. The EXAFS-determined Mn=O bond distances are reproduced best by DFT calculations when the oxo ligand includes strong hydrogen-bonding interactions with two second sphere TFE molecules. Similar calculations were performed for $[Fe^{IV}(O)(N4py)]^{2+}$ with two second sphere TFE molecules, where weaker hydrogen-bonding interactions were observed. This suggests that there may be a solvent stabilization of Mn^{IV}-oxo species that makes it difficult to form these complexes in aprotic solvent systems, whereas analogous Fe^{IV}-oxo species are formed in MeCN. To further understand the solvent stabilization of Mn^{IV}-oxo species in TFE, it would be insightful to form $[Mn^{IV}(O)(^{DMM}N4py)]^{2+}$, the most stable of the Mn^{IV}-oxo complexes, in an aprotic solvent, such as MeCN, acetone, or CH_2Cl_2. Upon examination of the EXAFS data, we would expect that the absence of hydrogen-bonding in an aprotic solvent would lead to a contracted Mn=O bond distance.

7.3 Oxygen Atom Transfer for Mn^{IV}-Oxo Complexes

The sulfoxidation of thioanisole by the series of Mn^{IV}-oxo complexes was investigated using temperature-dependent kinetic studies to obtain activation parameters ($\Delta H^{\ddagger}$ and $\Delta S^{\ddagger}$) for each reaction. The $\Delta H^{\ddagger}$, as well as the calculated activation free energy ($\Delta G^{\ddagger}$) at 25°C, strongly correlate with previously observed second-order rate constants (k_2). Additionally, investigation of *para*-substituted thioanisole derivatives allowed for a Hammett analysis across the Mn^{IV}-oxo series, yielding similar negative slopes, thereby suggesting they follow the same mechanism of

sulfoxidation. While the Hammett analyses are insightful, only thioanisole and two of its derivatives possessing electron-withdrawing substituents were investigated. Upon plotting the log(k_2) value for $[Mn^{IV}(O)(^{DMM}N4py)]^{2+}$ with 4-methoxythioanisole against the σ_p value, this point deviates from the Hammett analysis of the electron-withdrawing thioanisole deriviatves (Chapter 6, Figure 6.6). Unfortunately, 4-methoxythioanisole could only be investigated for $[Mn^{IV}(O)(^{DMM}N4py)]^{2+}$ because the other complexes exhibited reaction rates that were too fast to monitor with our equipment. The enhanced reactivity observed for the oxidation of 4-methoxythioanisole compared to regular thioanisole by $[Mn^{IV}(O)(^{DMM}N4py)]^{2+}$ may suggest a change in mechanism. Supporting this proposal, the reduction potentials for thioanisole and 4-methoxythioanisole are 1.18 V and 1.37 V (vs. SCE), respectively,[11] suggesting the former is more susceptible to an initial electron transfer reaction. Thus, there may be a change from a direct OAT mechanism to an initial electron transfer reaction followed by a fast OAT transfer for the more easily oxidized derivative.

While the three Mn^{IV}-oxo species studied exhibit strong correlations between the log(k_2) and the σ_p for thioanisole derivatives, the substrate scope is limited to a small range of electronic properties. Future efforts in the Jackson lab should be made to fill in the gaps for this Hammett analysis. Several thioanisole derivatives that are commonly investigated for these types of analyses are depicted in Figure 7.1. A commonly employed derivative in this Hammett analysis is 4-methylthioanisole, which possesses a σ_p value of -0.17. While kinetic information obtained for this substrate would help to fill in our analysis, specifically for $[Mn^{IV}(O)(^{DMM}N4py)]^{2+}$ where we lack a point between regular thioanisole and 4-methoxythioanisole, the substrate is suceptible to both HAT and OAT reactivity. The Mn^{IV}-oxo species investigated in this study have also been shown to cleave benzylic C–H bonds (including those of cumene, toluene, ethylbenzene, and

diphenylmethane), so 4-methylthioanisole, which also posesses benzylic C–H bonds, was exculded from this analysis. Additionally, 4-(methylthio)benzonitrile is commonly employed as an electron-withdrawing thioanisole derivitve. While this substrate is oxidized very slowly, preliminary investigation of the oxidation of 40 equivalents of 4-(methylthio)benzonitrile by $[Mn^{IV}(O)(2pyN2Q)]^{2+}$ suggests that a k_2 value could be obtained (Figure 7.2). Future work should include re-visiting this substrate across the series to expand on the scope of thioanisole deriviatves investigation. Additionally, future work should focus on *tert*-butyl-thioanisole to allow for sulfoxidation of a thioanisole derivaitve with. a negative σ_p value that is not suceptible to HAT. Additionally, inclusion of $[Mn^{IV}(O)(2pyN2B)]^{2+}$ in the Hammett analysis is necessary to fully explore the series of Mn^{IV}-oxo species.

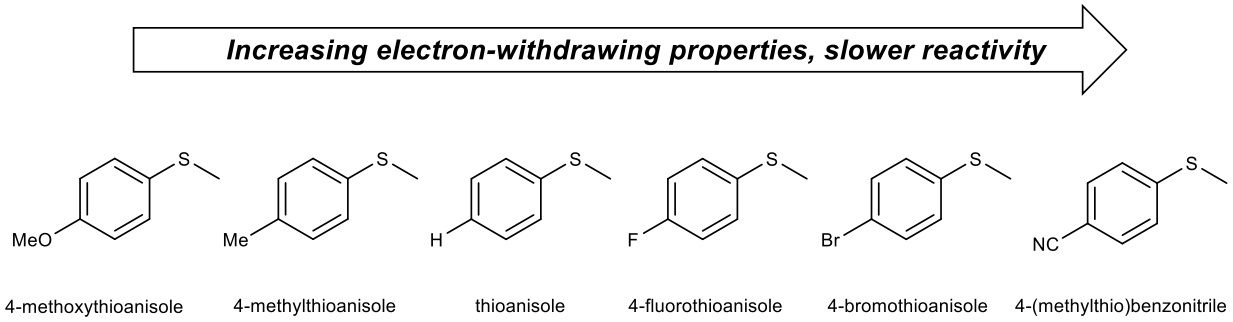

Figure 7.1. Commonly employed thioanisole deriviatves in Hammett analyses.

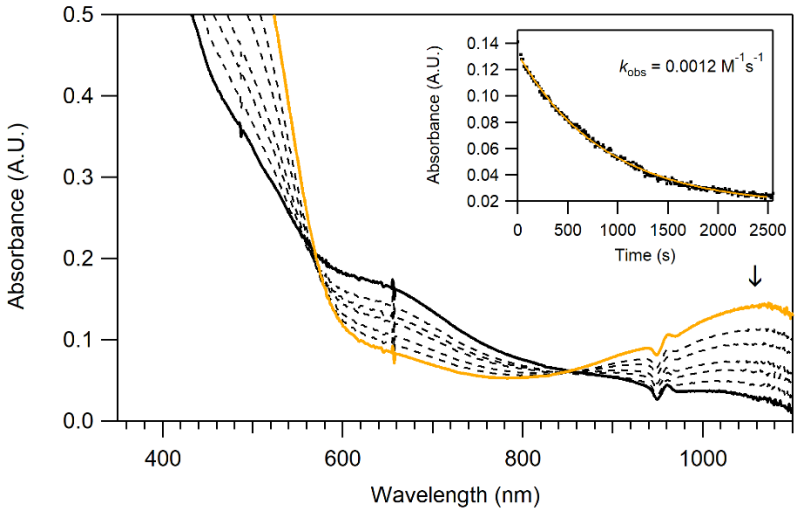

Figure 7.2. Reaction of 1.0 mM $[Mn^{IV}(O)(2pyN2Q)]^{2+}$ with 40 equivalents of 4-(methylthio)benzonitrile in TFE. Inset: decay of the fetaure at 1020nm over time.

Further insight into the scope of OAT reactivity for this series of Mn^{IV}-oxo species was obtained by investigating reactions with several other substrates, including styrene, triphenylphosphine, cyclohexene, and cyclooctene. Kinetic investigation of styrene epoxidation by $[Mn^{IV}(O)(2pyN2Q)]^{2+}$ expanded the oxidation ability for this series of Mn^{IV}-oxo series and revealed a new avenue of reactivity. To understand how the mechanism of epoxidation correlates across the series of Mn^{IV}-oxo species and compares to sulfoxidation of thioanisole, further investigation of styrene epoxidation is required. First, product analysis by ^{1}H NMR is required to support that epoxidation of the olefin substrate is taking place. Next, a Hammett analysis of styrene derivatives would allow for the investigation of how the reactivity trends across the series. Nam *et al*. have reported on styrene epoxidation reactions of $[Mn^{IV}(O)(N4py)]^{2+}$ in the presence of HOTf, suggesting the mechanism follows an outer-sphere electron transfer pathway.[12] Additionally, collection of activation parameters for styrene oxidation would allow for further comparisons to be made between sulfoxidation and epoxidation.

Additional experiments were attempted with triphenylphosphine (PPh_3), however, even the slowest complex, $[Mn^{IV}(O)(^{DMM}N4py)]^{2+}$, reacted with PPh_3 too rapidly to monitor using our equipment. To allow for kinetic investigation of these reactions, the temperature could be reduced, or electron-withdrawing substituents could be introduced to slow down the reactivity and allow for kinetics to be monitored on our equipment.

Finally, cyclohexene and cyclooctene were utilized to evaluate the chemoselectivity of $[Mn^{IV}(O)(2pyN2Q)]^{2+}$ for olefin oxidation when both epoxidation and allylic C–H bond abstraction are possible (Chapter 6). Cyclooctene possesses a slightly higher BDFE than cyclohexene (83 kcal/mol and 80 kcal/mol respectively). Upon the addition of cyclohexene to $[Mn^{IV}(O)(2pyN2Q)]^{2+}$, electronic absorption data showed the conversion of the Mn^{IV}-oxo species to a Mn^{III}-OH product, suggestive of a HAT reaction. However, upon addition of cyclooctene, which possesses a slightly stronger allylic C–H bond, electronic absorption showed the conversion of the Mn^{IV}-oxo species to a Mn^{II} product, suggestive of a two-electron epoxidation reaction. Taken together, these results suggest that the small difference in BDFE values (3 kcal/mol) between the two substrates was enough to change the mechanism of olefin oxidation. Product analysis of the oxidation of cyclohexene by $[Mn^{IV}(O)(2pyN2Q)]^{2+}$ revealed both epoxidation and C–H activation products, electronic absorption suggested a single oxidation process. The use of excess PhIO to form $[Mn^{IV}(O)(2pyN2Q)]^{2+}$ could allow for the reformation of the Mn^{IV}-oxo species following epoxidation, therefore leading to complications in determining stoichiometric oxidation products. Taking advantage of this catalytic efficiency, the series of Mn^{IV}-oxo species could be investigated for the catalytic oxidation of olefin substrates with allylic C–H bonds. Product analysis studies may give insight into what mechanism pathways are favored and how the ligand scaffold serves to control these pathways. Presumably, any unreacted PhIO in solution will

react with Mn^{II} (Mn-product following epoxidation) and re-form the Mn^{IV}-oxo center, thus supporting a catalytic cycle. While catalysis leads to complicated product analysis for stoichiometric substrate oxidation, a screening of the catalytic OAT reactivity could be performed. Product analysis by GC-MS methods can give insight into OAT reaction turnover numbers and catalyst efficiency, which have yet to be studied for derivatives of the N4py series.

7.4 References

1. Gómez, L.; Garcia-Bosch, I.; Company, A.; Sala, X.; Fontrodona, X.; Ribas, X.; Costas, M., Chiral manganese complexes with pinene appended tetradentate ligands as stereoselective epoxidation catalysts. *Dalton Trans.* **2007,** (47), 5539-5545.

2. Leto, D. F.; Ingram, R.; Day, V. W.; Jackson, T. A., Spectroscopic properties and reactivity of a mononuclear oxomanganese(iv) complex. *Chem. Commun.* **2013,** *49* (47), 5378-5380.

3. Massie, A. A.; Denler, M. C.; Cardoso, L. T.; Walker, A. N.; Hossain, M. K.; Day, V. W.; Nordlander, E.; Jackson, T. A., Equatorial Ligand Perturbations Influence the Reactivity of Manganese(IV)-Oxo Complexes. *Angew. Chem. Int. Ed.* **2017,** *56* (15), 4178-4182.

4. Cho, K.-B.; Shaik, S.; Nam, W., Theoretical Investigations into C–H Bond Activation Reaction by Nonheme MnIVO Complexes: Multistate Reactivity with No Oxygen Rebound. *J. Phys. Chem. Lett.* **2012,** *3* (19), 2851-2856.

5. Leto, D. F.; Massie, A. A.; Rice, D. B.; Jackson, T. A., Spectroscopic and Computational Investigations of a Mononuclear Manganese(IV)-Oxo Complex Reveal Electronic Structure Contributions to Reactivity. *J. Am. Chem. Soc.* **2016,** *138* (47), 15413-15424.

6. Chen, J.; Cho, K.-B.; Lee, Y.-M.; Kwon, Y. H.; Nam, W., Mononuclear nonheme iron(iv)–oxo and manganese(iv)–oxo complexes in oxidation reactions: experimental results prove theoretical prediction. *Chem. Commun.* **2015,** *51* (66), 13094-13097.

7. Mitra, M.; Nimir, H.; Demeshko, S.; Bhat, S. S.; Malinkin, S. O.; Haukka, M.; Lloret-Fillol, J.; Lisensky, G. C.; Meyer, F.; Shteinman, A. A.; Browne, W. R.; Hrovat, D. A.; Richmond, M. G.; Costas, M.; Nordlander, E., Nonheme Fe(IV) Oxo Complexes of Two New Pentadentate Ligands and Their Hydrogen-Atom and Oxygen-Atom Transfer Reactions. *Inorg. Chem.* **2015,** *54* (15), 7152-7164.

8. Rasheed, W.; Draksharapu, A.; Banerjee, S.; Young, V. G.; Fan, R.; Guo, Y.; Ozerov, M.; Nehrkorn, J.; Krzystek, J.; Telser, J.; Que, L., Crystallographic Evidence for a Sterically Induced Ferryl Tilt in a Non-Heme Oxoiron(IV) Complex that Makes it a Better Oxidant. *Angew. Chem., Int. Ed.* **2018,** *57* (30), 9387-9391.

9. Rana, S.; Dey, A.; Maiti, D., Mechanistic elucidation of C–H oxidation by electron rich non-heme iron(iv)-oxo at room temperature. *Chem. Commun.* **2015,** *51* (77), 14469-14472.

10. Halbach, R. L.; Gygi, D.; Bloch, E. D.; Anderson, B. L.; Nocera, D. G., Structurally characterized terminal manganese(iv) oxo tris(alkoxide) complex. *Chem. Sci.* **2018,** *9* (19), 4524-4528.

11. Chen, J.; Lee, Y.-M.; Davis, K. M.; Wu, X.; Seo, M. S.; Cho, K.-B.; Yoon, H.; Park, Y. J.; Fukuzumi, S.; Pushkar, Y. N.; Nam, W., A Mononuclear Non-Heme Manganese(IV)–Oxo Complex Binding Redox-Inactive Metal Ions. *J. Am. Chem. Soc.* **2013,** *135* (17), 6388-6391.

12. Lee, Y.-M.; Kim, S.; Ohkubo, K.; Kim, K.-H.; Nam, W.; Fukuzumi, S., Unified Mechanism of Oxygen Atom Transfer and Hydrogen Atom Transfer Reactions with a Triflic Acid-Bound Nonheme Manganese(IV)–Oxo Complex via Outer-Sphere Electron Transfer. *J. Am. Chem. Soc.* **2019,** *141* (6), 2614-2622.

Appendix 2

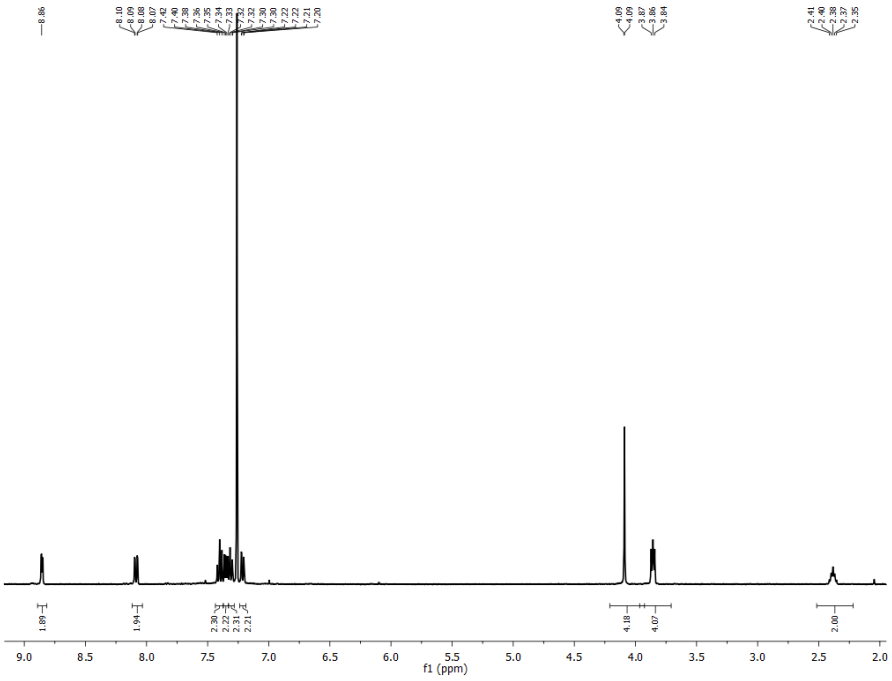

Figure A2.1. ^{1}H NMR spectrum of the $L^{7}BQ$ ligand collected in $CDCl_3$ under ambient conditions (collected on a 600 MHz).

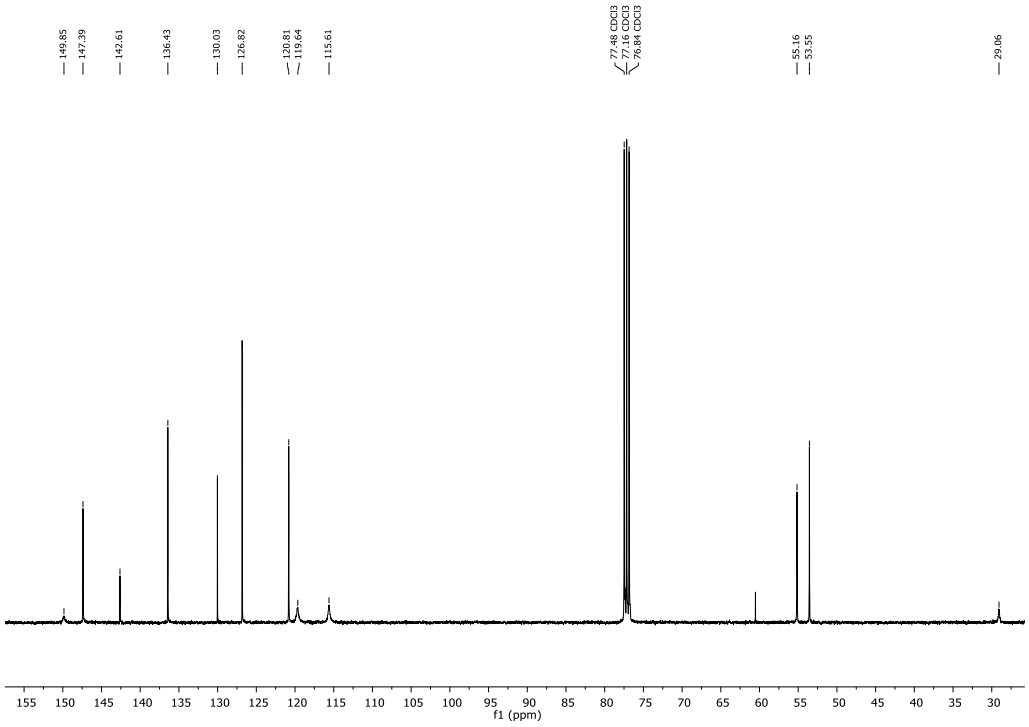

Figure A2.2. ^{13}C NMR spectrum of the $L^{7}BQ$ ligand collected in $CDCl_3$ under ambient conditions (100.62 MHz).

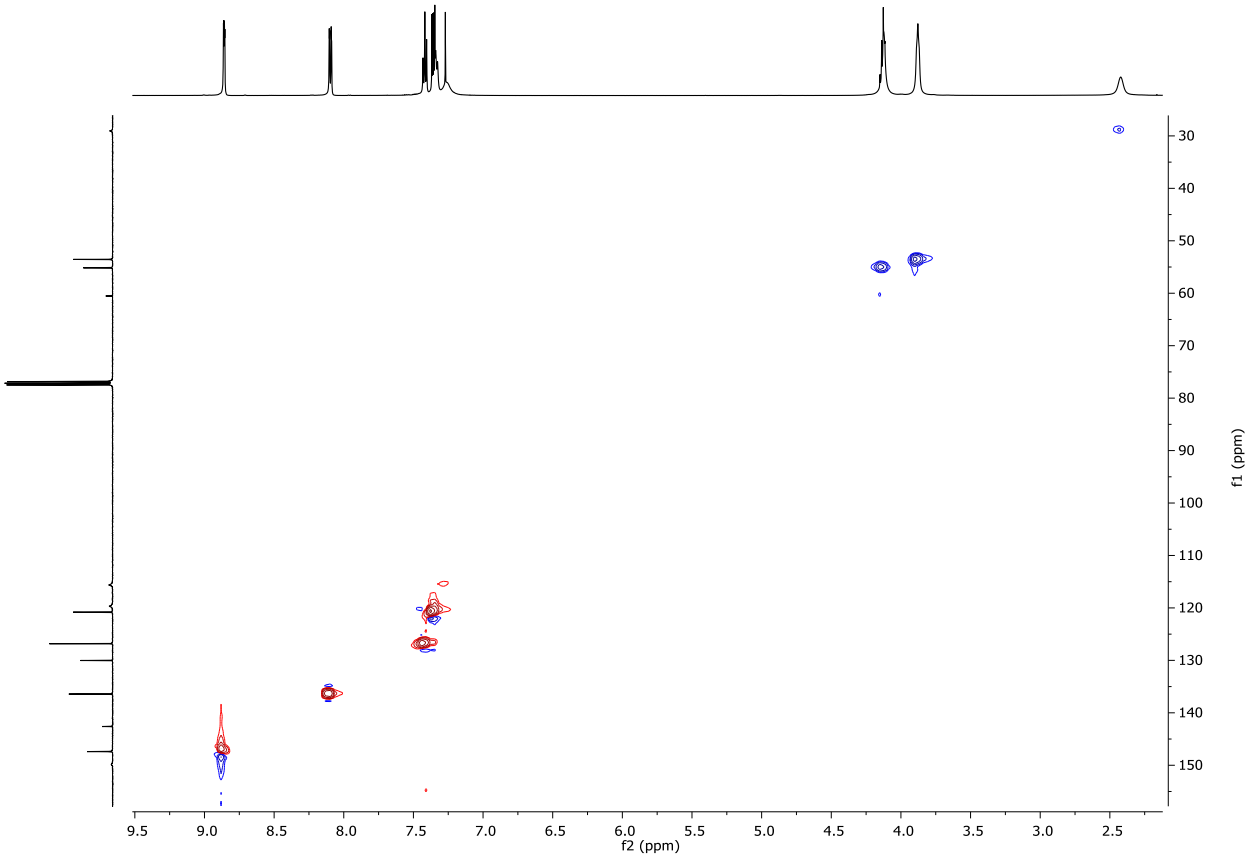

Figure A2.3. HSQC spectrum of the L^7BQ ligand collected in $CDCl_3$ under ambient conditions.

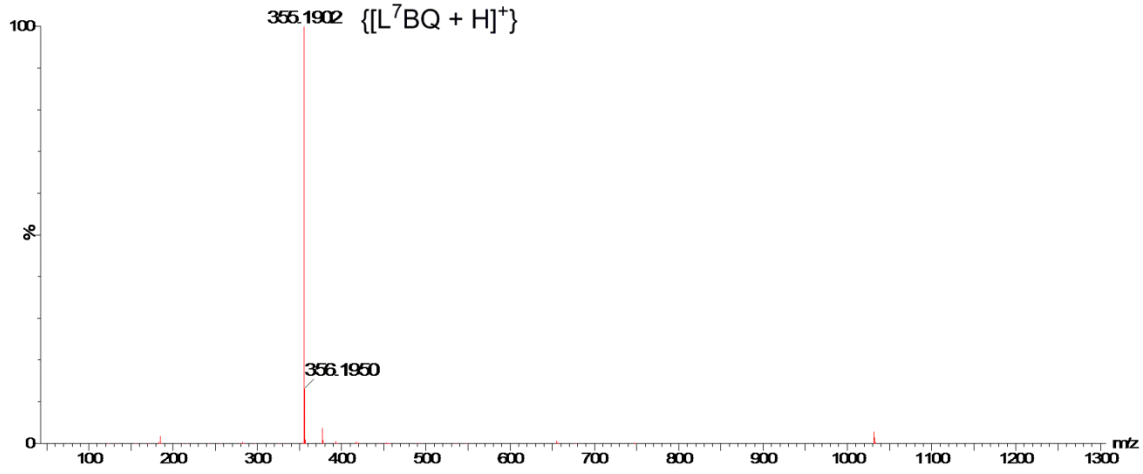

Figure A2.4. ESI-MS data showing the purified L^7BQ ligand in acetonitrile.

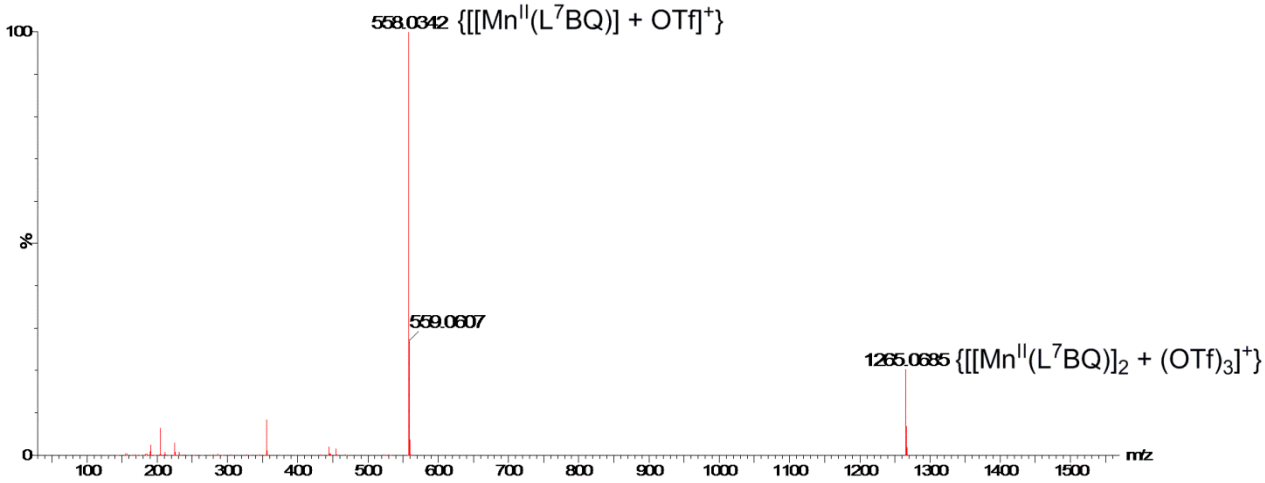

Figure A2.5. ESI-MS spectrum of $[Mn^{II}(L^7BQ)(OTf)_2]$ in acetonitrile.

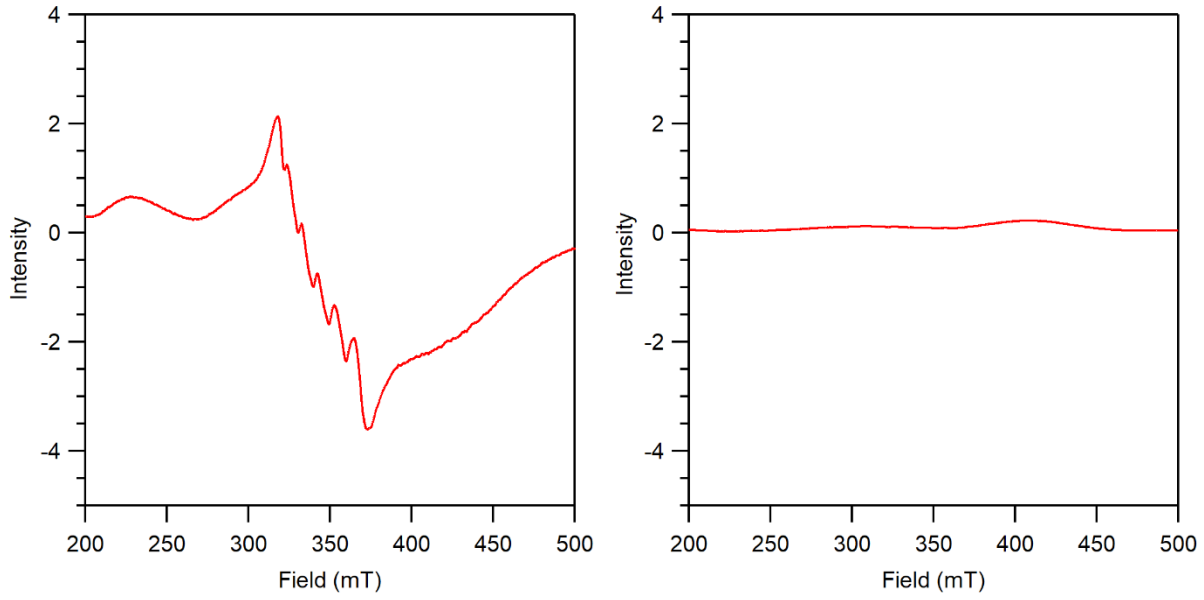

Figure A2.6. Perpendicular-mode (left) and parallel-mode (right) X-band EPR spectra of a 2.5 mM frozen MeCN solution of $[Mn^{II}(L^7BQ)(OTf)_2]$ collected at 5 K.

Table A2.1. Crystal Data and Structure Refinement for $[Mn^{II}(L^7BQ)(OTf)_2]$.

Empirical formula	$C_{27}H_{25}F_6MnN_5O_6S_2$
Formula weight	748.58
Temperature	100(2) K
Wavelength	1.54178 Å
Crystal system	Monoclinic
Space group[3]	$P2_1/n$ – alternate setting for $P2_1/c$ (No. 14 – C_{2h}^5)
Unit cell dimensions	**a** = 13.8379(4) Å **α** = 90.00°
	b = 14.1652(4) Å **β** = 105.211(1)°
	c = 16.3768(4) Å **γ** = 90.00°
Volume	3097.66(15) $Å^3$
Z	4
Density (calculated)	1.605 g/cm^3
Absorption coefficient	5.51 mm^{-1}
F(000)	1524
Crystal size	0.24 x 0.18 x 0.10 mm^3
Theta range for data collection	3.73° to 69.49°
Index ranges	$-15 \leq h \leq 16$, $-17 \leq k \leq 17$, $-13 \leq l \leq 19$
Reflections collected	26589
Independent reflections	5484 [R_{int} = 0.031]
Completeness to theta = 66.00°	97.0 %
Absorption correction	Multi-scan
Max. and min. transmission	1.000 and 0.787
Refinement method	Full-matrix least-squares on F^2
Data / restraints / parameters	5484 / 0 / 525
Goodness-of-fit on F^2	1.039
Final R indices [5432 I>2sigma(I)]	R_1 = 0.0293, wR_2 = 0.0748
R indices (all 5484 data)	R_1 = 0.0295, wR_2 = 0.0750
Extinction coefficient	0.00022(5)
Largest diff. peak and hole	0.40 and -0.34 $e^-/Å^3$

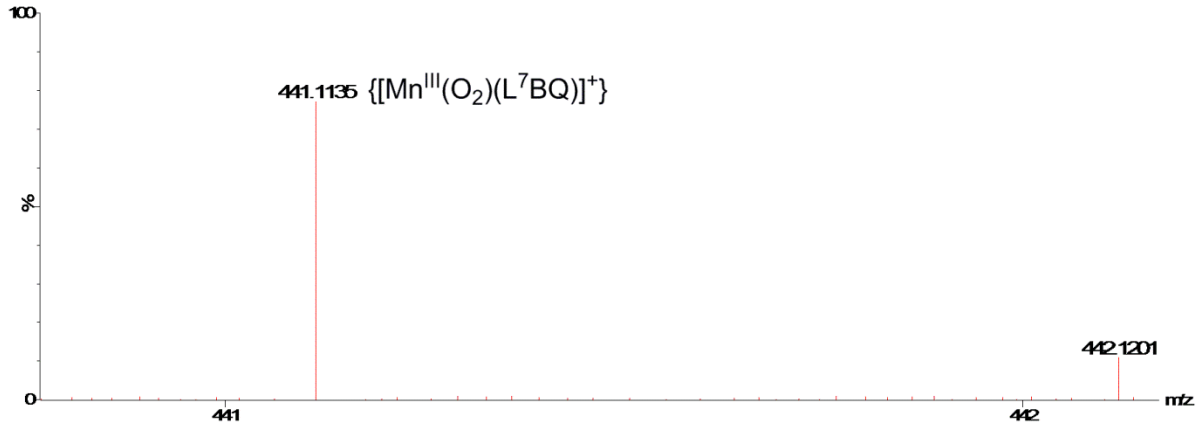

Figure A2.7. Low-temperature ESI-MS spectrum of $[Mn^{III}(O_2)(L^7BQ)]^+$ in acetonitrile.

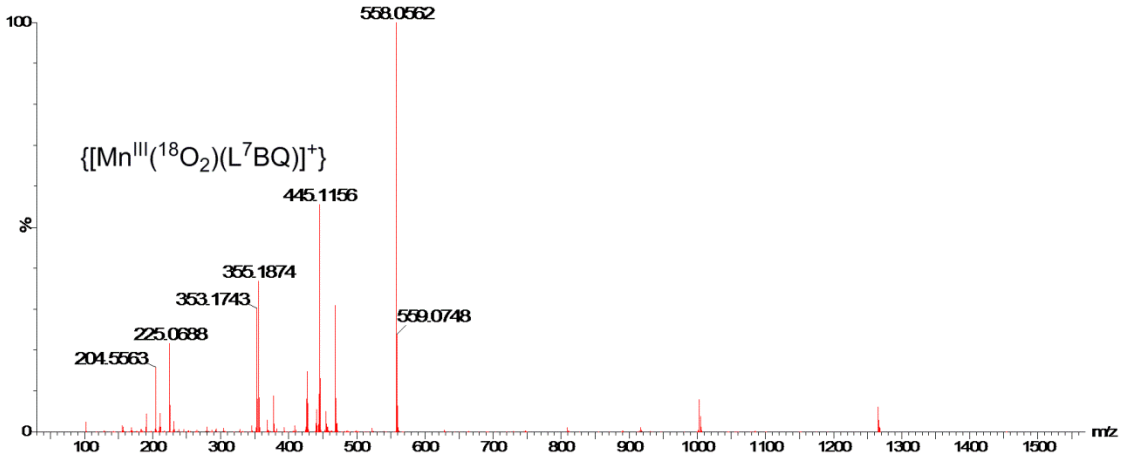

Figure A2.8. Low-temperature ESI-MS spectrum of $[Mn^{III}(^{18}O_2)(L^7BQ)]^+$ in acetonitrile. The major ion peak at 558.06 represents $[Mn^{II}(L^7BQ)(OTf)]^+$ (see Figure A2.5).

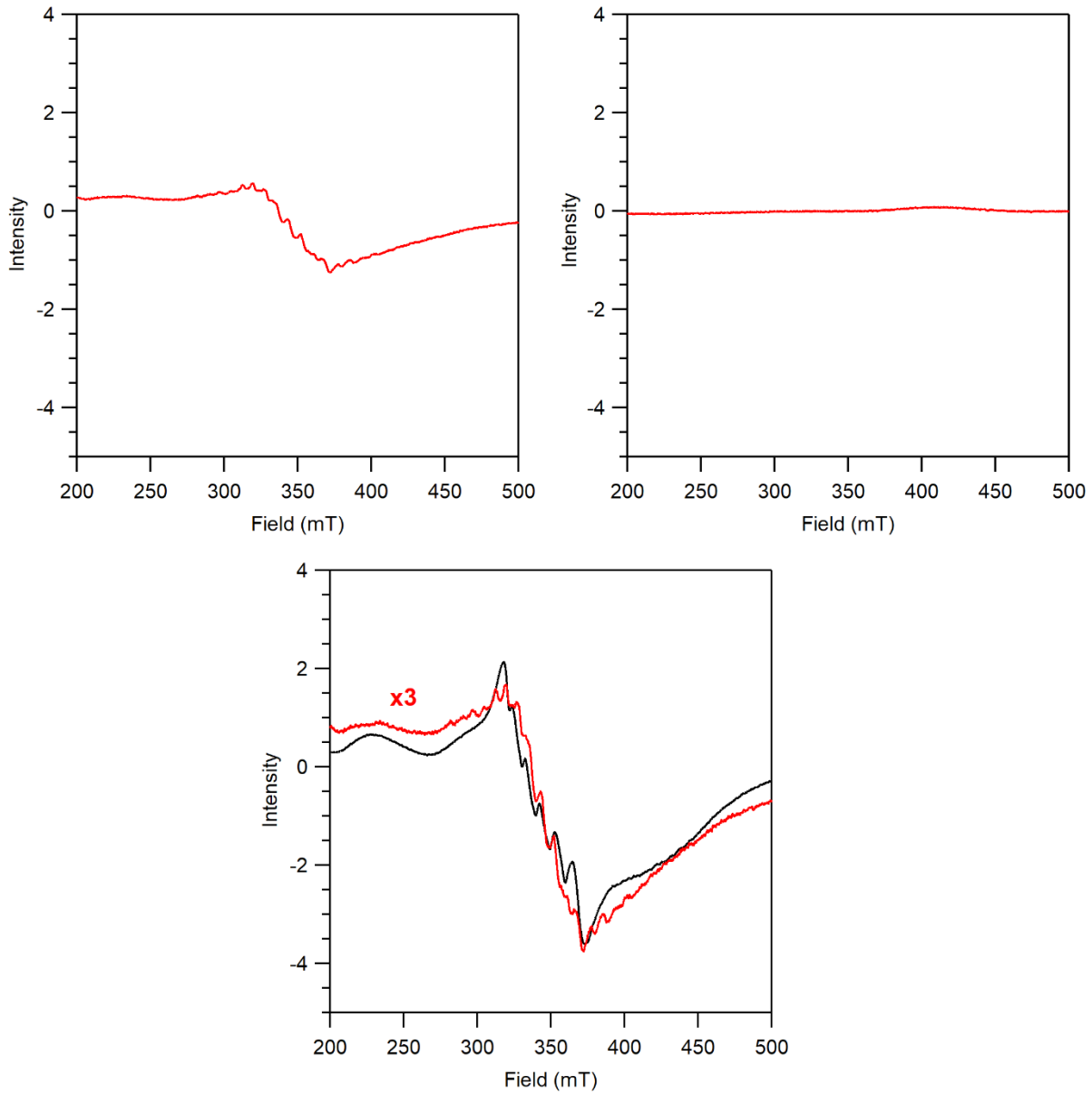

Figure A2.9. Perpendicular-mode (top left) and parallel-mode (top right) X-band EPR spectra of a 2.5 mM frozen MeCN solution of $[Mn^{III}(O_2)(L^7BQ)]^+$ collected at 5 K. Bottom panel: Overlay of perpendicular-mode X-band EPR spectra of $[Mn^{II}(L^7BQ)(OTf)_2]$ (black trace) and $[Mn^{III}(O_2)(L^7BQ)]^+$.

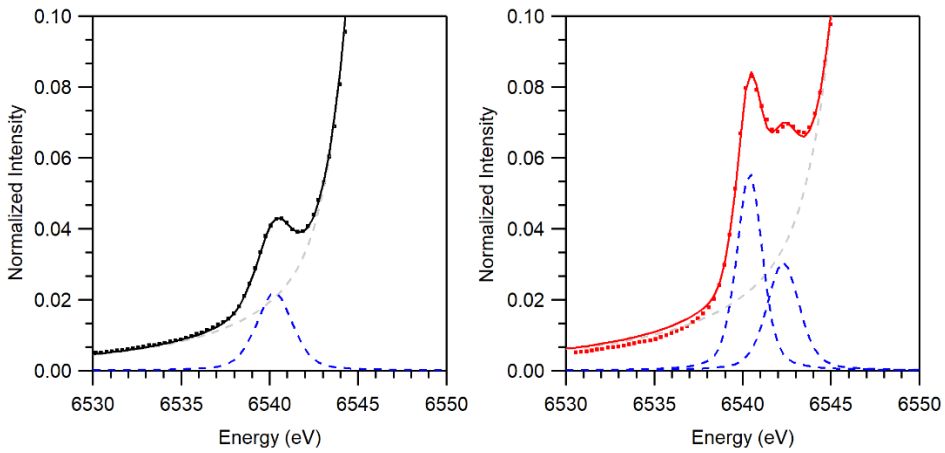

Figure A2.10 Comparison of the normalized XAS pre-edge data (doted line) and fits (solid line) for $[Mn^{II}(L^7BQ)(OTf)_2]$ (left) and $[Mn^{III}(O_2)(L^7BQ)]^+$ (right). The fit of the background and the fit of the pre-edge features are represented by the dashed blue traces.

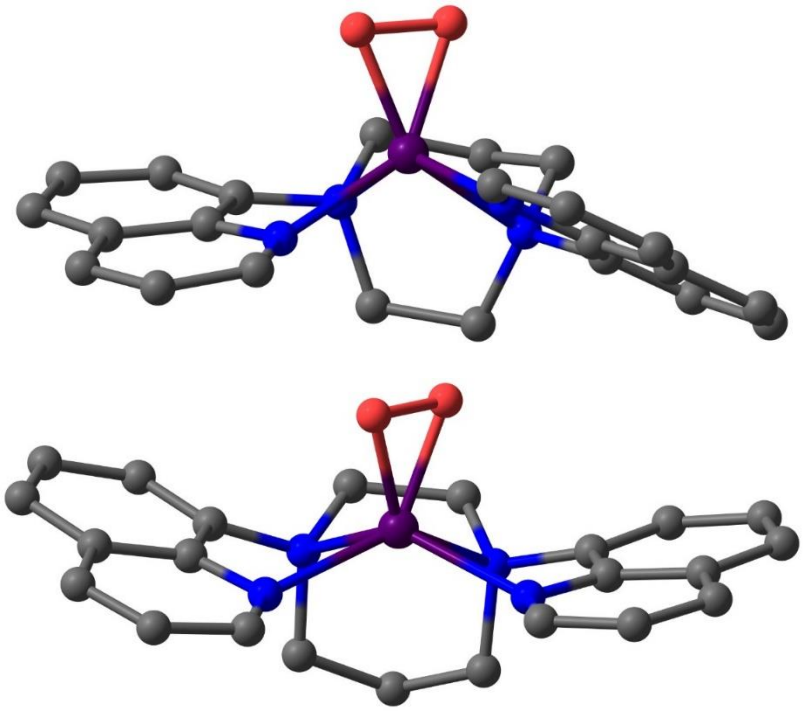

Figure A2.11. Predicted structures for $[Mn^{III}(O_2)(L^7BQ)]^+$ with the peroxo bound propyl- and ethyl-linked faces of the L^7BQ ligand (top and bottom, respectively).

Table A2.2. Selected Geometric Parameters for $[Mn^{III}(O_2)(L^7BQ)]^+$ with the Peroxo Bound to the Propyl-linked Face of the L^7BQ ligand (Figure A2.11, top).

Bond Length (Å)			
Mn–O1	1.862	Mn–N1	2.142
Mn–O2	1.856	Mn–N2	2.315
O1-O2	1.418	Mn–N3	2.204
		Mn–N4	2.199

Bond Angle (°)			
N1–Mn–O1	96.85	N1–Mn–N2	74.38
N2–Mn–O1	109.11	N1–Mn–N3	116.37
N3–Mn–O1	145.28	N1–Mn–N4	98.66
N4–Mn–O1	107.62	N2–Mn–N3	73.10
N1–Mn–O2	140.96	N2–Mn–N4	143.17
N2–Mn–O2	107.32	N3–Mn–N4	78.46
N3–Mn–O2	100.67	O1–Mn–O2	44.83
N4–Mn–O2	100.47		

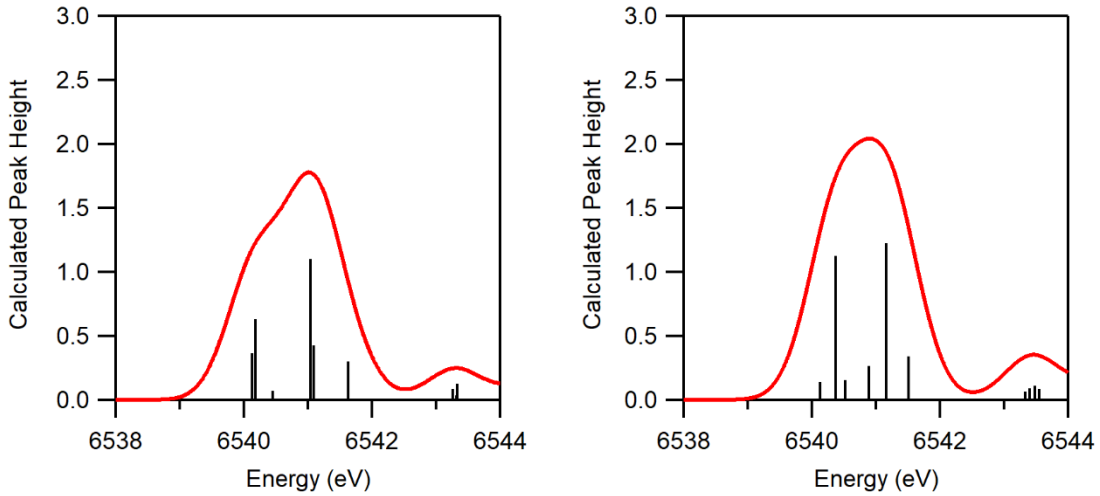

Figure A2.12. TD-DFT simulated pre-edge spectra with vertical lines showing transitions for $[Mn^{III}(O_2)(L^7BQ)]^+$ with the peroxo bound to the propyl-linked (left) and ethyl-linked faces (right) of the L^7BQ ligand (see Figure A2.11). The simulated spectra employed Gaussian functions with a 1 eV bandwidth.

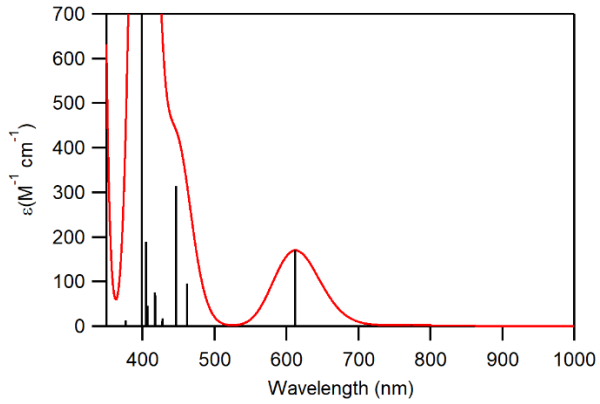

Figure A2.13. TD-DFT simulated UV-Vis absorption spectra with vertical lines showing transitions for the $[Mn^{III}(O_2)(L^7BQ)]^+$ with the peroxo bound to the propyl-linked face of the L^7BQ ligand (Figure A2.11, top). The transition at 612 nm corresponds to a transition involving a one-electron excitation from the Mn^{III} α-$3d_z^2$ to α-$3d_{xy}$ MO.

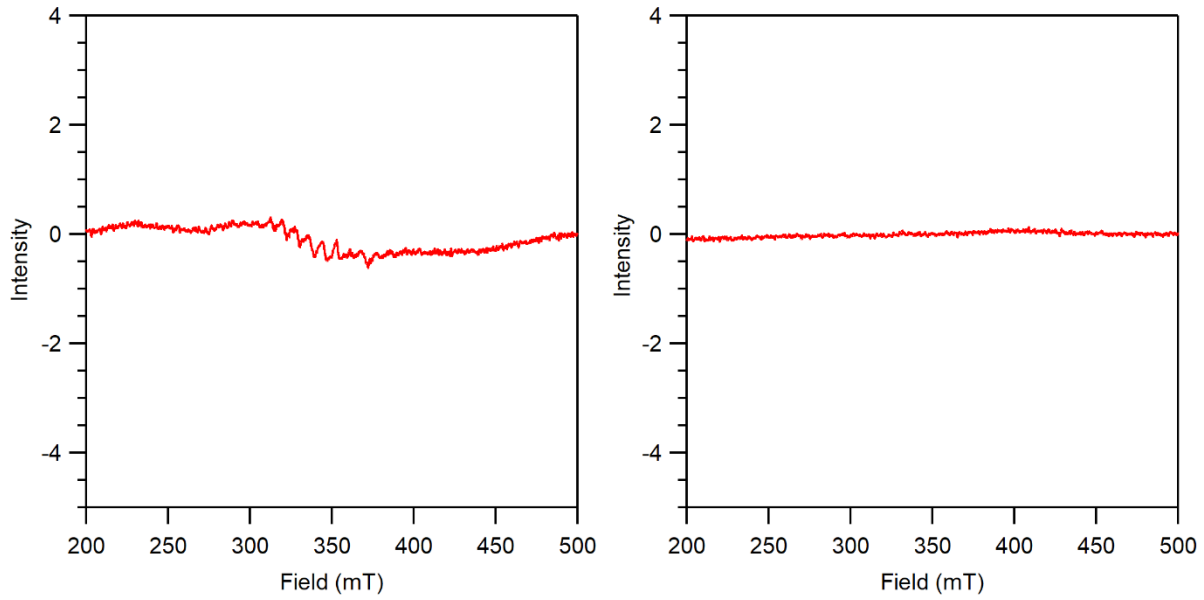

Figure A2.14. 10 K perpendicular- (left) and parallel-mode (right) X-band EPR spectra of a 2.5 mM frozen MeCN solution of the self-decay product of $[Mn^{III}(O_2)(L^7BQ)]^+$.

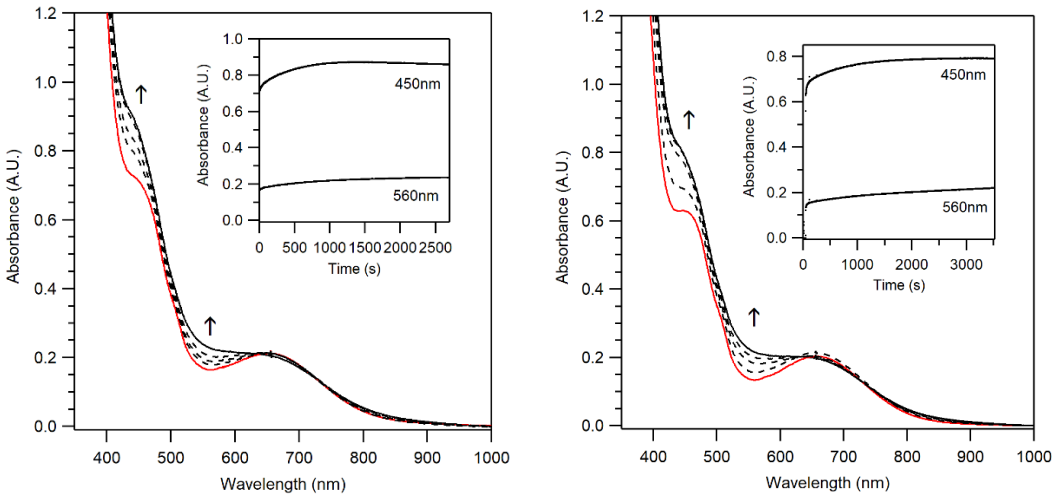

Figure A2.15. Left: Electronic absorption changes flowing the addition of 1.0 equivalents of $[Mn^{II}(L^7BQ)(OTf)_2]$ to $[Mn^{III}(O_2)(L^7BQ)]^+$ at -40°C in MeCN (the red and black traces are of the initial and final spectra, respectively). Right: Self decay of $[Mn^{III}(O_2)(L^7BQ)]^+$ at -40°C in MeCN (the red and black traces are of the initial and final spectra, respectively).

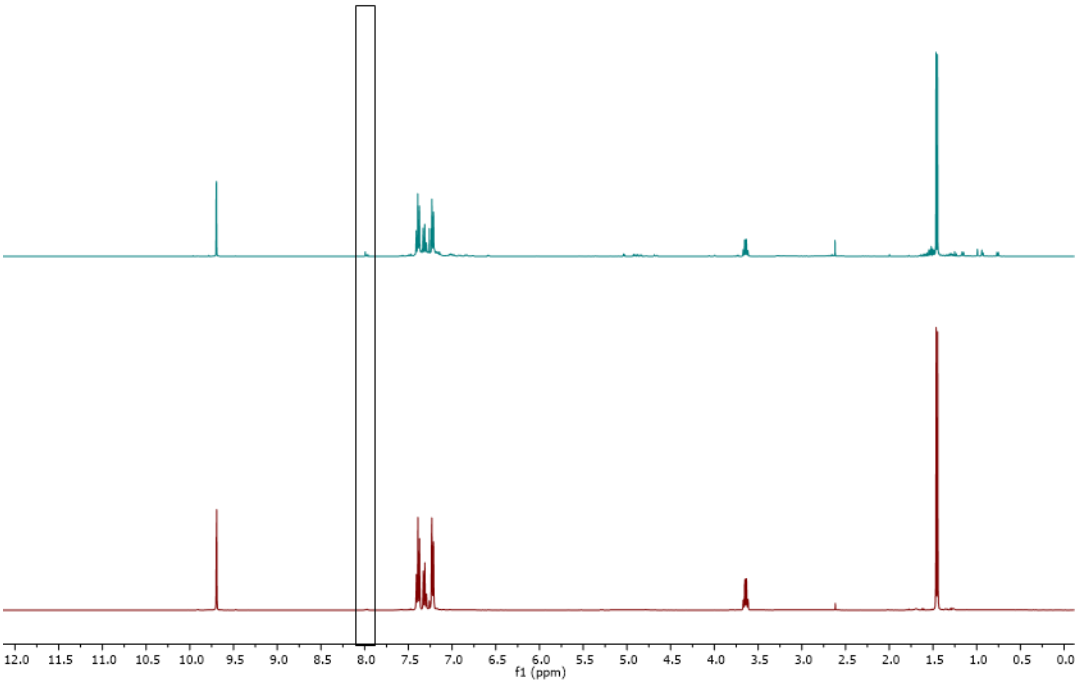

Figure A2.16. ^1H NMR spectra of PPA. Top: Spectrum of PPA with acid impurity at ~8.0 ppm. Bottom: Spectrum of fresh PPA with no acid impurity present.

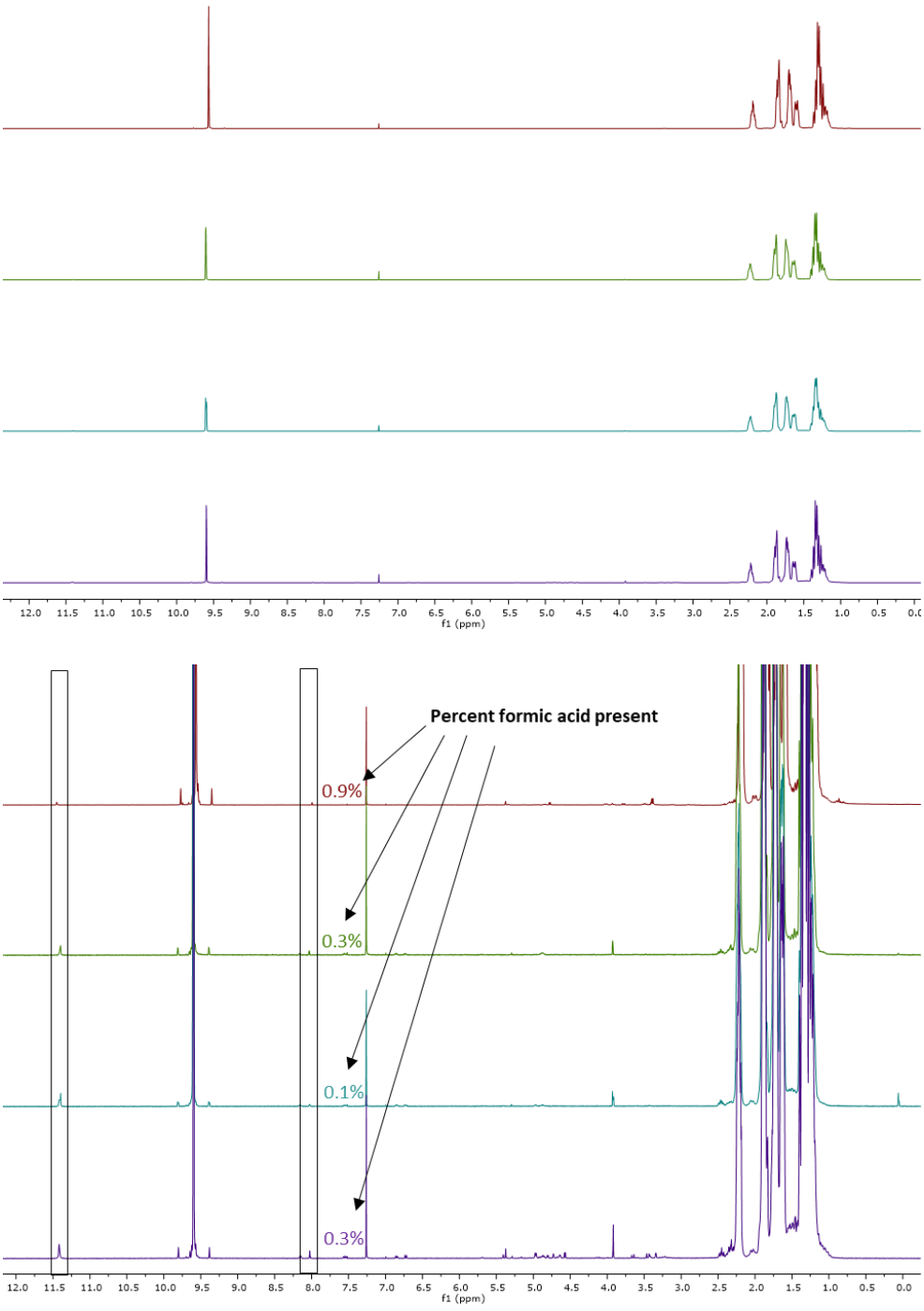

Figure A2.17. ^{1}H NMR spectra of CCA. The top red trace is of as-received CCA, while the other spectra are of CCA following distillation. Top: Complete spectra showing all resonances. Bottom: Expanded view spectra showing the resonances from acid impurities at 11.4 ppm and 8.0 ppm, which are attributed to cyclohexanecarboxylic acid and formic acid, respectively. The percentage of formic acid present was determined by integrating this peak relative to the aldehyde peak for CCA.

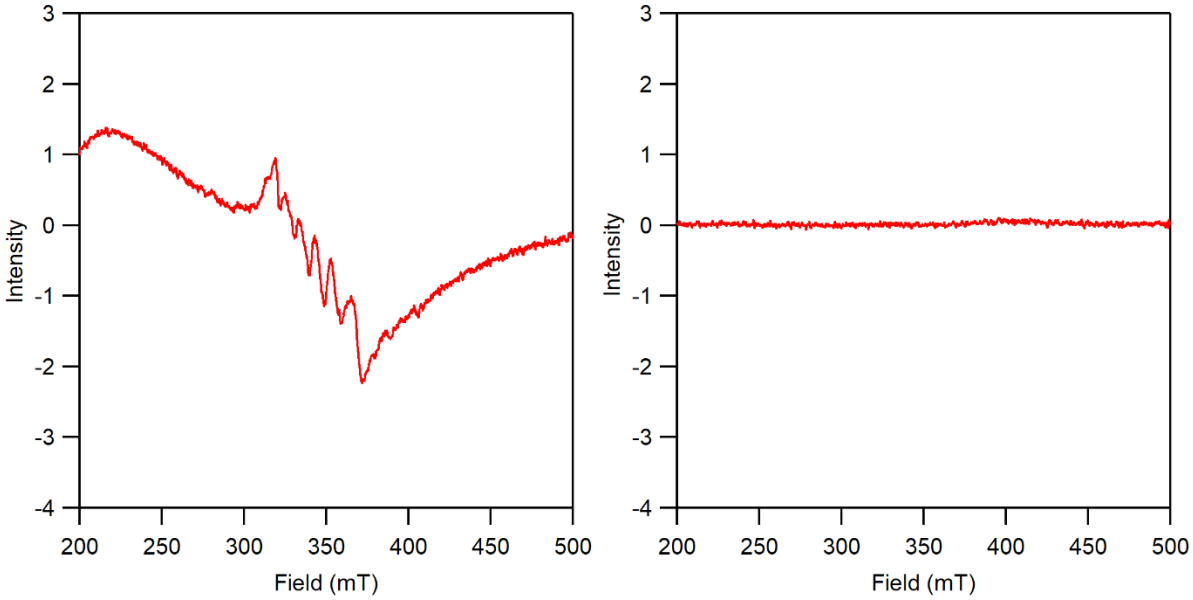

Figure A2.18. Perpendicular- (left) and parallel-mode (right) EPR spectra of $[Mn^{III}(O_2)(L^7BQ)]^+$ following the addition of cyclohexanecarboxylic acid.

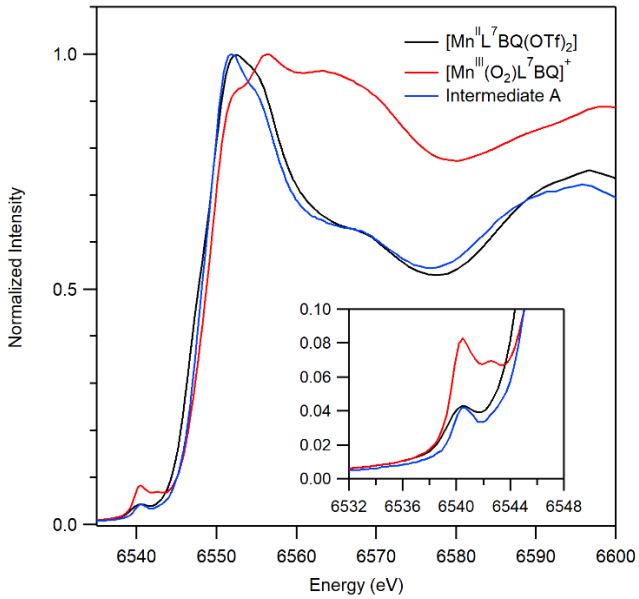

Figure A2.19. Comparison of X-ray absorption near edge structures of $[Mn^{III}(O_2)(L^7BQ)(OTf)_2]$ (black trace), $[Mn^{III}(O_2)(L^7BQ)]^+$ (red trace), and intermediate A (blue trace).

Table A2.4. Cartesian Coordinates for the DFT-optimized Structure of $[Mn^{III}(O_2)L^7BQ]^+$ with the Peroxo Bound on the Propyl-linked Face of the L^7BQ Ligand (Figure A2.11, top).

	X	Y	Z
Mn	-0.077993318	0.052291708	-0.037042407
O	-1.757596085	-0.741539254	0.092921937
O	-1.825512281	0.673309256	0.033004256
N	1.035216752	-1.752786393	-0.335699992
N	0.575766014	0.083285091	-2.257622547
N	1.013750677	1.940454871	-0.357466111
N	0.595304826	0.522698532	2.002320454
C	1.443193890	-2.576903757	0.614102789
C	1.659912611	-3.951873470	0.387104270
C	1.385059536	-4.475928812	-0.859040416
C	0.947859113	-3.618150484	-1.902214936
C	0.832923402	-2.230854116	-1.602619120
C	0.488223693	-1.298642774	-2.628056676
C	-0.315144102	1.017562870	-2.981807963
C	-0.003435419	2.469140515	-2.625758459
C	0.096713492	2.834878724	-1.147220821
C	0.357044357	-0.185020475	3.090251727
C	0.672490619	0.273188284	4.387549862
C	1.246213480	1.517976689	4.530210227
C	1.499281916	2.312421497	3.381124056
C	1.147392274	1.765572903	2.108296136
C	1.363830003	2.531678682	0.927202150
C	2.252225998	1.583811102	-1.108476050
C	1.990066297	0.547424868	-2.226471999
C	0.615679737	-4.067462715	-3.209823560
C	0.200860867	-3.161449880	-4.162543166
C	0.151673841	-1.771053063	-3.880919797
C	2.071642674	3.609739212	3.445929219
C	2.282171609	4.329012804	2.288744520
C	1.928993421	3.787721100	1.028866096
H	1.593951725	-2.151206061	1.607212378
H	2.008665290	-4.580286799	1.207462359
H	1.498770730	-5.544509661	-1.056192280
H	-0.194428717	0.909258808	-4.072261823
H	-1.350142304	0.752838247	-2.725130538
H	0.919130610	2.780322667	-3.137955469
H	-0.799558248	3.095913395	-3.056022426
H	-0.883514335	2.800971692	-0.655101855
H	0.461238828	3.870506118	-1.091183067
H	-0.109523286	-1.163038458	2.950708745
H	0.456681024	-0.360819507	5.248506958
H	1.506228425	1.908746571	5.516805115
H	2.718324260	2.492459768	-1.518871528
H	2.948281409	1.158514522	-0.375924872
H	2.265804157	0.947694010	-3.213939501
H	2.624025933	-0.326293867	-2.048348291
H	0.690508046	-5.132557873	-3.439796055
H	-0.067409773	-3.504787488	-5.164067732
H	-0.130552790	-1.079389823	-4.674721125
H	2.337937895	4.022493761	4.421523570
H	2.724539976	5.326277493	2.332091016
H	2.112710533	4.379401061	0.130621583

Table A2.5. Cartesian Coordinates for the DFT-optimized Structure of $[Mn^{III}(O_2)L^7BQ]^+$ with the Peroxo Bound on the Ethyl-linked Face of the L^7BQ Ligand (Figure A2.11, bottom).

	X	Y	Z
Mn	0.000000000	0.000000000	0.000000000
O	1.735718240	0.000000000	0.694846300
O	1.735718240	0.000000000	-0.711695357
N	-0.465025601	2.116366370	0.456228537
N	-0.869168113	-0.056669920	2.060354374
N	-0.960207236	-2.061479980	0.352805697
N	-0.820911559	-0.596390625	-1.904218033
C	-0.386078425	3.153416070	-0.356336573
C	-0.138743204	4.467151097	0.098316826
C	0.072335652	4.677597180	1.444277985
C	0.005555143	3.582989941	2.346681254
C	-0.303426365	2.302354474	1.801428673
C	-0.415996020	1.172530766	2.664907990
C	-2.373464777	-0.038347048	2.026840748
C	-2.972638606	-1.393357667	1.698967910
C	-2.456138525	-2.016053590	0.416088047
C	-0.944281441	0.148756046	-2.987542222
C	-0.868771407	-0.384505155	-4.292619363
C	-0.599677032	-1.727617635	-4.452838617
C	-0.457163403	-2.558103543	-3.309476110
C	-0.626630171	-1.947047490	-2.034959780
C	-0.575477142	-2.740187787	-0.849365824
C	-0.336098896	-2.479348630	1.620296424
C	-0.325670272	-1.305579969	2.650449435
C	0.245863139	3.699933770	3.742738977
C	0.177730647	2.584696507	4.550676700
C	-0.168602380	1.318168789	4.014373295
C	-0.148169600	-3.944886945	-3.368319879
C	-0.027740647	-4.677038028	-2.205250074
C	-0.263526028	-4.081080224	-0.939147809
H	-0.505354113	2.956739824	-1.424244645
H	-0.095723666	5.285028355	-0.622146453
H	0.297495904	5.675295762	1.828523136
H	-2.740889332	0.289511700	3.012418804
H	-2.676058704	0.718605518	1.288949157
H	-2.837175707	-2.084225758	2.543747816
H	-4.060667641	-1.261994399	1.594800808
H	-2.804678364	-1.445984966	-0.455607758
H	-2.845131178	-3.043902313	0.322528505
H	-1.089838024	1.220565154	-2.837812520
H	-0.992460013	0.279018688	-5.149344854
H	-0.492016471	-2.163632710	-5.448812782
H	-0.845684000	-3.355797041	2.050802786
H	0.697289572	-2.767144157	1.395808012
H	-0.884509342	-1.584742669	3.555498948
H	0.709187376	-1.101234416	2.943938973
H	0.488855369	4.680695502	4.157377311
H	0.371269625	2.669546340	5.622168774
H	-0.255902413	0.461028663	4.683803081
H	-0.005932087	-4.414175929	-4.344173149
H	0.220909722	-5.739575389	-2.250195743
H	-0.222999309	-4.696413243	-0.038757932

Appendix 3

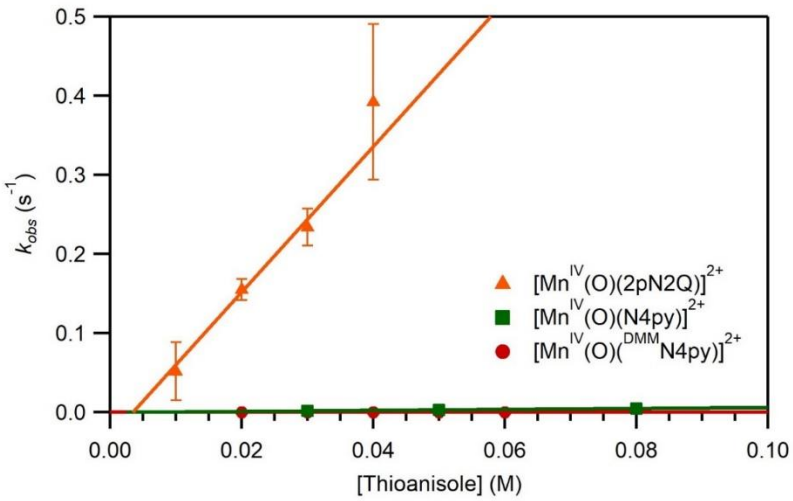

Figure A3.1 Full spectrum view of pseudo-first order rate constants (k_{obs}) versus thioanisole concentration for 1.0 mM of each complex in TFE at 298 K.

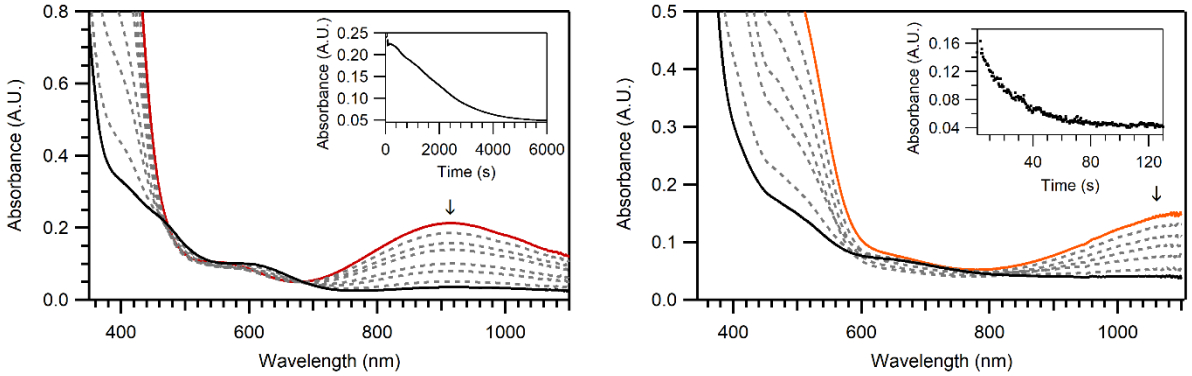

Figure A3.2 Electronic absorption spectra showing the disappearance of [Mn^{IV}(O)(^{DMM}N4py)]$^{2+}$ following the addition of 50 equiv. thioanisole (left) and following the addition of 10 equiv. thioanisole (right).

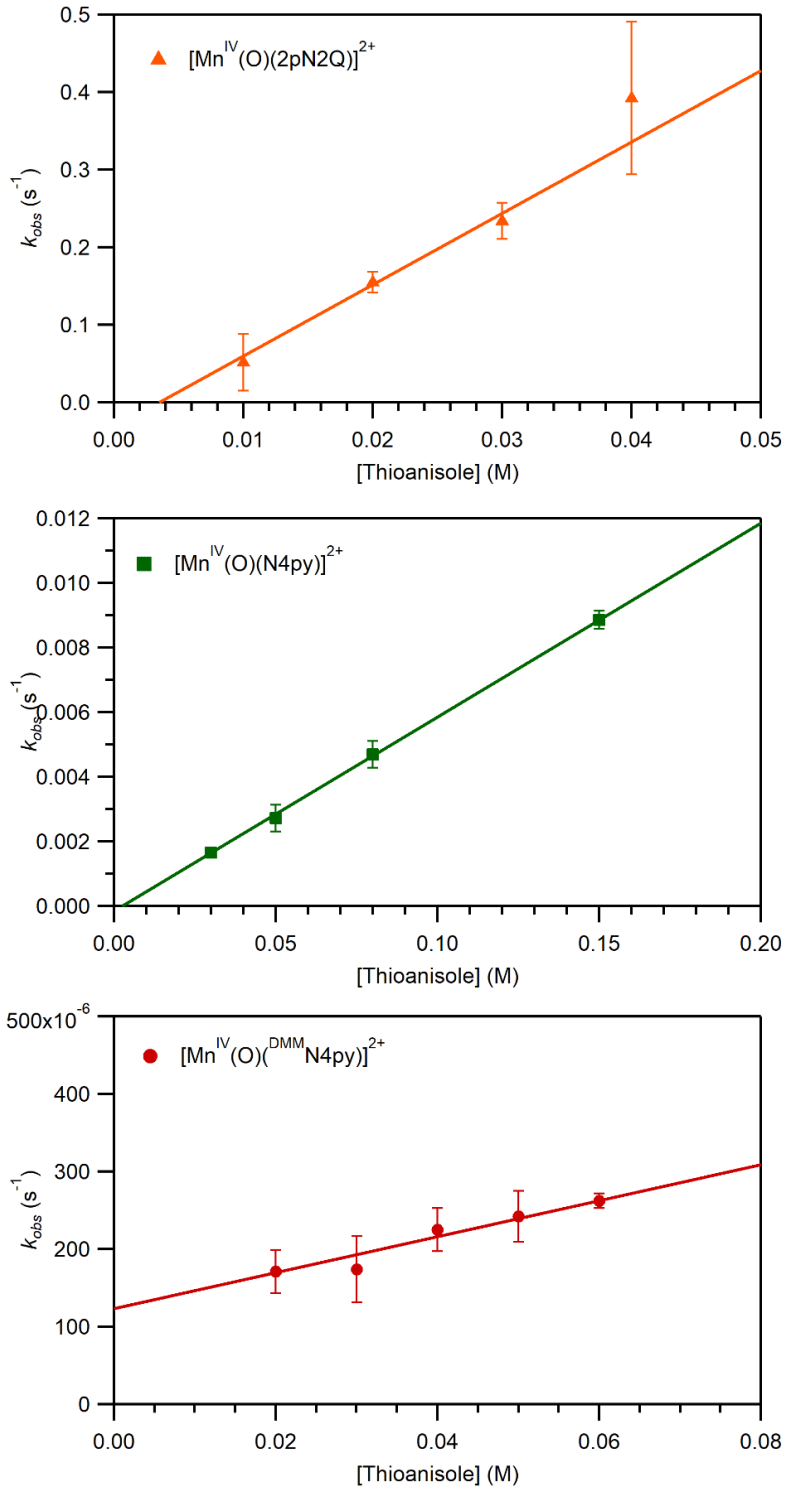

Figure A3.3 Plots of pseudo-first order rate constants for thioanisole oxidation by $[Mn^{IV}(O)(2pyN2Q)]^{2+}$ (top), $[Mn^{IV}(O)(N4py)]^{2+}$ (middle) and $[Mn^{IV}(O)(^{DMM}N4py)]^{2+}$ (bottom) as a function of thioanisole concentration.

Appendix 4

Table A4.1. Crystal Data and Structure Refinement

Identification	$Mn^{II}(OH_2)(2pyN2B)](OTf)_2$	
CCDC Identification Code	1874429	
Empirical formula	$C_{35}H_{39}F_6MnN_7O_8S_2$	
Formula weight	918.79	
Temperature	228 K	
Wavelength	0.71073 Å	
Crystal system	Orthorhombic	
Space group	Pnma – D_{2h}^{16} (No. 62)	
Unit cell dimensions	**a** = 19.166(2) Å	**α** = 90.000°
	b = 19.200(2) Å	**β** = 90.000°
	c = 11.2881(12) Å	**γ** = 90.000°
Volume	4153.9(8) Å3	
Z	4	
Density (calculated)	1.469 g/cm^3	
Absorption coefficient	0.50 mm^{-1}	
F(000)	1892	
Crystal size	0.450 x 0.180 x 0.180 mm^3	
Theta range for data collection	2.125 to 28.280°.	
Index ranges	$-25\leq h\leq 25$, $-25\leq k\leq 25$, $-15\leq l\leq 15$	
Reflections collected	55690	
Independent reflections	5299 [R_{int} = 0.059]	
Completeness to theta = 27.500°	99.9 %	
Absorption correction	Multi-scan	
Max. and min. transmission	1.000 and 0.768	
Refinement method	Full-matrix least-squares on F^2	
Data / restraints / parameters	5299 / 0 / 331	
Goodness-of-fit on F^2	1.053	
Final R indices [I>2sigma(I)]	R_1 = 0.048, wR_2 = 0.124	
R indices (all data)	R_1 = 0.071, wR_2 = 0.145	
Extinction coefficient	n/a	
Largest diff. peak and hole	0.53 and -0.45 e$^-$/Å^3	

Table A4.2. Comparison of Structural Properties of perchlorate and triflate salts of $[Mn^{II}(OH_2)(2pyN2B)]^{2+}$.

	$[Mn^{II}(OH_2)(2pyN2B)](ClO_4)_2$	$[Mn^{II}(OH_2)(2pyN2B)](OTf)_2$
CCDC Entry Number	1891620	1874429
Mn–O	2.076(7)	2.087(3)
$Mn–N_{benzimidazolyl}$	2.181(5)	2.193(2)
$Mn–N_{benzimidazolyl}$	2.181(5)	2.193(2)
$Mn–N_{pyridyl}$	2.311(5)	2.298(2)
$Mn–N_{pyridyl}$	2.311(5)	2.298(2)
$Mn–N_{amine}$	2.353(7)	2.375(3)
$Mn–N_{equatorial}$ [b]	2.246	2.246
$Mn–N_{total}$ [c]	2.267	2.271

[a] Average of the Mn–N bond distances in the equatorial positions. [b] Average of all Mn–N bond distances.

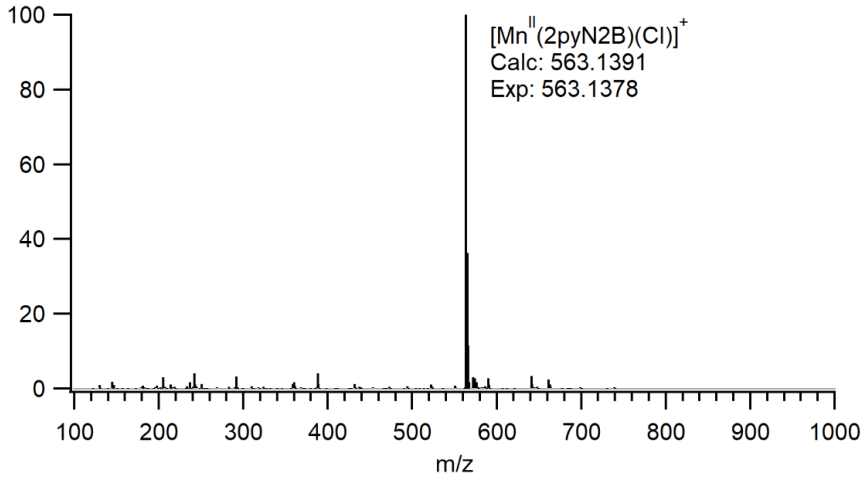

Figure A4.1. ESI-MS of $[Mn^{II}(OH_2)(2pyN2B)](OTf)_2$.

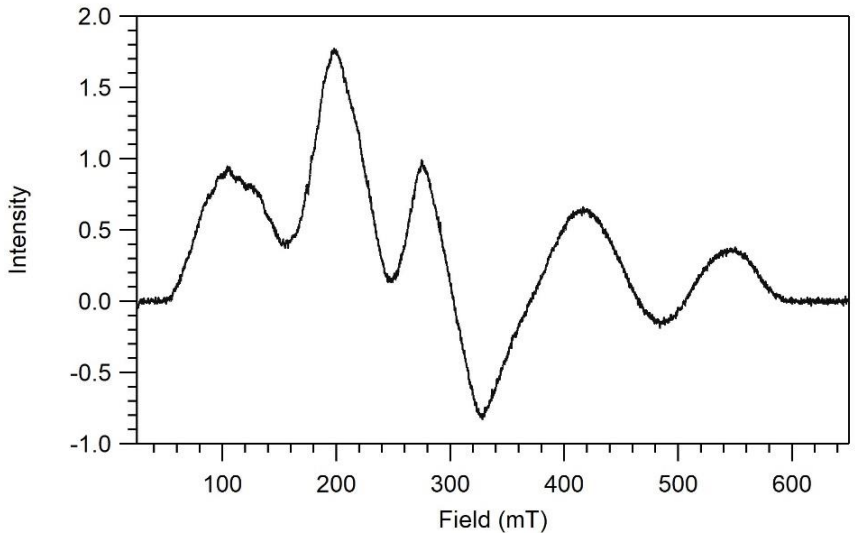

Figure A4.2. Perpendicular mode EPR of 1 mM $[Mn^{II}(OH_2)(2pyN2B)](OTf)_2$ in TFE at 10K.

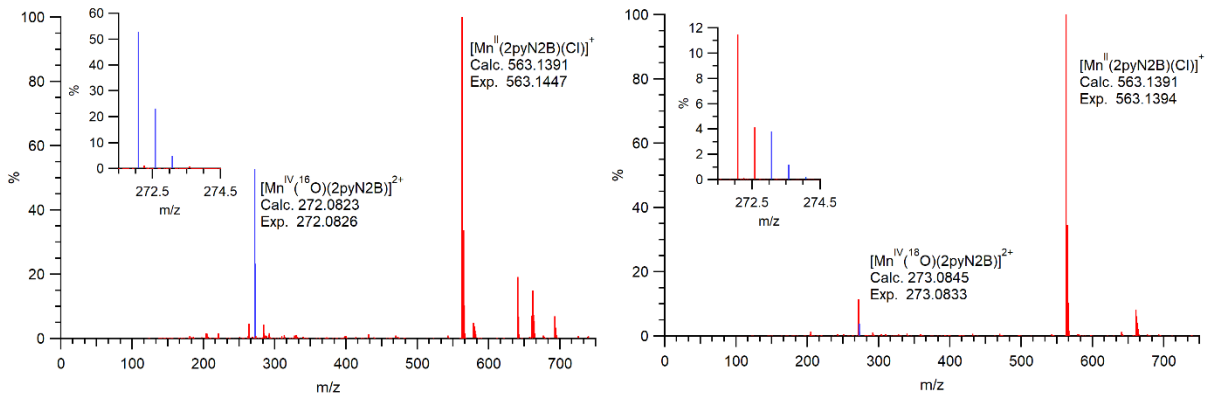

Figure A4.3. ESI-MS of $[Mn^{IV}(^{16}O)(2pyN2B)]^{2+}$ (left) and $[Mn^{IV}(^{18}O)(2pyN2B)]^{2+}$ (right).

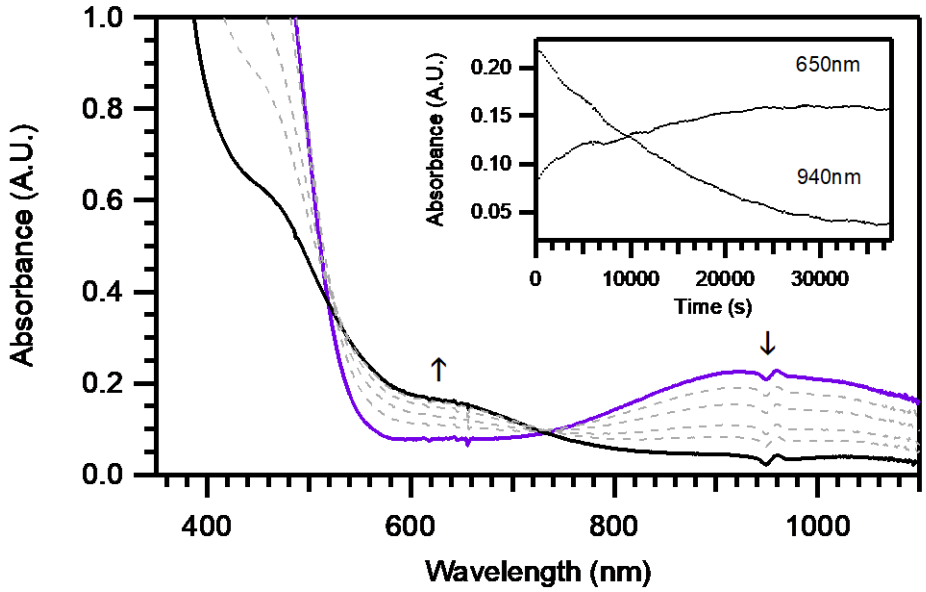

Figure A4.4. Electronic absorption spectra showing the thermal decay of 1 mM $[Mn^{IV}(O)(2pyN2B)]^{2+}$ in TFE at 25 °C.

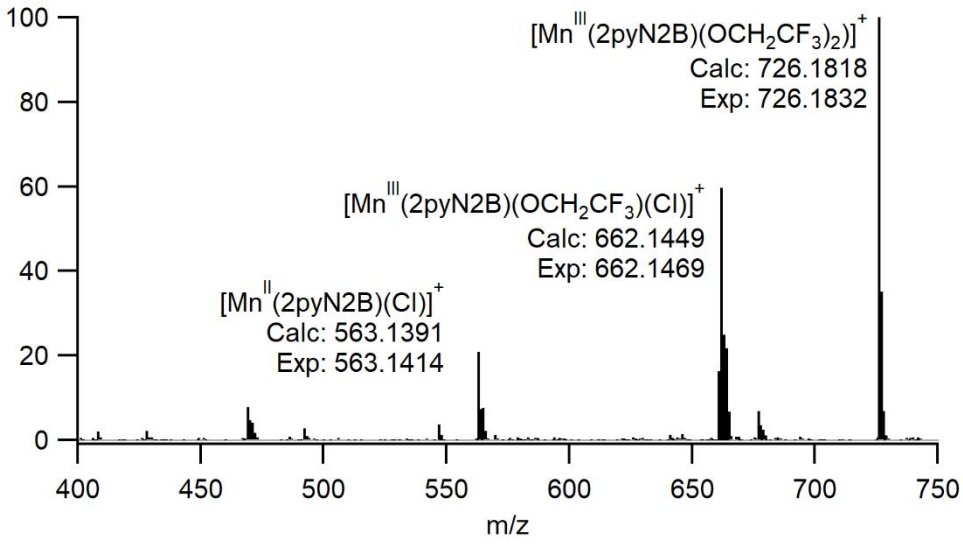

Figure A4.5. ESI-MS of the self decay of 1 mM $[Mn^{IV}(O)(2pyN2B)]^{2+}$ in TFE.

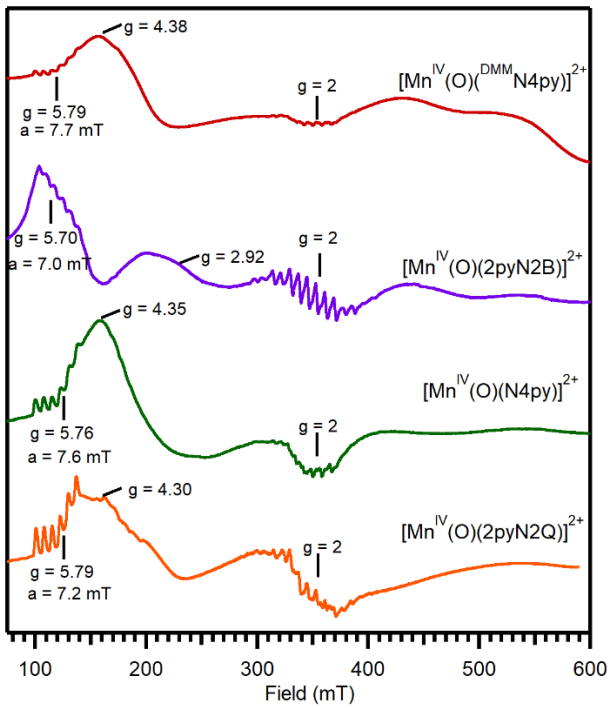

Figure A4.6. Perpendicular-mode X-band EPR spectra of $[Mn^{IV}(O)(^{DMM}N4py)]^{2+}$, $[Mn^{IV}(O)(2pyN2B)]^{2+}$, $[Mn^{IV}(O)(N4py)]^{2+}$, and $[Mn^{IV}(O)(2pyN2Q)]^{2+}$. All experiments were carried out at 5 K, except that of $[Mn^{IV}(O)(2pyN2B)]^{2+}$, which was collected at 10 K. Data for $[Mn^{IV}(O)(^{DMM}N4py)]^{2+}$, $[Mn^{IV}(O)(N4py)]^{2+}$, and $[Mn^{IV}(O)(2pyN2Q)]^{2+}$ are from references [1] and [2].

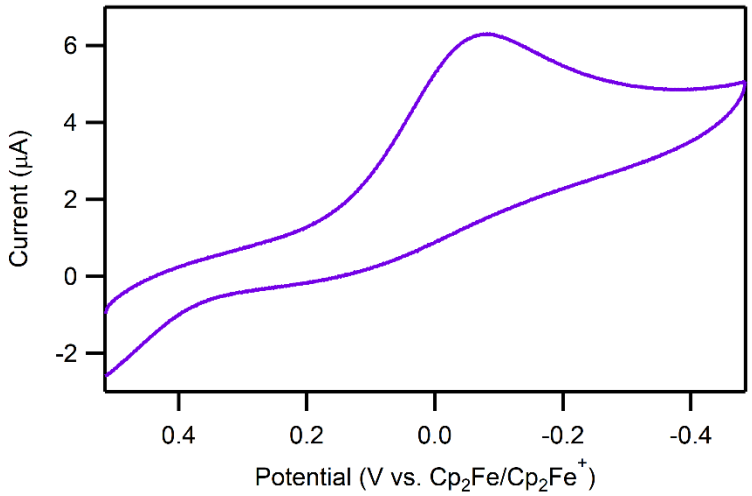

Figure A4.7. Cyclic voltammogram of $[Mn^{IV}(O)(2pyN2B)]^{2+}$ recorded in TFE with 0.1 M Bu_4NPF_6 electrolyte solution at 50 mV s^{-1}. This data was collected by Allyssa Massie.

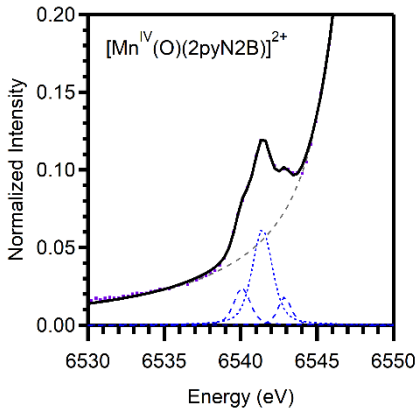

Figure A4.8. Comparison of the normalized XAS pre-edge data (dotted line) and fits (solid line) for the $[Mn^{IV}(O)(2pyN2B)]^{2+}$. The dashed traces represent the fit of the background and fits to the pre-edge peak. This data was fit by Allyssa Massie.

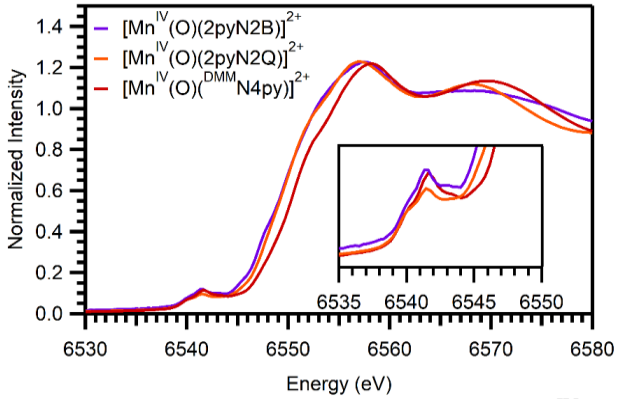

Figure A4.9. Comparison of experimental XANES regions for $[Mn^{IV}(O)(^{DMM}N4py)]^{2+}$, $[Mn^{IV}(O)(2pyN2B)]^{2+}$, and $[Mn^{IV}(O)(2pyN2Q)]^{2+}$.

Table A4.3. Selected Bond Lengths (Å) and Bond Angles for Oxomanganese(IV) Complexes $[Mn^{IV}(O)(N4py)]^{2+}$, $[Mn^{IV}(O)(^{DMM}N4py)]^{2+}$, $[Mn^{IV}(O)(2pyN2Q)]^{2+}$ and $[Mn^{IV}(O)(2pyN2Q)]^{2+}$ from DFT Computations.

	$[Mn^{IV}(O)(2pyN2B)]^{2+}$	$[Mn^{IV}(O)(N4py)]^{2+}$	$[Mn^{IV}(O)(^{DMM}N4py)]^{2+a}$	$[Mn^{IV}(O)(2pyN2Q)]^{2+a}$
Mn–O	1.671	1.673	1.678	1.678
$Mn–N_X$ [b]	1.974	2.025	1.988	2.066
$Mn–N_X$ [b]	1.974	2.026	1.989	2.066
$Mn–N_{pyridyl}$	2.047	2.012	2.041	2.043
$Mn–N_{pyridyl}$	2.048	2.011	2.041	2.042
$Mn–N_{amine}$	2.174	2.118	2.108	2.109
$Mn–N_{equatorial}$ [c]	2.011	2.018	2.015	2.054
$Mn–N_{total}$ [d]	2.043	2.038	2.033	2.065
$N_{amine}–Mn=O$	177.48	179.55	179.76	170.63

[a] From reference 1. [b] N_X is $N_{benzimidazolyl}$ for $[Mn^{II}(OH_2)(2pyN2B)]^{2+}$, $N_{pyridyl}$ for $[Mn^{II}(OTf)(N4py)]^{+}$, $N_{3,5\text{-dimethyl-4-methoxypyridyl}}$ for $[Mn^{II}(OTf)(^{DMM}N4py)]^{+}$, and $N_{quinolinyl}$ for $[Mn^{II}(OH_2)(2pyN2Q)]^{2+}$. [c] Average of the Mn–N bond distances in the equatorial positions. [d] Average of all Mn–N bond distances.

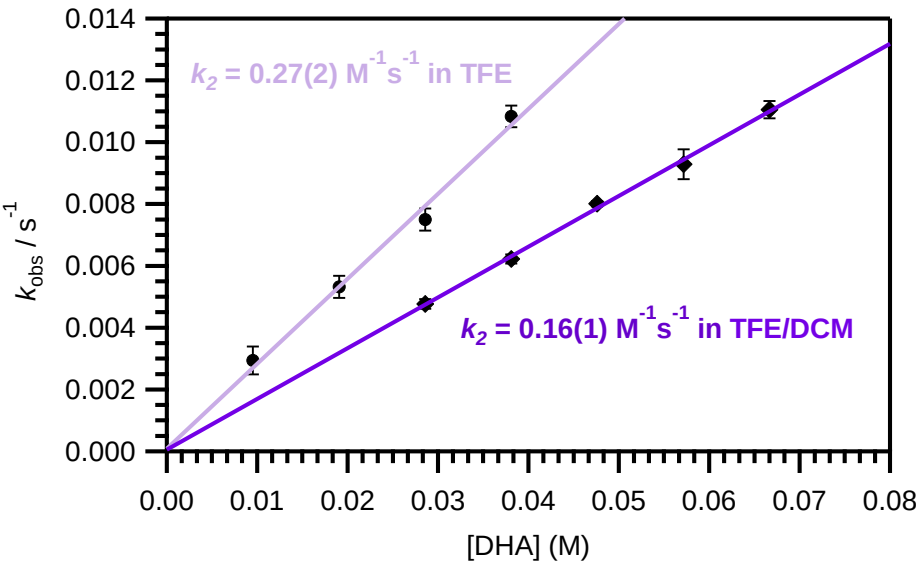

Figure A4.10. Pseudo-first-order rate constants (k_{obs}) vs. DHA concentration for $[Mn^{IV}(O)(2pyN2B)]^{2+}$ in TFE and TFE/DCM at 25 °C. The lines represent best fits to the data used to determine the second-order rate constants (k_2).

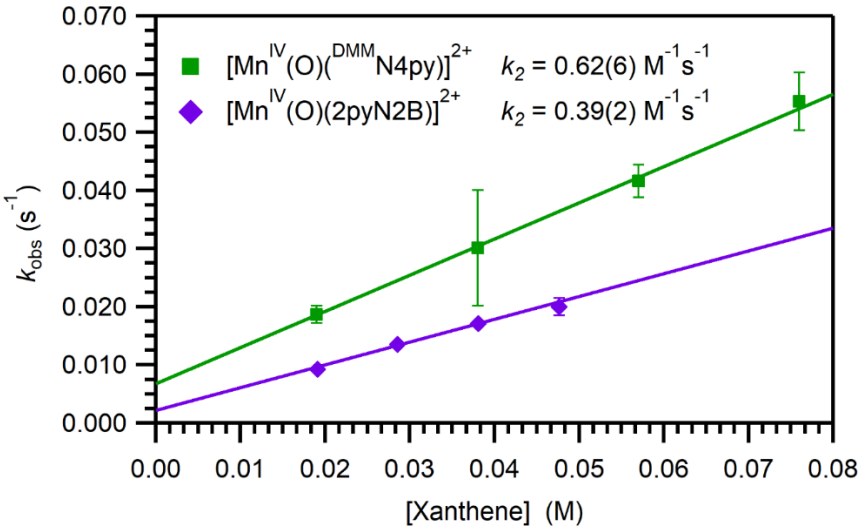

Figure A4.11. Pseudo-first order rate constants (k_{obs}) vs. xanthene concentration for [Mn^{IV}(O)(2pyN2B)]$^{2+}$ (purple) and for [Mn^{IV}(O)(^{DMM}N4py)]$^{2+}$ (green) in 1:1 TFE:CH_2Cl_2 at 25 °C. The lines represent best fits to the data used to determine the second-order rate constants (k_2).

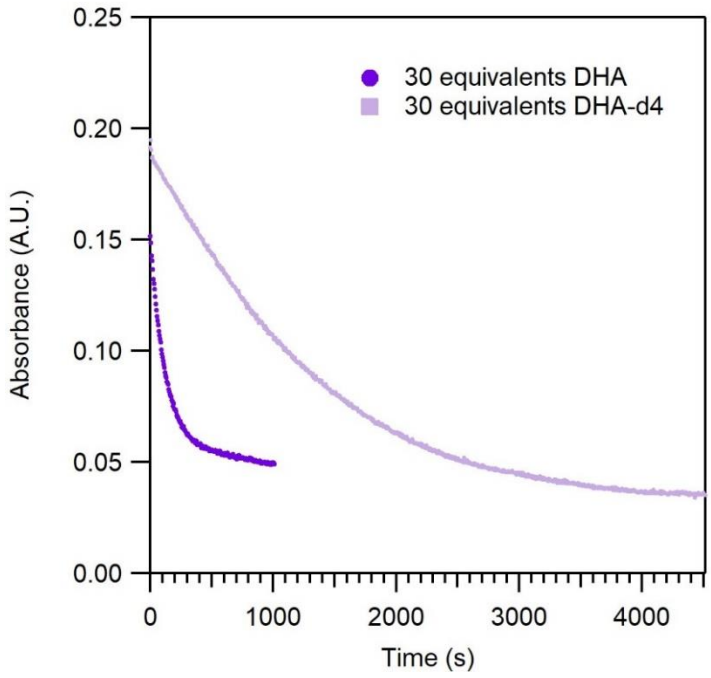

Figure A4.12. Time trace of the decay of the 940 nm electronic absorption signal of a 1 mM solution of [Mn^{IV}(O)(2pyN2B)]$^{2+}$ in TFE at 25 °C upon the addition of 30 equivalents DHA dark purple circles) and [D_4]-DHA (light purple squares).

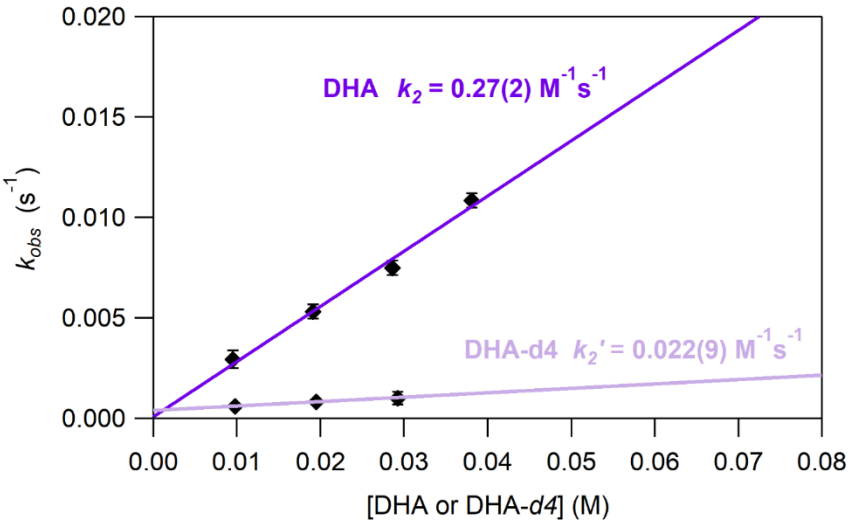

Figure A4.13. Pseudo-first order rate constants (k_{obs}) vs. DHA (dark purple) and DHA-d4 (light purple) $[Mn^{IV}(O)(2pyN2B)]^{2+}$ in TFE at 25 °C. The lines represent best fits to the data used to determine the second-order rate constants (k_2).

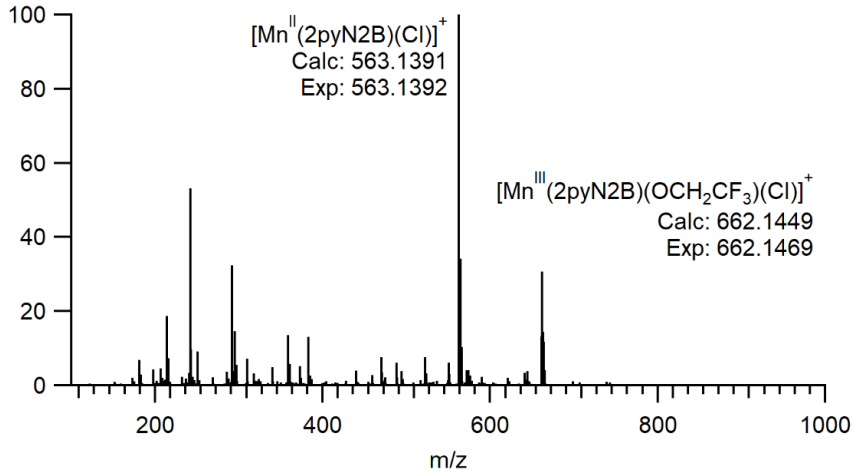

Figure A4.14. ESI-MS following the reaction of 1.0 mM $[Mn^{IV}(O)(2pyN2B)]^{2+}$ in TFE with 40 equivalents of DHA.

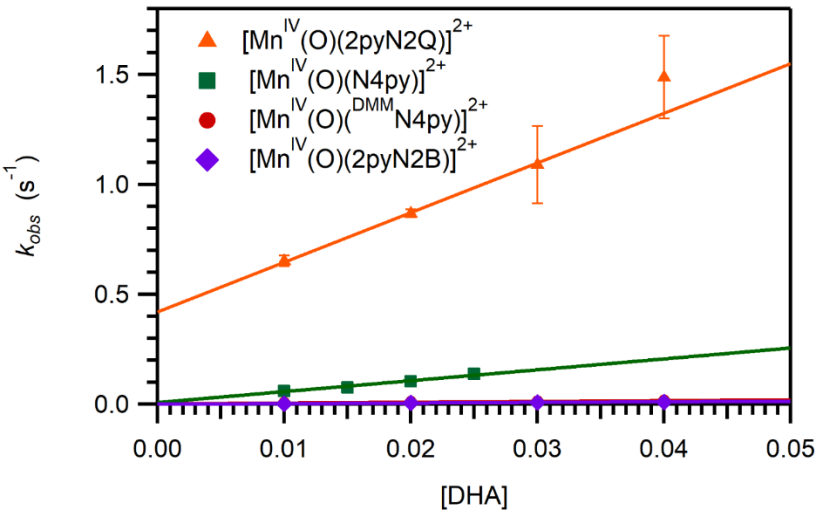

Figure A4.15. Pseudo-first-order rate constants (k_{obs}) versus DHA concentration for oxomanganese(IV) species, showing experimental data for $[Mn^{IV}(O)(2pyN2Q)]^{2+}$. Rate data for $[Mn^{IV}(O)(^{DMM}N4py)]^{2+}$ and $[Mn^{IV}(O)(2pyN2Q)]^{2+}$ are from reference [1]; data for $[Mn^{IV}(O)(N4py)]^{2+}$ are from reference [2].

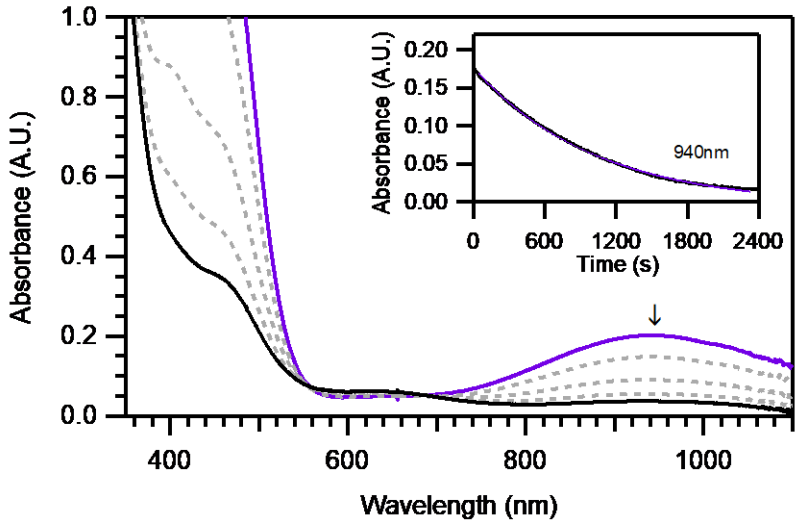

Figure A4.16. Electronic absorption spectra showing the reaction of 1.0 mM $[Mn^{IV}(O)(2pyN2B)]^{2+}$ (purple trace) with 40 equivalents of thioanisole in TFE at 25 °C. Inset: decay of the feature at 940nm over time.

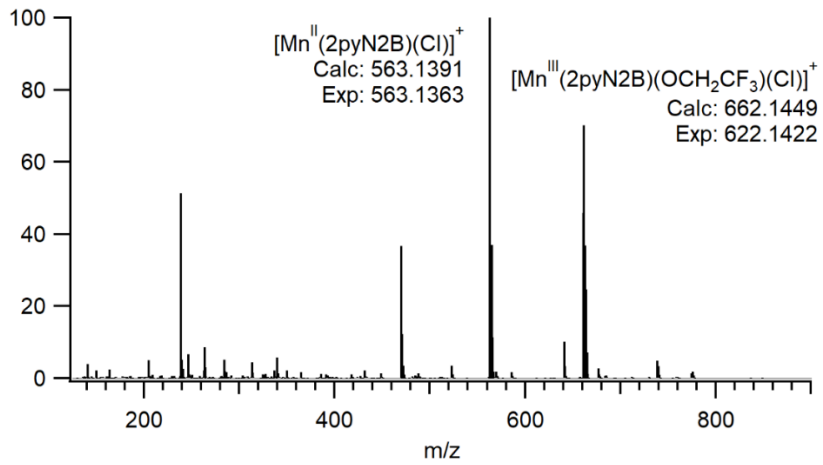

Figure A4.17. ESI-MS following the reaction of 1.0 mM $[Mn^{IV}(O)(2pyN2B)]^{2+}$ in TFE with 40 equivalents of thioanisole.

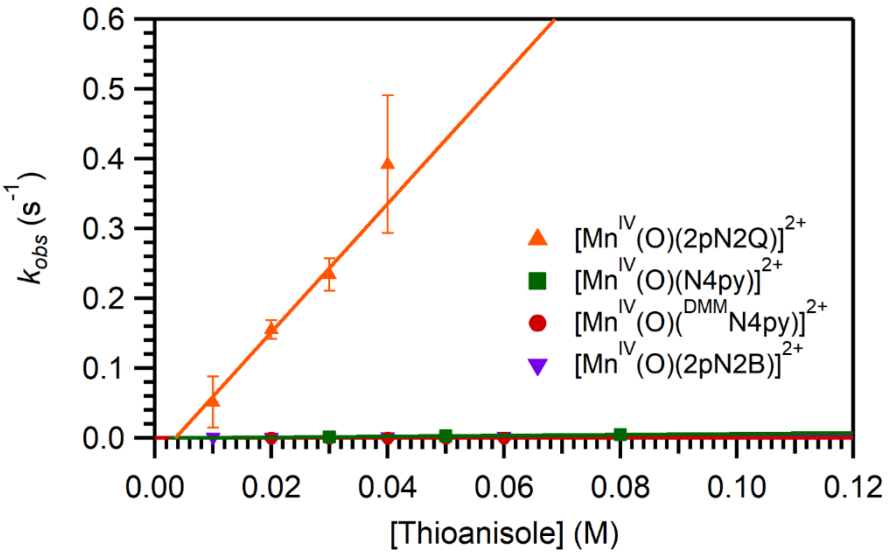

Figure A4.18. Pseudo-first-order rate constants (k_{obs}) versus thioanisole concentration for oxomanganese(IV) species showing experimental data for $[Mn^{IV}(O)(2pyN2Q)]^{2+}$. Rate data for $[Mn^{IV}(O)(^{DMM}N4py)]^{2+}$, $[Mn^{IV}(O)(N4py)]^{2+}$, and $[Mn^{IV}(O)(2pyN2Q)]^{2+}$ are from reference [1].

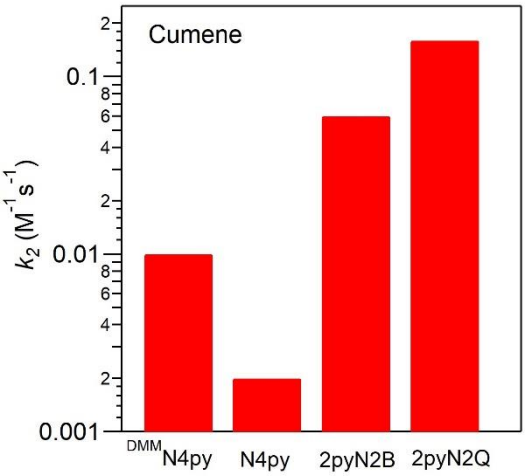

Figure A4.19. Comparison of second-order rate constants for cumene oxidation by $[Fe^{IV}(O)(^{DMM}N4py)]^{2+}$, $[Fe^{IV}(O)(N4py)]^{2+}$, and $[Fe^{IV}(O)(2pyN2B)]^{2+}$. Data taken from references [3], [4], and [5], respectively.

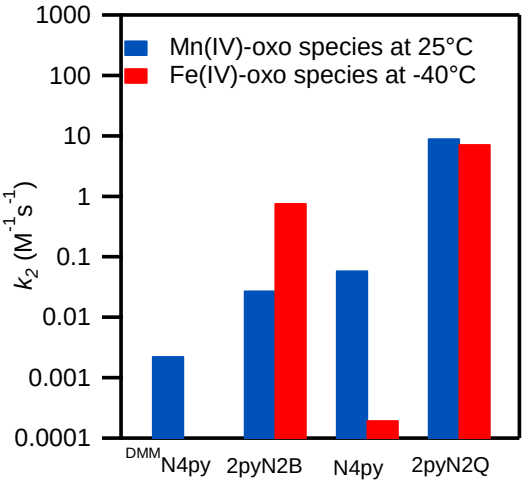

Figure A4.20. Comparison of the rates of reaction of thioanisole with oxomanganese(IV) at 25ºC and oxoiron(IV) species at -40ºC supported by N4py and its derivatives. Oxoiron(IV) species (excluding ^{DMM}N4py) are shown in red, oxomanganese(IV) species are shown in blue.

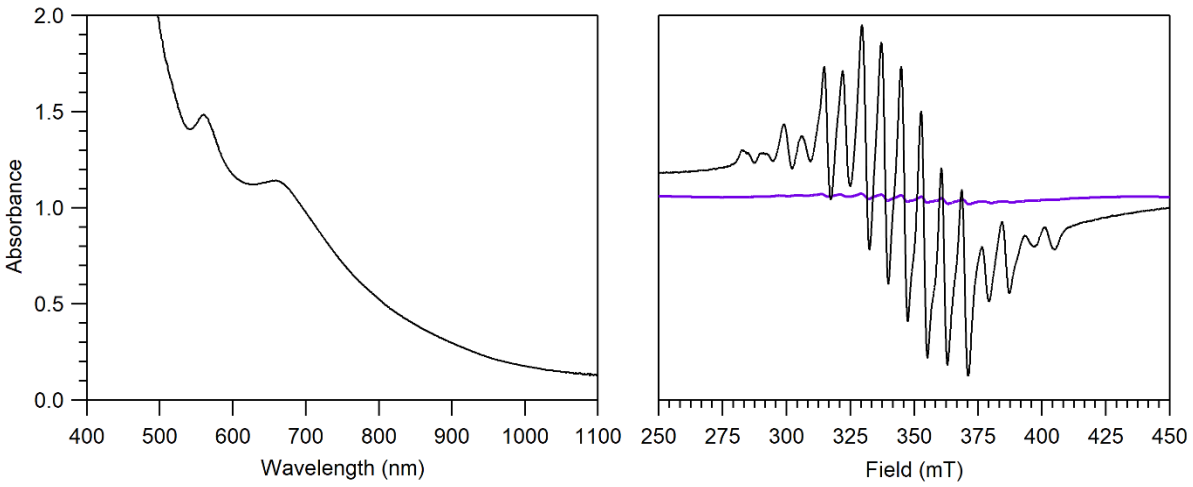

Figure A4.21. A sample of $[Mn^{III}Mn^{IV}(\mu\text{-}O)(^{DMM}N4py)_2)]^{2+}$ was prepared in TFE, according to a previously published protocol.[6] Left: Electronic absorption spectrum of 10mM $[Mn^{III}Mn^{IV}(\mu\text{-}O)(^{DMM}N4py)_2)]^{2+}$. Right: 5mM $[Mn^{III}Mn^{IV}(\mu\text{-}O)(^{DMM}N4py)_2)]^{2+}$ in TFE (black trace) and 10mM $[Mn^{IV}(O)(2pyN2B)]^{2+}$ (purple trace, see Figure 4.3 for full spectrum). The $Mn^{III}Mn^{IV}$ signal in the purple trace is very weak compared to that of pure dimer of a closely related complex, suggesting it represents a small fraction of the Mn in the sample.

Table A4.4. Cartesian Coordinates for $[Mn^{IV}(O)(2pyN2B)]^{2+}$ Optimized by DFT Computations.

Atom	x	y	z
Mn	-0.00097035663382	0.23022457549271	-0.60243137675133
O	-0.04306675263990	0.41759964354642	1.05757272577181
N	0.12312599294241	0.05209860938857	-2.76588936855174
N	-1.92537700337637	0.38798726502742	-1.01215777214240
N	-3.59790345194925	0.54791581668974	-2.48756868676180
N	2.03351311259927	0.19207611460063	-0.82871069685590
C	-1.18204945278439	0.49972488920407	-3.36974985003010
C	-2.25326594340202	0.45110494286929	-2.31182392906430
C	-3.11611281567467	0.44883307937452	-0.28213349948636
C	-4.18188741045777	0.55207571394838	-1.20819736504342
C	-4.34532616980656	0.66368366218846	-3.74916862061893
C	-5.52114228223479	0.63817473534084	-0.80160693064979
C	-5.75051966823919	0.61920009892809	0.57801880681712
C	-4.68930541040975	0.51757296202600	1.50995945560605
C	-3.35574180494736	0.42905981131732	1.10180566281541
C	1.26224086630206	1.04110661510544	-2.94253424264619
C	2.42377329272527	0.54804749782097	-2.08178453176260
C	2.94676363710445	-0.16030953482708	0.09703033951315
C	4.31300866010966	-0.18077501026841	-0.20889191601382
C	4.72738146774743	0.16919548069245	-1.50035872994253
C	3.76807115771406	0.54480543629904	-2.45715933324680
N	-0.04149917842910	-1.73979026076264	-0.72744191586075
N	0.06152483467532	-3.61716060490518	-1.93770638688253
N	0.24751165318749	2.20158826105203	-1.09766955836672
C	0.48067963461705	-1.36856479608596	-3.11702148028336
C	0.14069421318853	-2.26010919290603	-1.95108481057025
C	-0.25239950581609	-2.80834997724692	0.14866719046906
C	-0.18781184761323	-4.00275311477163	-0.60852905838872
C	0.22222391257045	-4.55030329730928	-3.06341006566399
C	-0.35817784256391	-5.26755054284148	-0.02766353356259
C	-0.59536206581882	-5.28751806719751	1.35053933401939
C	-0.65894739491675	-4.09674907911723	2.11459469193215
C	-0.49075605074528	-2.83747260251772	1.53266296304841
C	0.80846342768646	2.36282152934957	-2.32575341691500
C	-0.10697893531683	3.27305064587622	-0.36241289596025
C	0.07972223732698	4.57363031454978	-0.84688521774973
C	0.64124289912801	4.75366862200693	-2.11707209644554
C	1.01711954311395	3.62947783750489	-2.87338531447491
H	-1.06313684833705	1.53627388209681	-3.73266220812823
H	-1.43491929249199	-0.12152843671609	-4.24601340631399
H	-3.65473636236250	0.58065964176494	-4.59891029969759
H	-5.09222933737218	-0.14379713371336	-3.80654054569848
H	-4.85541401842777	1.63941700452368	-3.78839164835261
H	-6.34625517979383	0.71979122642154	-1.51439155894029
H	-6.77835380052529	0.68769613439485	0.94648681642882
H	-4.92340810320859	0.51035019138015	2.57884916388937
H	-2.52760000933402	0.35600220883053	1.81094144615493
H	1.56337475126307	1.16732751712954	-3.99676516403551
H	2.54872785600703	-0.41122815625696	1.08383973531408
H	5.03595047461784	-0.46203133201947	0.56168558301908
H	5.78966448708975	0.15885500202338	-1.76426687211040
H	4.06508999271172	0.83601807437826	-3.46893509842401
H	1.56592498088444	-1.41613115355139	-3.31970772680898
H	-0.03464381955914	-1.67896603837193	-4.04172444769668

H	0.36828855310304	-3.98772953495021	-3.99500167409681
H	-0.68108868284121	-5.17440771200321	-3.15205811694312
H	1.09799621691548	-5.19500574745335	-2.88691866134319
H	-0.30813373796553	-6.19131073740234	-0.61017035980153
H	-0.73431568679252	-6.25004281037415	1.85167455662552
H	-0.84489297726867	-4.16843447372878	3.19041446127178
H	-0.53263111095093	-1.91215593833031	2.11214631976379
H	-0.53033678368097	3.05376430540777	0.62126924255412
H	-0.20856956527432	5.42780415723255	-0.22845301083924
H	0.79469877901072	5.76019492672753	-2.51846081108764
H	1.46837432489423	3.74143870300788	-3.86344842155496

Table A4.5. Cartesian Coordinates for $[Mn^{IV}(O)(N4py)]^{2+}$ Optimized by DFT Computations.

Atom	x	y	z
Mn	-0.23633646371276	0.60328106557608	0.91458632057475
O	0.18624376401618	2.16543911466274	1.34036633424372
N	0.43421312984041	-0.30223186612636	2.58178711605595
N	1.48550802625649	0.12612225028571	-0.00871225846301
N	-2.13345191346404	0.58217995021707	1.62364209011379
N	-1.13231987443518	0.99140771618478	-0.86013086676241
C	0.19280989312914	-1.63978889468179	2.67260674519352
C	-2.89068861939440	-0.37358888148184	1.01662994780429
C	1.52323143716089	-1.10017122781278	-0.60083281027177
N	-0.75561114458402	-1.37907045842057	0.37864818316473
C	-1.98966456115381	-0.00354333078124	-1.22243977058740
C	-0.95053402681276	2.06503946821093	-1.65612294114020
C	-2.65801692876309	1.36371822614909	2.58919448782632
C	0.70673286844912	-2.38987967925658	3.73505125332755
C	-4.77084020085366	0.21067269832217	2.39962228836442
C	2.70504279608784	-1.58517051831976	-1.16928802459247
C	-0.72565828032329	-2.22893761985374	1.61780964579224
C	0.20330093301152	-1.84556081888592	-0.68091191821195
C	2.59228030870613	0.90694435631226	0.02227862549224
C	1.16547160317044	0.32802118519923	3.53278476714803
C	1.69192573777111	-0.36486872913064	4.62361351452081
C	-2.15112277463869	-1.05966643243667	-0.13091770227945
C	3.85584864159685	-0.78350180834461	-1.13998173798026
C	-2.49237797213144	1.15057344709359	-3.27384216584020
C	1.46542307679809	-1.74501077507588	4.72287947631398
C	-1.62177108050751	2.17501320672440	-2.87941922646567
C	3.79625656122614	0.48327276814988	-0.54207701022019
C	-3.98528165746621	1.20159842977850	3.00236407164961
C	-4.21855129621158	-0.59074952149901	1.38409998710551
C	-2.68653290246197	0.04151834506394	-2.43002445645423
H	-0.26616466582444	2.82884032132236	-1.27738044224007
H	-1.98877902552188	2.12114343107462	3.00609110945982
H	0.50913448405773	-3.46466241608803	3.79268959287058
H	-5.80944545366317	0.06179030104581	2.71054836781407
H	2.72333300081392	-2.57475770871569	-1.63509472725440
H	-0.43766175703439	-3.26560942655779	1.37412950135833
H	-1.74887797460305	-2.26812757268335	2.03077332365422
H	0.35708302000294	-2.93595996226629	-0.61621153454300
H	-0.25138344137920	-1.64223567219133	-1.66671509006290
H	2.46571768647782	1.87365397331598	0.51728910732544
H	1.30628691188510	1.40154036252504	3.37638398497758

H	2.27461644915710	0.17247661406573	5.37716816283863
H	-2.69434606145817	-1.94713761182281	-0.49690950629178
H	4.78935767645011	-1.14625842975516	-1.58108344123076
H	-3.02399888189002	1.21174032225063	-4.22829780332844
H	1.87444550117795	-2.31657008641444	5.56196721762989
H	-1.46246302110947	3.05695617483135	-3.50617150268894
H	4.67188967138323	1.13733218222497	-0.50499241062410
H	-4.39142678698938	1.84992598098266	3.78387072268048
H	-4.81371305336651	-1.36461459557718	0.89026864591723
H	-3.36905835887215	-0.76687184739008	-2.70940224368414

References

1. Massie, A. A.; Denler, M. C.; Cardoso, L. T.; Walker, A. N.; Hossain, M. K.; Day, V. W.; Nordlander, E.; Jackson, T. A., Equatorial Ligand Perturbations Influence the Reactivity of Manganese(IV)-Oxo Complexes. *Angew. Chem., Int. Ed. Engl.* **2017,** *56* (15), 4178-4182.

2. Leto, D. F.; Ingram, R.; Day, V. W.; Jackson, T. A., Spectroscopic properties and reactivity of a mononuclear oxomanganese(iv) complex. *Chem. Commun.* **2013,** *49* (47), 5378-5380.

3. Rana, S.; Dey, A.; Maiti, D., Mechanistic elucidation of C–H oxidation by electron rich non-heme iron(iv)-oxo at room temperature. *Chem. Commun.* **2015,** *51* (77), 14469-14472.

4. Kaizer, J.; Klinker, E. J.; Oh, N. Y.; Rohde, J.-U.; Song, W. J.; Stubna, A.; Kim, J.; Münck, E.; Nam, W.; Que Jr., L., Nonheme FeIVO Complexes That Can Oxidize the C−H Bonds of Cyclohexane at Room Temperature. *J. Am. Chem. Soc* **2004,** *126* (2), 472-473.

5. Mitra, M.; Nimir, H.; Demeshko, S.; Bhat, S. S.; Malinkin, S. O.; Haukka, M.; Lloret-Fillol, J.; Lisensky, G. C.; Meyer, F.; Shteinman, A. A.; Browne, W. R.; Hrovat, D. A.; Richmond, M. G.; Costas, M.; Nordlander, E., Nonheme Fe(IV) Oxo Complexes of Two New Pentadentate Ligands and Their Hydrogen-Atom and Oxygen-Atom Transfer Reactions. *Inorg. Chem.* **2015,** *54* (15), 7152-7164.

6. Lee, Y.; Jackson, T. A., Ligand Influence on Structural Properties and Reactivity of Bis(μ-oxo)dimanganese(III,IV) Species and Comparison of Reactivity with Terminal MnIV-oxo Complexes. *ChemistrySelect* **2018,** *3* (47), 13507-13516.

Appendix 5

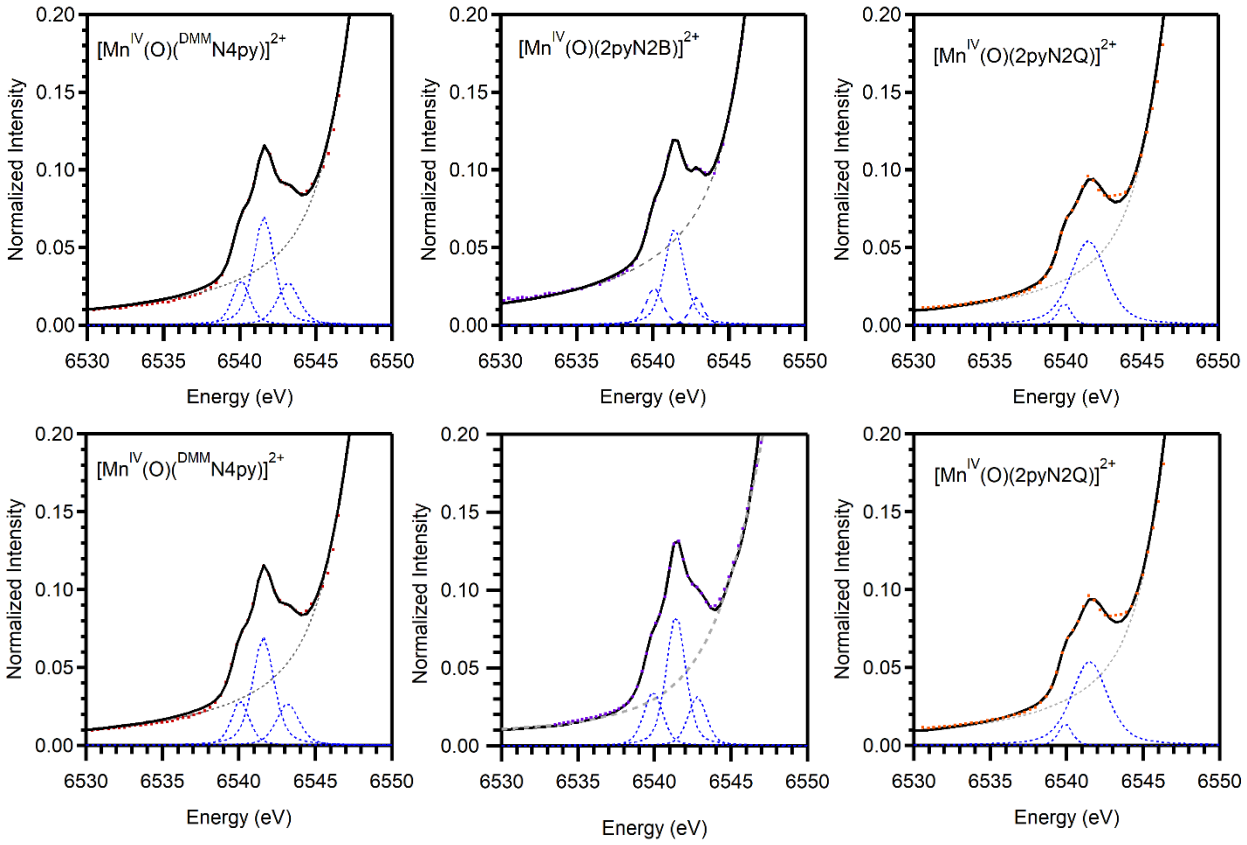

Figure A5.1. Comparison of the normalized XAS pre-edge data (dotted line) and fits (solid line) for the oxomanganese(IV) complexes. Dashed traces represent the fit of the background and fits to the pre-edge peak.

Table A5.1. EXAFS Fitting Parameters for $[Mn^{IV}(O)(^{DMM}N4py)]^{2+}$, *K 2-14*

	Mn-O/N			Mn-N			Mn•••C			Mn••N••C				
fit	N	r(Å)	σ^2	N	r(Å)	σ^2	N	r(Å)	σ^2	N	r(Å)	σ^2	E_0	R
1	6	2.19	30.8										10.7	0.746
2				6	2.15	24.2							7.47	0.729
3	1	1.70	1.00	5	1.99	11.6							-6.42	0.408
4	1	1.71	1.49	4	1.99	5.96							-3.37	0.341
				1	2.15	-0.13								
5	1	1.72	1.43	3	1.97	3.25							-2.58	0.334
				2	2.13	2.27								
7	1	1.72	1.65	3	1.98	3.97	3	2.92	3.80				0.565	0.247
				2	2.14	2.94								
8	1	1.71	1.23	3	1.96	4.27	3	2.92	2.28				-2.40	0.209
				2	2.12	3.63	4	2.74	10.8					
9	1	1.71	1.30	3	1.97	4.23	3	2.92	2.27				-2.06	0.211
				2	2.13	3.57	3	2.73	8.34					
10	**1**	**1.72**	**1.26**	**2**	**1.94**	**2.38**	**3**	**2.92**	**2.28**				**-1.79**	**0.208**
				3	**2.10**	**6.09**	**3**	**2.74**	**8.63**					
11	1	1.72	1.36	2	1.95	2.23	3	2.92	2.41				-1.35	0.211
				3	2.10	6.04	2	2.73	5.75					
12	1	1.72	1.50	2	1.95	1.93	3	2.92	4.50	4	3.30	-0.11	-0.36	0.228
				3	2.11	5.57								
13	1	1.72	1.51	3	1.97	3.88	3	2.92		4	3.29	0.20	-0.67	0.234
				2	2.14	2.96								
13	1	1.71	1.18	2	1.94	2.46	3	2.92	2.51	4	3.25	2.34	-2.87	0.199
				3	2.09	6.24	3	2.72	8.59					

Table A5.2. EXAFS Fitting Parameters for $[Mn^{IV}(O)(2pyN2B)]^{2+}$, *K 2-14*

	Mn-O/N			Mn-N			Mn•••C			Mn••N••C				
fit	N	r(Å)	σ^2	N	r(Å)	σ^2	N	r(Å)	σ^2	N	r(Å)	σ^2	E_0	R
1	6	2.24	37.7										14.3	0.761
2				6	2.23	32.7							10.1	0.758
3	1	1.66	2.16	5	1.98	16.2							-9.74	0.677
4	1	1.69	3.04	4	1.97	7.96							-6.29	0.383
				1	2.14	-1.54								
5	1	1.70	2.60	3	1.95	3.95							-5.04	0.366
				2	2.12	0.96								
6	1	1.69	2.50	3	1.94	4.12	3	2.81	16.8				-4.90	0.336
				2	2.12	1.07								
7	1	1.69	2.28	3	1.94	4.23	3	2.94	6.05				-4.84	0.317
				2	2.12	1.27	4	2.74	10.1					
8	1	1.69	2.33	3	1.94	4.25	3	2.93	6.39				-4.66	0.316
				2	2.12	1.26	3	2.73	7.66					
9	**1**	**1.70**	**2.12**	**2**	**1.92**	**1.31**	**3**	**2.94**	**5.97**				**-4.01**	**0.304**
				3	**2.10**	**4.10**	**3**	**2.74**	**7.74**					
10	1	1.67	2.41	5	1.99	17.5	3	2.69	4.41				-6.45	0.576
							3	2.89	4.92					
11	1	1.70	2.25	2	1.92	1.12	3	2.82	20.1	4	3.36	-1.12	-4.45	0.314
				3	2.10	3.83								
12	1	1.70	2.11	2	1.92	1.25	3	2.94	7.85	4	3.17	6.55	-4.42	0.300
				3	2.10	4.05	4	3.17	5.82					

Table A5.3. EXAFS Fitting Parameters for $[Mn^{IV}(O)(2pyN2Q)]^{2+}$, *K 2-14*

	Mn-O/N			Mn-N			Mn•••C			Mn••N••C				
fit	N	r(Å)	σ^2	N	r(Å)	σ^2	N	r(Å)	σ^2	N	r(Å)	σ^2	E_0	R
1	6	1.28	17.9										-371	1.00
2				6	2.29	27.7							12.4	0.525
3	1	1.76	24.4	5	2.27	23.7							13.0	0.503
4	1	1.76	8.17	4	2.11	11.0							4.90	0.383
				1	2.30	1.49								
5	1	1.77	8.92	3	2.09	7.00							6.10	0.360
				2	2.28	4.32								
6	1	1.77	7.75	3	2.07	6.62	4	2.91	15.5				2.81	0.297
				2	2.26	4.98								
7	**1**	**1.76**	**7.06**	**3**	**2.06**	**6.31**	**4**	**2.91**	**7.34**				**-0.65**	**0.268**
				2	**2.25**	**5.73**	**3**	**2.71**	**8.17**					
8	1	1.77	7.56	2	2.04	4.03	4	2.91	7.42				-0.36	0.269
				3	2.22	9.96	3	2.70	8.26					
9	1	1.74	5.67	5	2.08	16.7	4	2.71	9.34				-3.56	0.361
							3	2.90	5.92					
10	1	1.77	7.96	3	2.08	6.73	4	2.92	14.0	4	3.15	3.38	3.74	0.289
				2	2.27	4.83								
11	1	1.76	6.18	3	2.04	6.05	4	2.87	4.35	4	3.16	-1.88	-2.89	0.257
				2	2.23	6.08	3	2.68	5.39					

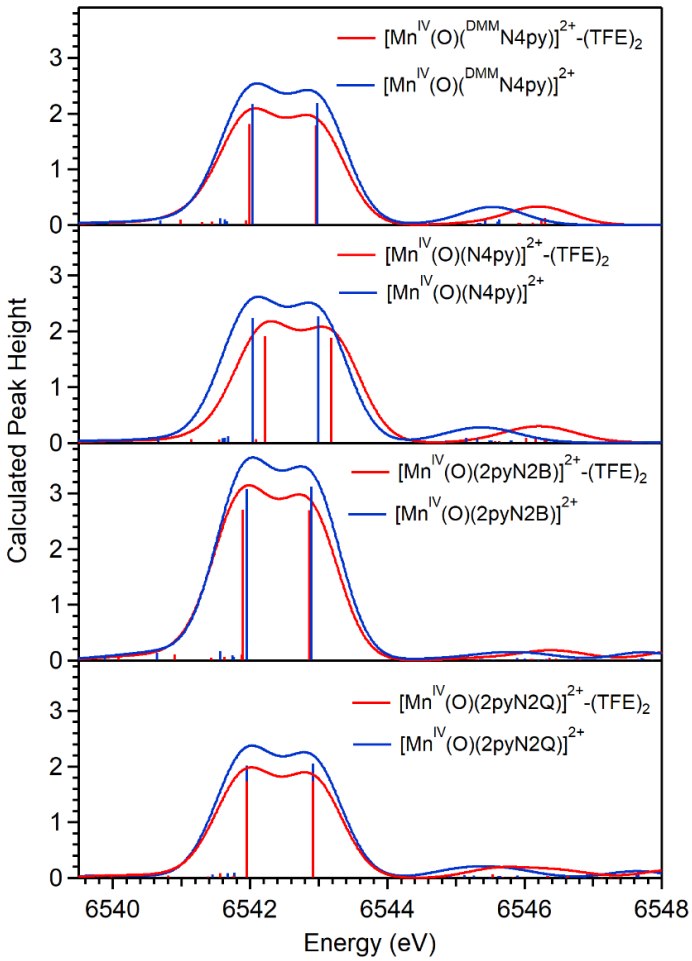

Figure A5.2. TD-DFT pre-edge regions for Mn^{IV}-oxo Complexes with and without 2,2,2-trifluoroethanol (TFE) molecules hydrogen-bonding with the oxo ligand.

Table A5.4. Comparison of TD-DFT Pre-edge Energies, Intensities, and Area for Mn^{IV}-oxo Complexes with and without 2,2,2-Trifluoroethanol (TFE) Molecules Hydrogen-Bonding with the Oxo Ligand.

complex	energy	intensity	area
$[Mn^{IV}(O)(^{DMM}N4py)]^{2+}\cdot(TFE)_2$	6542.1	2.58	17.3
	6542.9		
$[Mn^{IV}(O)(^{DMM}N4py)]^{2+}$	6542.1	3.14	20.6
	6542.9		
$[Mn^{IV}(O)(^{DMM}N4py)]^{2+}\cdot(TFE)_2$	6542.2	2.67	17.8
	6543.2		
$[Mn^{IV}(O)(^{DMM}N4py)]^{2+}$	6542.0	3.20	21.0
	6543.0		
$[Mn^{IV}(O)(2pyN2Q)]^{2+}\cdot(TFE)_2$	6542.0	2.34	15.9
	6542.9		
$[Mn^{IV}(O)(2pyN2Q)]^{2+}$	6542.0	2.87	19.0
	6542.9		
$[Mn^{IV}(O)(2pyN2B)]^{2+}\cdot(TFE)_2$	6542.0	3.80	24.7
	6542.8		
$[Mn^{IV}(O)(2pyN2B)]^{2+}$	6542.0	4.42	28.3
	6542.8		

Table A5.6. TD-DFT Energies (eV), Oscillator Strengths, and Percent Contributions from One-Electron Excitations[a] for the Major Pre-edge Transitions of $[Mn^{IV}(O)(^{DMM}N4py)]^{2+}\cdot(TFE)_2$, $[Mn^{IV}(O)(2pyN2B)]^{2+}\cdot(TFE)_2$, and $[Mn^{IV}(O)(2pyN2Q)]^{2+}\cdot(TFE)_2$.

complex	state	energy	$f_{osc} \times 10^6$	transition[b]	%	Mn 3d	Mn 4p	O 2p	N 2p
$[Mn^{IV}(O)(^{DMM}N4py)]^{2+}\cdot(TFE)_2$	1	6540.0	0.06	$1s\beta \rightarrow 193\beta$ (xy)	72	54.4	0.0	0.3	3.3
				$1s\beta \rightarrow 194\beta$ (xz)	6	47.6	0.0	15.8	6.8
	2	6541.0	1.7	$1s\alpha \rightarrow 196\alpha$ (x^2-y^2)	98	59.8	0.0	0.1	20.2
	3	6541.3	0.3	$1s\beta \rightarrow 194\beta$ (xz)	62	47.6	0.0	15.8	6.8
				$1s\beta \rightarrow 196\beta$ (xz/yz)	12	31.8	0.0	8.7	12.2
				$1s\beta \rightarrow 197\beta$ (xz/yz)	11	13.7	0.0	3.2	16.8
				$1s\beta \rightarrow 195\beta$ (yz)	10	46.9	0.0	19.0	5.7
	4	6541.4	0.6	$1s\beta \rightarrow 195\beta$ (yz)	57	46.9	0.0	19.0	5.7
				$1s\beta \rightarrow 196\beta$ (xz/yz)	30	31.8	0.0	8.7	12.2
	5	6541.9	1.0	$1s\beta \rightarrow 199\beta$ (x^2-y^2)	68	45.9	0.0	0.0	15.1
				$1s\beta \rightarrow 203\beta$ (x^2-y^2)	23	19.6	0.0	0.1	14.6
	6	6542.0	67.3	$1s\alpha \rightarrow 199\alpha$ (z^2)	95	52.7	1.5	16.6	11.3
	7	6543.0	66.3	$1s\beta \rightarrow 205\beta$ (z^2)	93	58.4	1.8	10.6	8.6
$[Mn^{IV}(O)(N4py)]^{2+}\cdot(TFE)_2$	1	6539.9	0.1	$1s\beta \rightarrow 161\beta$ (xy)	75	57.9	0.0	0.2	1.8
				$1s\beta \rightarrow 170\beta$ (xy)	11	20.5	0.0	0.3	13.0
				$1s\beta \rightarrow 168\beta$ (xy)	6	20.7	0.0	0.6	9.7
	2	6540.9	0.4	$1s\alpha \rightarrow 164\alpha$ (x^2-y^2)	98	60.7	0.0	0.0	20.4
	3	6541.4	0.4	$1s\beta \rightarrow 162\beta$ (xz)	69	48.6	0.0	17.6	6.0
				$1s\beta \rightarrow 163\beta$ (yz)	10	49.2	0.0	21.3	5.7
				$1s\beta \rightarrow 165\beta$ (xz/yz)	9	10.0	0.0	2.0	17.8
				$1s\beta \rightarrow 164\beta$ (xz)	7	23.2	0.1	6.9	15.9
	4	6541.5	0.9	$1s\beta \rightarrow 163\beta$ (yz)	63	49.2	0.0	21.3	5.7
				$1s\beta \rightarrow 164\beta$ (xz)	26	23.2	0.1	6.9	15.9

	5	6541.9	0.3	1sβ → 169β (x^2-y^2)	54	40.0	0.0	0.1	13.3
				1sβ → 166β (x^2-y^2)	19	13.7	0.0	0.1	18.1
				1sβ → 168β (xy)	12	20.7	0.0	0.6	9.7
				1sβ → 167β (x^2-y^2)	8	6.9	0.0	0.0	5.9
	6	6542.0	70.7	1sα → 167α (z^2)	80	45.0	1.5	13.7	13.3
				1sα → 166α (z^2)	15	9.9	0.2	2.7	19.6
	7	6543.0	69.9	1sβ → 173β (z^2)	96	59.8	2.0	11.5	8.6
$[Mn^{IV}(O)(2pyN2Q)]^{2+}\cdot(TFE)_2$	1	6540.0	0.4	1sβ → 187β (xy)	76	60.3	0.0	0.2	1.4
				1sβ → 193β (xy)	7	25.0	0.0	1.2	14.4
				1sβ → 192β (x^2-y^2)	5	35.9	0.0	0.6	14.9
	2	6540.8	0.1	1sα → 190α (x^2-y^2)	96	59.7	0.0	0.1	21.5
	3	6541.4	0.3	1sβ → 188β (xz)	71	56	0.0	19.8	3.4
				1sβ → 193β (xy)	8	25.0	0.0	1.2	14.4
				1sβ → 189β (yz)	6	28.1	0.0	13.8	12.9
				1sβ → 190β (yz)	6	32.3	0.2	11.6	11.1
	4	6541.6	2.3	1sβ → 190β (yz)	38	32.3	0.2	11.6	11.1
				1sβ → 189β (yz)	38	28.1	0.0	13.8	12.9
				1sβ → 192β (x^2-y^2)	7	35.9	0.0	0.6	14.9
	5	6541.8	0.4	1sβ → 194β (x^2-y^2)	47	37.5	0.0	1.1	16.4
				1sβ → 192β (x^2-y^2)	32	35.9	0.0	0.6	14.9
				1sβ → 193β (xy)	10	25.0	0.0	1.2	14.4
	6	6542.0	64.3	1sα → 194α (z^2)	54	32.0	0.8	9.5	14.4
				1sα → 192α (z^2)	29	17.0	0.6	4.3	17.4
				1sα → 193α (z^2)	14	8.9	0.2	2.3	17.4
	7	6542.9	64.2	1sβ → 199β (z^2)	82	52.6	1.5	9.7	7.6
				1sβ → 198β (z^2)	9	6.3	0.2	1.0	1.5
$[Mn^{IV}(O)(2pyN2B)]^{2+}\cdot(TFE)_2$	1	6540.0	0.3	1sβ → 189β (xy)	73	57.6	0.0	0.0	1.5
				1sβ → 190β (xz)	8	34.1	0.1	13.0	8.3
				1sβ → 196β (xy)	8	13.7	0.0	0.1	13.6
	2	6540.9	2.4	1sα → 192α (x^2-y^2)	98	62.4	0.0	0.1	14.3
	3	6541.4	0.7	1sβ → 191β (yz)	63	47.1	0.0	17.9	2.6
				1sβ → 190β (xz)	21	34.1	0.1	13.0	8.3
				1sβ → 193β (xz/yz)	10	9.1	0.0	2.1	8.6
	4	6541.6	0.9	1sβ → 192β (xz/yz)	68	47.3	0.0	17.8	4.9
				1sβ → 190β (xz)	23	34.1	0.1	13.0	8.3
				1sβ → 191β (yz)	6	47.1	0.0	17.9	2.6
	5	6541.9	2.0	1sβ → 195β (x^2-y^2)	90	65.2	0.0	0.1	10.5
	6	6541.9	100.3	1sα → 194α (z^2)	94	52.5	2.5	17.4	8.0
	7	6542.9	99.8	1sβ → 199β (z^2)	95	59.2	2.8	12.3	6.3

[a] One-electron excitations contributing greater than 5% to the state of interest are included. [b] The α and β designations correspond to spin-up (majority spin) and spin-down (minority spin) MOs, respectively.

Table A5.7. Cartesian Coordinates for DFT-optimized Model of $[Mn^{IV}(O)(N4py)]^{2+}$.

Mn	-0.12474546499286	0.58955373621768	0.81633948784617
O	0.43123226669255	2.14620862410101	1.11948799502889
N	0.57964679972054	-0.27007951989544	2.47073487289375
N	1.48710904155265	-0.08530604364627	-0.14206332923912
N	-1.94963997108373	0.74229132243416	1.63888427487429

N	-1.06009316576525	0.92503016712175	-0.92756982375046
C	0.24275772150730	-1.57358170300861	2.64703911121986
C	-2.82075895335147	-0.16387169061537	1.12367887815875
C	1.38827125350616	-1.34068424393714	-0.65007465590050
N	-0.82972142309539	-1.34778514174364	0.43443878195554
C	-2.02379624977349	0.00093162181409	-1.17768531113102
C	-0.78098576435721	1.89099427298359	-1.81790351218059
C	-2.32043569841571	1.57355252650904	2.62648981562715
C	0.79591329841252	-2.31422617142260	3.69314512789286
C	-4.52626679913021	0.60062901378701	2.62682082651775
C	2.50129401348691	-1.96823075523621	-1.21227939282145
C	-0.80111494237191	-2.12648419269261	1.71101779572885
C	0.01415232552854	-1.95957506730287	-0.63831092400693
C	2.65587782941213	0.58741710377153	-0.18051151144798
C	1.44403447631679	0.34109158662948	3.30704316914811
C	2.01823194763637	-0.34179588236235	4.37589706320026
C	-2.21779319331825	-0.96224888482940	-0.01923999292577
C	3.71974552812095	-1.28076962029039	-1.25813043072585
C	-2.47577198359864	1.02604258519604	-3.29839031861575
C	1.69386583080066	-1.69148007301432	4.56785420313785
C	-1.47924527261666	1.97016603786616	-3.02468897001582
C	3.79696658280122	0.01904562595761	-0.74029443594918
C	-3.61565503500969	1.52797717498122	3.14659536584748
C	-4.12569899368671	-0.26303685777140	1.59478075569823
C	-2.75748370851467	0.02104887177184	-2.35917857834705
H	0.00558219815332	2.59444160929445	-1.53829979702922
H	-1.56072706441288	2.27236631360904	2.98173784460873
H	0.52061539817291	-3.36444589219353	3.81618896146775
H	-5.54434218405893	0.54463991288300	3.02089946050663
H	2.40699520673106	-2.98189767283419	-1.60908830871041
H	-0.63720484077732	-3.19496181956523	1.51069713329690
H	-1.78704081551897	-2.03694606370149	2.19501669108387
H	0.06482170418876	-3.05139362930092	-0.51826898387813
H	-0.46507598806113	-1.76398243990114	-1.61114103480136
H	2.63837018243174	1.58844451547021	0.25527687226387
H	1.65634414687559	1.38846862477740	3.08293514417731
H	2.71405615915325	0.17849325584887	5.03795512895558
H	-2.83771252580170	-1.82609604560396	-0.29579139343426
H	4.60215593399875	-1.75794037132987	-1.69300395520681
H	-3.03281019241035	1.06642504438839	-4.23806614281490
H	2.13815359449481	-2.25710248186970	5.39136418652008
H	-1.23933079125073	2.76540222086492	-3.73397152155285
H	4.72971253059734	0.58726682874355	-0.75903074787004
H	-3.89844005678396	2.21496598476384	3.94728848136571
H	-4.81027026369439	-0.99970953975850	1.16861094261721
H	-3.52666366834627	-0.73246758772507	-2.54228516410026

Table A5.8. Cartesian Coordinates for DFT-optimized Model of $[Mn^{IV}(O)(N4py)]^{2+}\cdot(TFE)_2$.

Mn	-0.16271377549221	0.60237062295441	0.85631899954072
O	0.36207962602643	2.19031820432367	1.15683293620757
N	0.58341417767666	-0.27550718384847	2.48855486695243
N	1.45166103775356	-0.04325644631431	-0.09993395083884
N	-1.99022861408355	0.75375172192850	1.66972984743589
N	-1.04822580657307	0.90335473777044	-0.92731296098874
C	0.23562306788087	-1.57973112773427	2.65650365638397
C	-2.86429099725284	-0.13696985598145	1.13044274474157

C	1.36254382410834	-1.29690384825519	-0.61410798071533
N	-0.86048823172007	-1.31593176962063	0.47349059508310
C	-2.03415432872565	0.00021414646556	-1.16787784345276
C	-0.69880304176466	1.80648410380877	-1.86092760894260
C	-2.36712095951272	1.57189579787208	2.66817771345234
C	0.82778504816588	-2.35264863548953	3.65508227466023
C	-4.58794149471614	0.63400648725106	2.60799743270079
C	2.47770922992305	-1.90204247038519	-1.19479052251674
C	-0.85225797071362	-2.09296967391012	1.75354230917714
C	-0.00137363965690	-1.93777076260144	-0.58751862916733
C	2.60864337654203	0.65019044010386	-0.14425303061188
C	1.51305389961971	0.29405474785804	3.28406091324773
C	2.13041825180923	-0.42405672219497	4.30429320571594
C	-2.24932650282072	-0.94055599414166	0.00080395496177
C	3.68403612792954	-1.19396330355034	-1.25117499640048
C	-2.41078756245052	0.95957896958855	-3.33331287773301
C	1.78591176805015	-1.76825029679919	4.49183489354591
C	-1.37206619074060	1.86408572046528	-3.08237882308373
C	3.74956960765779	0.10253188428559	-0.72339394921787
C	-3.67300406348540	1.53755161393981	3.16000266382727
C	-4.17836379006744	-0.22424575375447	1.57515116974297
C	-2.74557101841046	0.00260195074222	-2.36290904719952
H	0.12480971528235	2.47846732975869	-1.61195981033659
H	-1.60827579225203	2.24694531153302	3.06507394279350
H	0.53834451810496	-3.39996352163904	3.76812357719038
H	-5.61409596252749	0.58812216714075	2.98138460850323
H	2.39445396859645	-2.91383650606383	-1.59833711754346
H	-0.74463431589940	-3.16854344538497	1.55349832547741
H	-1.82440605300995	-1.95104931694882	2.25176270559431
H	0.06664676043236	-3.02434632772880	-0.43633779431791
H	-0.48489072552692	-1.77938361200674	-1.56453774965692
H	2.58379501679179	1.64626715139896	0.30160556312824
H	1.75072048610009	1.33844799919107	3.08406661686445
H	2.87731669421898	0.06922945958266	4.93047878147050
H	-2.85793217233760	-1.81281123045229	-0.27129410919910
H	4.56737258057756	-1.65354095276670	-1.70235635836054
H	-2.95106950647188	0.98728281384620	-4.28283967306634
H	2.26335722397464	-2.36008611940443	5.27715720618389
H	-1.07754228019736	2.61142059849246	-3.82218874626664
H	4.67323898525931	0.68474342012289	-0.74910031870974
H	-3.95870848286061	2.21420132664638	3.96818824008820
H	-4.86198549465034	-0.95062246964966	1.13032140921519
H	-3.53516525846724	-0.73233619021073	-2.53268712037688
O	0.20417702333773	4.50568514784280	-0.11331076145194
C	-1.13949316677740	4.86318553771338	-0.37253260567870
C	-1.81481073369157	5.46731346180685	0.85019290395052
F	-1.91558932205716	4.57331702776612	1.87232337269140
F	-1.13589845564393	6.53487663699191	1.33761767213348
F	-3.06999095359714	5.88118621394351	0.55717620351866
H	0.22812774610858	3.62795134960641	0.37755626378119
H	-1.15213810602817	5.62556692258573	-1.16759279628201
H	-1.76369514884878	4.01089401220903	-0.69859895802180
O	0.55104314287008	3.40605932853551	3.50475130742020
C	1.24062579243625	4.64000505927425	3.42164662462714
C	2.69152213520359	4.44305680524059	3.00589265021431
F	2.80174035670338	3.97896544053144	1.72850422347986
F	3.37950299262904	5.60653429494722	3.06498874153708

F	3.33364691913149	3.54526165519107	3.79500997161950
H	0.46067865210415	3.01283647431089	2.58481168854502
H	1.24112768165495	5.10028796837948	4.42187517038272
H	0.77960748437045	5.34730447289018	2.70927719234967

Table A5.9. Cartesian Coordinates for DFT-optimized Model of $[Mn^{IV}(O)(^{DMM}N4py)]^{2+}$.

Mn	-0.12803777728742	0.68070176988292	0.82226345209217
O	0.33484499396320	2.26517463252519	1.14713409648667
N	0.66838215781048	-0.16645115057384	2.43429445687953
N	1.47838600070380	0.12278284000808	-0.18402121039249
N	-1.93737833193783	0.70200249136222	1.70878349274402
N	-1.14774639425399	0.99920453246329	-0.88194130988060
C	0.41749078538280	-1.48812423040746	2.60006938462142
C	-2.76586424646375	-0.24614070219812	1.20107978686968
C	1.45975322023108	-1.13050874869171	-0.71898224942564
N	-0.72770524776559	-1.27873486721684	0.41727138302061
C	-2.06071719549488	0.02321880633010	-1.12149096317628
C	-0.95904151028045	1.99818616361888	-1.75897046129449
C	-2.32520828088474	1.48129905886960	2.73098321543336
C	1.02521853147187	-2.22711564361931	3.62545822604648
C	-4.46187933371779	0.36564855940124	2.78273086616809
C	2.59796487132778	-1.67415910424832	-1.30742016557067
C	-0.60686307419993	-2.09062238250024	1.66804309823607
C	0.11330070063001	-1.81632897150341	-0.69800625394574
C	2.60921086149199	0.85071205254474	-0.20132920721576
C	1.50692788953159	0.49056494394728	3.26056926920766
C	2.17536743049084	-0.15310089499369	4.29953990851658
C	-2.15240202626080	-0.97616748430825	0.01869856649358
C	3.79273839502302	-0.88971880630425	-1.33253902543923
C	-2.64909234820641	1.06233352198138	-3.20142879915092
C	1.94148004519043	-1.53931914577835	4.45457327725411
C	-1.70259226207133	2.05994134342928	-2.93957859678510
C	3.81195056764225	0.41062744365577	-0.75552652386673
C	-3.59481852469080	1.33794509314430	3.29514553059097
C	-4.04384353305812	-0.44366998493574	1.71433660446821
C	-2.83558929830859	0.02226555430144	-2.27697705831492
C	0.67368479792597	-3.67278481124431	3.86327151583947
C	2.63012665333780	-3.03824801523257	-1.94258292521180
C	3.63696919508277	-3.09382195168814	5.12683892993338
O	4.81029317922180	-1.53605540233357	-1.92217943984182
O	2.57698947710692	-2.17476091826118	5.48023765339051
C	5.00741766233970	1.32891375774349	-0.63591573263963
C	3.11482787634090	0.57800257881218	5.21696917900227
C	6.04929083581200	-0.92613094448112	-2.33688827550356
H	-0.20646222981516	2.74184398253487	-1.48986705925347
H	-1.59944874589028	2.21918042705199	3.07854496445006
H	-5.45893117011600	0.23266908779601	3.21077901039082
H	-0.36333021417849	-3.13264533584457	1.41387087598231
H	-1.58720081680283	-2.10715685669717	2.17219105045689
H	0.20295187141997	-2.90727287277123	-0.60290424572278
H	-0.40504219179042	-1.61836380274154	-1.64985304354430
H	2.53268977837453	1.83362190374169	0.27004195909380
H	1.63595530924745	1.55453823893858	3.04890864367154
H	-2.72311042954538	-1.87317415290343	-0.25881044342256
H	-3.24003599175828	1.08814314013436	-4.12075485573074
H	-1.53624269178680	2.88285889591186	-3.63838165097208

H	-3.89201444551599	1.98439074846897	4.12398424553057
H	-4.69389678967423	-1.21359826088216	1.29275379367260
H	-3.56275523526647	-0.77378264963476	-2.45186566390365
H	1.17068943102269	-4.34225771782498	3.13754532465799
H	-0.41318724186356	-3.83491422347967	3.77396838112493
H	0.97589633808582	-3.97604169510379	4.87720802739728
H	3.39880654098005	-3.66901912012181	-1.46243851968578
H	1.66297040980897	-3.55631058220421	-1.88033196935423
H	2.90851309314740	-2.95414877956703	-3.00794343140517
H	3.97652787193075	-3.53877134815319	6.07244449893170
H	4.46822708069958	-2.54847837389443	4.64762985957570
H	3.27968600831451	-3.88750525783366	4.44962059222352
H	5.83236392188772	0.85203032226102	-0.08186946616581
H	5.39368368748119	1.65457963805283	-1.61463328177618
H	4.71365337680269	2.23261177096430	-0.07898663485436
H	2.79387907460912	0.47109072219551	6.26789298714238
H	3.15577819537898	1.64941698907664	4.96675098054827
H	4.13630777995807	0.16407236557877	5.14728485926777
H	6.67023474219710	-0.65498035104156	-1.47110590033812
H	5.85717486915646	-0.05448527567173	-2.97993443762076
H	6.55946748503399	-1.70478178756786	-2.92067769738443

Table A5.10. Cartesian Coordinates for DFT-optimized Model of $[Mn^{IV}(O)(^{DMM}N4py)]^{2+}\cdot(TFE)_2$.

Mn	-0.16016522440439	0.70839969836657	0.82328258867569
O	0.27972193455728	2.32236730140222	1.13820315001995
N	0.65228738127515	-0.14595912469396	2.43031228815402
N	1.45519040844367	0.15276568268824	-0.14735731614767
N	-1.97686577813003	0.75265456660242	1.67995134060129
N	-1.11806735816315	0.99049201125931	-0.93158938946779
C	0.38492581216269	-1.46670831877430	2.59671274997615
C	-2.81494504867563	-0.17658949135874	1.15165969249115
C	1.45483002607875	-1.11577960211331	-0.64607239234932
N	-0.76458613733695	-1.23217616361106	0.43454394234682
C	-2.05272795717379	0.03261995882584	-1.16227266657344
C	-0.85677584580131	1.93222095398587	-1.85520878889675
C	-2.36989167525368	1.54016388590939	2.69540601998792
C	1.02799632124703	-2.23101914346156	3.58046710806820
C	-4.54090105677476	0.49181278470937	2.67555804744956
C	2.61638510595759	-1.67353440123783	-1.17069386856775
C	-0.68649811576709	-2.03064765952940	1.69941123763924
C	0.10591885868193	-1.79707611759911	-0.65049733368437
C	2.58382119762532	0.88462024336516	-0.13763456321244
C	1.55960226481774	0.47639453094243	3.21056733349855
C	2.26891770577899	-0.19448928507627	4.20404421267296
C	-2.18288940142850	-0.93355191046409	-0.00194867706431
C	3.81231351854996	-0.88707344333855	-1.16351744138365
C	-2.55197850959930	1.00328477403751	-3.29764909864460
C	2.00868171308894	-1.57494779110974	4.36113347553691
C	-1.56849123029848	1.96986089217887	-3.05580430585538
C	3.80936555951886	0.43010363529065	-0.62388741415041
C	-3.66061329519300	1.43622124424416	3.21677719703840
C	-4.11272818121336	-0.33545182399641	1.62514650826511
C	-2.79640179744026	0.00932310195761	-2.33752858127811
C	0.64885984961940	-3.67077187108284	3.81386335101229
C	2.66883150349954	-3.05610288862324	-1.76189571038631
C	3.67609812173270	-3.21096253463697	4.91409349054474

O	4.85351770930251	-1.55320661661683	-1.69415828326328
O	2.68872744577743	-2.23401882848309	5.34957148806425
C	4.99100096532100	1.36338242105554	-0.47937626805123
C	3.28122050099349	0.51554595202588	5.05843842831604
C	6.14040582649107	-0.95705897033999	-1.99856482979603
H	-0.07514851051116	2.65467995882851	-1.61372216045076
H	-1.63338180234588	2.24765483587607	3.07661948761923
H	-5.55483948780873	0.39106925663548	3.07102104707334
H	-0.51302581132826	-3.08916915898922	1.45946801512286
H	-1.66087028056104	-1.97121914716504	2.21072879148873
H	0.18573821607758	-2.88540795721229	-0.52726574251373
H	-0.38691238328672	-1.61749926655831	-1.61888075198027
H	2.48534309574932	1.88229691278291	0.29466463533059
H	1.72069277827586	1.53755813318655	3.01777779149197
H	-2.74689795708020	-1.83676522203341	-0.26963875812586
H	-3.11986308399491	1.01304198248488	-4.23136148769795
H	-1.34585829392939	2.75010489074253	-3.78701478458342
H	-3.96282604130513	2.09021187921108	4.03765215432673
H	-4.76968330073134	-1.09012426293736	1.18759854462014
H	-3.54267571585391	-0.77124101324333	-2.49967711446674
H	1.09810616632942	-4.34158017802070	3.05892817283937
H	-0.44455000902746	-3.80137751865475	3.76690693809876
H	0.98112570795175	-4.00088022080773	4.80958033405228
H	3.41604221907173	-3.67428746715657	-1.23495149764965
H	1.69769831473501	-3.56853766982174	-1.71900482373614
H	2.98422950877145	-3.00692684933401	-2.81864614938563
H	4.03823295596924	-3.69397765954538	5.83198237533865
H	4.50573590618212	-2.69588909260145	4.40163803061200
H	3.23397972905538	-3.96338575632529	4.24201691045482
H	5.79972653409005	0.90937507717080	0.11494363103148
H	5.40753740534607	1.67261166834239	-1.45074535355987
H	4.66620999517772	2.27512867372987	0.04569321502661
H	2.98267014224953	0.48585192999893	6.12098518985426
H	3.38427577844744	1.56778460415967	4.75209989420493
H	4.26905397081594	0.02892496226621	4.98613409476944
H	6.68044542833634	-0.69925770275784	-1.07755045250754
H	6.01511452892955	-0.08402667723802	-2.65382930238269
H	6.68377119686051	-1.74664688127551	-2.53522620101944
O	-0.19239260968974	4.60811916598268	-0.07333932844841
C	-1.58535116456628	4.84871311581811	-0.09358320492969
C	-2.06966716704731	5.47707115372500	1.20669902131668
F	-1.91379467871460	4.63862104475488	2.26911570916242
F	-1.39769010672616	6.61345314535137	1.50960050843420
F	-3.38704499260716	5.78571541620003	1.13580021643466
H	-0.02172096303242	3.73179274364212	0.39506040116363
H	-1.81235332832683	5.55778827143233	-0.90596275866519
H	-2.18221473821345	3.93184103606268	-0.25595909241889
O	0.92991282796851	3.66006160617431	3.33173886630520
C	1.61230247910852	4.86713627005091	3.05304967814074
C	2.94515216151467	4.63021610537023	2.35393068038634
F	2.78788040328705	4.16276797582250	1.07992727509101
F	3.65799917363550	5.77634616065388	2.26541183851838
F	3.71506768026930	3.71703293785129	2.99825642565795
H	0.63637957636581	3.22767142925498	2.47439862009227
H	1.83144533631759	5.36257645094937	4.01194884136478
H	1.02512609193163	5.56135425446559	2.42501890751099

Table A5.11. Cartesian Coordinates for DFT-optimized Model of $[Mn^{IV}(O)(2pyN2B)]^{2+}$.

Mn	0.56682711319630	4.79923738036984	1.99182769986919
O	-0.99252118792105	4.79869499364974	2.56502688033484
N	2.80868895178243	4.79942032889468	1.33984585276750
N	0.55375112440134	6.20407165787160	0.61084968080879
N	1.53545363455146	7.46220711878434	-0.94027112982068
N	1.48480661951085	3.41051845881569	3.33648155974535
C	3.04049198344183	6.04870814950148	0.56009342213352
C	1.72657673033297	6.56856498206134	0.05410095398059
C	-0.45661184057781	6.89151924458642	-0.05917317494580
C	0.16099737027622	7.69872390693352	-1.04398427611300
C	2.56125979021777	8.11471317099373	-1.75347009200922
C	-0.57656687669286	8.52588597869147	-1.90000898636488
C	-1.96692251220236	8.50879907551337	-1.73419065637065
C	-2.59047913959706	7.70052951821214	-0.75306774461256
C	-1.84930094089271	6.87736069304143	0.10178901142484
C	3.37615312968485	4.79958965362620	2.73273418968711
C	2.82790767290900	3.57241736180047	3.44953856970812
C	0.86140200686599	2.39884864238089	3.95967985834122
C	1.57249444842543	1.48737810075788	4.74503428439564
C	2.95735396826429	1.63907706596505	4.87222306360681
C	3.59922708933662	2.69959538686431	4.21432723382921
N	0.55385260045467	3.39355283624242	0.61105065564182
N	1.53586815439423	2.13916996932427	-0.94301710249653
N	1.48327938649877	6.18667597268017	3.33634391216400
C	3.04065919197740	3.55013330423273	0.55986644681375
C	1.72678605129198	3.03046867956945	0.05357865044820
C	-0.45632664137237	2.70768550402493	-0.06081789274254
C	0.16149701143727	1.90258716831363	-1.04722886101175
C	2.56170305169302	1.48826017955487	-1.75745648904310
C	-0.57580868034543	1.07671034865130	-1.90474142279080
C	-1.96615116017787	1.09299989048128	-1.73880118256135
C	-2.58992344801216	1.89910172191557	-0.75602075493230
C	-1.84901119532276	2.72091011394913	0.10037299828291
C	2.82660194876288	6.02608687562554	3.44967320175668
C	0.85882648199422	7.19768724386083	3.95969519000103
C	1.56892237648343	8.10962793532689	4.74536206396969
C	2.95398424587633	7.95949537362803	4.87238804942881
C	3.59700909365521	6.89978404522258	4.21432559498623
H	3.50144261496410	6.80355995113381	1.21718817223093
H	3.74601135197263	5.86537173544517	-0.26345842228145
H	3.53539686084694	7.65003940840889	-1.55787929598756
H	2.31126639100039	7.99241609361071	-2.81754046803721
H	2.61150841155315	9.18490031589392	-1.50074757113947
H	-0.09742995077854	9.15255032570710	-2.65651386858276
H	-2.58734191942859	9.13794744536444	-2.37974240599894
H	-3.68074479838418	7.72242054998254	-0.66149766125597
H	-2.31634039407104	6.25210885828085	0.86675910645031
H	4.47596783601898	4.80019314431775	2.74059826491524
H	-0.22006863200928	2.33618210307994	3.81860545163795
H	1.04016300007245	0.67469683657512	5.24462717566962
H	3.53930671830389	0.93786663364998	5.47625871315281
H	4.67943497011473	2.84503759096779	4.28967595046828
H	3.50153180243159	2.79516897405100	1.21685219669012
H	3.74618787473625	3.73347175988319	-0.26386293018633
H	3.53542730128884	1.95432199232454	-1.56286821870083

H	2.31024651319303	1.61087651792306	-2.82114988072335
H	2.61356713552642	0.41794118970755	-1.50546885690634
H	-0.09647057163652	0.45168882554714	-2.66246830620458
H	-2.58639725517132	0.46489764881564	-2.38553881193635
H	-3.68016683982769	1.87651558685927	-0.66435154180524
H	-2.31621339241635	3.34431395215642	0.86674938303082
H	-0.22266312310328	7.25934332378471	3.81835776291114
H	1.03567973028065	8.92158222536219	5.24515743292301
H	3.53517908988173	8.66125149737484	5.47652365108401
H	4.67737367003869	6.75542448187315	4.28940472027142

Table A5.12. Cartesian Coordinates for DFT-optimized Model of $[Mn^{IV}(O)(2pyN2B)]^{2+}\cdot(TFE)_2$.

Mn	-0.00260313652403	0.34441069222393	-0.61305541256892
O	-0.12668670783256	0.52544907739161	1.05236676704203
N	0.11020062780220	0.15897566454284	-2.75757244152518
N	-1.91937561691681	0.44773201228429	-1.03057108993605
N	-3.59043405409994	0.53487679594397	-2.50243304008163
N	2.01918201310628	0.19793055908206	-0.84520232722523
C	-1.16602544876518	0.67373738128444	-3.35995188774225
C	-2.24603249248153	0.54612869305489	-2.32744677032211
C	-3.10658800865127	0.33654486275593	-0.30705932261966
C	-4.17654642055505	0.40765575899023	-1.23297319297861
C	-4.33933974976029	0.65966860831316	-3.75602948160110
C	-5.51779031636454	0.33138510824703	-0.83385551159129
C	-5.74674783748525	0.16715138754246	0.53701265644106
C	-4.68080834554582	0.07190042579846	1.46476479931552
C	-3.34450959390006	0.14940428079689	1.06206464283314
C	1.28698294274341	1.09025460593435	-2.94758280896120
C	2.41876156853688	0.53557732016151	-2.09999889985125
C	2.91016553668807	-0.24911583482250	0.05694783999304
C	4.26659097370725	-0.36365819961146	-0.27434275920380
C	4.69260416425232	-0.02267873797686	-1.56107380444487
C	3.74897160010699	0.43655333772869	-2.49774250329450
N	-0.08504908687351	-1.60402578178823	-0.70857484988030
N	-0.01896217997369	-3.49301139602191	-1.88267253483200
N	0.29828947183821	2.29536964673305	-1.11997469092564
C	0.39851833179537	-1.27382584086922	-3.11025085643025
C	0.07462413685063	-2.14164905942190	-1.92657689391886
C	-0.29511757403771	-2.64773153160254	0.19392728446023
C	-0.25261225660116	-3.85572210317861	-0.54618847961287
C	0.12464832074369	-4.44284767248029	-2.98927632798332
C	-0.42278770921293	-5.10933979606328	0.05530564824149
C	-0.63638714719373	-5.10522942189183	1.43823539663524
C	-0.67839424025116	-3.90195067842764	2.18364298102700
C	-0.51161319267860	-2.65193253428068	1.58076817713664
C	0.89018753243451	2.42482066151154	-2.33687333536806
C	-0.02058005184747	3.38519072827718	-0.39735880352901
C	0.24442916869327	4.67010185444992	-0.88714754484165
C	0.84080462767860	4.81958879912204	-2.14356054602341
C	1.17302669668593	3.67291190728382	-2.88626285089114
H	-1.01792608893161	1.73424967393301	-3.62627558023617
H	-1.40694788387096	0.13189932472281	-4.28942183550731
H	-3.64194603560357	0.69552991635953	-4.60352466142527
H	-5.00930244167517	-0.20671199859798	-3.87010912967006
H	-4.93701261983071	1.58486412767733	-3.73942696172881

H	-6.34491238208664	0.39202213399382	-1.54584406784811
H	-6.77667752589134	0.10207776405616	0.89962234167852
H	-4.90851552615571	-0.07021688080588	2.52552792042659
H	-2.52007901168496	0.05788375578765	1.76919190974393
H	1.58248415406915	1.19710518726040	-4.00440767553840
H	2.53378774001821	-0.47715123200476	1.06065174810378
H	4.97094377481735	-0.70461245151903	0.48826997553625
H	5.74749758862470	-0.10501488315311	-1.83960863218821
H	4.04630934940543	0.71725363631123	-3.51221395669527
H	1.47014084502818	-1.36379196353840	-3.35963543062913
H	-0.17056993533791	-1.56831840474849	-4.00732759048747
H	0.26538176168715	-3.89731360810966	-3.93193980210912
H	-0.78192648302051	-5.06390618594492	-3.05951301280744
H	0.99814513559356	-5.08982211465677	-2.81043640778997
H	-0.38843413216713	-6.04184253265862	-0.51387573496470
H	-0.77108872446617	-6.05836787550488	1.95768902339446
H	-0.84160806384846	-3.95343469401369	3.26385421176199
H	-0.53599979156390	-1.72456888855757	2.15534040668297
H	-0.47450020331771	3.21796362372881	0.58549528142986
H	-0.01348553739295	5.53745769922903	-0.27376743317438
H	1.05402007909991	5.81498395357034	-2.54478374643266
H	1.64910971166427	3.75132318605691	-3.86782252201867
O	-0.85634276178279	2.67753905913729	2.53885586132653
C	-1.99679026861331	2.62251054881504	3.37805740870701
C	-1.86622228713679	1.53680845097470	4.44249797087427
F	-1.62974791834355	0.31664403618507	3.85210317296010
F	-2.99929480709458	1.42255098278667	5.15480569346314
F	-0.84406083061564	1.75944795998296	5.28710936365546
H	-0.72690824382923	1.80232951663119	2.08527338364315
H	-2.93274570163269	2.42946017643085	2.81924265382673
H	-2.08557501912087	3.59366979659107	3.88966834505692
O	1.71501656537426	-0.06750038758805	2.95864375566994
C	2.15321242036517	1.08175474458477	3.66958753737098
C	2.98527969713916	2.00524064462071	2.78618795511971
F	4.11168576023969	1.39576181691930	2.33214894575849
F	3.34798941779399	3.11918073176084	3.43591166693833
F	2.28957082088405	2.38780300168507	1.66561399296492
H	0.96750941827580	0.19967984352966	2.36421252804850
H	1.31511053761681	1.66895252399582	4.08089716038351
H	2.79483790120677	0.74436370306644	4.49902374178395

Table A5.13. Cartesian Coordinates for DFT-optimized Model of $[Mn^{IV}(O)(2pyN2Q)]^{2+}$.

Mn	-0.22312665076367	0.32584536517864	0.12447826629630
O	-0.12043586159640	1.98028764057743	-0.16989614440930
N	0.66271455396885	0.08706901565476	1.95947644420499
N	1.51607677332266	-0.43207188896577	-0.65597316414126
N	-2.04709920695080	0.47003767721773	0.96022555932411
N	-1.21456191654798	-0.03576195303766	-1.58758342473364
C	0.51083829547477	-1.15710322704250	2.45188819033428
C	-2.80927628133860	-0.63796852132066	0.77727610548846
C	1.53309517398165	-1.77848724050101	-0.67599548087629
N	-0.68861898198677	-1.69466063367480	0.37381048288518
C	-2.06447955982056	-1.09036163604213	-1.50203056870249
C	-1.06617825848877	0.63998425334414	-2.73824119444840
C	-2.50586591674246	1.51463146925894	1.66819041756627
C	1.23968068437914	-1.63307196126513	3.56098389090303

C	-4.57880153981071	0.34661459477357	2.06074694764132
C	2.70531332751610	-2.52336016097006	-0.91875857343177
C	-0.53370221081394	-2.03230835267256	1.81480190011758
C	0.22062034576586	-2.49083975983618	-0.49425353355495
C	2.68188467151334	0.27013826668655	-0.93095035631466
C	1.53517276597122	0.96772142211834	2.58499274071234
C	2.31551999304402	0.52801501210182	3.71298500436320
C	-2.11913542808503	-1.66438319976212	-0.09970517012319
C	3.89395552627340	-1.85842272213642	-1.14984682335445
C	-2.66108638020807	-0.81841266166889	-3.80812883526974
C	2.15050889875791	-0.79955637783418	4.18057183414707
C	-1.78137866124749	0.26813572181462	-3.87858160092246
C	3.91086898988570	-0.44154129032392	-1.17127909906146
C	-3.78013103871058	1.48236556318228	2.23860730230358
C	-4.08862870574381	-0.73619998656497	1.31377049166261
C	-2.81055562865776	-1.51262853958670	-2.59715339612511
C	2.68622014117023	1.68508874407985	-0.99299435228300
C	1.66693152990689	2.30613576128421	2.14087349035007
C	3.22397279952361	1.43408397336504	4.33005717427011
C	5.10414750445758	0.29150781915580	-1.42785602015939
C	2.55326449365493	3.16555342797872	2.77291649171079
C	3.34568278842844	2.73189568126139	3.86600101449462
C	3.86470219660500	2.36692938285757	-1.25743114499403
C	5.08441972220760	1.67447713204404	-1.46637805382803
H	-0.37153543610890	1.48136080724704	-2.71968034501177
H	-1.83478912020523	2.37031714411465	1.75887946135399
H	1.07711614021265	-2.65775757842491	3.90212247152968
H	-5.57855618907374	0.29891705896254	2.50019323179935
H	2.65222003393661	-3.61417014376335	-0.90837773212291
H	-0.29799140498808	-3.09878251921077	1.94403257639927
H	-1.49328297388205	-1.84933129209734	2.32486143151049
H	0.36445305703974	-3.50225096133349	-0.08701945826264
H	-0.24835053038751	-2.60537364221097	-1.48489482746080
H	-2.60849714812603	-2.64696538862755	-0.06456947591326
H	4.82170183108777	-2.41239624585644	-1.31961943040394
H	-3.22939502580723	-1.12823571296046	-4.68899685205833
H	2.74393636224865	-1.15097499449954	5.02956143009042
H	-1.64569469814112	0.83071211152578	-4.80493510807823
H	-4.13422618255141	2.34242858193529	2.81126061564960
H	-4.68294155051244	-1.63910334997829	1.15665968082318
H	-3.48587735373248	-2.36635302222589	-2.50629252671356
H	1.74381126954875	2.21417550994223	-0.83571608054851
H	1.05120704313018	2.63729432098120	1.30182853441221
H	3.81499200178604	1.08104318921176	5.18067027660071
H	6.03067450722444	-0.26477726638586	-1.59983475371360
H	2.63972321959951	4.19798187159403	2.41998950955420
H	4.04285049731148	3.42676101518663	4.34356519476962
H	3.84984357481927	3.46024278647561	-1.30638301019494
H	6.00237335981290	2.23519040758991	-1.66613875473674

Table A5.14. Cartesian Coordinates for DFT-optimized Model of $[Mn^{IV}(O)(2pyN2Q)]^{2+}\cdot(TFE)_2$.

Mn	0.13678741656775	1.26336568616145	0.61831088868595
O	0.39969079202197	2.77035065171100	-0.12911386034058
N	1.23163537012071	1.44485224042629	2.33267014598066
N	1.63084866194308	0.07599423923073	-0.09259402853387

N	-1.57096932741458	1.89616577751738	1.50380759333916
N	-1.03461393748096	0.50127645666499	-0.83593811766093
C	0.85059878289739	0.59569379409084	3.30461290365680
C	-2.47920243120479	0.89931825835333	1.66556465771762
C	1.56289296589877	-1.17363698529303	0.40732001077189
N	-0.51091757647973	-0.46592960960613	1.55382587479757
C	-1.97395682364970	-0.35585990781166	-0.36039081566413
C	-0.90971061749600	0.71680633291185	-2.15620114088061
C	-1.86074388630950	3.15079607684649	1.88948059225492
C	1.47380672672726	0.55297080820577	4.56865437998887
C	-4.05688891408248	2.44440861658256	2.59777771525592
C	2.63252735471337	-2.08514899487816	0.31400553160503
C	-0.31248652933672	-0.31108978725941	3.02480815131891
C	0.24936807914041	-1.61874241759924	0.99134604583724
C	2.74063059889301	0.46311999932945	-0.83058387849679
C	2.33099607978066	2.26887184842151	2.53901114634405
C	2.99951073696297	2.26980620385035	3.81330967378593
C	-1.96598174637202	-0.42837715339581	1.15019609529778
C	3.79222280831053	-1.70278236428528	-0.33409489675817
C	-2.74398134896258	-0.78793926289070	-2.58949789371223
C	2.53135055333821	1.40047156511806	4.83044376020947
C	-1.76115399622313	0.08649153558496	-3.06547905113377
C	3.86709327014693	-0.42647069114073	-0.94493382295198
C	-3.10483570435477	3.45801424566393	2.44387243738606
C	-3.73854046172903	1.13537622254574	2.20497466312523
C	-2.85216865813245	-1.01996238837264	-1.20959629844963
C	2.78062349336699	1.70727396513589	-1.50580184179596
C	2.83968618575393	3.08694045009615	1.50358933548664
C	4.13104956149651	3.11084214606968	4.00883590321205
C	5.01257868619936	-0.01053820176161	-1.68147201074911
C	3.95876071428044	3.87890840841772	1.71929056709174
C	4.60763044262657	3.90279965373086	2.97842895399917
C	3.90504890775068	2.07359064419247	-2.23027948588988
C	5.03524787683455	1.22153595496324	-2.31093748067918
H	-0.12554792460915	1.40170083048587	-2.47580758681094
H	-1.08789317004017	3.90718977730226	1.74712103477144
H	1.10791908873673	-0.15519276195012	5.31520732987476
H	-5.03802326575546	2.66430275079877	3.02608552936404
H	2.52647442670048	-3.07567380181014	0.76135139876656
H	-0.17072782156798	-1.29361436670999	3.49914996505287
H	-1.22323190443554	0.12470353752257	3.46436887599213
H	0.38835826636696	-2.39898536051168	1.75273924411993
H	-0.34391712464768	-2.06507039195964	0.17645684479108
H	-2.53794270223304	-1.28236451527363	1.53596892108259
H	4.64648669730377	-2.38263972510867	-0.39817047109147
H	-3.41970463402295	-1.29375537891910	-3.28370971281194
H	3.02988693106714	1.39029267401733	5.80381020819880
H	-1.64566458961466	0.28764429201968	-4.13256108399786
H	-3.31517001848098	4.48650003195769	2.74553773779275
H	-4.44757193590498	0.31298806614100	2.32253886514580
H	-3.59904041642838	-1.70352060673098	-0.80036489933034
H	1.91718461153372	2.37031772988055	-1.44231038903302
H	2.34058735642041	3.08219823477026	0.53739831674539
H	4.62157523641046	3.10392490481405	4.98680102870614
H	5.86504339548532	-0.69326436300410	-1.74716876074022
H	4.34673547871704	4.49059831480067	0.89899138787660
H	5.48448706595474	4.53914713234037	3.12822987355635

H	3.91505270171867	3.03806007210473	-2.74689739967103
H	5.91456473273849	1.53541936532854	-2.88074503576348
O	0.15891941807742	5.32098866866592	0.65145253612510
C	1.27667779055365	6.18903818280816	0.62121886236937
C	1.88285771819695	6.29280892161484	-0.77042919904121
F	2.35514567889810	5.08655115672848	-1.20561836919848
F	2.93198367435209	7.14889671936649	-0.77666918061996
F	0.99635790038857	6.71976645267320	-1.69637472098543
H	0.42428483055687	4.39030648710932	0.39683864044452
H	2.07823030495804	5.87851581142330	1.31574950988765
H	0.93383135809341	7.19328057851474	0.91351683537786
O	-0.54833718803146	3.90788530676704	-2.35816939218541
C	-1.68871983648882	4.70012700204578	-2.08870800795577
C	-2.95627253906188	3.85784616825035	-2.04365771272927
F	-3.13801031734220	3.13310104508355	-3.17265654736959
F	-4.05300640206886	4.63504053835384	-1.87373916403500
F	-2.94314469194752	2.96453199781699	-1.01058296055467
H	-0.23744944922502	3.49087691940922	-1.50380276877669
H	-1.60795460661022	5.24639484749487	-1.13190711611838
H	-1.81008423125574	5.43179873603941	-2.90359787067337

References

1. Massie, A. A.; Denler, M. C.; Cardoso, L. T.; Walker, A. N.; Hossain, M. K.; Day, V. W.; Nordlander, E.; Jackson, T. A., Equatorial Ligand Perturbations Influence the Reactivity of Manganese(IV)-Oxo Complexes. *Angew. Chem., Int. Ed. Engl.* **2017,** *56* (15), 4178-4182.
2. Leto, D. F.; Ingram, R.; Day, V. W.; Jackson, T. A., Spectroscopic properties and reactivity of a mononuclear oxomanganese(iv) complex. *Chem. Commun.* **2013,** *49* (47), 5378-5380.
3. Rana, S.; Dey, A.; Maiti, D., Mechanistic elucidation of C–H oxidation by electron rich non-heme iron(iv)-oxo at room temperature. *Chemical Communications* **2015,** *51* (77), 14469-14472.
4. Kaizer, J.; Klinker, E. J.; Oh, N. Y.; Rohde, J.-U.; Song, W. J.; Stubna, A.; Kim, J.; Münck, E.; Nam, W.; Que Jr., L., Nonheme FeIVO Complexes That Can Oxidize the C−H Bonds of Cyclohexane at Room Temperature. *J. Am. Chem. Soc* **2004,** *126* (2), 472-473.
5. Mitra, M.; Nimir, H.; Demeshko, S.; Bhat, S. S.; Malinkin, S. O.; Haukka, M.; Lloret-Fillol, J.; Lisensky, G. C.; Meyer, F.; Shteinman, A. A.; Browne, W. R.; Hrovat, D. A.; Richmond, M. G.; Costas, M.; Nordlander, E., Nonheme Fe(IV) Oxo Complexes of Two New Pentadentate Ligands and Their Hydrogen-Atom and Oxygen-Atom Transfer Reactions. *Inorg. Chem.* **2015,** *54* (15), 7152-7164.